

THERMOPLASTIC COMPOSITE WIND TURBINE BLADES

AN INTEGRATED DESIGN APPROACH

Proefschrift

ter verkrijging van de graad van doctor
aan de Technische Universiteit Delft,
op gezag van de Rector Magnificus prof.ir. K.C.A.M. Luyben,
voorzitter van het College voor Promoties,
in het openbaar te verdedigen op dinsdag 13 juli 2010 om 10:00 uur

door

Simon JONCAS

Master in mechanical engineering,
Université du Québec, Canada
geboren te Montréal, Québec, Canada.

Dit proefschrift is goedgekeurd door de promotoren:

Prof.dr.ir. G.A.M. van Kuik

Copromotor:

Dr.ir. H.E.N. Bersee

Samenstelling promotiecommissie:

Rector Magnificus, voorzitter

Prof.dr.ir. G.A.M. van Kuik, Technische Universiteit Delft, promotor

Dr.ir. H.E.N. Bersee, Technische Universiteit Delft, toegevoegd promotor

Prof.ir. A. Beukers, Technische Universiteit Delft

Prof.dr.ir. M.J.L. van Tooren, Technische Universiteit Delft

Prof.dr. H. Champlaud, École de Technologie Supérieure, Montréal, Canada

Dr.ir. O.K. Bergsma, Technische Universiteit Delft

Ir. P. A. Joosse, Composite Technology Centre, Hengelo, Nederland

Copyright © 2010: S. Joncas

All rights reserved

No part of the material protected by this copyright notice may be reproduced or utilized in any form or by any means, electronic or mechanical, including photocopying, recording or by any information storage retrieval system, without permission from the author.

ISBN: 978-2-921145-73-2
École de technologie supérieure

Cover design: S. Joncas and A. Michaud

Photography: D.P.N. Vlasveld, Karine Thiblaut-Libiron and S.Joncas

Printed at Ipskamp Drukkers, The Netherlands

À Estelle et Félix

SUMMARY

Technology advancements over the past three decades have helped wind turbines mature dramatically in efficiency and reliability. Driven by the fact that cost per kW generated generally decreases as the rated power of a wind turbine increases, their rated power has also increased dramatically over this period. With power being proportional to rotor swept area, blades have increased in length by a factor of 10 from the 1980s to now. With some blades currently measuring more than 60 meters in length, wind turbine blade designers and manufacturers face problems due to weight and length that were never encountered when building smaller blades. Moreover, in view of the very large amount of blade material to be recycled in the near future and the legislation that is already affecting other industries concerning composite waste management, it seems likely that recyclability will soon become a key design requirement for large wind turbine blades.

In this context, this thesis proposes a new structural design concept for future large wind turbine blades using fully recyclable thermoplastic composites (TPC). Based on material properties, cost and processing, reactively processed anionic polyamide-6 (APA-6) has been identified as the most promising thermoplastic polymer system for these future wind turbine blades. After mechanically characterizing *in situ* polymerized APA-6/glass composites and assessing their recyclability, TPC oriented blade designs were developed following an integrated finite-element approach based on topology and size optimization techniques. The main contributions to large thermoplastic wind turbine blade design presented in this thesis are summarized below:

APA-6 composite material and processing: Because of the very low viscosity of the anionic polyamide-6 resin system (10 mPa·s, i.e. 35 times lower than epoxy) fiber wettability is excellent and infusion times are very short. Processing temperatures of 170-180°C are higher than what is usually used for thermosetting infusion resin systems (cure and/or post-cure) but standard high-temperature epoxy tooling could still be used up to these temperatures. A slight increase in tooling cost is to be expected due to the possible reduced life of the molds (aggressive thermal cycling) and the more expensive heating system to be used. However this increase in cost is expected to be compensated by a faster cycle time (faster infusion and polymerization) and significantly lower cost of the resin (20% cheaper than epoxy).

Under dry conditions, the APA-6 0°/90° composites tested in static tension, compression and shear surpassed its epoxy-based counterpart in strength and stiffness. On the other hand, fatigue performance in tension-tension was found to be significantly less for APA-6 composites. Under moist conditions, mechanical properties of APA-6 composites were reduced due to matrix swelling and fiber/matrix interface degradation. Ongoing research to improve the manufacturing process and fiber/matrix interface is expected to improve the fatigue properties of the composite significantly, which is essential for fatigue-driven components such as wind turbine blades.

APA-6/glass long-fiber composites were mechanically recycled into APA-6 short-fiber reinforced composites by regrinding and injection molding. Tensile tests showed that the strength and modulus of the recycled material could be up to 10% higher than those of commercial short-fiber glass-reinforced polyamide-6 resins at equivalent fiber weight content. From these encouraging results, given a big enough market to absorb end-of-life materials, the development of recyclable wind turbine blades could diminish the

uncertainties and environmental impact related to the dismantling and recovery of composite waste in the wind energy sector.

Design loads: Based on a generic 75m-long blade geometry and associated main physical and structural characteristics, different design load cases were studied according to the IEC-61400-1 standard. Four critical load cases were identified. Two of these arise from power production design situations while the other two are related to parked design situations. It is important to note that although the root bending moments produced by these four load cases can be considered similar, they are actually very different from each other because the aerodynamic load comes mostly from the outer part of the blade in power production load cases but from the inner part of the blade in parked situations. This creates very different bending moment and shear force distributions over the blade length. Because these load cases are very different in nature, they will not affect specific chord stations in the same manner. For this reason, all load cases were conserved during the design process in order to be sure that the structure would perform well under all loading conditions.

Structural design: The most natural load path to sustain the different load cases was identified with a finite-element-based (FE) structural topology optimization technique. A structure characterized by heavily reinforced spar caps (upper and lower surface) extending from approximately 15% to 50% of the chord length was identified. These spar caps were joined using either a single shear web (close to blade tip) or double shear webs (close to blade root). Topology-optimized blade structures also showed the distinctive presence of ribs in the trailing edge section (1 to 2m pitch between ribs). Composite sizing optimization (thickness and fiber orientation) was performed on a shell element model built based on the results of topology optimization. Capable of modeling blades with rib spacings of one or two meters equipped with a single or a double shear web, this customisable shell FE model helped explore different design configurations with respect to stress, stiffness and buckling stability. Based on dry-condition mechanical properties, results showed that PA-6-based composite blades could be of very similar weight to epoxy-based blades for identical structural designs ($\pm 1\%$). The PA-6-based blade structure using two webs and a rib spacing of two meters (35 ribs) was found to be the best design. With this new design, compared to today's classic epoxy-based blade design, mass could be reduced by 3% for identical structural performance. Furthermore, due to the presence of ribs, aerodynamic profile and web distortion was significantly reduced when compared to classic wind turbine blade designs.

SAMENVATTING

In de afgelopen drie decennia hebben technologische verbeteringen een indrukwekkende bijdrage geleverd aan de efficiëntie en betrouwbaarheid van windturbines. Gedurende deze periode, werd ook een toename van het nominale vermogen waargenomen, welke de prijs per opgewekt kW over het algemeen deed afnemen. Doordat het vermogen evenredig is met het omschreven oppervlak van de rotor, zijn de huidige windturbinebladen in vergelijking met de jaren 80 een factor 10 langer geworden. Sommige van deze bladen overschrijden zelfs een lengte van 60 meter. Hierdoor ondervinden ontwerpers en fabrikanten problemen betreffende gewicht en lengte die nog niet aanwezig waren bij de bouw van kleinere windturbinebladen. Een bijkomend aspect is het feit dat er in de toekomst grote hoeveelheden bladmateriaal gerecycleerd dienen te worden. Dit in combinatie met de wetgeving die inmiddels al andere industrieën een afvalbeleid voor composieten oplegt, lijkt het waarschijnlijk dat de recycleerbaarheid een belangrijke ontwerpeis zal zijn voor toekomstige grote windturbinebladen.

Vandaar dat in dit proefschrift een nieuw constructief ontwerp wordt voorgesteld voor toekomstige grote windturbinebladen op basis van volledig recycleerbare thermoplastische composieten (TPC). De keuze van het materiaal werd gemaakt op basis van materiaaleigenschappen, materiaalkosten en materiaalverwerking. Hiervoor werd reactieve, anionische polyamide-6 (APA-6) geïdentificeerd als meest veelbelovende thermoplastisch harssysteem voor grote windturbinebladen. Eerst werden de *in situ* gepolymeriseerde APA-6/glas composieten mechanisch gekarakteriseerd, waarna hun recycleerbaarheid werd vastgesteld. Uiteindelijk werden bladontwerpen op basis van TPC ontwikkeld met behulp van een geïntegreerde eindige elementen (FE) methode. Hierbij werden de topologie en de afmetingen van het windturbineblad geoptimaliseerd. De belangrijkste bijdragen met betrekking tot het ontwerp van grote thermoplastische windturbinebladen die in dit proefschrift gepresenteerd worden zijn hieronder samengevat:

APA-6 composietmateriaal en verwerking: Vanwege de heel lage viscositeit van het anionische polyamide-6 harssysteem (10MPa.s, 35 keer lager dan epoxy), is de benatting van de vezel uitstekend en de infusietijd kort. De verwerkingstemperaturen van 170-180 °C zijn hoger dan wat normaal gebruikelijk is voor thermohardende harssystemen (cure en/of post-cure). Echter, bij deze temperaturen kan nog steeds de standaard tooling voor hoge temperatuur epoxy gebruikt worden. Er wordt wel een lichte stijging van de tooling kosten verwacht doordat de hogere verwerkingstemperaturen en de hierbij gepaard gaande thermische cycli, respectievelijk een duurder verwarmingssysteem en een mogelijk verminderde levensduur tot gevolg kunnen hebben. Naar verwachting zal deze stijging echter worden gecompenseerd door de snellere doorlooptijd (snellere infusie en polymerisatie) en de substantieel lagere kostprijs van de hars (20% goedkoper dan epoxy).

Vergeleken met epoxy composieten, vertonen de APA-6 0°/90° composieten een hogere sterkte en stijfheid in statische trek, compressie en afschuiving uitgevoerd in droge omstandigheden. De sterkte van de APA-6 composieten bleek echter bij de op trek belaste vermoeiingstesten aanzienlijk minder te zijn. Onder vochtige omstandigheden

namen de mechanische eigenschappen van de APA-6 composieten af als gevolg van swelling van de matrix en degradatie van de vezel-matrix hechting. Lopend onderzoek naar verbetering van het productieproces en de vezel-matrix hechting zal naar verwachting de vermoeiingssterkte aanzienlijk verbeteren, wat essentieel is voor windturbinebladen, die vooral op vermoeiing belast worden.

In de studie naar het recycleren, werden de lange glasvezelversterkte APA-6 composieten vernalen en spuitgegoten tot korte glasvezelversterkte APA-6 composieten. Trekproeven hebben aangetoond dat de sterkte en stijfheid van het gerecycleerde materiaal tot 10% hoger kan zijn dan de commerciële korte glasvezelversterkte PA-6 composieten met vergelijkbaar vezelvolumegehalte. Zowel deze bemoedigende resultaten als het feit dat de markt omvangrijk genoeg is voor de verwerking van end-of-life materialen, zorgen ervoor dat de ontwikkeling van recycleerbare windturbinebladen een antwoord kan geven op de onzekerheden en de milieu-impact van de ontmanteling en de herwinning van composiet afval in de windenergie sector.

Ontwerp belastingen: Aan de hand van de geometrie van een generiek 75m lang blad en zijn bijbehorende belangrijkste fysische en structurele eigenschappen, werden in overeenstemming met de IEC-norm 61400-1, verschillende ontwerpbelastingen bestudeerd. Hierbij werden vier kritische belastingen geïdentificeerd. Twee van deze belastingen komen voort uit de dynamische toestand tijdens energieproductie van de windturbine terwijl de andere twee kritieke belastingen optreden in statische, stilstaande toestand. Hoewel de buigende momenten in de wortel van het blad in alle vier de belastingen als gelijkaardig kunnen worden beschouwd, is het belangrijk te vermelden dat de belastingen toch heel verschillend van elkaar zijn. Voor de belastingen bij het opwekken van elektriciteit, komt het grootste deel van de aërodynamische belasting uit het buitenste gedeelte van het blad, terwijl dit in stilstaande situaties uit het binnenste gedeelte van het blad komt. Dit leidt tot een groot verschil in de verdeling van het buigend moment en de dwarskracht over de bladlengte. Omdat deze belastingen en de verdelingen over het blad zo verschillend zijn, zullen zij de specifieke koorde secties van het blad ook niet op eenzelfde manier beïnvloeden. Om die reden werden alle belastingsgevallen tijdens het ontwerpproces behouden, om ervan verzekerd te zijn dat de constructie alle ontwerpbelastingen kan dragen.

Constructief ontwerp: Door middel van een FE-gebaseerde techniek om de structurele topologie te optimaliseren, werd het meest natuurlijke belastingspad geïdentificeerd om de verschillende belastingen te dragen. Uit deze analyse, werd een constructie gevonden die gekenmerkt wordt door sterk verstevigde flenzen van de ligger, zowel aan de boven- als onderkant, die zich tussen 15% tot 50% van de lengte van de koorde bevinden. Deze flenzen werden met elkaar verbonden door middel van ofwel een enkele ligger (dichtbij de tip van het blad) ofwel een dubbele ligger (dichtbij de wortel van het blad). Ook werden bij deze door topologie geoptimaliseerde bladen duidelijk ribben onderscheiden aan de achterrand van het profiel (met een afstand van 1 tot 2m tussen de ribben).

Gebaseerd op de resultaten van de structurele topologie optimalisatie, werd een FE-model opgebouwd aan de hand van schaalelementen voor de optimalisatie van de composiet constructie (dikte en vezeloriëntatie). Dit aanpasbare schaalelementen model bleek geschikt voor het modelleren van bladen bestaande uit een enkele of een dubbele ligger en ribben met afstand van 1 of 2 meter. Het model hielp bij het bestuderen van verschillende ontwerpconfiguraties waarbij gekeken werd naar spanningen, stijfheid en

knikstabiliteit. Wanneer gebruik gemaakt wordt van de mechanische eigenschappen in droge omstandigheden, tonen de resultaten aan dat bladen bestaande uit epoxy of PA-6 een vergelijkbaar gewicht opleveren ($\pm 1\%$) voor een identiek structureel ontwerp. De constructie van het PA-6-gebaseerde blad met 2 liggers en een ribafstand van 2 meter (35 ribben) werd vastgesteld als het beste ontwerp. Dit nieuw ontwerp heeft een gewichtsreductie van 3% tot gevolg vergeleken met de huidige epoxy-gebaseerde bladontwerpen terwijl de structurele eigenschappen behouden werden. Ook wordt door de aanwezigheid van de ribben, de verstoring van het aërodynamische profiel en de liggers aanzienlijk verminderd in vergelijking met de huidige windturbinebladen ontwerpen.

Contents

SUMMARY	i
SAMENVATTING	iii
CHAPTER 1	1
THERMOPLASTIC COMPOSITE WIND TURBINE BLADES	
<i>GENERAL INTRODUCTION</i>	
1.1 THE WORLD'S HUNGER FOR ENERGY	1
1.2 TRENDS IN UTILITY-SCALE WIND TURBINES	3
1.3 THE HOLY TRINITY OF DESIGN	5
1.4 STRATEGY FOR UP-SCALING BLADES	6
1.5 S-CURVE JUMP AHEAD?	9
1.6 RESEARCH GOALS	12
1.7 THERMOPLASTIC COMPOSITE WIND TURBINE TECHNOLOGY PACKAGE	13
1.8 THESIS PLAN	14
1.9 REFERENCES	16
CHAPTER 2	19
BLADE MATERIAL AND STRUCTURAL DESIGN	
<i>AN HISTORICAL OVERVIEW</i>	
2.1 WINDMILLS USED FOR MECHANICAL WORK	19
2.1.1 Vertical axis machines	19
2.1.2 Horizontal Horizontal axis machines	20
2.1.2.1 European windmills	20
2.1.2.2 Blade concepts on ancient windmills	22
2.1.2.3 American windmills	23
2.2 PIONEERING WORK IN WIND-POWERED GENERATION OF ELECTRICITY	24
2.3 POST WORLD WAR II ACHIEVEMENTS	26
2.4 LARGE WIND TURBINE FEDERAL R&D PROGRAMS - 1970-1990	31
2.4.1 Technology development and subcontractors	31
2.5 LARGE WIND TURBINE BLADE STRUCTURAL DESIGN – 1970-1990	33
2.5.1 Aluminum and steel blades	33
2.5.2 Wood and laminated wood blades	39
2.5.3 Fiber reinforced composite blades	42
2.5.3.1 Filament or tape winding concepts	42
2.5.3.2 Structural skin concepts	48
2.5.3.3 Bladder approach	49
2.6 SMALL AND MEDIUM SIZE WIND TURBINE BLADE DEVELOPMENT	50
2.6.1 Small monolithic skin blades	51
2.6.2 I-Shaped web blades	52
2.6.3 Box-spar blades	53
2.7 MODERN LARGE WIND TURBINE BLADE DESIGN	54
2.8 CONCLUSIONS	55
2.8.1 Material issues	55

2.8.2	Structural and manufacturing issues	56
2.8.2.1	Steel designs	57
2.8.2.2	Composite designs	57
2.9	REFERENCES	60
CHAPTER 3		63
THERMOPLASTIC COMPOSITE MATERIALS AND MANUFACTURING PROCESSES		
<i>POTENTIAL BENEFITS FOR BLADES</i>		
3.1	INTRODUCTION	63
3.2	THERMOPLASTIC COMPOSITE RAW MATERIALS	66
3.2.1	Impregnation techniques	68
3.2.2	Consolidated laminates	69
3.2.3	Pre-impregnated materials	69
3.2.4	Core materials	69
3.2.5	Reactive molding resin systems	70
3.3	MANUFACTURING PROCESSES FOR THERMOPLASTIC COMPOSITES	70
3.3.1	Press-forming processes	71
3.3.1.1	Elastomeric tool forming	71
3.3.1.2	Hydroforming	73
3.3.1.3	Matched-metal die forming	73
3.3.2	Vacuum-forming processes	74
3.3.2.1	Atmospheric or autoclave processing	74
3.3.2.2	Diaphragm forming	75
3.3.2.3	Bladder inflation forming	76
3.3.3	Automated fiber placement processes	77
3.3.4	In-situ polymerization processes	79
3.3.4.1	Resin transfert molding	79
3.3.4.2	Vacuum infusion	80
3.3.4.3	Pultrusion	81
3.3.5	Joining techniques	81
3.4	THERMOPLASTIC COMPOSITE WIND TURBINE BLADES	82
3.4.1	Physical and mechanical property issues	82
3.4.2	Sustainability issues	83
3.4.3	Manufacturing issues	85
3.4.4	Demonstrator projects	86
3.5	CONCLUSIONS	87
3.6	REFERENCES	89
CHAPTER 4		93
ANIONIC POLYAMIDE-6 COMPOSITES FOR WIND TURBINE BLADES		
<i>MATERIAL PROPERTIES</i>		
4.1	INTRODUCTION	93
4.2	EXPERIMENTAL PROCEDURES	94
4.2.1	Laminate description	95
4.2.2	Processing of epoxy and HPA-6 composite plates	95

4.2.3	Processing of Anionic Polyamide-6 composites	95
4.2.3.1	Ring-opening polymerization	96
4.2.4	Physical property measurements	97
4.2.4.1	Moisture absorption	97
4.2.4.2	Material constituents	97
4.2.4.3	Degree of conversion	99
4.2.4.4	Cristallinity	99
4.2.5	Mechanical property measurements	100
4.2.5.1	Tensile, compressive and shear properties	100
4.2.5.2	Inter-laminar shear strength properties	100
4.3	RESIN FORMULATION AND FIBER SURFACE TREATMENT	100
4.3.1	Fiber volume fraction and void content	101
4.3.2	Degree of conversion	102
4.3.3	Moisture uptake	104
4.3.4	Interlaminar shear strength	106
4.3.5	Discussion	107
4.4	BENCHMARKING ANIONIC POLYAMIDE-6	108
4.4.1	Basic laminate properties	109
4.4.2	Static properties	110
4.4.2.1	Dry-as-molded	110
4.4.2.2	Moisture-conditioned	110
4.4.2.3	Discussion	111
4.4.3	Fatigue properties	113
4.4.3.1	Fatigue mechanisms	113
4.4.3.2	The effect of void content	114
4.4.3.3	Results and discussion	115
4.5	DEVELOPMENT OF A RECYCLING STRATEGY	117
4.5.1	Methodology	117
4.5.2	Material processing	118
4.5.2.1	Grinding of laminates	118
4.5.2.2	Dilution resins	119
4.5.2.3	Injection Molding	119
4.5.3	Mechanical properties	120
4.5.4	SEM micrographs of fractured surfaces	122
4.5.5	Discussion	123
4.6	CONCLUSIONS	124
4.7	REFERENCES	127
CHAPTER 5		129
AERODYNAMIC AND STRUCTURAL DESIGN AND ANALYSIS TOOLS		
5.1	INTRODUCTION	129
5.2	AERODYNAMIC DESIGN AND ANALYSIS: THEORY	131
5.2.1	Blade Element Theory	132
5.2.2	Momentum Theory	133
5.2.3	Blade element momentum theory	135
5.2.4	Tip and root loss factors	136
5.2.5	Turbulent wake state	137

5.3	DESIGN AND ANALYSIS TOOL: ITERATION PROCEDURE	138
5.3.1	Algorithm	139
5.3.2	Airfoil characteristics	140
5.4	STRUCTURAL DESIGN AND ANALYSIS TOOLS	141
5.4.1	Stress Analysis	141
5.4.2	Weighted area moment of inertia	143
5.4.3	Tip Deflection Analysis	144
5.4.4	Natural Frequency Analysis	146
5.5	REFERENCES	150
CHAPTER 6		151
GENERIC BLADE MODEL AND DESIGN LOADS		
6.1	INTRODUCTION	151
6.2	GENERIC BLADE DESIGN	152
6.2.1	Blade geometry	152
6.2.2	Rotor performance	154
6.2.3	Blade mass, mass moment of inertia and natural frequency	155
6.2.3.1	Estimated blade stiffness and natural frequency	155
6.3	DESIGN LOADS	159
6.3.1	IEC-61400-1 design situations	160
6.3.2	Power production design situation load cases	161
6.3.2.1	In-plane and out-of-plane bending moments	162
6.3.3	Parked design situations	162
6.4	LOAD CASES FOR THE OPTIMIZATION PROBLEMS	163
6.5	CONCLUSIONS	164
6.6	REFERENCES	168
CHAPTER 7		169
PRELIMINARY DESIGN OF LARGE THERMOPLASTIC COMPOSITE WIND TURBINE BLADES		
<i>A TOPOLOGY OPTIMIZATION APPROACH</i>		
7.1	INTRODUCTION	169
7.2	METHODOLOGY	170
7.2.1	Finite-element-based structural optimization tools	170
7.2.2	Topology optimization method	172
7.2.3	Problem formulation	173
7.2.4	Preliminary design development strategy	174
7.3	STEP 1: TOPOLOGY OPTIMIZATION OF A BLADE SECTION	176
7.3.1	Finite element model	176
7.3.2	Model loading	178
7.3.3	Optimization variables, objective function and constraints	180
7.3.4	Results	180
7.3.4.1	Edgewise individual load case solutions	180
7.3.4.2	Flapwise individual load case solutions	181
7.3.4.3	Multiple Load Case Solutions	182
7.3.5	Discussion	184

7.4	STEP 2: TOPOLOGY OPTIMIZATION USING A HALF-BLADE MODEL	185
7.4.1	Finite element model	185
7.4.2	Model Loading	186
7.4.3	Optimization variables, objective function and constraints	187
7.4.4	Results	187
7.5	CONCLUSIONS	189
7.5.1	Spar cap and webs	190
7.5.2	Presence of ribs	190
7.6	REFERENCES	191
CHAPTER 8		193
PRELIMINARY DESIGN OF LARGE THERMOPLASTIC COMPOSITE WIND TURBINE BLADES		
<i>STRUCTURAL ELEMENT SIZING OPTIMIZATION</i>		
8.1	INTRODUCTION	193
8.2	BLADE MODEL AND FORMULATION OF THE OPTIMIZATION PROBLEM	194
8.2.1	Generic shell element model	194
8.2.2	Model loading and material property description	195
8.2.3	Design variables, objective function and constraints	196
8.3	BASELINE EPOXY/GLASS WIND TURBINE BLADES	198
8.3.1	Material properties	199
8.3.2	Design solutions based on stiffness and strength	199
8.3.3	Design solutions based on stiffness, strength and buckling	201
8.4	POLYAMIDE-6/GLASS COMPOSITES WIND TURBINE BLADES	204
8.4.1	Material properties	204
8.4.2	Design solutions based on stiffness and strength	205
8.4.3	Design solutions based on stiffness, strength and buckling	208
8.5	DISCUSSIONS AND CONCLUSIONS	212
8.5.1	Preferred topology for TPC wind turbine blades	212
8.5.2	The presence of ribs in wind turbine blade structures	213
8.5.3	General considerations	214
8.6	REFERENCES	217
CHAPTER 9		219
CONCLUSIONS AND RECOMMENDATIONS		
9.1	MAIN CONCLUSIONS ON MATERIALS AND MANUFACTURING	219
9.1.1	Manufacturing issues	219
9.1.2	APA-6 composite mechanical properties	220
9.1.3	Material recycling	221
9.2	MAIN CONCLUSIONS REGARDING STRUCTURAL DESIGN	221
9.2.1	Box-spar configuration	221
9.2.2	Rib reinforced aerodynamic surfaces	222
9.2.3	Proposed designs	222
9.3	RESEARCH OBJECTIVE ASSESSMENT	223
9.3.1	Identifying a potential thermoplastic resin system	223
9.3.2	Benchmarking PA-6/glass against epoxy/glass composites	224

9.3.3	Proposal of an integrated TPC large wind turbine blade design	225
9.3.4	Benchmarking TPC blades against a classic blade design	226
9.4	POTENTIAL BENEFITS FOR THE WIND ENERGY INDUSTRY	227
9.4.1	Potential blade cost reduction	227
9.4.2	Blade recycling and the fear of legislation	228
9.4.3	TPC structural design benefits	229
9.5	RECOMMENDATIONS FOR FUTURE WORK	229
9.5.1	Manufacturing issues	229
9.5.2	Material issues	230
9.5.3	Structural design issues	230
9.5.4	Cost analysis	231
9.6	REFERENCES	232
APPENDIX A		233
APPENDIX B		237
APPENDIX C		241
ACKNOWLEDGEMENTS		247
ABOUT THE AUTHOR		249
LIST OF PUBLICATIONS		251
NOMENCLATURE		253

CHAPTER 1

THERMOPLASTIC COMPOSITE WIND TURBINE BLADES *GENERAL INTRODUCTION*

A scientist studies what is, whereas an engineer creates what never was.
- Theodore von Karman

The aim of this introductory chapter is to position the work presented in this dissertation within the current context of wind energy. Recent trends in wind energy and their effects on blade structures will be summarized and an overview of future challenges facing wind turbine blade design and manufacturing will be presented. Finally the motivation for this work will be exposed and a brief outline of the following chapters will be given.

1.1 The world's hunger for energy

Today's world population of 6 billion is growing fast and is expected to soar to 9 billion by 2050 [1]. With growth observed mainly in developing countries that are expected to increase their energy consumption significantly as they modernize their infrastructures, world demand for energy is expected to increase by more than 50% by 2030. Under current governmental policies, the International Energy Agency (IEA) predicts that fossil fuel will provide more than 80% of this energy demand, leading to CO₂ emissions growing even faster than our primary energy usage [2]. An alternative scenario was also evaluated by the IEA based on the assumption that countries would adopt today all of the new energy and CO₂ emission policies that they are currently considering. Figure 1.1 shows that even under this optimistic scenario, CO₂ emissions would still increase rapidly and that only significant technological breakthroughs in primary fields of conventional energy production methods could help keep our emissions at a stable level. This underscores the inevitable environmental crisis the

planet faces if the world's hunger for energy is not reduced significantly and if environmentally sound and renewable energy production methods are not fast-tracked.

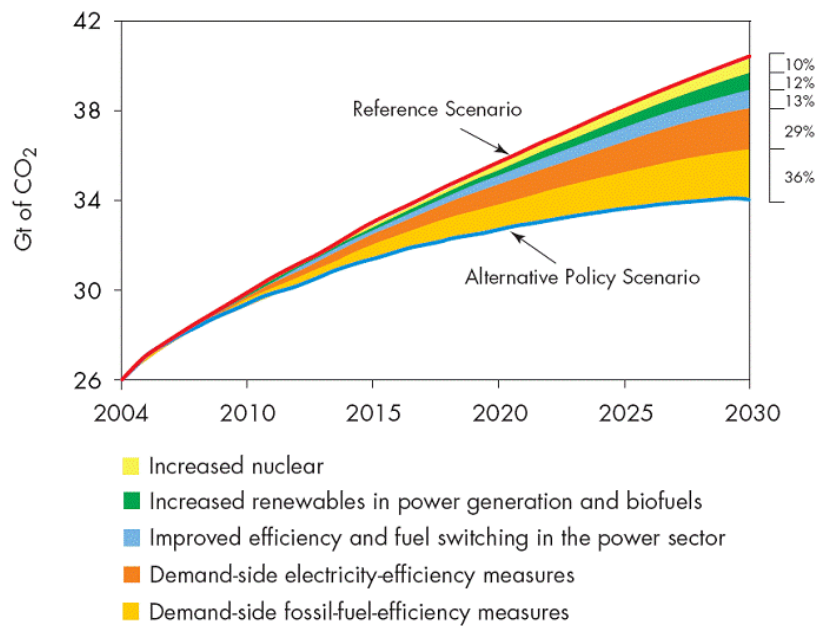


Figure 1.1: Global savings in CO₂ emissions. Alternative scenario versus reference scenario [2]

There is no doubt that governmental policies with respect to energy production must change in order to at least be able to preserve the current state of our ecosystems. In this context, it is clear that renewable energy sources such as wind energy will play a key role in our ability to respond to the increase in energy demand in an environmentally sound manner.

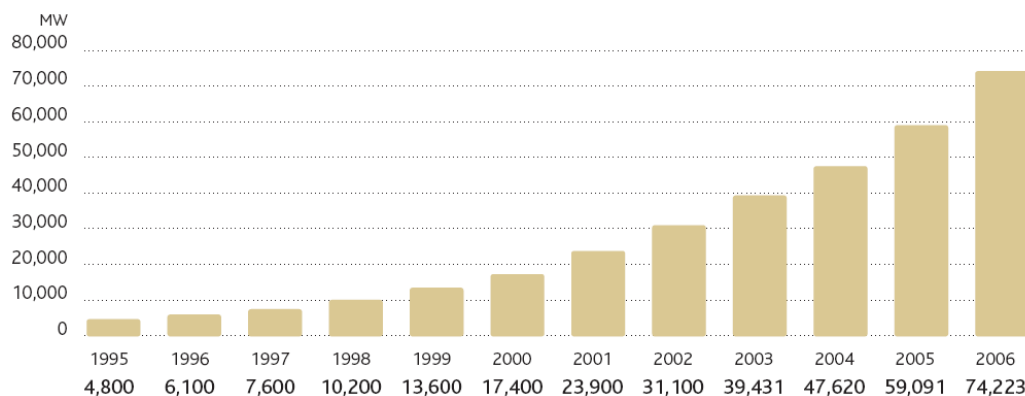


Figure 1.2: Global cumulative wind energy installed capacity 1995-2006 [3].

As depicted in Figure 1.2, the wind energy sector over the past ten years has seen an incredible increase in its total capacity installed. With a large portion of this growth owing to European energy policies, it is expected that with other countries taking similar initiatives, wind power capacity installed worldwide will reach close to 300GW by 2015 [3].

1.2 Trends in utility-scale wind turbines

Recent technology advancements have helped wind turbines mature dramatically in efficiency, reliability and power rating. As depicted in Figure 1.3, their average size has been increasing steadily over the past 25 years. Early development of grid-connected wind energy converter systems occurred in the seventies in reaction to the oil crisis. This so-called “wind rush” gave birth to the famous Californian wind farms equipped with thousands of small turbines with rated power output in the 50-100kW range. Since then, the power output of commercially sold wind turbines has increased by a factor of more than a fifty with state-of-the-art turbines now being able to generate above 5MW of nominal power output.

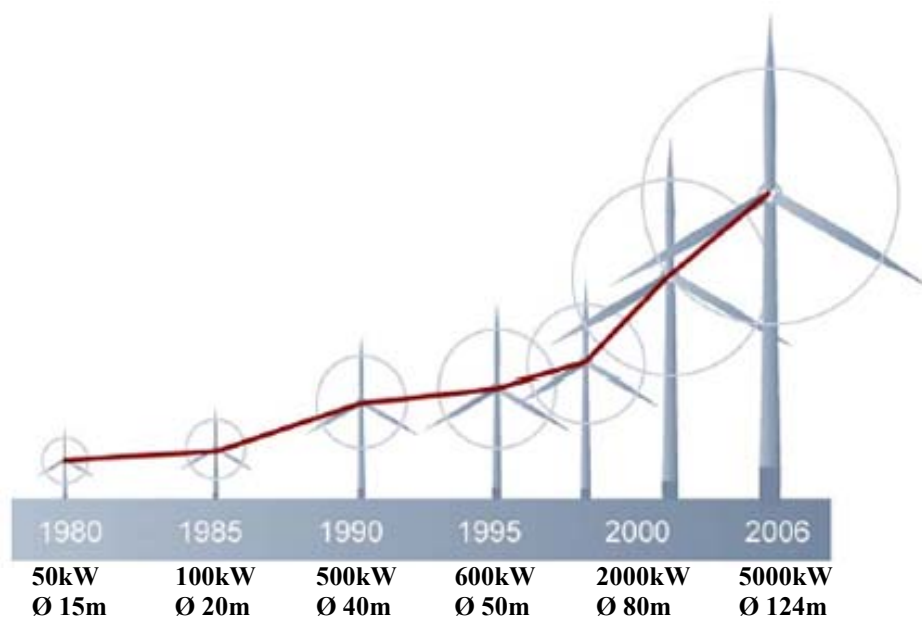


Figure 1.3: Wind turbine rated power output and rotor diameter at year of market introduction [3].

The industry’s desire to build such large machines is driven primarily by the fact that as the rated power of wind turbines increases, the cost per kW generated decreases. This increase in size combined with more carefully selected sites now makes wind

energy as affordable as conventional energy production methods (see Figure 1.4) [2]. In the next few years, with the now rising popularity of offshore wind farms, manufacturers will be tempted to build even larger machines simply to compensate for the higher individual unit installation, operation and maintenance cost of these wind turbines. With carefully planned commissioning and maintenance scenarios, the cost of energy of these new offshore wind farms is expected to become lower than onshore installations [4].

Since the power generated by wind turbines is in theory proportional to the rotor swept area, blades have also increased significantly in size over the years. Using a similar scaling rule, it can also be found that if the blade material and structural design concept are kept unchanged, weight should scale in theory to the cube of blade length. This increase in blade weight now gives an important role to gravity loads that were not a real concern for smaller blades but are now contributing to a complex loading spectrum influenced by aerodynamic loads and blade weight. With blades now reaching over 60 meters in length, wind turbine blade designers and manufacturers face problems due to weight and length never encountered when building smaller blades. These new problems coupled with the persistent challenge of producing low cost blades now make wind turbine blades very challenging composite parts to design and build.

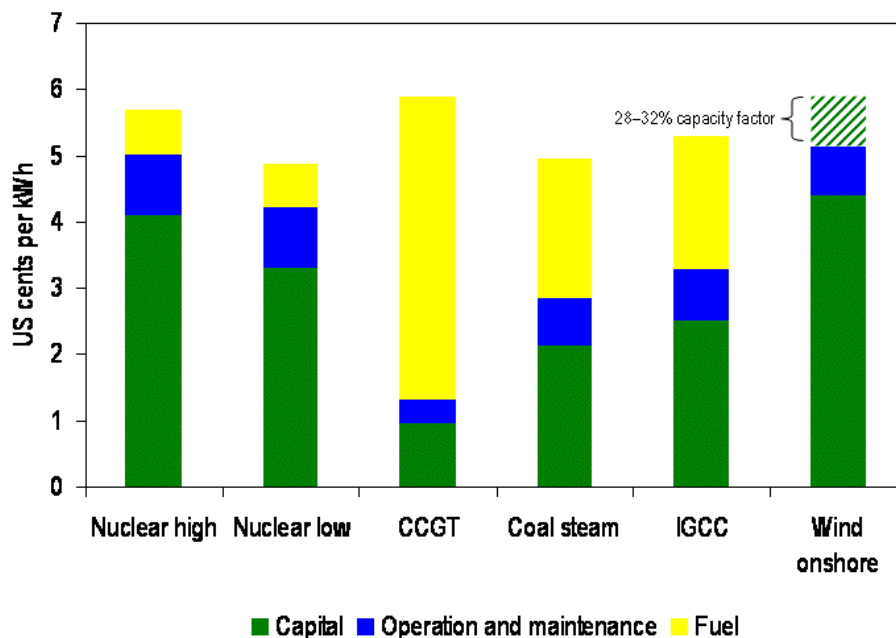


Figure 1.4: Electricity generating costs for different production methods. CCGT- Combined cycle gas turbine, IGCC-Integrated gasification combined cycle [2].

1.3 The Holy Trinity of design

All engineered products can be defined in terms of the materials from which they are made, the manufacturing technique with which they were processed and the structure (shape, topology, structural layout, etc...) on which they rely in order to bare their function. The strong interaction between these three fundamental aspects of engineered products can be visualized as a “Holy Trinity” of design in which material, structure and process each have their own distinctive nature, but form the engineered product when combined (see Figure 1.5) [5]. In the early steps of the design process, engineers are confronted with the fact that materials, processes and structures are “spiritually” united and must be treated collectively. Ultimately, the role of the engineer is to find the best structure for a specific function within the constraints imposed by the materials (cost, strength and stiffness limits, etc.) and processes (cost, size and shape limits, etc.) readily available at the time of design.

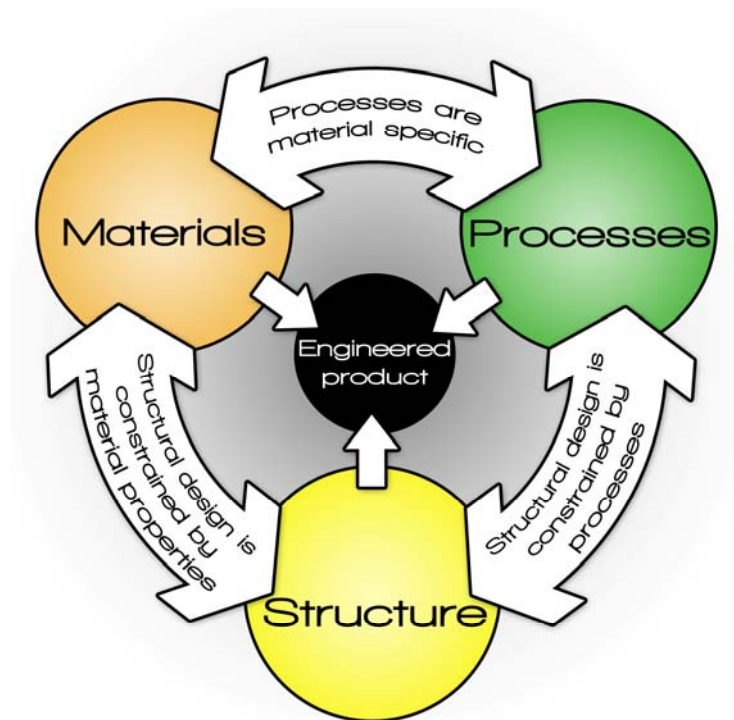


Figure 1.5: The “Holy Trinity” of design - Materials, processes and structural concepts strongly interact to form an engineered product.

When reengineering an existing product, designers can make changes to all three constituents of the trinity or simply concentrate on one or two. Unfortunately, manufacturing processes are often dedicated to specific material families (metals, plastics, wood, concrete, etc.), while structural concepts likewise are usually compatible

with only certain manufacturing processes. Therefore, when evaluating the financial risks of reengineering a product, the options are usually very limited. Significant changes to the structural design (shape) are rarely considered due to the strong causality effects that shape has on other elements of the trinity. Also, material upgrades are usually made within the same family of material to remain compatible with original manufacturing processes. The introduction of carbon-fiber composites in aircraft structures (black aluminum) is a perfect example of using a different material within the design trinity of a metal-based concept. Although carbon-fiber composite had to be processed differently than the aluminum parts, the change in material did not affect the structural design or the overall manufacturing strategy, therefore limiting the impact on the original design concept.

Slightly modifying one aspect of the trinity usually works well when the function of the product stays the same and improvements in cost or weight are desired. On the other hand, when significant changes are made to the function of the product (new loading, change in size, etc.), altering only one aspect of the trinity is often not enough. In this case, rethinking materials, processes and structural design as a group generally yields a more efficient design with respect to the new required function.

1.4 Strategy for up-scaling blades

While steel, aluminum and wood were used in early stages of wind energy development, fiber-reinforced polymer (FRP) composite is undoubtedly the most common material used today for blade structures. When up-scaling large composite parts such as wind turbine blades, designers were inevitably faced with the causality effects between material, design and process just discussed. Their goal in increasing the length of blades is to improve the design while minimizing costs and still ensure structural integrity. Over the years, the original concept of FRP composite blades was modified with the introduction of new manufacturing processes, new materials, and changes to the internal structural topology (see chapter 2 for more details on FRP composite blade design evolution).

Although the first FRP composite wind turbine rotor blade built can be traced back to 1959 (Ulrich Hutter's 17m W34 blades), widespread use of composite for blades truly began in the mid 1970s with the early development of small Danish commercial turbines. Hutter's pioneering effort inspired most of the designs seen in Denmark at that

period, which were generally based on monocoque-monolithic skin structures as illustrated in Figure 1.6. The only difference from Hutter's original design concept was that blades were often filled with polyurethane foam for better stability of the skins. At the end of the 1970s and early 1980s, in an effort to reduce tip deflection and further improve the stability of the skins, the single shear web concept appeared and the use of unidirectional fibers placed above and below this shear web became more and more common. Finally, the introduction of sandwich panels at the leading and trailing edge section contributed to establishing the basis of a design that would be considered the industry norm until the early 1990s. During the past 15 years, largely due to increasing gravity loads with length, one last significant change in structural topology occurred when a second shear web was introduced. This configuration helped concentrate the loads within a "box spar" included between the shear webs, therefore relieving the leading edge and trailing edge section from in-plane loads. Two main strategies are now favored by manufacturers to construct blades with this configuration. They either build the spar in a single step on a dedicated mandrel and later cover it with non-structural skins or use secondary bonding of the two skins and shear webs to form the blade structure.

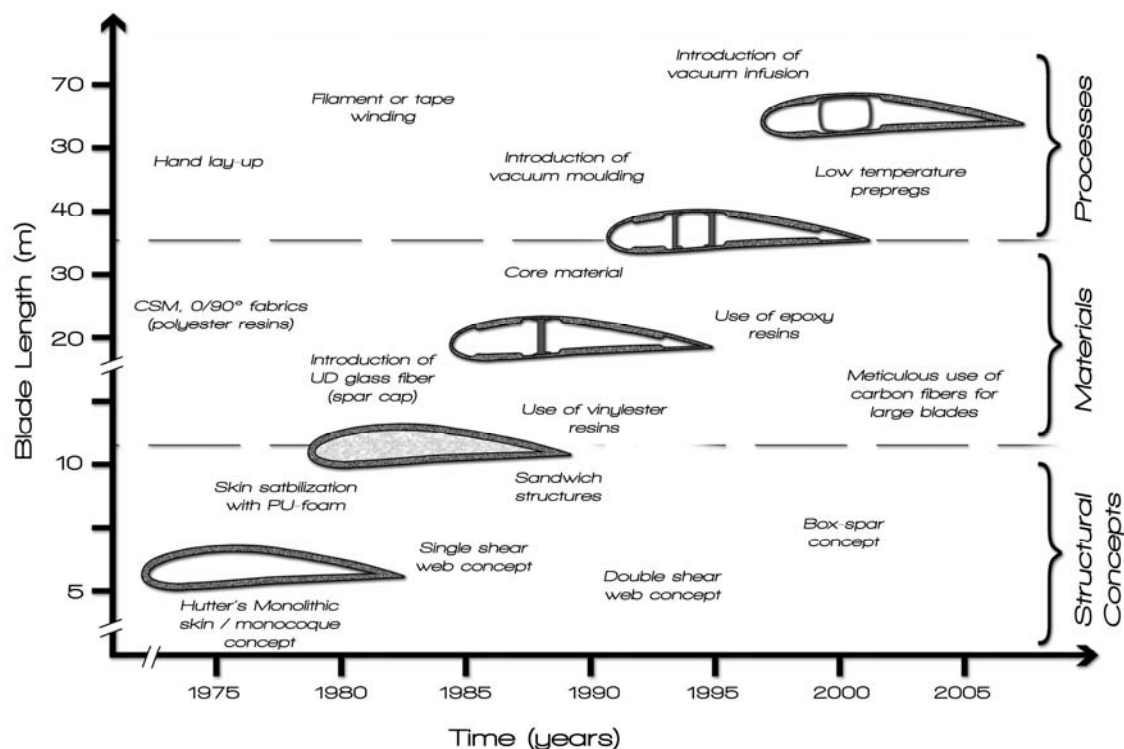


Figure 1.6: Evolution of structural design concepts, materials and processes for FRP composite wind turbine blades (1975-present).

In retrospect, the last 30 years of FRP composite wind turbine blade development have yielded three distinct structural concepts: the monolithic skin monocoque concept (Hutter's design), the single shear web design and the double shear web/box spar concept.

The past three decades also saw non-negligible improvements in manufacturing techniques as most manufacturers moved from the classic hand lay-up process to vacuum infusion methods or pre-pregging [5]. Measures were also taken to improve the design in terms of materials. New glass fabrics were introduced and meticulous use of carbon fibers for highly stressed areas is now common for large blades. Resin systems also evolved from basic polyester-based systems to vinylester and epoxy systems [6]. Finally, numerous improvements were also made to blade root details with manufacturers refining their design from first-generation heavy one-piece metallic flanges to lighter flange designs and bonded-in sleeves and stud connections.

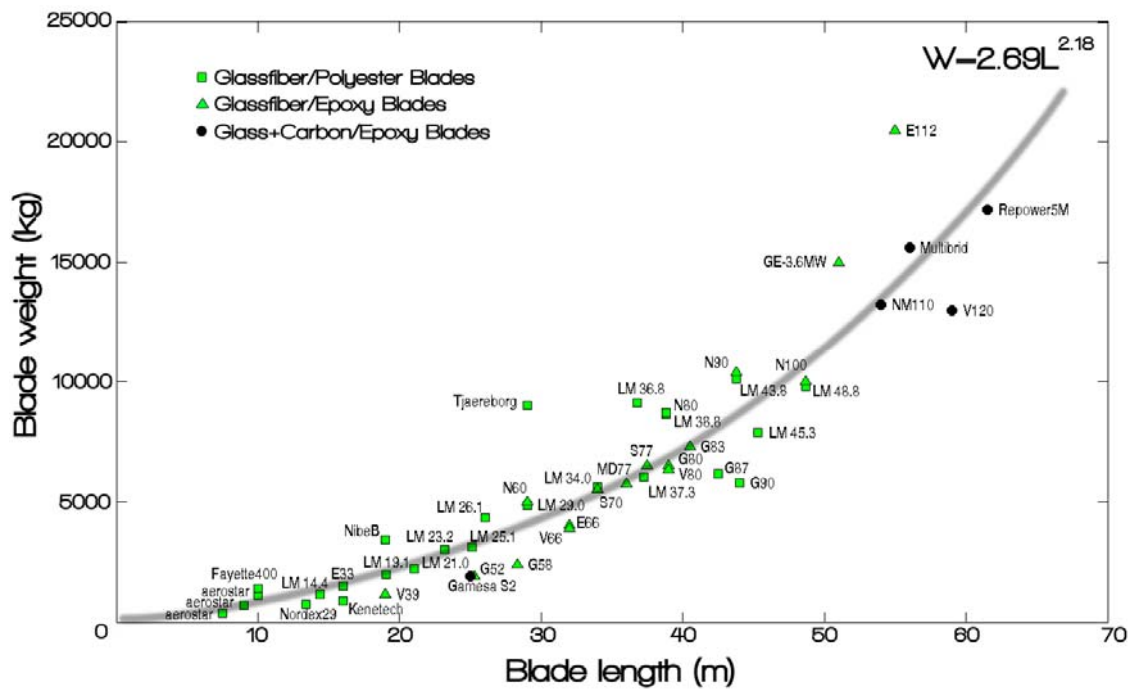


Figure 1.7: Evolution of FRP composite blade mass (kg) with respect to blade length (m).

As a result of these improvements, manufacturers have controlled FRP composite blade weight with respect to length remarkably well. As discussed earlier, if materials and structural concepts are kept unchanged during an up-scaling process, mass should evolve as a cubic function of blade length. Figure 1.7 shows on the contrary that due to

the above-mentioned improvement to the design, blade mass scaled closer to a square law over the years. It is interesting that decisions made during the aerodynamic design phase also had significant influence on blade weight since high tip speed ratio decreases blade loading. This effect is noticeable with large blades dedicated to offshore applications showing a particularly low weight for their lengths.

1.5 S-curve jump ahead?

Experts in the wind energy business believe that through the design improvements discussed above, manufacturers have already pushed currently used technology to its limits. Their conclusion suggests that current blade design has reached maturity and that without major design changes, no significant weight and cost reduction will be possible [7-11]. Basic principles of engineering design remind us that once such a level has been reached in product development, investments in technology often exceed the possible benefits to be gained as a result. It is usually just a matter of time until a new technology takes over and later on an even newer technology forces its way in. This concept is illustrated in Figure 1.8. The aeronautical industry is most certainly an interesting case to illustrate what can be considered one of the most important S-curve jumps in this early 21st century: aluminum stressed-skin design slowly being taken over by composite-material-oriented design.

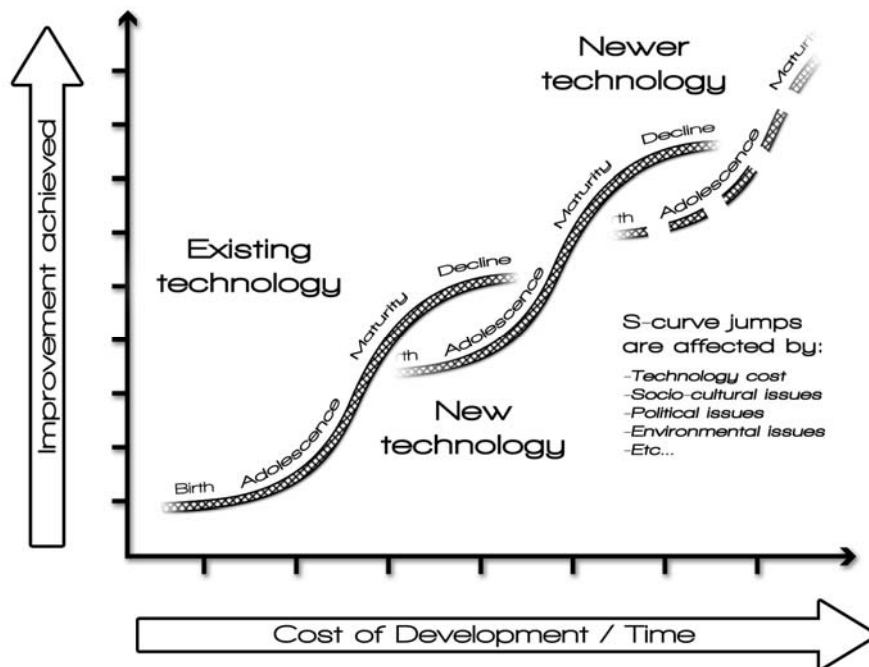


Figure 1.8: S-curves showing maturity levels and important factors capable of triggering S-curve jumps.

From a pure engineering perspective, technological S-curves should evolve solely with respect to technological advancements. In other words, as new and more efficient technologies are developed and made readily available, obsolete ones are simply replaced. In reality, technological rise and fall is intrinsically related to the perception that society has of both mature and emerging technology (see Figure 1.8). Obviously, cost is an important factor affecting industrial society, but more recently, political, environmental and socio-cultural issues have played an important role in the rise and fall of certain technologies. The impact that legislation, directives and regulations have had on the automotive industry is proof that non-technological issues like waste management and recycling can dramatically affect an industry and easily trigger S-curve jumps.

Directly related to the wind turbine blade manufacturing industry, the technological switch from hand lay-up to vacuum infusion techniques (VI) can be viewed as an interesting S-curve jump example influenced by both technological advancement and socio-political aspects. From a technical point of view, VI brought the possibility of building better quality composites, but because of the associated cost, it is doubtful that this S-curve jump would have ever occurred without governmental legislation on styrene and other volatile gas emissions.

As with manufacturing, it is possible that new materials for blades will be pushed up the S-curve slope due to social, environmental and political pressures. Major manufacturers have already engaged in life-cycle analysis (LCA) to demonstrate their commitment to sustainable development and prepare for imminent governmental legislation forcing them to take responsibility for their product from cradle to grave, as is the case in the automotive industry with the EU “end of life” directive. Vestas published in 2001, 2004 and 2006 their life cycle assessment of offshore and onshore wind power plants with the latest being based on V90-3MW machines [12]. An important conclusion to their study is that scrap blades are usually sent to landfill due to their unsuitability for recycling. Compared to the rest of the turbine (mostly steel), blades have the greatest environmental impact as “bulk waste” (26.1% of what is sent to landfill comes from blade waste). Similar conclusions were drawn at the 38th International Energy Agency Topical Expert meeting on material recycling and life cycle analysis of wind turbines in 2003, where blades were identified as problematic components to be managed from a LCA perspective [13].

It is likely that due to the impressive growth rate of the wind energy industry and limited blade life expectancy, recyclability will soon become a key design requirement for wind turbine blades. Indeed, the wind energy composite market has witnessed an impressive steady growth rate of 20% over the past couple of years and should surpass the aerospace market with 618,000 tons consumed per year compared to 515,000 tons by 2013 [14]. As a consequence of blade life being limited to 20 years, blade scrap tonnage should be in the same order of magnitude by 2025 and rise by 20% a year. Judging from these numbers, blade recycling should become a lucrative industry in less than two decades.

General common practice when dealing with waste management is to follow the routes enumerated below in order of decreasing desirability [15]:

- Simply use less material (prevention at source with better designs and more efficient manufacturing processes)
- Fully reuse of the product (breakdown the product into fully reusable materials)
- Mechanical recycling of the material
- Incineration:
 - With material and energy recovery
 - With energy recovery
 - Without energy recovery
- Landfill

Since resin systems used in the wind energy industry are exclusively thermoset, matrix recovery will never be possible. Thermosetting polymers are cross-linked and cannot be remolded in contrast with thermoplastics, which can be reprocessed. Two options are therefore possible for recycling blades today: Mechanical recycling (shredding) and reuse as filler for other materials, or incineration (with energy and fiber recovery in the best-case scenario). Mechanical recycling was demonstrated recently in a project funded by LM Glasfiber, in which shredded blades were used as filler for fiber reinforced concrete [16]. In a different project, Vestas showed the potential of incineration without material recovery. In this case, energy recovery was made possible since blade particles were incinerated in power stations but 20% of the blade material still had to be sent to landfill in the form of ash [17]. In view of the very large amount of blade material to be recycled in the near future and the legislation that is already

affecting other industries concerning waste management, it seems likely that an S-curve jump concerning wind turbine blade materials is imminent because of recycling issues.

1.6 Research goals

Designers of large wind turbine blades are preoccupied mostly with blade stiffness, weight, lifespan (fatigue life prediction), and of course cost.

Over the years, important contributions from blade manufacturers and researchers have helped to address some of these aspects. For example, numerous studies on blade scaling helped target the most important factors to be dealt with when up-scaling blades. Colossal work on material characterization has also helped better predict fatigue life. Finally, recent work on load mitigation and health monitoring techniques has also contributed to finding ways of extending or monitor blade life. Although some of these contributions are not material dependent, most of them are valid only for the thermoset-based composites used in current large wind turbine blade structures. The knowledge acquired therefore cannot be transferred directly to TPC-based blade designs. This leaves a large technological gap to be filled before TPC can be used for large wind turbine blade structures.

Although the recycling capabilities of TPC are certainly appealing to wind turbine blade designers, insufficient knowledge concerning manufacturing and material properties (strength, stiffness, fatigue life, etc.) prevents them from seriously considering TPC for wind turbine blade structures. This is not specific to the wind energy industry but rather a general trend in the composite industry, in which people are specialized either in thermoset composites or thermoplastic composites.

From earlier discussions, it is clear that simply changing the resin system and keeping the existing blade design is not an ideal solution for TPC blades. This is due mainly to the fact that TPC are processed and assembled very differently than thermoset composites.

The work presented in this dissertation proposes an integrated approach to the design of large wind turbine blades, one that will take into account the fragile equilibrium among the material, structural design, and process limitations of TPC. In order to obtain such a design, the following goals have been formulated:

- Identify potential thermoplastics resin systems suitable for large wind turbine blades based on cost, physical properties, strength and stiffness, processing and recycling capability.
- Benchmark mechanical properties of TPC against their thermoset counterpart and propose solutions for a sustainable end-of-life for these new materials.
- Considering material and process limits, propose an integrated design solution that maximizes the potential of TPC when used for large wind turbine blades.
- Benchmark the proposed TPC blade design concept against a conventional blade design.

By achieving these goals, this thesis will contribute to bridging the extremely large knowledge gap that remains before TPC can be used successfully in large wind turbine blade structures.

1.7 Thermoplastic Composite Wind Turbine Technology Package

In 2003, in an effort to improve blade design with respect to sustainability, manufacturing costs and structural efficiency, the Design and Production of Composite Structures research group (DPCS) of the Delft University of Technology began to investigate the possibility of using fully recyclable thermoplastic composites (TPC) for wind turbine blade structures. Through a partnership with the Delft University Wind Energy Research Institute (DUWIND), a complete technology package covering design, manufacturing and material issues was set up to develop the necessary tools for TPC blade manufacturing. As will be discussed in Chapter 3, one of the key issues for the successful use of TPC for wind turbine blade structures lies in the ability to manufacture large parts. TPC manufacturing processes in use today are mostly melt processes dedicated to the production of relatively small parts (up to 1-2m in length and 1-5mm thick) and are not suitable for the production of thick and large composite shells such as those found in wind turbine blade structures. An essential aspect of the TPC blade technology package therefore was to select the appropriate matrix material and develop a reactive processing technique that could make the manufacturing of large parts possible. The dissertation of Kjelt van Rijswijk on vacuum infusion technology for anionic polyamide-6 composites forms the base of this effort [18].

Since DPCS has been contributing to TPC development for more than two decades now in the automotive and aerospace industry, past and ongoing projects at DPCS have helped nurture and inspire the development team in the field of assembly technologies (welding), material development, and press forming technologies. Figure 1.9 shows the interactions between the different projects at DPCS and the beneficial effects they have had on technology development.

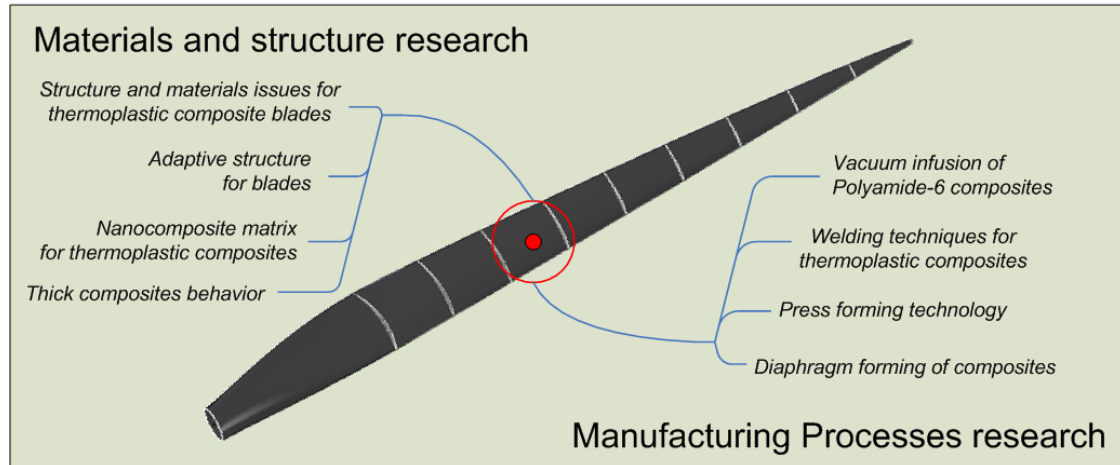


Figure 1.9: The different R&D projects at DPCS and their interaction with the development of TPC blades.

1.8 Thesis plan

Since design problems are “open-ended” and certainly do not have unique or “optimal” solutions, engineers must keep an open mind especially in the first stages of the design process. This willingness to consider all options is key to finding the correct balance between performance and cost when constrained by the complex interaction between shape, material and process. Bearing this in mind, the second chapter of this thesis will review the history of wind turbine blade materials and structures. Through this broad literature survey, the reader will witness the very diverse approaches followed for blade design and manufacturing over the years. Chapter 3 will concentrate on the state of the art of thermoplastic materials and processes and their potential use for wind turbine blade structures. Intrinsic properties of the material will be discussed and potential benefits for blade design will be outlined, including sustainability issues. In Chapter 4, polyamide-6 composites will be benchmarked against traditional epoxy-based composites commonly used for wind turbine blade structures. Different physical

properties and mechanical properties such as tensile, compressive and shear moduli and strengths will be used to establish an overall comparison of composites. The recyclability of the continuous polyamide-6 composites will also be addressed at the end of this chapter.

While chapters 3 and 4 focus purely on material and processing issues, the following chapters will deal with structural aspects of blade design. Chapter 5 will present the analytical design tools built to determine blade loading and analyze different design concepts. In Chapter 6, these tools will be used to set the geometry of the generic blade used in this thesis and define associated critical load cases for the topology-optimization-based preliminary blade design presented in Chapter 7. In Chapter 8, this preliminary TPC wind turbine blade design will be refined further through different composite sizing optimization techniques to yield a final blade design concept. Using this design, the end of Chapter 8 will conclude by benchmarking this new design concept against conventional thermoset wind turbine blade structures. The final chapter of this dissertation will draw conclusions and formulate recommendations for future work on large thermoplastic composite blade design.

1.9 References

- [1] *Global Population Profile: 2002*, U.S. Bureau of the Census, Washington, D.C.: International Programs Center Population Division, March 2004, PASA HRN-P-00-97-00016-00.
- [2] *World Energy Outlook 2006, Summary and conclusions*, International Energy Agency, Paris, France, 2006.
- [3] *Global Wind 2006 Report*, Global Wind Energy Council, 2006.
- [4] *20% Wind Energy by 2030 - Increasing Wind Energy's Contribution to U.S. Electricity Supply*, DOE/GO-102008-2567, May 2008.
- [5] Beukers, A., Van Hinte, E., *Lightness: The Inevitable Renaissance of Minimum Energy Structures*. Rotterdam, 010 Publishers, 1998.
- [6] P.S. Veers, T.D. Ashwill, H.J. Sutherland, D.L. Laird, D.W. Lobitz, D.A. Griffin, J.F. Mandell, W.D. Musial, K. Jackson, M.D. Zuteck, A. Miravete, S.W. Tsai, J.L. Richmond, *Trends in the Design, manufacture and Evaluation of Wind Turbine Blades*, Wind Energy, Vol. 6, No. 3, July-September 2003, pp. 245-259.
- [7] Griffin, D.A., *Alternative materials, manufacturing processes and structural designs for large wind turbine blade*, 40th AIAA Aerospace Sciences Meeting and Exhibit, AIAA, Washington, DC, 2002, pp. 27-39.
- [8] Malcolm, D.J., Hansen A.C., *WindPACT Turbine Rotor Design Study*. NREL/SR-500-32495. National Renewable Energy Laboratory. Golden, CO, 2002.
- [9] Griffin, D. A., *Blade system design studies volume 1 : composite technologies for large wind turbine blades*. SAND2002-1879. Sandia National Laboratories, Albuquerque, NM, 2002.
- [10] Griffin, D.A., *WindPACT Turbine Design Scaling study technical area 1 – Composite blades for 80 to 120 meter rotor*. NREL/SR-500-29492. National Renewable Energy Laboratory. Golden, CO, 2001.
- [11] Brondsted, P., Lilholt, H., Aage, L. *Composite Materials for Wind Power Turbine Blades*, Annual review of Materials Research, 2005, 35:505-538.
- [12] Vestas Wind Systems A/S, *Life cycle assessment of offshore and onshore sited wind power plants based on Vestas V90-3.0 MW turbines*, June 2006.
- [13] Thor Sven-Erik, *Proceedings of the 38th IEA Topical Expert Meeting – Material Recycling and Life Cycle Analysis of Wind Turbine*. Roskilde, Denmark, March 2002.

- [14] JEC Composites, *Global Market Scenario Dynamic of the Composites Industry – 2009 Release*. Strategic Studies, 2009.
- [15] Pickering, S. J. (2006). *Recycling technologies for thermoset composite materials--current status*. Composites Part A: Applied Science and Manufacturing, 37(8): 1206-1215.
- [16] LMGlasfiber Newsletter, *From waste problem to raw material in cement*, September 2004.
- [17] Advanced Materials & Composites News. *New Use Found for Old FRP Wind Turbine Blades*. Advanced Materials & Composites News, Composite Worldwide Inc., March issue, 2004.
- [18] van Rijswijk, K., *Thermoplastic Composite Wind Turbine Blades – Vacuum Infusion Technology for Anionic Polyamide-6 Composites*. PhD dissertation, Delft University of Technology, Delft, 2007.

CHAPTER 2

BLADE MATERIAL AND STRUCTURAL DESIGN *AN HISTORICAL OVERVIEW*

Rien ne sert de courir; il faut partir à point
(Slow and steady wins the race)

- Jean de La Fontaine

This thesis proposes a new structural design concept for future large wind turbine blades. History has shown that good design solutions are often forged on past experiences (successes or failures). It is therefore of prime importance to any engineer striving to improve an existing design to acknowledge and to understand previous and present-day attempts at solving similar problems. This chapter presents these landmark achievements and failures in wind turbine design and blade structural design history. After reviewing the early days of windmill and wind turbine use, the rest of this chapter will focus on the most important milestones of wind turbine blade development in the twentieth century.

2.1 Windmills used for mechanical work

2.1.1 Vertical axis machines

The discovery of ancient Egyptian pottery showing vessels under sail moving upstream on the Nile suggests that man has been harnessing wind for more than 5000 years. Most probably due the experience gained on sailing vessels, man soon began to harvest wind for “on-land” applications. It is unclear whether the Chinese or the Persians should be credited with the invention of the first vertical-axis wind turbine but history recalls that as early as the 7th century, both civilizations used similar versions of the so-called panemone turbine to pump water (drain rice fields) and grind grain [1-3]. These simple drag machines relied on wood as their main structure and used either bamboo sticks or cloth for their sails (blades) (see Figure 2.1).

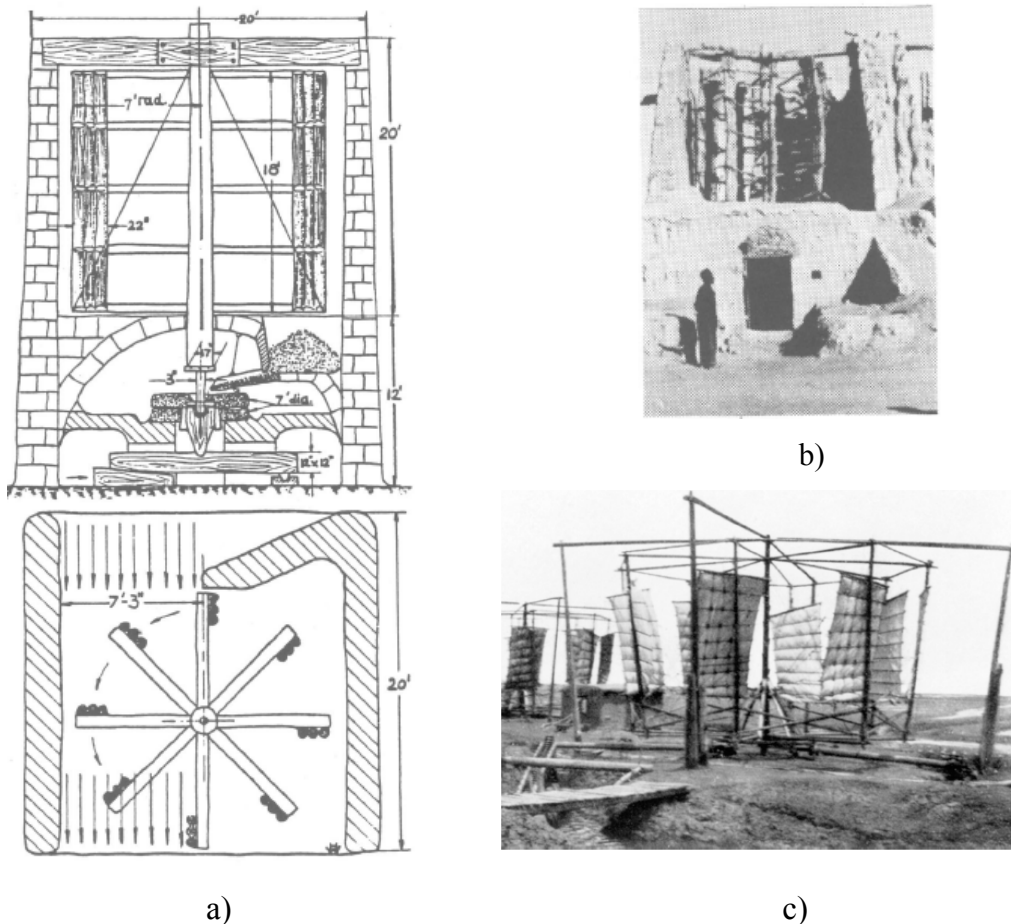


Figure 2.1: Ancient Persian and Chinese windmills. a) Persian vertical axis windmill with millstone placed below the rotor; sails are made with bundles of reeds [1]. b) Downwind view of the Persian windmill [1]. c) Chinese vertical-axis windmill [3].

2.1.2 Horizontal Horizontal axis machines

2.1.2.1 European windmills

It is interesting to note that some four hundred years later, northwestern Europeans started using horizontal axis wind turbines to perform exactly the same tasks. Two contradicting theories exist to explain the birth of the horizontal-axis wind turbine in Europe. The first one, known as the diffusion theory, suggests that the vertical axis machine would have spread west simply by virtue of the different trade routes and returning crusaders and evolved into the traditional four-blade horizontal-axis design. This theory proposed by Debeir et al was linked to the discovery of written proof that the first horizontal axis windmill likely stood in the North of France in Normandy around 1180 [4]. This same “diffusion” theory is normally used to explain the discoveries of other ancient windmills in Belgium and Holland with the oldest one

found in the province of Brabant as early as 1119. Conversely, Kealey suggested that the design of horizontal-axis windmills originated in England and was never influenced by the achievement of the Persians or the Chinese [2]. The design would have instead evolved from earlier watermill designs. Using financial records from the 12th century, Kealey estimated that the first English windmills would have been built around 1137.

Nevertheless, historians generally agree that the original design of horizontal-axis windmills in England and on the European main land was the so-called “post windmill”, taking its name from the central post used as the main structure (see Figure 2.2). Different versions of this design found in England, France, Holland and Germany were reported to be used to mill grain or cut wood. A hollow-post version with a scoop wheel at the base was also used to pump water. Around the fourteenth century, driven by the need to build larger windmills, the tower-mill design started to gain in popularity. Rotating only the head of the windmill instead of the entire structure, millers were able to operate larger mills and used the tower for storage and living quarters (see Figure 2.3). Within a couple of centuries, the Dutch became the ultimate tower-mill builders, improving the blade design with elements such as blade twist, leading edge camber, and fractional chord position of the main blade stock [1]. Around the mid-nineteenth century, the Dutch pushed their use of wind energy to extremes with some areas of the country populated by more than 400 windmills per square kilometer. At the same period, other countries such as Germany, England and Denmark also made extensive use of tower mills, raising the level of “mechanical” power available in Europe to 1500 MW [5]. This level of wind energy use was to be surpassed only by electrical wind energy production late in the 1980s.



Figure 2.2: Typical Dutch post mill.



Figure 2.3: Typical Dutch tower mill.

2.1.2.2 Blade concepts on ancient windmills

European windmills have seen various changes in blade design over the centuries. On early models, such as those found in the near East and around the Mediterranean, blades were short, used stocks centered in the middle of a flat sail and had no twist or camber (Figure 2.4a). This blade concept prevailed until the middle of the second millennium, at which time the stock was moved forward to 33% of the chord length. According to Drees [6], this was done in order to reduce the torsion that was increasingly present with longer being built. In the first half of the 17th century, the famous Dutch mill builder and hydraulic engineer Jan Adriaanszoon (also known as Leeghwater, which literally means “Empty-water” – a name given to him because he reportedly emptied 27 lakes during his lifetime!) improved this design by moving the stock forward to the quarter-chord, by introducing a cambered leading edge board (droop snoot) and by using furling sails (see Figure 2.4b). The reason behind this last design change was primarily to maintain better control over the windmill during storms. With the original concept, if the windmill was caught with wind blowing from its back during a storm, the sails could inflate. The brake system not being able to manage reverse torque, the windmill could start in reverse, over-speed and possibly suffer serious damage.

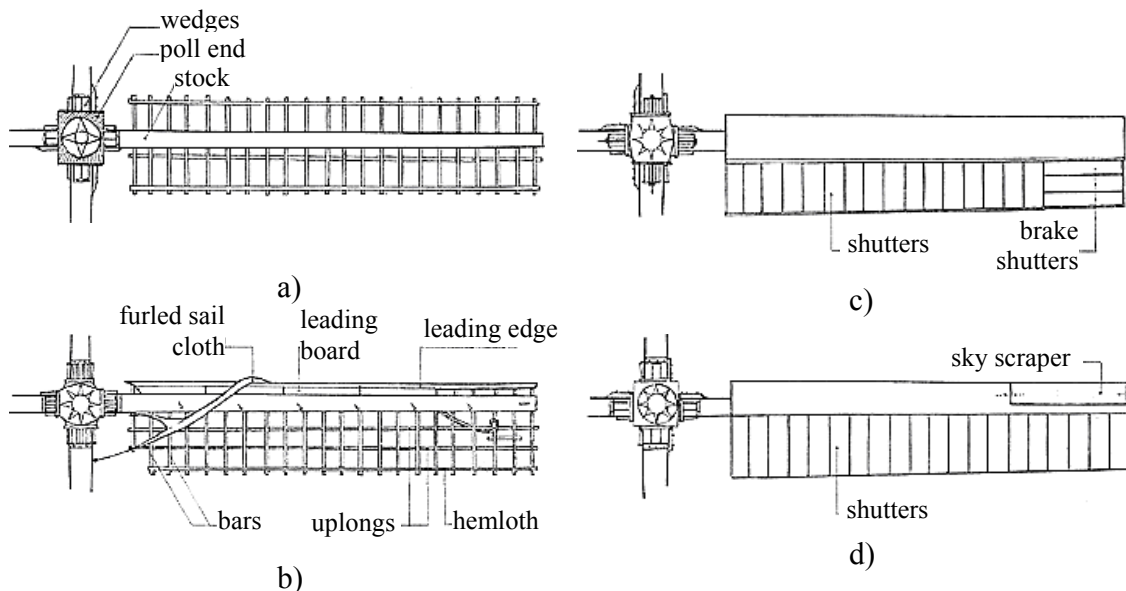


Figure 2.4: Windmill blade concepts. a) original concept with a symmetric sail over the stock, b) improved concept with stock at quarter-chord, leading edge boards and furling sail cloth, c) shutter concept with shutter brake, d) shutter concept with sky scraper [7].

Another interesting concept found on ancient windmill was the shutter sail design, also known as the “spring sails” concept shown in Figures 2.4c and 2.4d. Found as early as the end of the 18th century, these sails used a series of hinged shutters like those of Venetian blinds. In normal operation, the shutters would form a uniform blade surface. Generally controlled by centrifugal force, the shutters would gradually open with increasing wind speed. Spilling wind through the open shutters regulated the rotational speed of the windmill and provided control during storms. Different variations of this concept were developed through the years with one of them having the shutters controlled by a system of rods going through the pole end and another one with longitudinal shutters (also known as sky scrapers, see Figure 2.4d) used as air-brakes [7].

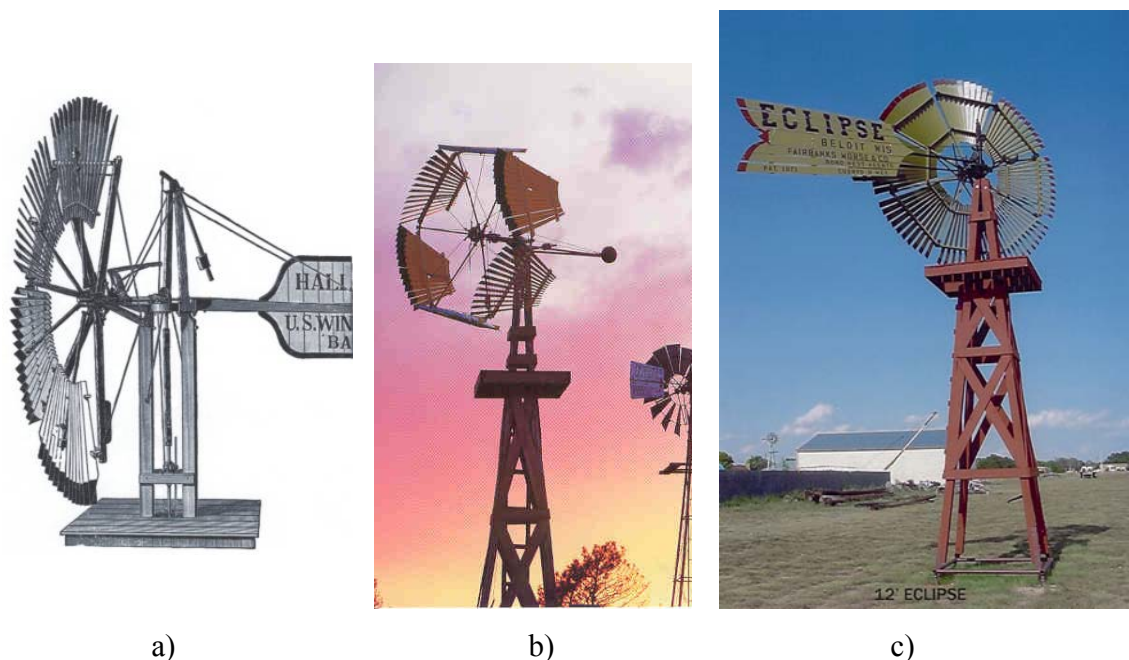


Figure 2.5: American windmills. a) the Halladay concept with a multi-bladed sectional wheel and tail vane, b) the Halladay windmill under strong winds (or parked), c) Reverend Wheeler's Eclipse solid wheel windmill in parked mode.

2.1.2.3 American windmills

Early prototypes of the so-called “American windmill” were first developed in the mid-nineteenth century. Daniel Halladay is credited with being the first to commercialize the American windmill as early as 1854. Halladay's first concept, which was quite different in design from its European counterpart, used four hinged blades and

a tail vane attached perpendicular to the rotor plane [8]. In operation, the blades swept out a cone and found equilibrium between centrifugal forces and aerodynamic thrust loads. A couple of years later, Halladay developed a new concept using instead a multi-bladed rotor composed of a large number of thin wooden blades fasten to a wooden rim placed at blade mid-span (the hinge pivot). Usually the rotor was composed of a dozen sections of five or six blades attached together to force a folding motion similar to that of an umbrella. This type of rotor shown in Figures 2.5a and 2.5b is commonly known as the *sectional wheel* concept and is one of the two main styles of American windmills.

The other windmill style found late in the 19th century in America was the *solid wheel* concept developed by Reverend Leonard R. Wheeler. As shown in Figure 2.5c, the rotor consists of a large number of thin blades mounted together in a single rigid section. Wheeler, who generally used a small lateral vane to force the rotor out of the wind in severe conditions, favoured yaw control over hinged blades. As with Halladay's design, a tail vane was used to control the windmill but Wheeler improved the concept, since he was the first to use a hinged tail vane that could be secured parallel to the rotor plane when the windmill needed to be shut down. Wheeler's pioneering effort inspired most of the water-pumping solid wheel windmill designs to follow in the late 19th century and early 20th century.

2.2 Pioneering work in wind-powered generation of electricity

The previous section discussed the early use of wind power for mechanical work with grinding, milling and pumping water being the most common applications. According to the literature, the first time wind power was used to produce electricity can be traced back to 1888 as a result of Charles F. Brush's desire to power a large number of incandescent lights at his large estate in Cleveland, Ohio [5]. Brush, an industrialist in the electrical field, erected on his land a large Wheeler-type windmill equipped with a rotor 18m in diameter (see Figure 2.6). Using belts and pulleys, Brush stepped up the rotor's RPM by a ratio of 50 to provide 500 RPM to a 12kW DC generator.

Although Brush was the first to achieve this milestone in wind-powered electricity generation, his effort did not have a large impact on technology development in America. It took 40 years before some form of industrial electrical wind power exploitation occurred in America with the effort of Marcellus and Joseph Jacobs. Recognizing the need for an off-grid electrical energy source (only large cities had grid

connection capabilities at the time), the Jacobs Wind Electric Company started the production of their “wind charger” model in the 1920s (see Figure 2.7). Very popular for providing power to isolated farms and ranches (battery charging), thousands of these machines were manufactured and sold throughout the world from 1925 to 1950 [9].

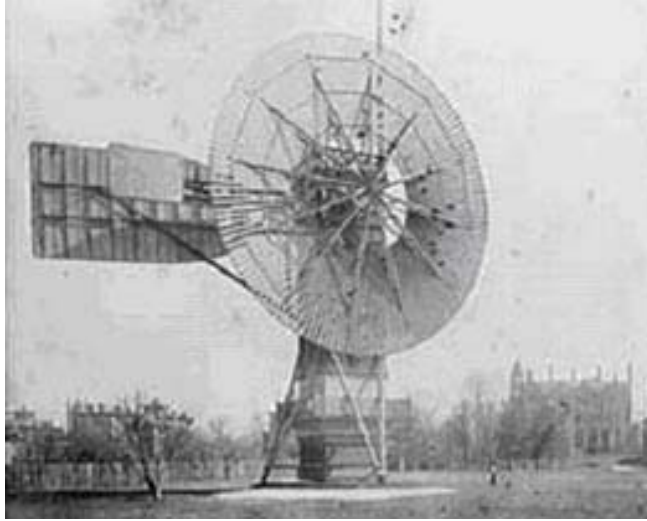


Figure 2.6: Charles F. Brush's 12kW wind turbine, 1888.



Figure 2.7: Jacobs “wind charger”, 1932.

In Europe, the Dane Poul LaCour, experimenting with wind-powered electricity as early as 1891, is recognized as the father of modern electrical power generating wind turbines. Compared to Brush's effort, LaCour's contribution led to a countrywide revolution in electricity production by means of wind power with more than a hundred 25kW units installed in Denmark by 1920 [5]. His merit is measured not only in kilowatts installed but also through his pioneering effort in numerous aspects of wind turbine technology development. Amongst other things, LaCour was the first to test a wind turbine in a wind tunnel that he had built himself. He was also the first to produce hydrogen with electricity coming from his turbines and is known to have powered gas lamps at his school from 1885 to 1902 with this hydrogen. He also made a substantial contribution to education with lectures on wind energy and by publishing the world's first journal on wind energy. Commercialized by the Lykkegard Company as early as 1908 in power outputs ranging from 10 to 35 kW, LaCour's concept used four wooden shutter sails for power limitation and relied on fantail-type side wheels for yawing (see Figure 2.8) [9]. It is interesting to note that the generator was placed at the base of the tower and was coupled to the rotor via a long shaft and 90° gearbox.

Some years after World War I, as fossil fuel prices came down again, interest in wind energy also crumbled and Lykkegard's business went bankrupt. As is always the case, wind energy became popular again when oil prices soared, which this time occurred with the outbreak of World War II. This led to the birth of an important player in wind turbine development in Denmark, the F.L. Smidth Company. They manufactured machines using the brand name "aeromotor" using solid wood blades and applied the concept of struts for stress relief in the blade roots. Benefiting from their experience in the concrete business (Smidth was originally a manufacturer of machines for the production of cement), they were also the first to use concrete for towers. Figure 2.9 shows their 70kW model, which served as the base concept for another very famous Danish turbine erected in 1957, Johannes Juul's Gedser turbine.

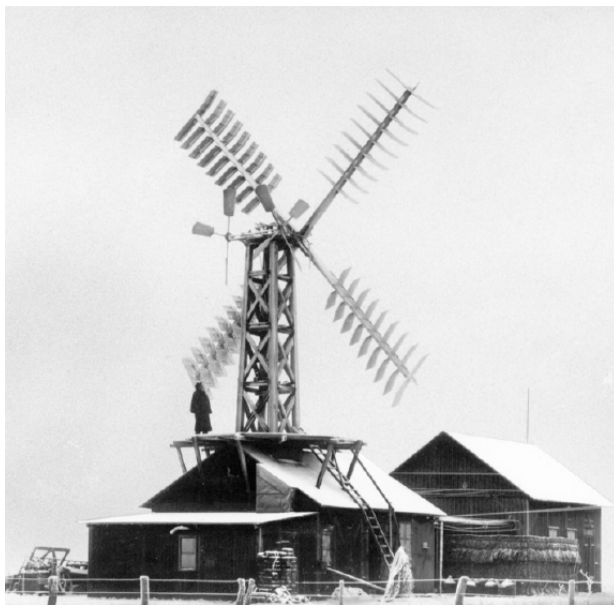


Figure 2.8: Poul LaCour's first prototype, 1891.



Figure 2.9: Smidth's aeromotor 70kW turbine, 1942.

2.3 Post World War II achievements

In the period between 1940 and 1960, three very important figures marked the course of wind turbine development: The German Ulrich Hütter, the Dane Johannes Juul and the American Palmer Cosslett Putnam.

Hütter, an aeronautical engineer backed with a PhD on optimal wind turbine design, developed the W34 turbine following principles of low weight, high tip speed ratio and maximum efficiency. His design, put in service at a low-wind site near Stuttgart in

1958, reflected exactly this philosophy and yielded a concept using a very lightly loaded downwind teetering rotor (see figure 2.10). Most importantly, on a blade design and manufacturing point of view, Hütter was the first to use advanced glass-fibre composite materials for his 17m long blades. Often referred to as the father of composite wind turbine blade design, Ulrich Hütter's ideas significantly influenced later composite blade designs both in Germany and elsewhere. His contribution was two fold as he proposed a relatively simple but efficient solution to connect the blades to the hub and he proved that a simple monolithic-skin composite construction could be used successfully for blade structures. His method for load transfer from the blade to the rotor hub, now simply referred to as the "Hütter root", relied on heavy glass roving strings individually looped around a series of flange bolts or bushings mounted on a metallic ring as illustrated in figure 2.11. Once wetted with resin, the flange bolts and loop-strings assembly offered a smooth load transition to the blade structure. Variants of this concept are known to have been used up to the late eighties by different blade manufacturers.



Figure 2.10: The W34 wind turbine (rotor dia. 34m, rated power, 100kW), Stötten, Germany, 1959 [9].

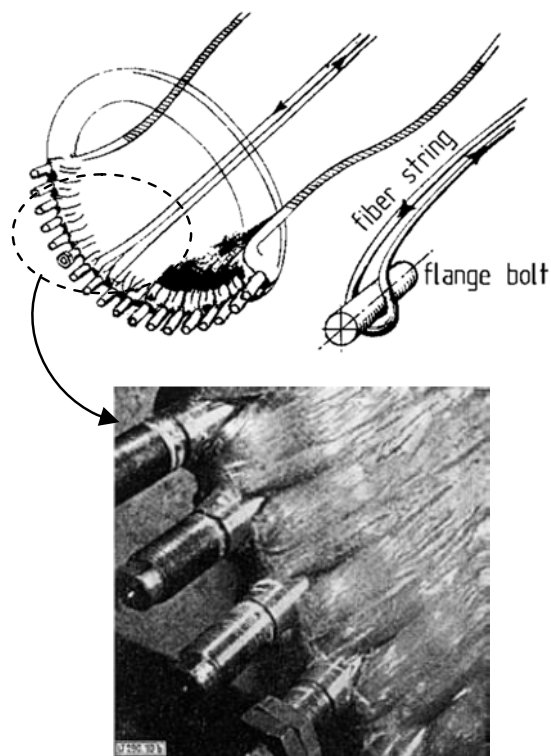


Figure 2.11: The "Hütter root", also known as the loop connection [9].

Hütter was also the first to propose the blade manufacturing technique so widely used today. His monolithic structure was built using two female molds in which the upper surface and lower surface of the blade skins were laminated. In a third and final step the two half blades were bonded together at the leading edge and trailing edge to form the blade. Again, variants of this manufacturing technique are widely used today with extra c-shaped or I shaped shear webs included in the structure.

The wind energy industry owes a debt of gratitude to Hütter's vision with respect to the aesthetics of wind turbines. As related by Heymann [10], unlike many of the engineers who followed in his footsteps, Hütter emphasized the importance that aesthetics would have on subsequent decades of wind energy development. The following passage from his thesis clearly reflects his view in this regard:

"These (wind turbines) must for that reason in a deeper sense be of a timeless beauty, so that they do not in three or four decades hence burden a later generation with the heavy task of removing angular skeletons, by our indifference to the imponderable value of our environment."

In the neighboring country of Denmark, Johannes Juul would not have been given a perfect score for the aesthetic features of his turbine installed at Gedser but can surely be credited with setting the baseline characteristics of most modern wind turbines using a low-speed upwind three-bladed rotor configuration.

His design, shown in Figure 2.12, was commissioned in 1957 by the Danish utility company SEAS and was one of the first AC wind energy converters ever built. It proposed a series of new concepts with one of them being a simple yet very efficient method of preventing over-speeding and providing control: the tip brake. Using centrifugal force to drive a spring-loaded curvilinear slot mechanism, blade tips could be placed perpendicular to the incoming flow when a certain rotational speed was reached. Adapted to fiber-reinforced composite blades, his concept is still in use today on numerous medium-sized turbines. With regard to blade structure, one of the key design features is the use of struts and stays (originally proposed on Smidth machines) to reduce root-bending moments. This odd-looking concept later inspired other Danish and European rotor designs such as the NibeA, Windmatic or Polenko turbines. Compared to Hütter's glass-fiber-reinforced composite blades, Juul's blades relied on common 1950s construction principles using a steel spar to carry the load and wooden

ribs covered with aluminum skins to give the blade its desired aerodynamic characteristics.

Fifteen years prior to Juul's work on the Gedser turbine, Palmer Cosslett Putnam formed a group composed of renowned scientists of the Massachusetts Institute of Technology (MIT) such as Theodore von Karman and talented engineers from the S. Morgan Smith Company, a manufacturer of hydroelectric turbines, to design and build the largest wind turbine yet to exist. Erected in 1941 at Grandpa's Knob in the state of Vermont, the Smith-Putnam turbine used a 53m-diameter downwind rotor equipped with hinged blades to produce 1.25MW of power at rated wind speed (see Figure 2.13).



Figure 2.12: The Gedser turbine. The mother of modern low speed 3 bladed upwind wind energy converters.

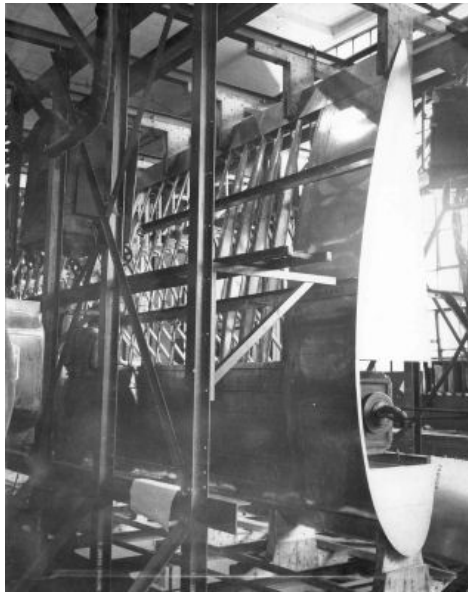


Figure 2.13 Smith-Putnam 1.25MW wind turbine (1941).

The technology preferred for the machine fairly reflected the background of the different men involved in the design. The tower, drive train and hub were characteristic of the heavy steel industry in which the S. Morgan Smith Company was involved at the time. As for the blades, their construction borrowed technology typical of the aeronautical industry of the 1930s and 1940s. Figure 2.14 depicts the inner-frame structure of the blades and method of assembly of the riveted skins. The blades are

known to have been all stainless steel and weighed around six tons each. In service for four years, the machine suffered a fatal blade fatigue failure in 1945 and was unfortunately never repaired.

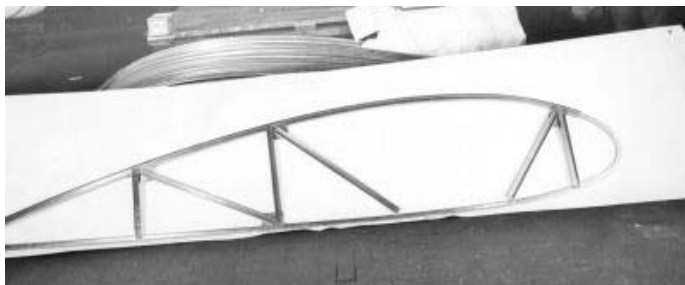
As related in many wind energy history review articles and book chapters [5,9,10], these three particular projects are considered to be the starting points of most of the wind energy R&D projects started in the 1970s.



a)



b)



c)



d)

Figure 2.14: The Smith-Putnam turbine blade structure. a) Blade section with skin and inner tubular structure apparent, b) fully assembled blade shown from tip to root, c) typical rib station structure, d) fully assembled rotor

2.4 Large wind turbine Federal R&D programs - 1970-1990

With oil prices soaring as a result of the oil embargo imposed on the United States and most European countries at the beginning of the 1970s, numerous countries engaged in intensive government-funded R&D programs aimed at achieving energy self-sufficiency. While some cast their lot solely with nuclear technology, others like the United-States, Germany, Sweden, the United-Kingdom and Denmark invested in wind energy R&D programs. After a brief historical survey of the most important turbines emerging from those Federal programs, the subsequent sections will trace the history of some of the most popular designs for blade structures at this early stage of large horizontal axis wind turbine development.

2.4.1 *Technology development and subcontractors*

Managed by NASA, the United-States Federal R&D programs favored the development of wind turbines producing 1 MW of power or greater, which were believed at the time to have the greatest potential for application in utility networks due to the economies of scale [5,10]. From 1975 to 1988, more than 80% of the program's funding (\$427 million) went to large wind turbine development. Companies like Boeing, McDonnell Douglas, Lockheed, Grumman Aerospace and Kaman were preferred for wind energy technology development, with Westinghouse being the only non-aerospace related company known to have received a contract at the time. With such a strong presence of the aerospace industry in their R&D program, the concepts emerging from the American design teams were strongly influenced by the technology used in that industry at the time. Metallic stressed-skin blade design is a great example of this influence and will be discussed in more detail in the next section. From 1975 to the end of the 1980s, NASA's "modification" program (MOD) sponsored the design and manufacturing of five different wind turbine concepts with capacities ranging from 100kW to 3.2MW (see Table 2.1).

Efforts in Germany were also aimed at developing MW-size machines and their R&D bore the stamp of their aeronautical industry since the program was strongly influence by Ulrich Hütter, director of the Institute of Aircraft Construction at Stuttgart University and top German wind energy expert at the time [10]. Based on his recommendations, Germany engaged in different turbine design projects including the

WKA turbine, the Aeolus turbines, the very odd-looking one-bladed Monopteros turbines and the very large Growian (Große Windkraft-anlage) turbine, an up-scaled 3MW version of his W34 turbine (see table 2.1 for turbine specs).

Finally, the United Kingdom, Sweden and Denmark with their federal programs also contributed at the time to the development of very large wind turbines. Their most important projects are also listed in Table 2.1. It is interesting to note that the Danish Tvind turbine was the only non-federally funded project. Designed and built between 1975 and 1978, the Tvind turbine was financed entirely by the Teacher group of the schools at Tvind and was built entirely by volunteers.

Table 2.1: Large wind turbine blades built for 750kW+ wind turbines, 1970-1990.

<i>Country</i>	<i>Blade Manufacturer</i>	<i>Turbine model</i>	<i>Blade mat.</i>	<i>Manuf. Proc.</i>	<i># of blades</i>	<i>Up or down wind</i>	<i>Rotor dia. (m)</i>	<i>Rated power (kW)</i>	<i>Year of oper.</i>
USA	Lockheed	MOD-0	Al	Riveted	2	D	38	100	1975
USA	Lockheed	MOD-0A	Al	Riveted	2	D	38	200	1977
USA	Gougeon Bros.	MOD-0A	WE	Vacuum	2	D	38	200	1979
USA	SCI	MOD-0A	GFRP	Tape wound	2	D	38	200	1981
USA	NASA LeRC	MOD-0A	S/foam	Welded	2	D	38	200	1980
USA	Boeing	MOD-1	S/foam	Welded	2	D	60	2000	1979
USA	Kaman aero.	MOD-1	GFRP	Tape wound	2	D	60	2000	1980
USA	Boeing	MOD-2	S	Welded	2	U	91	2500	1982
USA	Boeing	MOD-5B	S	Welded	2	U	98	3200	1987
USA	Hamilton Stan.	WTS-4	GFRP	Fil. wound	2	D	78	4000	1982
Germany	MAN	WKA60	GFRP	Tape wound	3	U	60	1200	1989
Germany	MBB	Monop 50	G-CFRP	Hand lam.	1	D	50	640	1989
Germany	Erno GmbH	Aeolus I	S/GFRP	Welded	2	U	75	2000	1983
Germany	MBB	Aeolus II	G-CFRP	-	2	U	80	3000	1991
Germany	MAN	Growian	S/GFRP	Welded	2	D	100	3000	1983
Denmark	Elsam	NibeA	W	-	3	U	40	630	1980
Denmark	Elsam	NibeB	GFRP	Tape wound	3	U	40	630	1980
Denmark	DWT	Windane40	GFRP	Tape wound	3	U	40	750	1986
Denmark	DWT	Tjaereborg	GFRP	Tape wound	3	U	61	2000	1988
Denmark	Tvind school	Tvind	GFRP	Hand lam.	3	D	54	900	1978
Italia	Hamilton Stan.	Gamma 60	GFRP	Fil. wound	2	U	66	1500	1990
Nederland	Polymarin	NEWECs 45	GFRP	Hand lam.	2	U	45	1000	1985
Spain	Asinel-MAN	AWEC-60	GFRP	Bladder	3	U	60	1200	1989
Sweden	Erno GmbH	WTS-75	S/GFRP	Welded	2	U	75	2000	1981
Sweden	Hamilton stan.	WTS-3	GFRP	Fil. wound	2	D	78	3000	1982
UK	Howden	HWP-1000	WE	Vacuum	3	U	55	1000	1989
UK	Howden	HWP-750	WE	Vacuum	3	U	45	750	1988
UK	British Aero.	LS-1	S	-	2	U	60	3000	1988

Blade materials: Al- Aluminum, WE- Wood/epoxy, GFRP- Glass-fiber reinforced plastic, S- Steel, W- Wood, G-CFRP- Glass and Carbon fiber reinforced plastic.

2.5 Large wind turbine blade structural design – 1970-1990

As shown in Table 2.1, an impressive number of different materials and manufacturing processes were used to build very large blades through federally funded projects. Steel, aluminum, wood and composites were the most commonly used materials from 1970 to the end of the eighties. Although steel or aluminum might sound today like a strange choice of material, they were quite often used at an early stage of large wind turbine development, mainly because they were better characterized than their more modern alternatives. This advantage clearly influenced puzzled designers dealing with uncertain stochastic loads and long life expectancy design criteria typical for wind turbine blade design [11]. Obviously, due to the strong interaction between material, design and manufacturing processes, the structural design concepts and manufacturing processes used were strongly linked to the chosen material. For the sake of clarity, the next sections will review large wind turbine blade structural design with respect to their construction material rather than any other blade characteristic.

2.5.1 *Aluminum and steel blades*

Aluminum was used for the first blade set installed on the American MOD-0 machine (see Figure 2.21a). NASA had initially sponsored Hamilton Standard, a division of the United Technology Corporation, to design and build composite blades but delays and escalating costs forced the space agency to abandon this idea and opt instead for the aluminum stressed-skin design proposed by Lockheed.

As shown in Figure 2.15a, the main structural element of these blades was a 2024-T3 aluminum D-spar consisting of a skin, ribs and stringers [12]. The trailing edge was semi-structural and was composed of a thinner aluminum skin assembled into a series of ribs. From the manufacturing perspective, the skins of the D-spar were all brake-formed into shape and riveted flush to the ribs and stringers for good aerodynamic performance. Welding instead of riveting was used to assemble the trailing edge section. Aerodynamic and gravity load transfer to the turbine hub was ensured by means of a steel tube mating the two innermost ribs as shown in Figure 2.15b. These aluminum blades are known to have performed relatively well for over 15,000 hours without significant damage (only minor fatigue repairs). On the other hand, due to their prohibitive manufacturing cost (\$250,000US per piece in 1980), the technology was later abandoned for a more low-cost approach [13].

Steel was the material of choice of Boeing, Maschinenfabrik Augsburg-Nürnberg (MAN) and Messerschmidt-Bölkow-Blohm (MBB), three important players in the American and German federally funded wind energy programs.

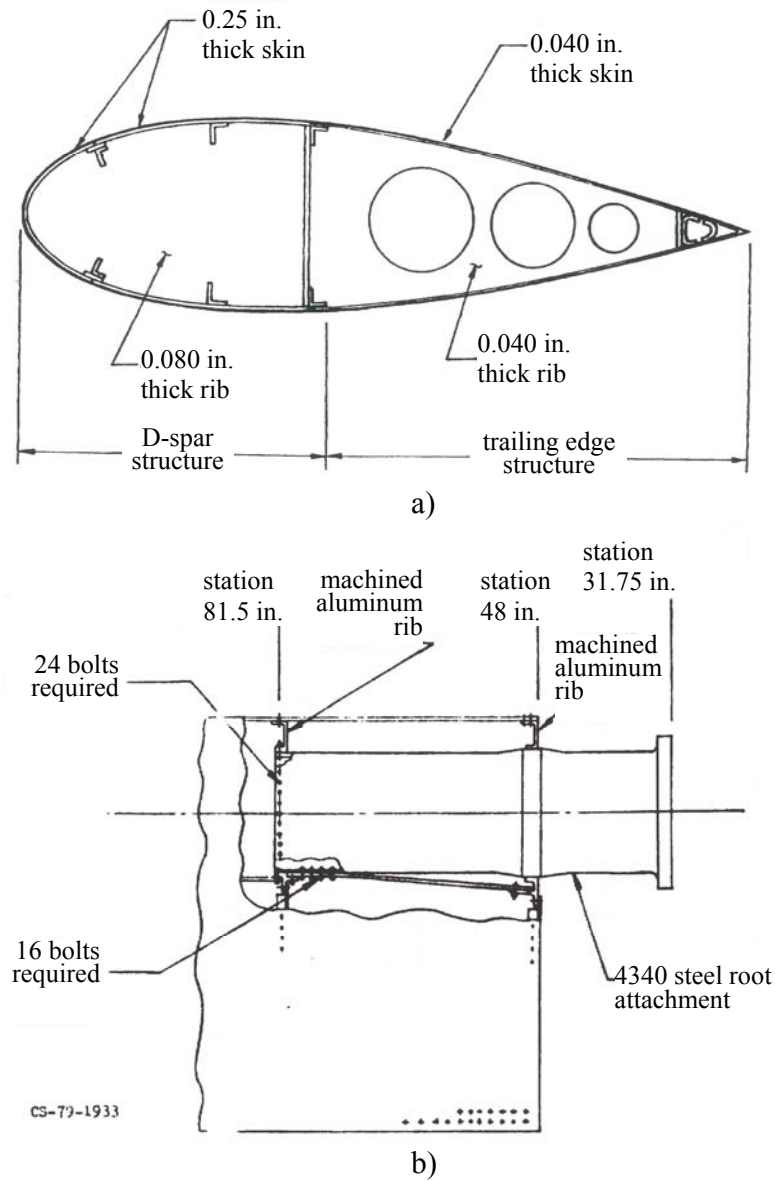


Figure 2.15: Lockheed's MOD-0 2024-T3 aluminum blade design [12]. a) cross-section details showing skin, rib and stringer construction, b) root attachment details.

Boeing introduced their first steel blade concept on the 2MW MOD-1 turbine (see Figure 2.21b). The blade consisted of a stiffened steel shell leading-edge spar onto which a foam trailing-edge section was assembled (see Figure 2.16a). The spar sections were manufactured by first brake-forming the lower and upper skins. As shown in Figure 2.16b, after welding the T-stiffener and partial ribs in place, the upper and lower

skins assemblies were welded together to form one of six spar sections to be welded later at different chord stations to give the spar its final shape. As shown in Figure 2.16a, the trailing edge sections were assembled on the spar using foamed-in and cut-into-shape polyurethane foam blocks covered with stainless steel skins [14].

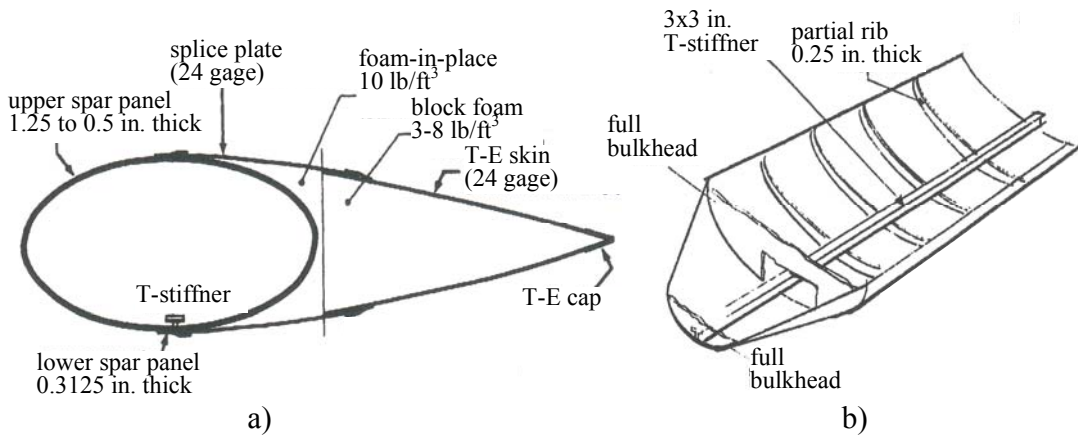


Figure 2.16: Boeing’s MOD-1 stainless steel blade [14]. a) cross-section details showing steel spar and foam trailing edge section covered with stainless steel skins, b) lower spar panel details.

After the completion of the experimental MOD-0 turbine, NASA engaged in a series of new blade designs in an effort to reduce cost. These new blades were tested on four different MOD-0A turbines for short periods of time. One of these designs was the so-called “utility pole” design named after the steel poles often used for highway lights. As shown in Figure 2.17a, the concept used a circular axisymmetric spar for the main structural element of the blade. Once the spar was prepared, leading-edge wooden ribs were glued on the spar, foam blocks were inserted between the ribs and a first GFRP (glass fiber reinforced polymer) over-wrap was performed to secure the leading edge section to the spar. In a similar fashion, the trailing edge portion of the blade was assembled and a thin layer of GFRP was over-wrapped to give the blade its final shape [15]. This design yielded a significant reduction in cost compared to the original aluminum design with blades being produced at \$30,000US (in 1979) per piece. On the other hand, limitations on the type of airfoil compatible with the axisymmetric spar compromised the aerodynamic design of the blades. Unfortunately, a redesign of the spar to accommodate thinner airfoils cancelled out the cost savings obtained with the conventional utility pole and as a result this blade concept was not reused as such for later MOD blade designs but did prove that blade cost could be reduced significantly.

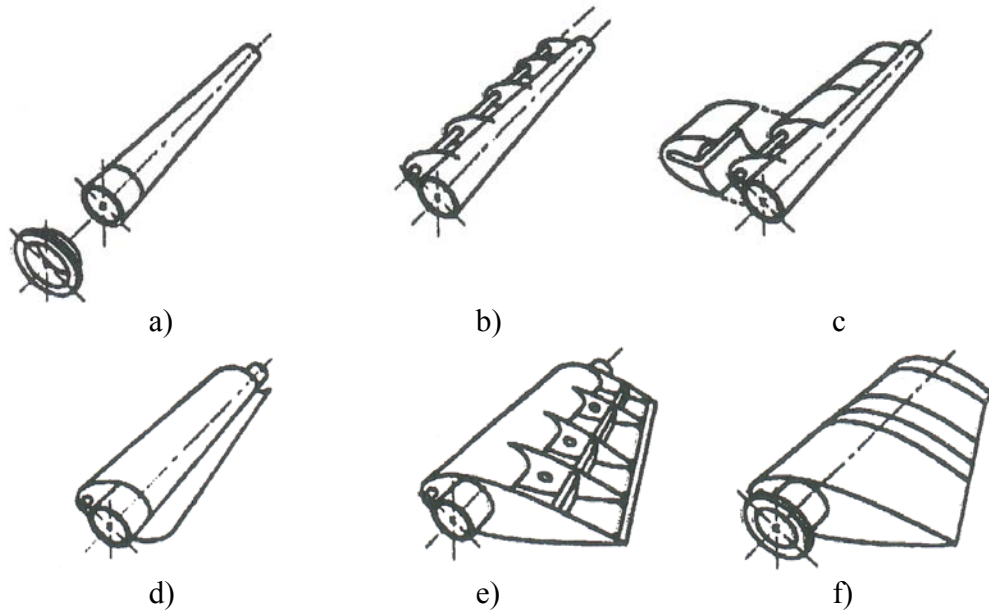


Figure 2.17: Manufacturing steps of the MOD-0A “utility pole” blades [15]. a) preparation of the axisymmetric steel spar, b) installation of the leading edge ribs, c) installation of the foams, d) first GFRP over-wrap, e) installation of the trailing edge ribs and foams, f) second GFRP over-wrap.

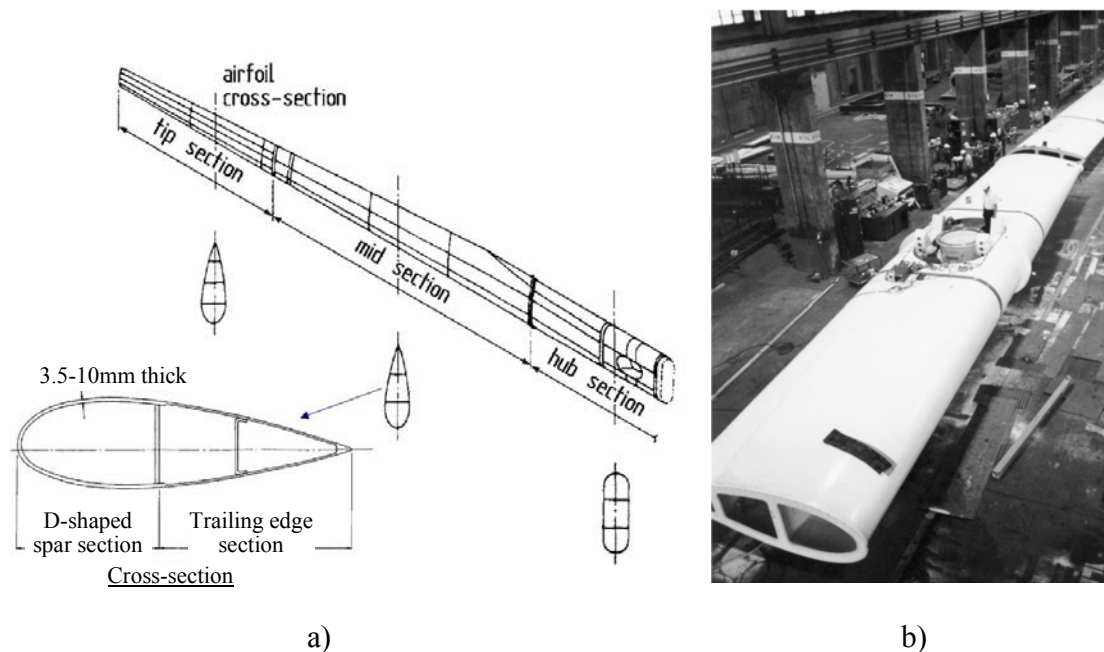


Figure 2.18: Boeing’s MOD-2 steel blade [9,16]. a) blade configuration and cross-section, b) blade hub section showing connecting flange to mid-section.

The last steel design developed for the American MOD program was a fully welded concept proposed again by Boeing for the MOD-2 and MOD-5b wind turbines (see Figure 2.21c and 2.21d). The entire 92-meter rotor (two blades) was constructed using

five sections bolted together: a hub section, two mid sections and two tip sections. Each of these sections was made with a skin of constant thickness welded to internal ribs and webs. As shown in Figure 2.18a, the blade cross-section was similar to a D-spar design with an extra web at the trailing edge. Compared to the aluminum blade skins discussed earlier, the skins for this steel design were rolled-formed prior to being welded [16]. Blade cost for 100 units produced was estimated at \$2,10US/lb or \$400,000US (in 1980) for a full rotor assembly.

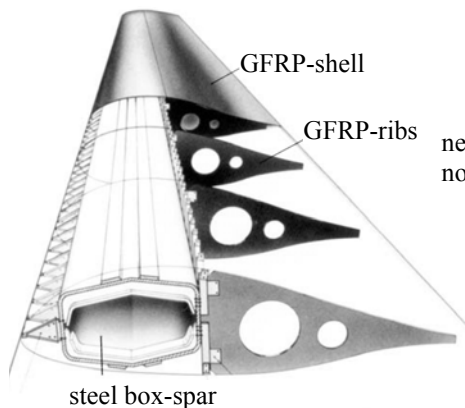


Figure 2.19: M.A.N. hybrid steel/GFRP concept [9].

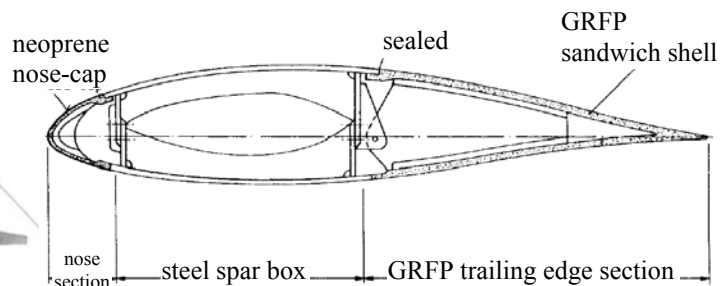


Figure 2.20: M.B.B. hybrid steel/GFRP concept [9].

M.A.N., the contractor for the Growian 3MW experimental turbine (see Figure 2.21e), was the first German company to propose a steel design for very large wind turbine blades. As shown in Figure 2.19, compared to the American MOD-2 and MOD-5b blades, M.A.N. favored a hybrid construction using steel for an inner spar section and GFRP to form aerodynamic surfaces. The spar evolved from a circular section at the blade root to a hexagonal shape for airfoil cross-sections. Fixed to the spar was a series of sandwich construction GFRP trailing-edge ribs and sheet metal leading-edge mini-ribs used to secure in place a GFRP-sandwich shell [9,17]. Weighing 28 tons a piece, the Growian blades are to this day the heaviest wind turbine blades ever built. Since the Growian machine suffered from fatal cracks in the pendulum-frame traverse of its teetering hub, these blades were not used over a long period. Nevertheless, they operated without significant problems for the 420 hours that the turbine was in operation [10].

Another steel blade design reviewed in this chapter is the one used on the Swedish Nasudden experimental machine later commercialized under the name WTS-75 (see Figure 2.21f). The manufacturer of these blades was the German firm ERNO GmbH

(MBB) [18]. As with the previous design, a hybrid steel/GFRP concept was favored. Instead of being fully embedded inside a GFRP skin as with the Growian design, the steel spar conformed to the aerodynamic profile, leaving only the leading edge and trailing edge sections to be made of GFRP (see Figure 2.20). The spar was constructed into two lengthwise sections (upper and lower surface) bolted together approximately at mid-thickness of the airfoil cross-section. In order to solve the problem of detecting the fatigue cracks that are typical of these large steel blades, MBB took the audacious approach of making the spar airtight and pressurizing its inner volume so that cracks could be detected as a drop in pressure [19].



Figure 2.21: Aluminum and steel bladed wind turbines. a) MOD-0 – aluminum blades, b) MOD-1 – steel spar design with foam trailing edge section, c) MOD-2- full steel blade design, d) MOD-5b – full steel blade design, e) GROWIAN – steel spar with GFRP aerodynamic surfaces, f) Nasüdden/WTS-75 - steel spar with GRFP aerodynamic surfaces.

Finally, one last steel blade design has been identified in the literature for which few construction details are known. The Wind Energy Group (WEG) designed, manufactured and installed the 3MW LS-1 wind turbine, the largest wind turbine that the United Kingdom has ever produced. Blades for the LS-1 were subcontracted to British Aerospace and were known as being made of steel. According to Price [20] who reviewed some of the wind energy R&D activities of the UK from 1970 to 1990, the design concept used a stressed-skin concept.

2.5.2 Wood and laminated wood blades

As discussed in the first section of this chapter, wood was the most common material used for blades in the early development of wind energy. In this section, wood blade design will be reviewed with respect to two different construction approaches used between 1970 and 1990: the plain wood construction and the laminated wood construction.

Plain-wood wind turbine blade construction is based on wooden boat-building techniques. The only known large-scale wind turbine blades built using this technique were those built for the Danish Nibe-B turbine in 1980 (see Figure 2.22) [9]. From a structural point of view, the blades performed well but long-term weathering issues such as rot made this concept unrealistic for the 20+ years for which modern turbines are designed.

Laminated wood blades were developed primarily in the United States and in the United Kingdom respectively at the Gougeon Brothers Company and the James Howden Company.

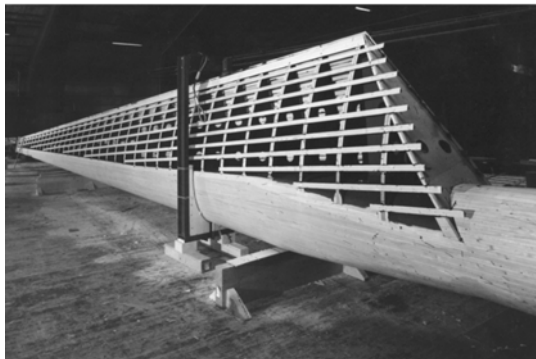


Figure 2.22: Nibe-B plain wood blades showing inner structure [9].

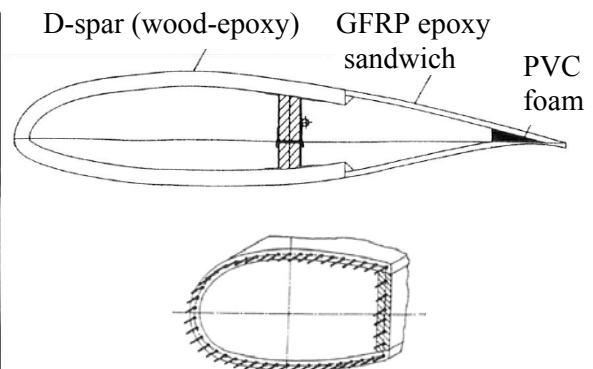


Figure 2.23: Cross-section of Howden's laminated wood blade (top) and blade root stud system (bottom) [21].

Involved in the UK's federally funded projects from day one, the James Howden Company developed a series of wind turbines ranging from 60kW to 750kW. All of these machines were equipped with laminated wood epoxy blades. Based on this experience, Howden was given the contract to design and build blades for a 1MW machine to be installed at Richborough, a wind turbine test facility in Kent, UK (see Figure 2.25a). As shown in Figure 2.23, a hollow laminated wood D-spar covering more than 50% of the chord length was used as the main structural element of the blade while GFRP-sandwich panels completed the trailing-edge section of the blade [21]. Howden's laminated wood blades were known to be especially lightweight mostly because their concept did not use a heavy metallic root-to-hub flange connection like most other designs did at that period. Instead, as depicted in Figure 2.23, Howden relied on a series of high tensile studs simply glued directly in the blade root with a carbon fiber/epoxy grout.

In the United States, Gougeon Brothers Inc. first experimented with wood laminate blades when awarded the contract to supply blades for some of the MOD-0A machines. The blades were made in two half-molds with 1.5mm thick Douglas fir veneers pressed under vacuum after being impregnated with epoxy. The upper and lower laminates of the spar were later assembled by joining them at the leading edge and to the rear flat section of the D-spar (see Figure 2.24). The trailing edge section was a sandwich construction made of plywood skins and an epoxy-impregnated paper honeycomb. As shown in Figure 2.24 where construction details are depicted, Gougeon Brothers inc. also used bonded studs to secure the blade to the hub [13].

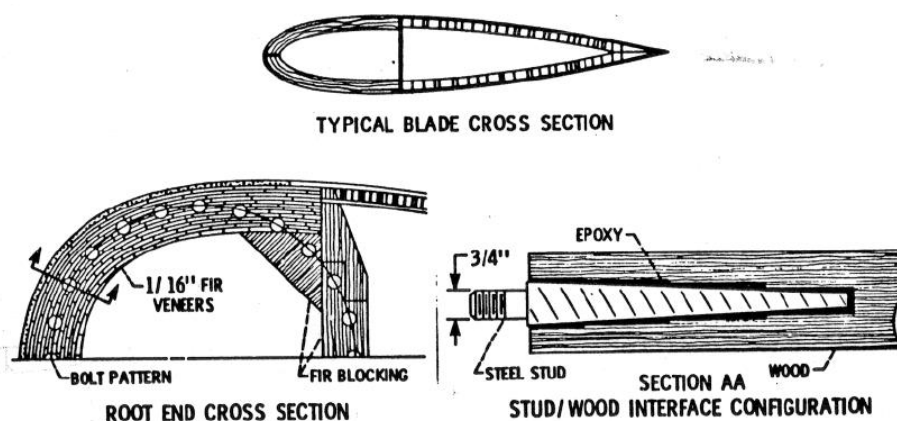


Figure 2.24: Laminated wood/epoxy MOD-0A blade construction details [13].

Both the Howden and the Gougeon Brothers blades were very successful designs and proved to be very reliable. The good fatigue properties of wood coupled with the fact that these blades were relatively light contributed to the good reputation that laminated wood blades earned during that period.

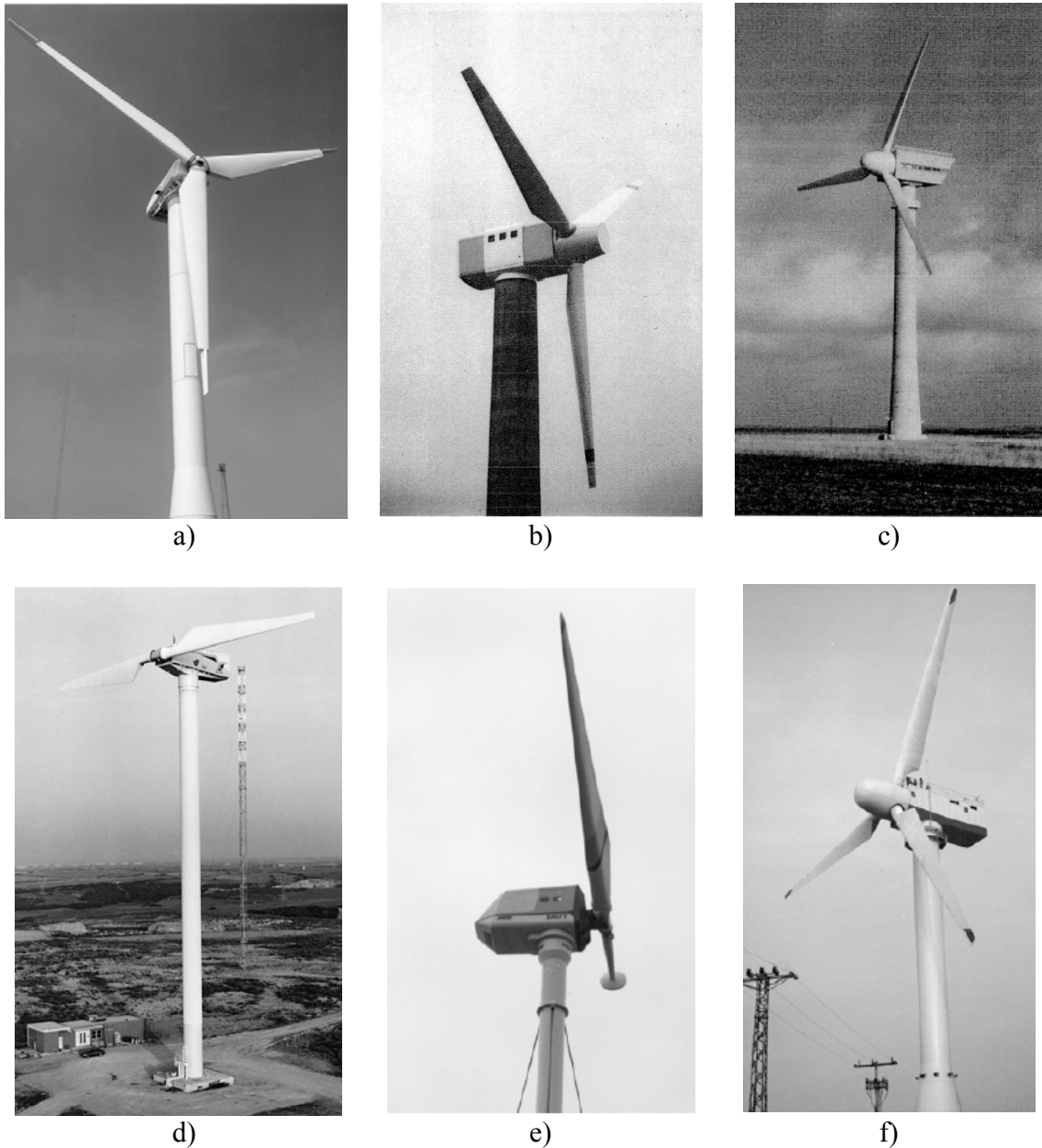


Figure 2.25: Wood laminate and GFRP bladed wind turbines. a) HWP-1000 - wood laminate blades, b) Windane 40 – Tape-wound D-spar and GFRP trailing edge blades, c) Tjaereborg – Tape-wound spar covered with GFRP skins, d) Gamma 60 – Fully filament-wound blades (Hamilton Standard), e) Monoporteros 30 - Monolithic skins bonded at leading edge and trailing edge, blade is foam-filled for skin stability. f) AWEC-60 – bladder molded D-spar with GFRP trailing edge.

2.5.3 Fiber reinforced composite blades

2.5.3.1 Filament or tape winding concepts

Filament or tape winding was a very popular method for blade manufacturing in the United-states and Denmark in the late 1970s and early 1980s. Since only convex shapes can be manufactured with this technique, most blades manufactured with this process used either D-spars or elliptically shaped spars covered with non-structural GFRP skins.

Hamilton Standard, a division of United Technologies, was the first company to experiment with filament winding for the fabrication of the MOD-0 wind turbine blades back in 1976 (see Figure 2.26) [22]. Although NASA never exercised its filament-wound option due to cost and blade weight issues, Hamilton standard pursued the development of the concept and supplied blades for numerous large wind turbines in the 1980s such as the Gamma 60 (Figure 2,25d), the WTS-3 and the WTS-4.

On a structural point of view, the blade used a glass-epoxy D-spar for load bearing. As shown in Figure 2.27, the spar extended to nearly half the chord length of the symmetric airfoil section used for the blade. In order to provide buckling stability of the monolithic skins of the spar, a fiberglass and foam web was glued in place after winding the spar.



Figure 2.26: Filament winding set-up for blade manufacturing at Hamilton Standard [22].

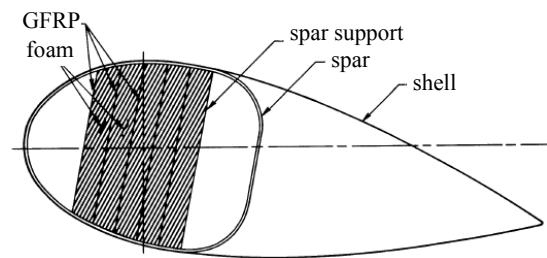


Figure 2.27: Cross section details of the Hamilton standard filament wound blades [23].

On a manufacturing point of view, the blade was fully filament-wound but unidirectional fiberglass fabric was also hand-laid in between some of the filament winding passes of the spar. As shown in Figure 2.28, the spar section was first wound over a two-part mandrel. Once the spar completed, a collapsible trailing edge mandrel was installed on the spar and a final winding pass was done to complete the blade structure. After post-cure, the two mandrels were removed, the mandrel ends of the

blade were capped and the blade was sent off for paint [22]. Although the blade weight could be kept relatively low and the process was fully automatic, the big drawback of this technique was that the winding process proved to be extremely long because of the large laminate thicknesses involved. Properly laying the UD fiberglass fabric in between passes and making sure glass filaments would not bridge in subsequent steps was reportedly another major challenge.

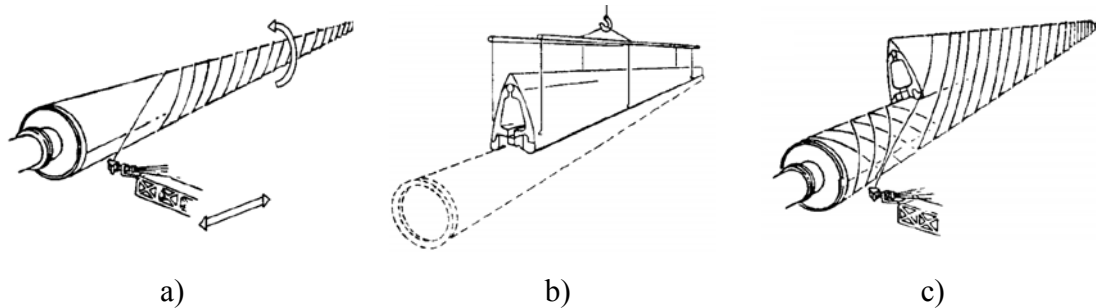


Figure 2.28: Manufacturing process of fully filament-wound blade. a) winding the spar over the spar mandrel, b) placing the trailing edge mandrel, c) winding the final shape of the blade [22].

As an alternative to the continuous filament winding approach proposed by Hamilton Standard, NASA awarded contracts to Structural Composite Industries (SCI) and to Kaman Aerospace to investigate blades made with a tape winding technique [13]. This technique was originally developed by Kaman aerospace for a 150-ft blade demonstrator project in 1978 [24], but was later used for MOD-0A, MOD1 and MOD2 blade designs contracted to either SCI or Kaman [16, 25, 26].

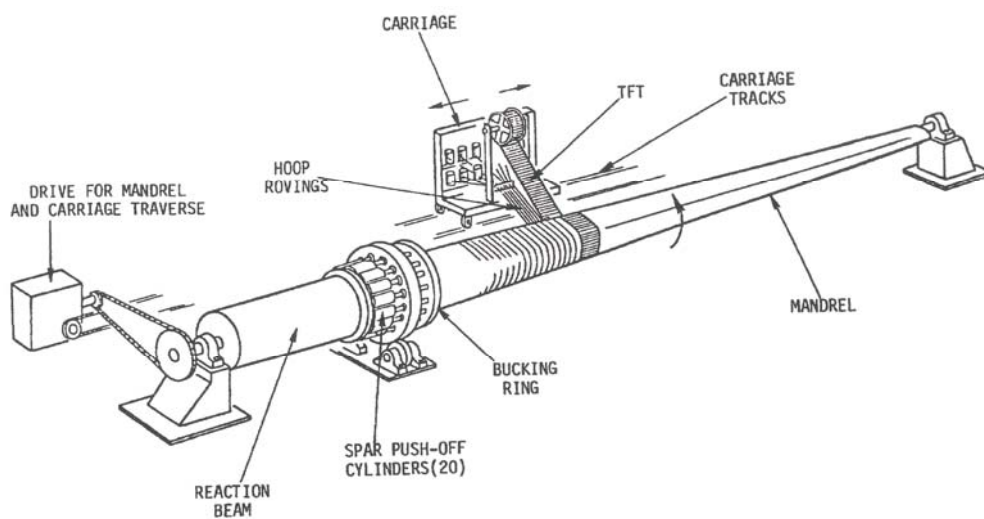


Figure 2.29: Typical transverse filament tape (TFT) winding machine [27].

Instead of using a single filament, the technique uses a wide tape (typically 7 to 30 inches wide) composed primarily of fibers oriented perpendicular to the length of the tape. Due to this particularity of the winding material, the technique is often called transverse filament tape winding (TFT). To provide adequate shear and transverse properties, $\pm 45^\circ$ and longitudinal fiber tapes or rovings were also used in between TFT layers. Figure 2.29 shows the configuration of the winding machine typically used for this manufacturing process (ring winders instead of translational carriages were also used).

The tape winding process offered several advantages over the filament winding process, the most important being the capacity to deposit material at a very rapid rate. In addition, the material could be tapered more easily from root to tip and fibers could be laid down automatically in the span-wise direction with this winding process. As seen later in this chapter, due to its low-cost and versatility, this technique was also exploited in Europe.

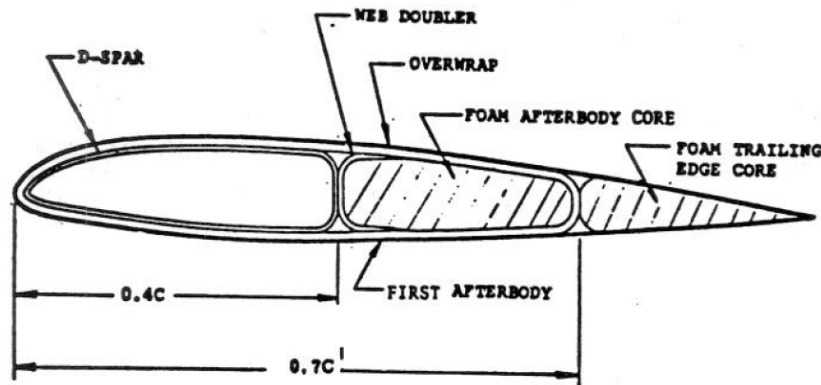


Figure 2.30: Cross-sectional view of the MOD-0A blade manufactured by Structural Composite Industries using a Transverse Filament Tape winding technique [24].

As Hamilton Standard did for their blade, SCI also only used winding to manufacture MOD-0A blades but with a very different topology. As shown in Figure 2.30, the blade cross-section consisted of three cells. According to Gewehr [24], this three-cell topology was favored because of its better resistance to buckling, compared to the single D-spar approach. The two first cells from the leading edge were designed to be the load-bearing cells while the trailing edge cell was used only to complete the airfoil shape. On a manufacturing point of view, the leading edge cell was first wound over a removable steel mandrel while the two other cells were wound subsequently over

foam mandrels, which remained embedded in the structure. These composite blades were installed in 1981 on the MOD-0A machine at Clayton and reportedly performed fairly well without significant damage. Their cost was evaluated at \$65,000US (in 1981) per piece, which was significantly cheaper than the original aluminum blades of the MOD-0 machine [13].

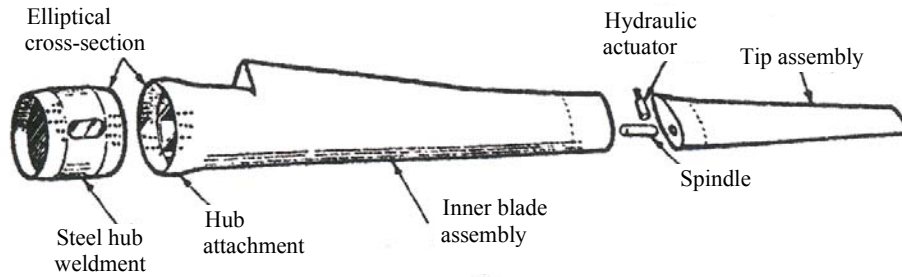


Figure 2.31: MOD-2 composite blade configuration to match the original steel blade design of Boeing [16].

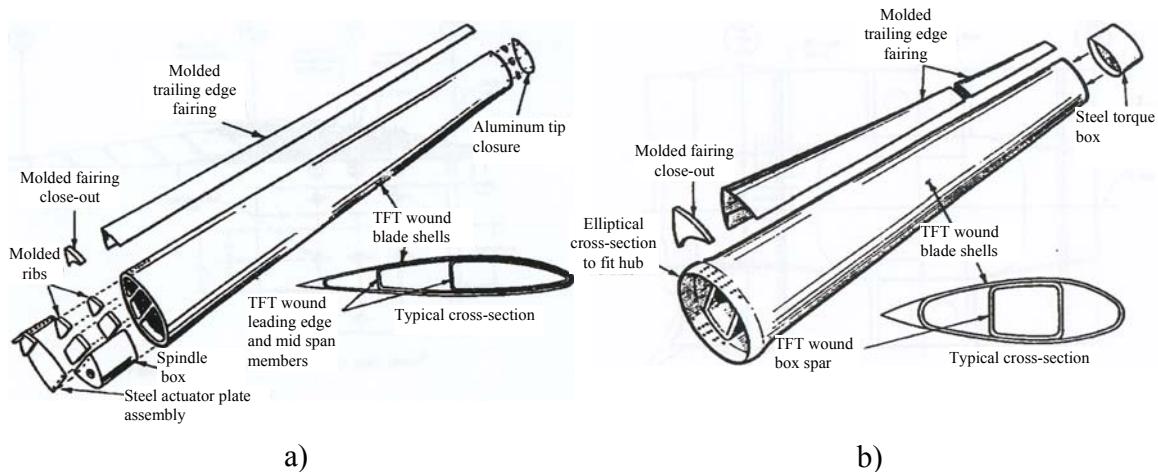


Figure 2.32: MOD-2 composite blade preliminary design construction details [16]. a) blade tip assembly, b) inner blade assembly.

In a second project contracted for NASA, SCI investigated the possibility of using composite blades for the 3.2-MW MOD-2 turbine [13]. At the time NASA asked SCI to develop composite blades for this machine, the conceptual design phase of the turbine was completed and the preliminary design phase was already started using steel blades to be manufactured by Boeing. Because of that, the composite blades were required to respect a series of design specifications for compatibility with the steel blades including matching their first flapwise natural frequency and the use of a tip brake (see Figure 2.31). Due to this late entry in the design phase of the MOD-2 machine, the composite blades were never really intended for manufacturing but did help refine the technology for later TFT-wound blades to be manufactured by Kaman. As with the MOD-0A

blades, SCI used a multi-cell configuration for both the tip and inner blade assembly. Again, as shown in Figure 2.32, the blade sections were planned to be fully tape-wound.

In 1979, based on technology developed for their 150-ft prototype blade [25], Kaman Aerospace designed a new set of blades for the MOD-1 following the principles of a classic single D-spar construction. As presented in Figure 2.33 and 2.34, Kaman used TFT winding first to manufacture a D-spar onto which autoclave-cured honeycomb after-body panels were later bonded [26-27]. Since these composite blades were meant to replace the original MOD-1 steel blades manufactured by Boeing, NASA required that Kaman's design duplicate the stiffness and natural frequency characteristics of the steel blades. Consequently, due to the difference in the elasticity modulus of the materials, matching the stiffness and natural frequency requirement forced significant increases in blade spar depth and thickness that forced compromises in terms of blade weight and cost.

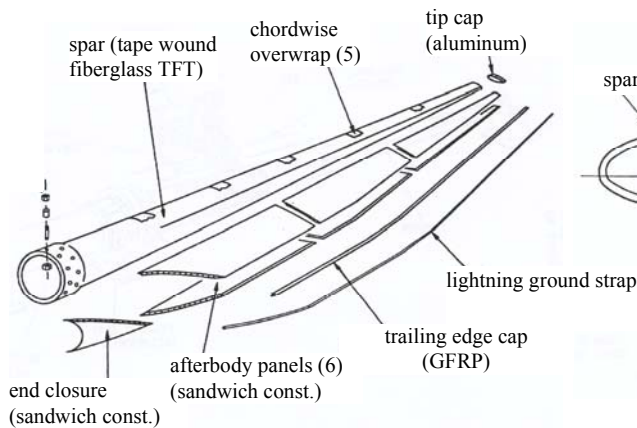


Figure 2.33: Exploded view of Kaman's MOD-1 TFT-wound blades [26].

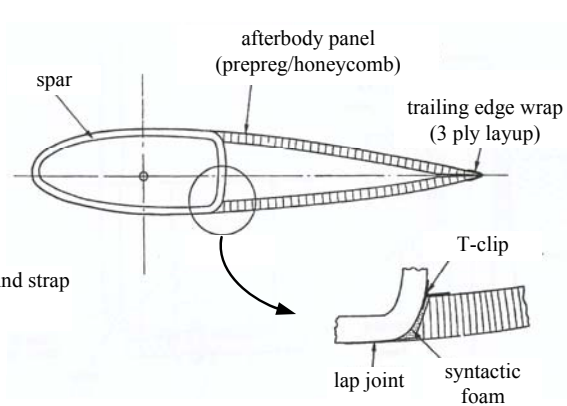


Figure 2.34: Cross section details of Kaman's MOD-1 TFT-wound blades [26].

These composite blades were built but were unfortunately never used because the MOD-1 turbine suffered fatal damage and was dismantled in 1981, the year Kaman was ready to deliver the blades. Nevertheless, the work of Kaman proved the potential of composites for very large blades since the MOD-1 blades were the largest (30m) composite blades ever produced in the United States at the time.

On their side of the ocean, the Danish proposed similar blade designs and manufacturing processes for large wind turbine blades. At the end of the 1970s, as part of the Nibe project, Vølund and OL Boats worked together to produce GFRP blades. Vølund manufactured the D-spar of the blade using TFT winding while OL Boats

produced the trailing edge skins (see Figure 2.36). As depicted in Figure 2.35, the construction was very similar to the previously discussed MOD-1 blade except for the blade skins being produced by hand lay-up, a much cheaper process than pre-pregging. Polyester resin was also used for the D-spar, further reducing the cost of the blades. Another interesting feature of these blades is that the D-spar was not directly used as an aerodynamic surface but rather fully embedded inside the CSM skins. This way, the labor-intensive surface finishing of the rough TFT-wound part was avoided.

At the beginning of the 1980s, *Dansk Vind Teknik* or Danish Wind Technology (DWT) was formed as a result of a partnership between Vølund and other partners. DWT commercialized the Windane turbines with blades ranging from 4.5m to 19m in length using the same technology. The largest of the DWT wind turbines, the Windane 40 is shown in Figure 2.25b.

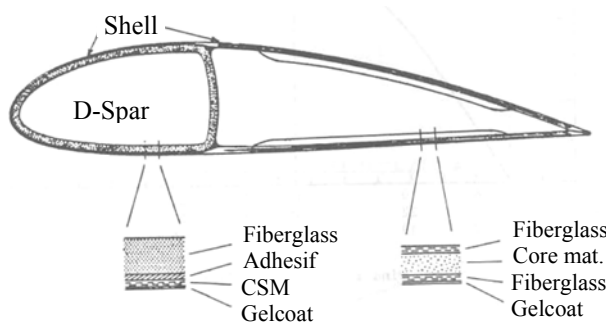


Figure 2.35: Typical cross section details of Danish TFT wound D-spar blades [28].

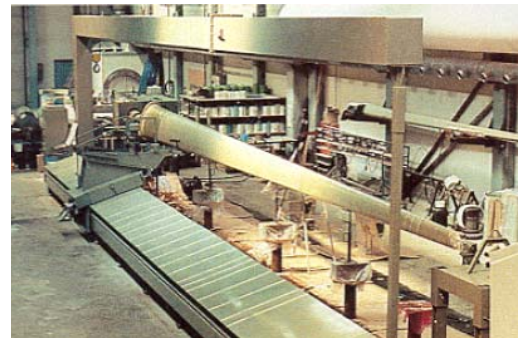


Figure 2.36: Manufacturing of a D-spar at Danish Wind Technology A/S [29].

At the end of the 1980s, the same manufacturing process was adapted by the Danish to build the large blades of the WKA-60 and Tjaereborg turbines (see Figure 2.25c) [30]. The difference in this case was that the spar had an elliptical shape and was placed in the middle of the blade's cross-section (see Figure 2.37a). Again, non-structural skins were produced separately and bonded over the spar to give the blade its desired aerodynamic profile. As with all other previously discussed Danish wound spar designs, a steel flange ensured blade root connection to the hub. In this case, a 1.5m-long 2600-kg forged steel flange was both bonded and bolted as shown in Figure 2.34b. The weight of the 30m Tjaereborg turbine blades including this metallic flange was 9033kg.

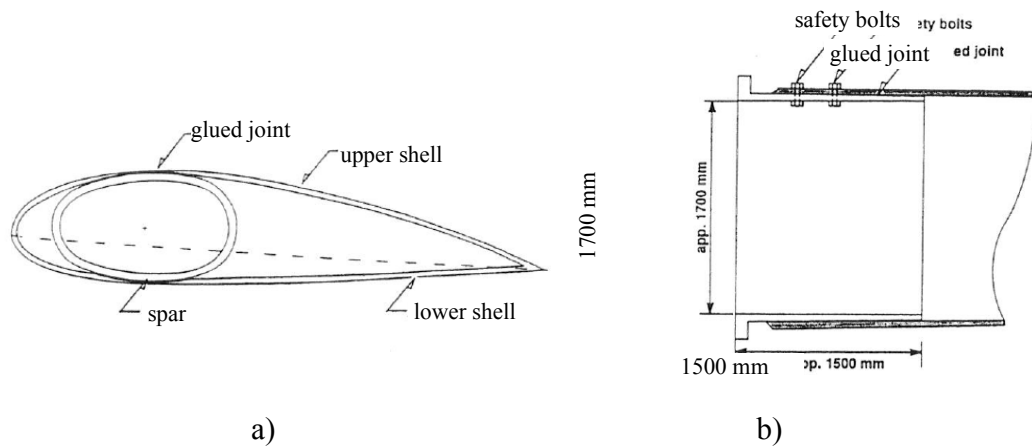


Figure 2.37: Construction details of the Tjaereborg turbine blades [21]. a) cross-section details, b) steel flange attachment details.

2.5.3.2 Structural skin concepts

As mentioned earlier, Hütter was the first to use GFRP for large wind turbine blades (the W34 turbine). His monocoque concept inspired a large number of designs including one of the first concept using carbon fiber laminates. The Monopteros M30 machines (figure 2.25e) were equipped with blades constructed of two monolithic half-skins (upper and lower surface) bonded at the leading edge and trailing edge [31]. The complete structure was built in female molds from tip to counterweight (single bladed concept). The stability of the skins was ensured by later filling this hollow structure with polyurethane foam (see figure 2.38).

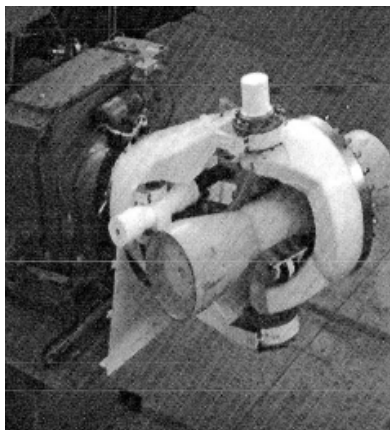


Figure 2.38: Hub assembly of the Monopteros M30 machine showing foam filled inner blade structure [30].

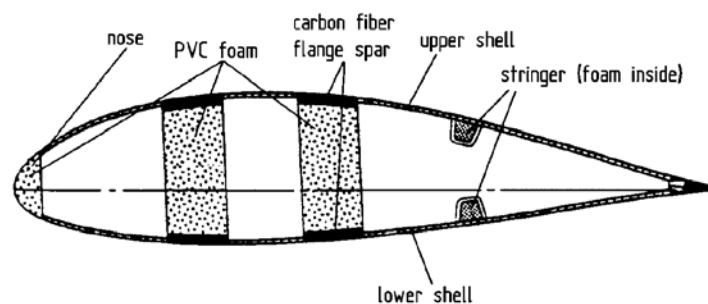


Figure 2.39: Cross-section details of the 40m long Aeolus II blades [9].

Another structural skin design inspired by Hütter's approach was the design favored for the 3MW Aeolus II machine. As depicted in Figure 2.39, the blade designers traded the fully filled inner foam structure with PVC foam sections to link the upper and lower skins. Foam filled stingers were also used aft of the blade's cross-section for skin stability [9].

2.5.3.3 Bladder approach

One innovative approach to blade manufacturing during the "Federal project" era of wind energy development was the use of bladder molding. The main advantage of this technique is that it can yield great exterior surface finishes, thus eliminating the need for spars to be covered with non-structural skins or hand polished as was the case for most of the D-spars earlier discussed. In a collaborative effort between Spanish and Germans, an improved version of the 1.2-MW WKA-60 blades was designed using this approach. As shown in Figure 2.40, the blade structural concept is similar to Kaman's MOD-1 blade design, but in this case, since the spar is manufactured by bladder molding, the labor-intensive surface finishing steps needed for wound composite parts can be eliminated [21].

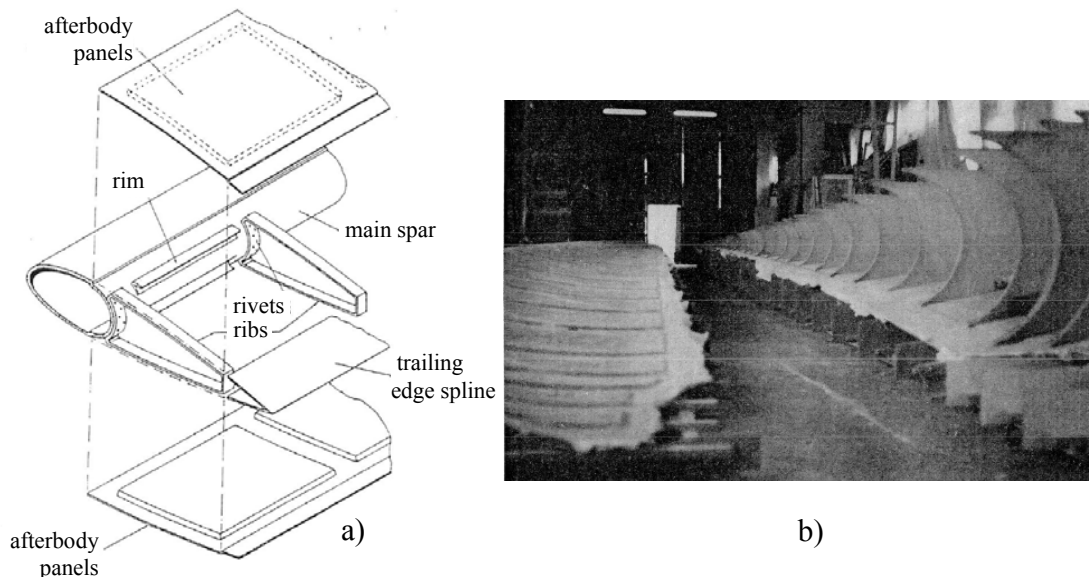


Figure 2.40: The AWEC-60 wind turbine blades. a) exploded view showing structural details [21], b) trailing edge components ready for assembly onto spar [32].

According to reference 21, the manufacturing process of the GFRP D-Spar (3500kg) is a conformation of hand lay-up by means of an inner pressurized bag (bladder

molding). The GFRP trailing edge ribs, trailing edge spline and sandwich-construction skins were produced separately and riveted to the spar to give the blade its final shape. The total weight of the secondary structure was 600kg. With a two-piece forged steel flange weighing 1900kg (+ 500kg of bolts) added to the blade, the fully assembled blade weighed 6500kg.

2.6 Small and medium size wind turbine blade development

At the same period Federal projects were investing significant sums of money for large-scale wind energy development, small companies (mostly Danish) with little or no funding were slowly shaping the industry by their simple and straightforward craftsmanship approach. As a matter of fact, the key players of small and medium size wind turbine development were not engineers nor scientists but rather skilled carpenters, blacksmiths or boat-builders. Beginning in the mid 1970s, approaching the energy self-sufficiency problem from a local perspective, these artisans committed themselves to the development of small wind turbine systems intended for household use. One of the first and most influential of these skilled artisans was Christian Riisager who was the first to connect a turbine to the Danish grid since the Second World War [10]. His turbine, a three-bladed upwind 22kW machine based on the Gedser turbine, was fitted with 4.5m composite blades manufactured by Økær, a small blade manufacturing company owned by Erik Grove-Nielsen. In these early days, as was the case for Riisager's turbines, most Danish wind turbine manufacturers were outsourcing blade manufacturing due to their lack of expertise in composites. Interestingly, the industry ready to fill this technological gap at that period was the boatbuilding industry, which had been manufacturing large composite boats for a number of years. As previously mentioned, one example of this technology transfer from boatbuilding to wind turbine blade manufacturing was the involvement of the OL Boat Company in the development of the Nibe and Windane wind turbine blades.

Unfortunately, small and medium-scale wind turbine development is not well documented in lengthy technical reports as it is the case for Federal projects. These pioneers of wind energy development were obviously more concerned about generating energy at low-cost than writing reports. Due to this lack of literature, personal communications with Erik Grove-Nielsen, early blade designer and manufacturer, will form the base of this small and medium size wind turbine blade structural design

historical review. The next section will discuss these changes and trace back the structural design evolution of Økær blades leading to today's commonly used topologies for large commercial wind turbine blades.

2.6.1 Small monolithic skin blades

The first blades manufactured by Økær were 4.5m blades. These blades were structurally similar to Hütter's design and used hand-laminated upper surface and lower surface skins bonded together at the leading edge and trailing edge. The laminates were composed of 0/90 woven fabric (600g/m^2) and CSM (300 g/m^2) wetted in polyester resin. The root flange design was also based on Hütter's concept and used fiber bundles looped around bushings to secure a metallic flange to the blade's structure (see Figure 2.41 and 2.11). Finally, unlike Hütter's original design, which was hollow, the inner volume of the blade was filled with polyurethane foam to improve the stability of the skins.

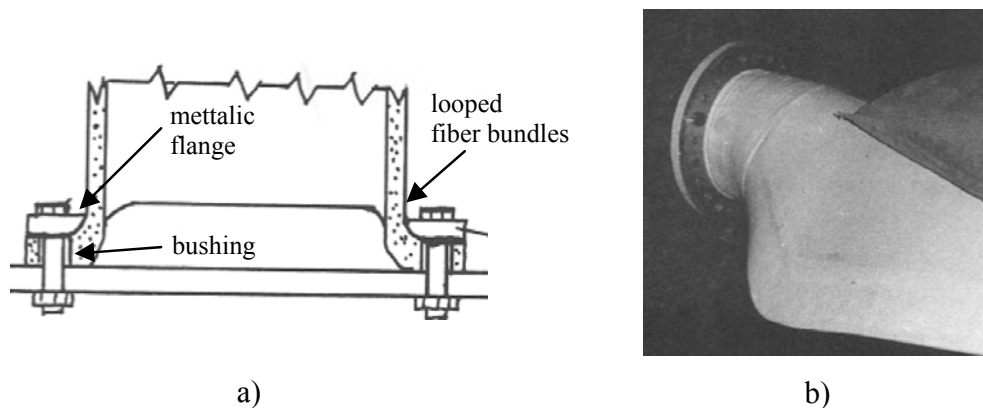


Figure 2.41: Hütter root concept used on Økær 4.5m blades [33]. a) sketch showing bushing and metallic flange, b) blade root showing metallic flange.

In 1978, Økær started the production of a 5m blade. The aerodynamic design was improved, but structurally, it was a scaled-up version of the 4.5m blade. This blade model quickly became quite popular in the “self-builders” community, bringing orders to Økær from Holland, Sweden and other neighboring countries of Denmark. Usually installed on custom-made 20-30kW machines rarely equipped with control devices for over-speed, a series of catastrophic runaways due to storms or loss of load motivated Økær to develop their first tip brake inspired by the design used on the Gedser turbine some 30 years earlier. Soon enough Økær started to sell 5m blades equipped with tip brakes to commercial wind turbine manufacturers such as Nordtank (later merged with

Micon, who later merged to Neg-Micon who was bought by Vestas!) and Bonus (now Siemens) for their 22kW machines.

2.6.2 I-Shaped web blades

In 1980, Økær started the production of a 7.5m blade to equip the Vestas 55kW machine, a new model that would earn its reputation by being so widely used in Californian wind farms during the following years. The blade structural design was again just a simple scale-up of the original 4.5m blade.

Within the first year of blade production, disaster struck one of the Vestas 55 kW machines during a storm at a wind farm in Hinnerup, Denmark. One of the blades suffered from buckling at one third of the blade length, leading to catastrophic failure. After statically loading a blade until failure at their facility, Økær drew the conclusion that the type of failure led to believe that the skin and foam structure might have reached the limit of its load bearing capability for that size of blade. Following this test, Økær redesigned their 7.5m blades in collaboration with Vestas and the material department of the Risø National laboratory in order to attempt to solve the skin stability problem. The new design incorporated a large amount of unidirectional fiber in the skins in the area between 25% and 50% of the blade's cross-section length. Surprisingly enough, since UD material was not standard from industrial weaving companies back then, blade manufacturers like Økær had to self-produce their own UD fabrics using roving bundles [34]. The other important feature of the redesigned 7.5m blade was the introduction of an I-shaped web (built in a separate mold) connecting the two skins in the middle of the area where UD material was placed. The final redesigned concept is illustrated at Figure 2.42. It is worth noting that these blades were still injected with polyurethane foam for a certain period of time until a sandwich construction (Coremat® was originally used) was introduced for the leading edge and trailing edge sections of the blade [34].

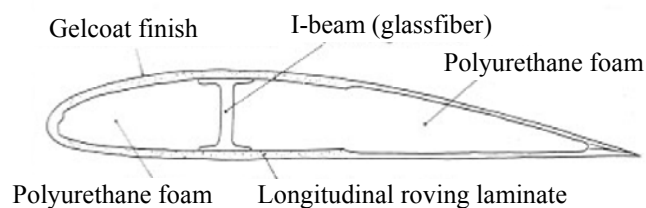


Figure 2.42: Cross-section details of the re-designed Økær 7.5m blades (adapted from [34]).

2.6.3 Box-spar blades

As from 1981, Coronet Boats was licensed to manufacture the Økær blades under the name Aerostar while Grove-Nielsen pursued the design of larger blades. That same year a second blade failure revealed another weakness of the 7.5m blade design. One of the fiber bundles of the Hütter root failed in fatigue. Due to this event, a second important design change occurred with the replacement of the Hütter root by a bonded steel flange. This concept proved less susceptible to fatigue failure but unfortunately significantly increased blade weight and cost. Figure 2.43 shows the static test performed to validate the steel flange blade design. At the same period, Ventilatoren Storck Hengelo B.V. (VSH), the largest Dutch blade manufacturing company at the time, used a similar root concept [35]. Among the thousands of VSH blades in operation in Californian wind farms, hundreds broke down due to root failure (which put an end to the activities of VSH).



Figure 2.43: Økær 7.5m blade under static testing at Risø laboratories to validate the steel flange root design, 1982 [36].

During the following years, wind turbine manufacturers commercialized machines in the 100kW range requiring blades of 9 to 12 meters. With increasing lengths and gravity loads (Aerostar's 12m blade weighed 1200 kg), the introduction of a second web was found necessary in order to increase torsional stiffness and better contain in-plane loads. The I-shaped web of the smaller blades was then traded off for two C-shaped webs placed at beginning and the end of the UD-reinforced area to form a box-spar. In addition, these new 12m blades introduced the use of steel studs for root connection as an alternative to the steel flange, providing a lighter and cheaper solution for load transfer to the rotor hub.

2.7 Modern large wind turbine blade design

Figure 2.44 illustrates the blade design evolution leading to today's common blade structural topology and root connection for large composites wind turbine blades. Although most blade manufacturers have switched to epoxy systems and some of them incorporate carbon fibers in highly stressed areas of the blades, the construction method they favor still relies on a two-blade skin assembly bonded at the leading edge and trailing edge. Box spars are either formed using the two C-shape web approach just discussed (typical of LM glassfiber blades) or produced separately on a spar mandrel (approach preferred by Vestas, Gamesa and others). Once released from the mandrel, non-structural skins are bonded to the spar to complete the blade structure.

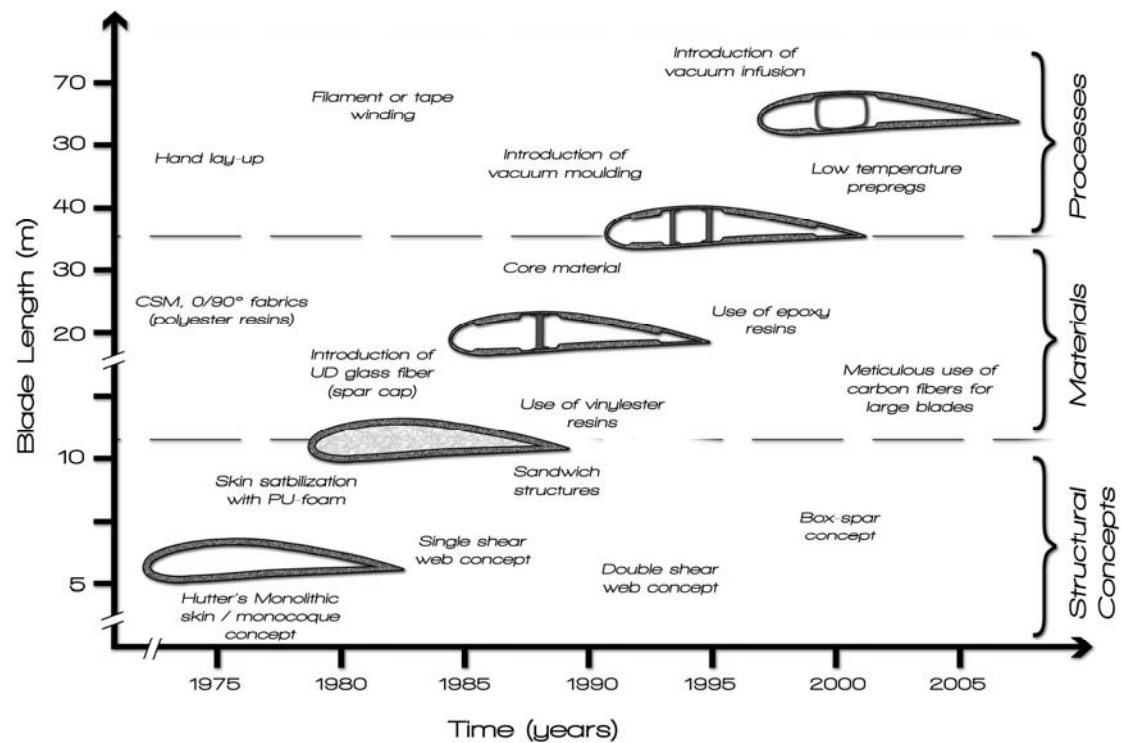


Figure 2.43: Evolution of FRP composite wind turbine blade structural design concepts, materials and manufacturing processes.

Core materials such as balsa, PVC or SAN foams are generally used for sandwich panels. Fiber architecture has evolved over the years with heavy ($1\text{kg}/\text{m}^2$) stitched Triaxial and UD fabrics now in widespread use. Manufacturing generally involves either resin infusion or low temperature pre-pregs [37]. Compared to hand lay-up, these two techniques brought the possibility of building better quality laminates, but also helped

manufacturers comply with governmental legislation on styrene and other volatile gas emissions. It is worth noting that wood laminate blades are still produced by some manufacturers in lengths up to 40 meters.

Non-material and process-related aspects such as specific wind turbine design changes have also affected blade mass over the years. For example, the introduction of full-span blade pitching in replacement of tip breaks has helped reduce blade weight. First introduced simply to brake the turbine for wind speed above cut-out wind speed, this system helped eliminate the tip brake mechanism, which was vulnerable to lightning strikes. Later on, the same concept was used to control the turbine above rated wind speed instead of using stall for power control. This helped further reduce blade mass since pitch-regulated machines are more lightly loaded above rated wind speed than stall regulated machines.

2.8 Conclusions

2.8.1 *Material issues*

As seen in this chapter, metals (steel and aluminum), wood, wood laminates and fiber reinforced polymer (FRP) composite have been used for blade structures over the years. Interestingly, in the beginning of large wind turbine development, blade material selection was influenced mostly by the level of confidence the designer had in a specific material rather than based on engineering merit indexes as is usually the case in design [11,37]. Early steel blade design is a good example of a material not being selected because of its high bending merit index ($E^{1/2}/\rho$) but rather because it was far better characterized than most other materials at the time (especially in terms of fatigue).

Since composite materials are now much better understood, using steel for modern wind turbine blades no longer makes any sense. Current material selection is done exclusively within the composite material family and is driven primarily by cost issues since the cost of energy (\$/kWh) is what matters most. Polyester resins still being used by LM Glassfiber reflect this tendency of favoring cost against mechanical properties for resin selection. The same principle applies to carbon fibers, of which cost is the main factor delaying their use for very large blades rather than their merit index.

It is likely that due to the impressive growth rate of the wind energy industry, recyclability will soon become a key factor in addition to cost for material selection.

Indeed, the wind energy composite market has witnessed an impressive steady growth rate of 20% for the last couple of years and should surpass the aerospace market, with 618,000 tons consumed per year compared to 515,000 tons by 2013 [38]. As a consequence of blade design life being limited to 20 years, blade scrap tonnage should be in the same order of magnitude by 2025 and rise every year by 20%. Judging from these numbers, it is likely that the wind energy industry will eventually be forced to manage their product from cradle to grave, as is currently the case in the automotive industry because of the European Union “end of life” directive.

Since resin systems used today are exclusively thermosets, matrix recovery will never be possible. Therefore, two options are currently possible to recycle blades: Mechanical recycling (shredding and reuse as filler for other materials), or incineration with or without energy recovery. If these methods for recycling are not compliant with future governmental directives, thermoplastic matrixes will most probably force their way in the industry because of their capacity to be fully recycled. It is ironic that thermoplastic composites are facing today the same difficulties thermoset composites were facing in the 1970s when benchmarked against steel: 1- The level of confidence in their mechanical properties is insufficient for their use in blade design, 2- Manufacturing processes need further development to allow the production of large parts.

2.8.2 Structural and manufacturing issues

Over the years, blade structural design has been influenced strongly by the technology used in the industries involved in wind energy development. In retrospect, early wind energy technology development followed two very distinct paths: Multi-MW wind turbine development (Federally funded projects) or small and medium size wind turbine development. Due to the significant difference in size of the machines and distinct backgrounds of the key players involved in the development, very different structural designs and manufacturing techniques were used depending on the approach followed. The following two sections will review structural and manufacturing issues of blade design with respect to these two very different paths followed for wind energy development.

2.8.2.1 Steel designs

As seen in section 2.4, Federal R&D programs favored the development of large-scale wind energy and generally awarded contracts to large well-established companies. In the United States, since the aerospace industry was highly involved in wind energy development, the original concepts emerging from their program drew inspiration from aircraft structures of the 1970s, with most blades being metallic stressed-skin designs using ribs and stringers. In Germany, contracts were also often awarded to companies in the aerospace industry (M.B.B.) but also involved machine engineering industries like M.A.N. Their early designs also used steel but heavy spar designs covered with aerodynamic secondary structures were preferred over the stressed skin approach often preferred by the Americans.

Soon enough, both Americans and Germans engineers realized that apart from sharing some common aerodynamic principals, the wind energy business and the aeronautical business were very different. The cost of energy, which depends strongly on the capital cost of the machine and its reliability during operation, is the ultimate criterion for measuring the performance of a wind energy system. Early projects led by the aeronautic industry were simply off-track with respect to this criterion since they used expensive materials and manufacturing processes borrowed from the aeronautical industry and also failed with respect to reliability since most machines showed very poor availability.

2.8.2.2 Composite designs

In an effort to reduce cost, Federal programs looked into composite blades in the mid 1970s. Since the goal of most Federal programs was to develop MW-sized wind turbines, engineers faced the challenge of developing both manufacturing processes and structural designs for these very large composite parts. At that time, the only industry having experience with such large composite parts were companies building large pipes and reservoirs using filament or tape winding. Consequently, most large composite blades produced at the end of the seventies and early eighties were either filament or tape wound. Due to the limitations of the winding process, blade designs used either symmetric or flat lower surface airfoils and relied on single or multi-cell spars for load bearing.

Conversely, small and medium size blade designers evolving at the same period did not face the same problems as large-scale wind turbine blade designers building composite structures 20-30 meters in length. They thus decided to rely on technology transfer from the composite boat business to build their wind turbine blades of 5 to 10 meters in length. Like composite boats using a hull and a deck bonded together at a partition line, the blades they built were hand-laminated in two separate molds and bonded at the leading edge and trailing edge.

As shown earlier in Figure 2.43, this original hand-laminated monolithic-skin design evolved over a 30-year period into the single-shear web design typical of the 8 to 12 meter blades built in the 1980s, and eventually transformed into the double-shear web or box spar concept used today. The introduction of longitudinal fibers in spar caps and the use of sandwich constructions also played a significant role in structural design evolution from the 1970s to the present.

Improvements to manufacturing techniques with the conventional hand lay-up process being replaced by vacuum infusion methods or pre-pregging also contributed to lowering the weight and improving the quality of the laminates. Finally, numerous design changes to blade root details helped refine the design, with first generation heavy one-piece metallic flanges being replaced by bonded-in sleeves and stud connections.

Figure 2.44, showing different three-bladed wind turbine's specific blade mass plotted against their length, illustrates the effects of some of the above-mentioned improvements to blade design. The top group shows the early heavy metallic flange blades produced by hand lamination using polyester resin and glass fiber. Just below, displaying a lower specific blade mass are blades refined in design because of the use of bonded-in stud root connections and improved laminate properties (lengthwise UD fibers and sandwich constructions). Finally, in the lower specific blade mass group are the latest generation of blades in which carbon fibers, epoxy resin systems, vacuum infusion or pre-preg technology are often used. It is worth noting that although care was taken to present only blades dedicated to three-bladed upwind turbines, factors not related to structural or manufacturing issues can also influence blade mass. Early blades equipped with tip brakes are obviously a bit heavier and stall control blades could also be considered slightly heavier than pitch-control blades. Nevertheless, these effects are considered marginal compared to the effect of tip speed on blade loading. This effect is clearly visible among large blades dedicated to offshore applications showing a particularly low weight for their lengths.

As seen in this chapter, wind turbine blade manufacturing is now a well-established industry with thousands of blades being produced worldwide every year. Successfully introducing a new material such as thermoplastic composites in the industry can only be done if proven that it's economically sound. As it will be presented in later chapters, manufacturing cost reductions may be possible since thermoplastic composites are usually produced faster than thermoset composites. In terms of materials, some thermoplastic resins are cheaper than epoxy systems and could provide additional cost reductions.

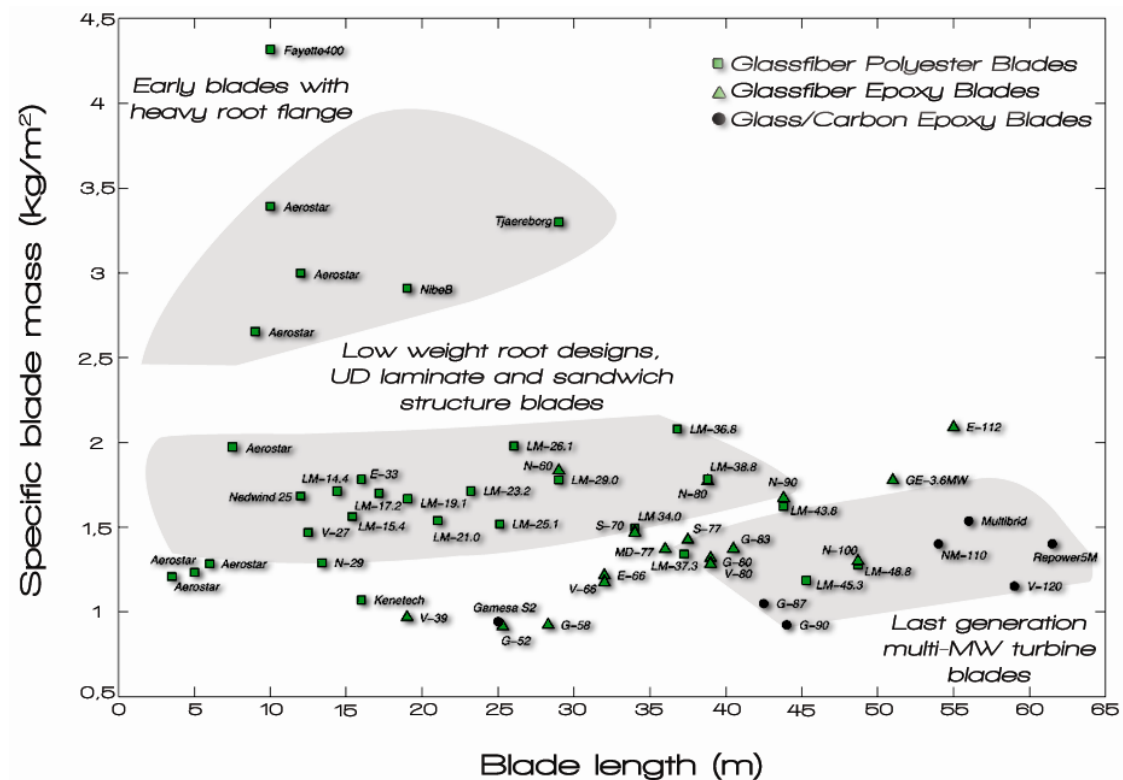


Figure 2.44: Evolution of composite blade specific mass (mass/rotor swept area) as a function of blade length showing blades grouped with respect to design characteristics..

2.9 References

- [1] Shepherd, D. *Historical Development of the Windmill*. National Aeronautics and Space Administration, DOE/NASA/5366-1, Lewis Research Center, Ohio, 1990.
- [2] Kealey, E.J. *Harvesting the Air: Windmill Pioneers in the Twelfth-Century England*. Berkeley, University of California Press, 1987.
- [3] Sian-Sheng, G. *Wind Power for Pumping Water in China*. Proceedings of the European Wind Energy Conference, Hamburg, Germany, October, 1984.
- [4] Debeir, J-C., Deléage, J-P, Héméry, D. *In the Servitude of Power: Energy and Civilization through the Ages*. trans. John Barzman, Zed books, London, 1991.
- [5] Gipe, P. *Wind Energy Comes of Age*. John Wiley & Sons, New-York, 1995.
- [6] Drees, J., M., *Blade twist, Droop Snoot, and Forward Spars*, Vertiflite, American Helicopter Society, September/October, 1976.
- [7] Stokhuyzen, F., *The Dutch Windmill*. Bussum van Dishoeck n.d., 1962.
- [8] Baker, L. *A field Guide to American Windmills*. Norman, Ok: University of Oklahoma Press, 1985.
- [9] Hau, E. *Wind turbines: Fundamentals, Technologies, Application and Economics*. second edition, Springer-Verlag, Berlin Heidelberg, 2006.
- [10] Heymann, M., *Signs of Hubris: The Shaping of Wind Technology Styles in Germany, Denmark and the United-States, 1940-1990*. Technology and Culture, Vol. 39, October 1998.
- [11] Bowen, D.H., Maskell, C.W.A., Phillips, D.C., Thorpe, T.W., Wells, G.M., Wilkins, N.J.M., *Materials Aspects of Large Aerogenerator Blades*. Proceedings of the European Wind Energy Conference – Hamburg, 1984, pp. 281-286
- [12] Lindscott, B.S., Shaltens, R.K., Eggers, A.G., *Aluminum Blade Development for the MOD-0A 200kW Wind Turbine*. NASA TM 82594, DOE/NASA/20370/20, 1981.
- [13] Faddoul, J.R., *An Overview of Large Horizontal Axis Wind Turbine Blades*. Proceedings of the European Wind Energy Conference – Hamburg, 1984, pp. 113-149
- [14] Van Bronkhorst, J., *The MOD-1 Steel Blade*. The Boeing Engineering and Construction Company, Report, N80-16476, 1979

- [15] Keith, T.G. Jr, Sullivan T.L., Viterna, L.A., *Performance of a Steel Spar Wind Turbine Blade on the MOD-0 100kW Experimental Wind Turbine*. NASA TM-81588, DOE/NASA/1028-27, 1980.
- [16] Boeing Engineering and Construction Company, *MOD-2 Wind Turbine System Concept and Preliminary Design Report, Volume II- Details Report*. NASA CR 159609, DOE/NASA/0002-80/2, July 1979.
- [17] Maschinenfabrik Augsburg-Nürnberg (MAN) Neue Technologie, *Large Wind Energy Converter GROWIAN*. Brochure, 1981.
- [18] Boving KMW Turbin AB (BKT), *Wind Turbine System Nasüdden*. Brochure, 1986.
- [19] National Swedish Board for Energy Source Development, *The Maglarp and Nasüdden Turbines*. 1982.
- [20] Price, T.J., *UK Large-Scale Wind Power Programme From 1970 to 1990: The Carmarthen Bay Experiments and the Musgrove Vertical-Axis Turbines*. Wind Engineering, Vol. 30, no. 3, 2006.
- [21] Hau, E. Lagenbrinck, J., Palz, W., *Wega: Large Wind Turbines*. Springer-Verlag, Berlin, 1993.
- [22] Boving KMW Turbin AB (BKT), *Wind Turbine System WTS-75-3*. Brochure, 1986.
- [23] Griffiee, D.G., Jr., Gustafson, R.E., *Design, Fabrication, and Test of a Composite Material Wind Turbine Rotor Blade*. DOE/NASA/9773-78/1, report, 1978.
- [24] Gewehr, H.W., *Design, Fabrication, Test and Evaluation of a Prototype 150ft Long Composite Wind Turbine Rotor Blade*. NASA CR-159775, DOE/NASA/0600-79/1, 1979.
- [25] Weingart, O., *Design, Evaluation and Fabrication of Low-Cost Composite Blades for Intermediate-Size Wind Turbines*. NASA CR-165343, 1981.
- [26] Batesole, W.R., *Fiberglass Composite Blades for the 2MW MOD-1 Wind Turbine Generator*. Second DOE/NASA workshop on large horizontal axis wind turbine proceedings, Cleveland, Ohio, 1981, p.215-238.
- [27] Batesole, W.R., Gunsallus, G.T., *Design and Fabrication of Composite Blades for the MOD-1 Wind Turbine Generator, Final Report*. NASA-CR-167987, DOE/NASA/0131-1, 1981.
- [28] Vølund Fiberglass division A/S, *Wind Turbine Brochure*. Brochure, 1981.
- [29] Danish Wind Technology A/S (Dansk Vindteknik), *Windane 31 Wind Power Plant*, Brochure. 1983.

- [30] International Energy Agency (IEA), *IEA Large-Scale Wind Energy 1989 Annual Report*. National Energy Administration Sweden, 1989.
- [31] International Energy Agency (IEA), *IEA Large-Scale Wind Energy 1988 Annual Report*. National Energy Administration Sweden, 1988.
- [32] International Energy Agency (IEA), *IEA Large-Scale Wind Energy 1987 Annual Report*. National Energy Administration Sweden, 1987.
- [33] Økær Vind-Energi, *Økær 4.5m Blade Technical Data Sheet*. 1977.
- [34] Grove-Nielsen, E., *Personal communications*. 2007.
- [35] de Boer, W., E., *Design, Construction and performance of WPX Wind Turbine Rotor Blades*, Proceedings of the European Wind Energy Conference, Hamburg, Germany, October, 1984.
- [36] Altenergy, *Aerostar Rotor Blades*. Brochure, 1986.
- [37] Brondsted, P., Lilholt, H., Aage, L. *Composite Materials for Wind Power Turbine Blades*, Annual review of Materials Research, 2005, 35:505-538.
- [38] JEC Composites, *Global Market Scenario Dynamic of the Composites Industry – 2009 Release. Strategic Studies*, 2009.

CHAPTER 3

THERMOPLASTIC COMPOSITE MATERIALS AND MANUFACTURING PROCESSES

POTENTIAL BENEFITS FOR BLADES

Ideas undergo a process of emergence by emergency. When they are needed badly enough, they are accepted.
 - Richard Buckminster Fuller

Chapter three will focus on the state of the art of thermoplastic materials and processes and their potential use for wind turbine blade structures. Material properties, raw material form, manufacturing techniques and process characteristics will be reviewed. At the end of this chapter, potential benefits and drawbacks of using thermoplastic composites for blade structures will be outlined with respect to material functionality, cost and sustainability issues.

3.1 Introduction

As discussed earlier in this dissertation, thermoplastic polymers differ from their thermoset counterpart primarily by their melt temperature being lower than their decomposition temperature, while thermoset polymers have melting temperatures higher than their decomposition temperature, meaning that they cannot be reshaped upon melting. In molecular terms, this characteristic can be correlated to molecular weight, since an increase in molecular weight increases the melting temperature. Thermoset have very high molecular weights because of the cross-links between their polymer chains, while thermoplastics have lower molecular weight since they are generally not cross-linked. This fundamental difference in physical properties between thermosets and thermoplastics has governed the development of their respective manufacturing techniques over the years with thermoplastic usually being melt processed while thermosets are exclusively reactively processed.

In order to position current state of the art thermoplastic composites clearly with respect to thermoset composites, it is interesting first to compare thermoplastic and

thermoset polymers from a global perspective. With respect to market share, each polymer type has its own specific niche in the very broad plastic and composite market, which includes all products made with a polymeric resin, whether non-reinforced and fiber-reinforced. In this global market, fiber-reinforced plastics (short and long fibers) only take 20% of the total market, leaving 80% of the market to non-reinforced plastic goods. Within this large non-reinforced plastic sub-market, thermoplastics clearly dominate with 80% of the market share [1]. The reason why thermoplastics so massively dictate the non-reinforced product market is due mainly to their ability to be processed using fast melt manufacturing techniques such as injection molding, extrusion or thermoforming instead of the longer chemically reactive processes typically used for thermoset parts.

It is noted with interest that the fiber-reinforced plastics market is dominated by thermosets rather than thermoplastics, with thermosets claiming approximately 80% of this market. Again, as was the case with non-reinforced goods, process capability is the main reason why thermosets are usually preferred for fiber-reinforced parts. Long-fiber reinforced parts are generally large and not well suited for melt processes requiring a significant amount of heat and pressure. In contrast, room or low temperature cure thermoset systems offer virtually unlimited part size. Also, since fiber to matrix adhesion is the key to getting full benefits out of the reinforcement in long-fiber composites, the polymer systems must provide proper fiber impregnation and adhesion. These aspects being more difficult with highly viscous molten thermoplastic polymers, low viscosity chemically reacted thermoset resin systems have often been preferred up to now for large structural parts.

Fiber-reinforced polymer composites are usually classified in two different categories: Engineering composites and high-performance composites. As shown in Table 3.1, engineering composites typically use low-cost resin systems, glass reinforcements and conventional manufacturing processes, while high-performance composites generally rely on more expensive materials and high-tech custom manufacturing processes. In support of the above discussion on manufacturing, it is interesting to note in Table 3.1 that thermoplastic and thermoset engineering composites are processed very differently. Engineering thermoset composites are produced using traditional reactive processes (spray-up, RTM, etc.) while thermoplastic composites are usually molded with classic plastic manufacturing techniques such as injection molding or extrusion. The main difference from the originally developed processes for non-

reinforced thermoplastic materials lies in the fact that plastic pellets are compounded prior to injection to introduce short fibers at a volume content of up to 40-50%. Since advanced thermoplastic composites use long fibers, these conventional engineering plastic manufacturing techniques obviously cannot be used. Therefore, typical processes for advanced thermoplastic composites are either processes developed initially for thermosets and adapted for thermoplastics (e.g. autoclave processed semi-pregs), or specific thermoplastic composite processes such as thermoforming or new automated fiber placement and consolidation techniques.

Over the past decade, a slow but steady shift from thermoset-based composites towards thermoplastic composites has been observed for both engineering and high performance composites [2-3]. For engineering composites, this shift was due primarily to recent legislation regarding land-fill, forcing the automotive industry to move away from non-recyclable compression-molded thermoset-based parts (SMC) in favor of sustainable short-fiber thermoplastic injection molded parts (GMT). Concerning advanced composites, cost has been the main factor driving the technology switch towards thermoplastics instead of recycling. Long and expensive autoclave-processed thermoset parts are slowly being reengineered for production with cheaper press-forming technology using thermoplastic materials.

Table 3.1: General characteristics of thermoplastic and thermoset engineering composites and advanced composites (adapted from [1]).

	Engineering Composites		Advanced Composites	
	Thermosets	Thermoplastics	Thermosets	Thermoplastics
Resin types	Low cost polyester, vinylester or epoxy	Traditional commodity plastics: PP, PC, PET, ABS, etc.	Epoxy, phenolics, polyimides, etc.	High performance plastics: PEEK, PPS, PEI, etc.
Reinforcement types	Glass (chopped or woven)	Glass (short fibers)	Carbon, aramids and other high performance fibers (long fibers)	Carbon, aramids and other high performance fibers (long fibers)
Fiber volume content	Up to 50%	Up to 40%	50% to 75%	50% to 75%
Manufacturing Processes	Traditional thermoset reactive processes: spray-up, lay-up, resin transfert molding, pultrusion, filament winding, etc.	Traditional thermoplastic processes: injection molding, extrusion, thermoforming, blow molding, etc.	Precision placement methods, prepregging, autoclave cure, etc.	Adapted methods from thermosets: semi-pregs, autoclave cure, etc. Specific high performance plastic melt processes.

Since continuous fiber composite is the topic of interest in this thesis, the focus of this chapter will be kept on associated processes and raw materials when reviewing the current state of the art of thermoplastic composite manufacturing. At the end of this chapter, these processes will be evaluated with respect to their potential usage for wind turbine blade manufacturing. Process limitations, cost and overall sustainability will be the main factors used for evaluation.

3.2 Thermoplastic composite raw materials

Long-fiber thermoplastic composites are commercially available typically in the form of consolidated sheets, prepregs or semi-preg unidirectional laminates or fabrics. Reaction injection molding resin systems are also available for *in-situ* polymerization processes such as RTM, RIM or vacuum infusion. As mentioned in the introduction, since fiber impregnation is one of the main concerns when processing thermoplastic composites, manufacturers have developed different techniques to ensure proper fiber wet-out with a variety of different matrix systems (see Table 3.2 for common thermoplastic composite matrix systems). After first reviewing these techniques, each form of commercially available thermoplastic composite material will be discussed. Table 3.3 summarizes the current most popular commercially available products.

Table 3.2: Physical and mechanical properties of the most common thermoplastic polymers used as matrices for long-fiber reinforced composites. Typical thermoset matrices are given for comparison (adapted from [2,4]).

Matrix system	Density	E _{tens} (GPa)	σ _{tens} (MPa)	ε _{failure} (%)	T _m (°C)	T _{process} (°C)	Cost* (€/kg)
Polypropylene (PP)	0.9	1.4	31-42	100-600	165	190-230	1.64
Polybutylene terephthalate (PBT)	1.3	2.5	56	50-300	235	240-275	2.75
Polyethylene terephthalate (PET)	1.3	3.5	48-73	30-300	250	260-350	4.55
Polymethylmetacrylate (PMMA)	1.2	2.8	60-78	2-6	150	200-250	3.31
Polyamide 6 (PA6)	1.1	3.0	35	50	220	230-285	3.00
Polyamide 66 (PA66)	1.1	1.3	55	50	260	270-285	5.40
Polyamide 12 (PA12)	1.0	1.1	40	50	175	180-275	8.5
Polyphenylene sulfide (PPS)	1.35	3.4	48-87	1-4	285	310-335	7.99
Polyetherimide (PEI)	1.26	3.4	62-150	5-90	-	340-370	17.93
Polyetheretherketone (PEEK)	1.3	3.6	70-105	15-30	335	340-400	83.70
Polyester (thermoset)	1-1.1	2.5-3.5	30-50	2-3	-	rt-100	3-5
Epoxy (thermoset)	1.15	3-3.5	55-120	3-6	-	rt-175	4-6

* based on 2006 prices (Source: Steinhall inc. and [3])

Table 3.3: Principal characteristics of the most common commercially available long-fiber reinforced thermoplastic composites (from data sheets).

Brand name	Material form	Fiber/matrix	M _f	Details
Twintex® P PP Vetrotex	Consolidated plate from commingled fabric	Glass/PP	60%	<ul style="list-style-type: none"> - Used in diaphragm, vacuum or press forming processing. - 0.5-2mm thick plates available with plain weave fabric. - Automotive/sports and leisure market.
Twintex® T PP Vetrotex	Commingled fabric	Glass/PP	60%	<ul style="list-style-type: none"> - Used in diaphragm, or vacuum forming processing. - 0.5-1mm thick twill, twill 2/2 or plain weave fabric made of commingled yarns. - Automotive, marine and sports and leisure market.
Twintex® R PP Vetrotex	Commingled roving	Glass/PP	60%	<ul style="list-style-type: none"> - Used in filament winding. - Tanks and vessels market.
Twintex® R PP Vetrotex	Commingled roving	Glass/PP	60%	<ul style="list-style-type: none"> - Used in filament winding. - Tanks and vessels market.
TEPEX® Dynalite Bond Laminates	Consolidated plates	See details	35-85% V _F (%)	<ul style="list-style-type: none"> - Glass, carbon and aramid fibers available (and hybrids). - PP, PBT, PA6, PA66, PA12, TPU and PPS melt impregnated matrix systems available - up to 4mm thick plate available - numerous fiber architecture available
TEPEX® semipreg Bond Laminates	Semipreg	See details	35-85%	<ul style="list-style-type: none"> - All Dynalite products are offered in a semipreg version.
TEPEX® Flowcore Bond Laminates	Sandwich panels flow moldable core	See details	35-85%	<ul style="list-style-type: none"> - Skins are TEPEX Dynalite. - Processed using GMT's technology - Used mostly in the automotive industry
TEPEX® Sandwich Bond Laminates	Sandwich panels with rigid core	See details	35-85%	<ul style="list-style-type: none"> - Skins are TEPEX Dynalite. - Core is Rohacell® - Thermoformable
PiPreg® Porcher Industries	Semipreg and consolidated plates	See Details	38-60%	<ul style="list-style-type: none"> - Glass, carbon and aramid fibers available. - PEEK, PPS, PEI, PC, TPU and PA12 powder impregnated matrix systems available. - Porcher consolidates their powder impregnated semipreg material for the consolidated plate market.
CETEX® PEI CETEX® PPS TenCate	Semipreg and consolidated plates	Glass, Carbon and Aramid/PPS or PEI	-	<ul style="list-style-type: none"> - Qualified at Airbus and Boeing. - Used in primary and secondary aircraft structures, aircraft interiors, radomes and military helmets.
CETEX® System3 TenCate	Sandwich panels with honeycomb core	Glass, Carbon or Aramid/PEI	67%	<ul style="list-style-type: none"> - Thermoformable (single curvature). - Marketed for the aircraft interior business.
Thermo-lite® TenCate	Prepregs (UD, Slit UD, fabrics and towpregs)	See details	50-74%	<ul style="list-style-type: none"> - Dedicated to the automated fiber placement market - Glass, Carbon and aramid fibers and PEEK, PEKK, PPS, PEI, PMMA, PP and PE matrices are available.
CURV® Propex fabrics	Consolidated plates	PP/PP	-	<ul style="list-style-type: none"> - 0.3-3mm thick laminates available - Thermoformable and fully recyclable - Automotive, and consumer goods market.
APC/APC-2® Cytec	Prepreg tape, towpreg, prepreg fabrics and consolidated plates	See Details	-	<ul style="list-style-type: none"> - Glass, carbon and aramid fiber available. - Wide range of advance polymer matrix system available. - Products marketed for the aerospace press forming, semi-preg and AFP industry.
Comfil	Roving, fabrics and consolidated plates from commingled yarns	See details	28-71%	<ul style="list-style-type: none"> - Very large selection of polymer available (engineering and advanced polymers) - Glass, Carbon, Aramid, Basalt and other specialty fibers available.

3.2.1 Impregnation techniques

One of the most common ways to impregnate fibers with thermoplastic polymers is to introduce polymer films between fiber layers (see figure 3.1a). The film/fiber layer assembly can then be either pulled through a series of heated rolls or simply pressed between hot plates to consolidate the laminate. After cooling the material below the polymer melting temperature, these two techniques yield products sold in the form of rolls or consolidation laminated plates.

Since this melt impregnation technique is difficult or impractical for some polymers due to thermal degradation at temperatures close to their melting point (T_m), a solvent impregnation technique was developed to impregnate at temperature well below T_m (see Figure 3.1b). The polymer being dissolved, its viscosity is significantly reduced which greatly improves fiber impregnation and fiber wet-out.

To facilitate fiber impregnation for some polymers, a powder impregnation technique was also developed where yarns or fabrics are first coated with polymer powder (see Figure 3.1c). After being sintered in an oven, the powder coated material can be sold as prepreg or consolidated into plates (using fabrics).

In a similar manner of joining fiber and matrix on an intra-bundle level like with powder impregnation, commingling offers the possibility of merging conventional reinforcement fibers with thermoplastic fibers within the same fiber bundle (see Figure 3.1d). Again, as with powder coated fibers, these commingled yarns can be further processed to be sold as roving or fabric. For polymers providing good impregnation, co-weaving techniques can also be used to produce thermoplastic composites. As illustrated in Figure 3.2e, co-weaving simply consists of introducing polymer yarns (fibers or split films) to reinforcement fibers either in the weft or warp direction during weaving.

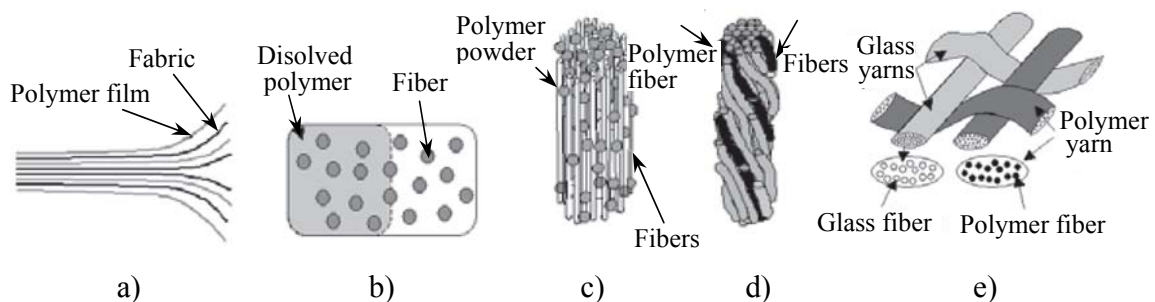


Figure 3.1: Impregnation techniques for thermoplastic composites (adapted from [4]). a) film stacking, b) solvent impregnation, c) powder impregnation, d) commingling, e) co-weaving.

3.2.2 Consolidated laminates

Manufacturers generally supply consolidated laminates in the form of large sheets (1m x 1m or 1m x 3m) a few millimeters thick. These sheets are composed of multiple layers of fabric and are processed in finished products using different melt processes such as elastomeric tool forming, hydroforming or matched metal tool forming (to be reviewed in later sections). As shown in Table 3.3, material sold under the brand names CETEX, Curv, TEPEX, APC-2, Comfil or Twintex offer a range of different fibers (glass, carbon, polypropylene, etc.) combined with a variety of engineering or high performance matrix systems such as PP, PA-12, PEEK, PEI, PPS and so on. Fiber mass fraction can vary from 35% to 85% with high fiber mass contents usually reserved for advanced composites. Depending on the manufacturer's expertise, these hot-press consolidated plates can be produced using simply film stacking with conventional reinforcement fabrics or fabrics pre-processed using powder impregnation, commingling or solvent impregnation.

3.2.3 Pre-impregnated materials

Prepreg thermoplastic materials are usually supplied on rolls in the form of roving, tape or fabric (see Table 3.3 for examples). While tapes are generally dedicated to automated fiber placement and consolidation processes, fabrics are generally used for vacuum molding or diaphragm molding. In contrast, roving is used typically for filament winding or pultrusion (these processes will be reviewed in later sections). Again, as with consolidated plates, different impregnation techniques can be favored by different manufacturers to produce prepregs. For fabrics, the possibility of co-weaving polymer fibers in the warp or weft direction yields a product with better drape properties than bulk, commingled or powder impregnated fabrics. However, for similar process parameters, co-weaved fabrics will exhibit longer impregnation times when compared with the intra-bundle-based impregnation techniques just mentioned.

3.2.4 Core materials

For sandwich structures, core materials developed for thermoset composites usually can be used for thermoplastic composites. Of course, the core material must be able to withstand the temperature and pressure applied during processing. Closed-cell foam,

balsa and aluminum honeycomb are known to have been used already with thermoplastic composites [1]. Some manufacturers also offer thermoformable pre-consolidated sandwich panels (see TEPEX sandwich or CETEX System3 in Table 3.3).

3.2.5 Reactive molding resin systems

Thermoplastic reactive molding systems are meant for use in RTM, vacuum infusion or pultrusion processes. As with thermoset reactive processes, the different components of these systems are first mixed and then injected or infused in dry fiber beds. Due to the very low viscosity of most of these systems, fiber impregnation is usually not a concern when compared to the molten polymer impregnation techniques earlier discussed. Compared to reactive thermoset systems, thermoplastic systems generally exhibit shorter infusion times (because of their very low viscosity) and shorter polymerization times. However, they require significantly higher processing temperatures.

To date, four engineering polymer systems are known to have being sufficiently developed to be used for continuous fiber composites:

- Fulcrum®, a thermoplastic urethane system developed for pultrusion,
- APNylon® (formerly DSM's Nyrin) from Brüggemann Chemical, a polyamide-6 ring-opening polymerization system,
- APLC12® from EMS-CHemie A.G., a polyamide-12 ring-opening system.
- Cyclics®, ring-opening PET, PBT and PC systems commercialized by Cyclics Corporation.

Apart from Fulcrum®, a system used successfully to mass produce fiber-reinforced pultruded rods and profiles [5], all other systems are at the stage of development or still have not found a specific niche for commercial success. Some work has been done on high-performance polymer systems (PEEK, PPS, etc.) but these systems have not yet been used on an industrial scale [6].

3.3 Manufacturing processes for thermoplastic composites

Manufacturing processes for thermoplastic composites can be separated in two distinct families: melt processes and reactive processes. Within these two families, processes can be grouped either as isothermal or non-isothermal, since all processes for thermoplastic composites require heat. Isothermal processing techniques involve heating

both the mold and the material at the same rate to provide the necessary thermal cycle to produce the part. Thermal cycling for isothermal melt processing involves a pre-heating step in which the melt temperature of the thermoplastic is reached, a consolidation step in which temperature and pressure are kept constant for a certain period of time, and a cooling step to allow the polymer to re-solidify so that the part can be de-molded. In non-isothermal processing, the mold and part to be produced are subjected to different thermal cycles. Usually, the material is pre-heated outside the mold and quickly transferred to a cool mold (temperature usually kept at 50-60% of T_m) to be formed to its final shape. Due to the high heat transfer rate attainable with non-isothermal processing, significantly shorter cycle times are possible when compared to isothermal processing.

Pressure is another distinct processing parameter commonly used to differentiate thermoplastic composite manufacturing techniques. Low-pressure and high-pressure processing methods include processes that use pressures of either a few bars or 10-50 bars respectively for consolidation. Since pressure is inversely proportional to the time required to impregnate the fibres, high pressure is generally used for non-isothermal processing, since the part needs to consolidate fully and be impregnated properly in a very short period of time.

With these different manufacturing characteristics in mind, the following section will review processes dedicated to long-fiber thermoplastic composites with respect to processing temperature, pressure, cycle time, part size and level of automation attainable.

3.3.1 Press-forming processes

3.3.1.1 Elastomeric tool forming

Elastomeric tool forming is a non-isothermal process using a metal mold half and a matched elastomeric mold half. As shown in Figure 3.2, the first step of the process involves pre-heating a pre-consolidated laminate. Infrared is usually the preferred method for heat generation but use of hot air or radiant heat is also known to have been used. Once the polymer melting temperature is reached, the laminate is quickly transferred to a press in which the elastomeric and metal mold halves are joined. During this critical step, blank holders are used to keep a membrane stress applied to the laminate while it is being formed. Careful positioning and tensioning of these blank

holders provides control over wrinkling, interply slip and intraply shear. Since the metal mold is kept at a temperature well below T_m , the laminate is cooled down quickly while the consolidation pressure is maintained (5-10 bars - depending on the material and the tool geometry and rigidity). Once the part has cooled sufficiently, it can be de-molded and trimmed if necessary. Typical cycle times are within minutes for this process [7].

The main advantage associated with the flexibility of the elastomeric mold half is that variations in ply thickness can be accommodated and relatively uniform consolidation pressure ensured, compared to fully metallic molds. On the other hand, due to the thermal insulation properties of rubber, elastomeric forming cycle times are generally longer than those of matched-metal die forming. Elastomeric molds are also limited in the number of cycles they can withstand since they are known to degrade rapidly [7].

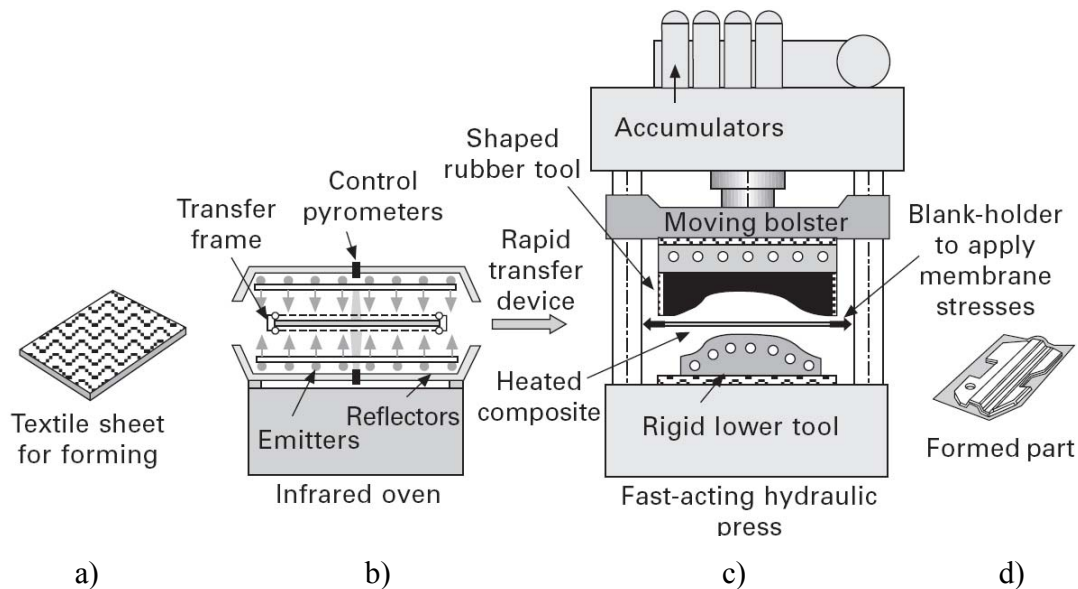


Figure 3.2: An elastomeric tool forming process [4]. a) pre-consolidated composite sheet to be formed, b) pre-heating of the composite sheet, c) stamp-forming, d) formed part.

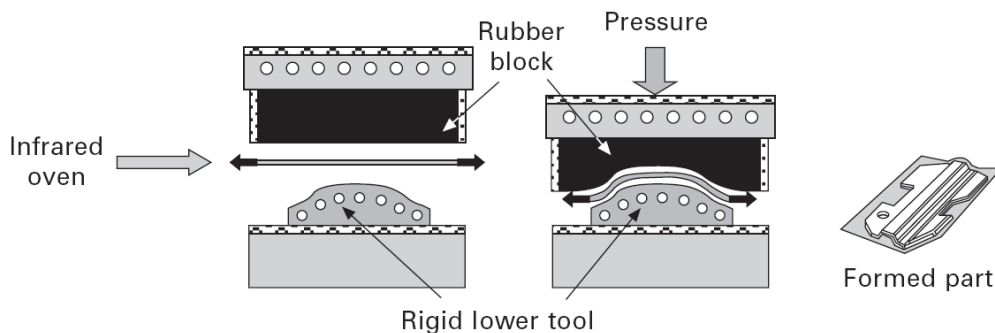


Figure 3.3: Elastomeric pad (rubber block) forming [4].

A variant of the elastomeric forming method just described uses a flat elastomeric pad instead of a matched elastomeric mold half (see Figure 3.3). This approach further simplifies the process but obviously can be used only with relatively flat shapes.

3.3.1.2 Hydroforming

Hydroforming is a process commonly used for sheet metal forming. It utilizes fluid pressure applied behind a 10-20mm thick rubber diaphragm to shape materials against a metallic mold. To form thermoplastic composites by hydroforming, the same basic principles as with elastomeric pad forming are applied. The only difference is that a hydraulic unit applies pressure behind a rubber diaphragm instead of using a rubber pad (see Figure 3.4). One of the key features of hydroforming is its ability to apply a very high uniform pressure over the mold surface. Also, since only one mold half needs be produced, the process can be considered a bit cheaper than elastomeric or matched-metal die forming. Despite these advantages, the relatively fragile nature of the rubber diaphragm and its limited deformability makes hydroforming suitable only for producing simple shapes made with low melting temperature thermoplastic composites.

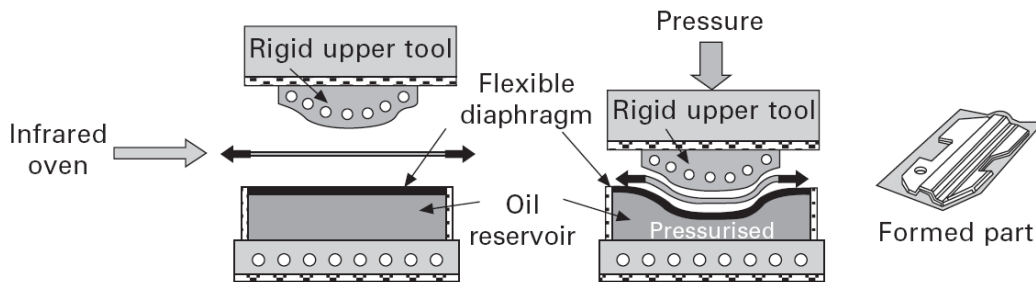


Figure 3.4: Hydroforming processing of thermoplastic composites [4].

3.3.1.3 Matched-metal die forming

Matched-metal die forming is used extensively in the automotive industry for the production of glassmat thermoplastic parts (GMT). In response to the end-of-life directive of the EU, polyester SMC (sheet molding compound) has mostly been abandoned in favor of GMTs because of their recyclable nature (polypropylene is the most common matrix). From a manufacturing perspective, matched-metal die processing is again very similar to elastomeric forming. As shown in Figure 3.5, composite sheets are pre-heated, stamped (typically 5-15 bars) and released from the mold once they have been sufficiently cooled below their melting temperature.

Matched-metal die forming offers very high production rates due to the rapid heat transfer from the laminate to the cool metal molds. Cycle times as short as 30 to 60 seconds are typical for this process [2]. However, the process is less forgiving due to the rigid nature of the molds when processing continuous fiber composites. Pressure is more difficult to apply uniformly over the part, with the vertical wall being subjected to very low pressures. Furthermore, differences in ply thickness due to intraply shear must be known precisely in order to determine mold cavity dimensions correctly for uniform pressure distribution, otherwise significant pressure differences leading to important variations in fiber volume content can occur during molding [4].

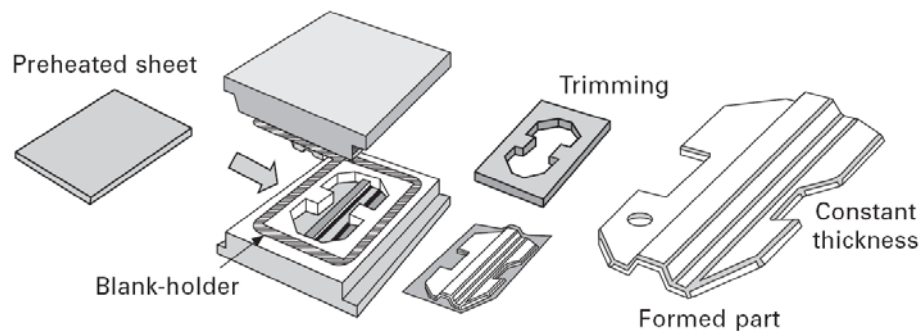


Figure 3.5: Matched-metal die forming of thermoplastic composites [4].

3.3.2 Vacuum-forming processes

3.3.2.1 Atmospheric or autoclave processing

When using semi-preg materials, thermoplastic composites can be processed with classic vacuum-assisted and autoclave processes used for thermoset composites. As with thermosets, thermoplastic composites are first hand-laid, then vacuum-bagged and finally heated in an oven or placed in an autoclave for consolidation. The main difference from thermosets concerns lay-up since thermoplastic preregs have absolutely no tack compared to thermoset preregs. Therefore, pressure-sensitive adhesives or fusion bonding must be used to position and secure the different plies during lay-up. Concerning processing temperatures, most engineering thermoplastic composites can be consolidated within the range of temperatures normally used to process thermoset preregs ($T_m \approx 200^\circ\text{C}$). Standard high-temperature epoxy tooling and consumables can then be directly used. For high-melt-temperature advanced composites ($T_m \approx 400^\circ\text{C}$), specialty tooling and consumables are necessary (polyimide films, high-temperature sealant tape, etc.). As with any other isothermal melt process, cycle times

are directly linked to the time the mold will take to reach the composite melt temperature. After a short consolidation period, the mold can be cooled and the part can be released. Typical processing times are from 1 to 2 hours (excluding lay-up).

Vacuum and autoclave forming are generally used for large complex parts impossible to produce with press forming technology. Numerous engineering thermoplastic parts and high-performance thermoplastic composite parts have been produced using oven or autoclave consolidation, including the J-nose of the Airbus A-340-600 (Fokker, Netherlands), robot arm sections for the international space station (FRE Composites, Canada) and countless large boat hulls made with polypropylene/glass.

3.3.2.2 Diaphragm forming

As the name suggests, diaphragms are at the base of this manufacturing process. To manufacture a part with diaphragm forming, the material is first placed flat between two thin films (the diaphragm) maintained under vacuum. Depending on the processing temperature, these films are made of materials such as polyimide for high temperature applications or silicon sheets for lower temperature applications. Different versions of the process have been developed over the years using either isothermal or non-isothermal manufacturing schemes. In isothermal processing (see Figure 3.6), autoclaves are often used to obtain gradual heating of the diaphragm and mold assembly. Once the forming temperature is reached, vacuum and autoclave pressure is applied to the diaphragm to force the assembly to mate with the mold surface. After a consolidation period, the assembly is cooled, the pressure is removed and the part is released. Due to the isothermal nature of the process, cycle times of less than 30 minutes are difficult to attain [4].

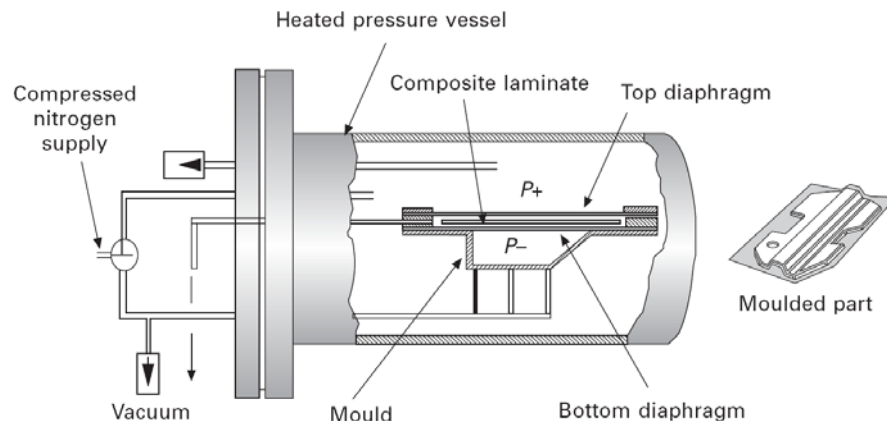


Figure 3.6: Isothermal autoclave diaphragm forming [4].

In the non-isothermal version of the process (see Figure 3.7), the diaphragm and laminate assembly is first heated close to the melting temperature of the thermoplastic (hot plate, ovens, or infrared can be used) and then transferred quickly above the mold surface. Single-surface molds (for which only vacuum is applied to pull the assembly towards the mold surface) and clamshell molds (for which a combination of vacuum and pressure can be used to increase consolidation) can both be used.

The main difference between this process and the press forming techniques earlier discussed is the fact that diaphragms can maintain a biaxial tension on the material as it is being formed, which helps prevent ply wrinkling. Since diaphragm stiffness plays a critical role in laminate control during, forming pressure, temperature and film type were heavily researched over the last 15 years to perfect the process [8, 9]. Unfortunately, this method has not yet gained much commercial importance but does have potential for the production of large parts since no press is necessary.

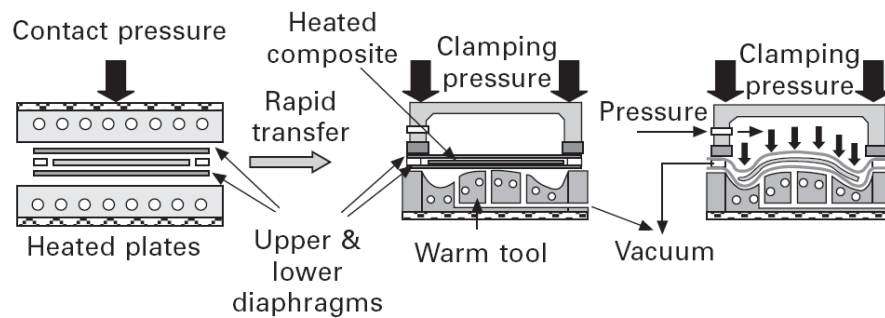


Figure 3.7: Non-isothermal diaphragm forming where pre-heating is provided by hot plates [4].

3.3.2.3 Bladder inflation forming

Bladder inflation forming is commonly used to produce hollow structures such as pressure vessels, tennis rackets, or bicycle frames. As with diaphragm forming, bladder molding can be performed isothermally or non-isothermally. In both cases, material is first laid over a lightly inflated pre-shaped bladder. This bladder can be either removed once the part has been processed or integrated into the structure as an internal liner (common for pressure vessels). For isothermal processing (see Figure 3.8), the material and bladder are placed at room temperature inside a clamshell mold. The mold can then be placed inside an oven or embedded heating elements can be used to raise the temperature of the assembly. Once the polymer melting temperature is reached, pressure

is increased in the bladder to fully impregnate and consolidate the part. After cooling the mold sufficiently below the melting point, the part can be released.

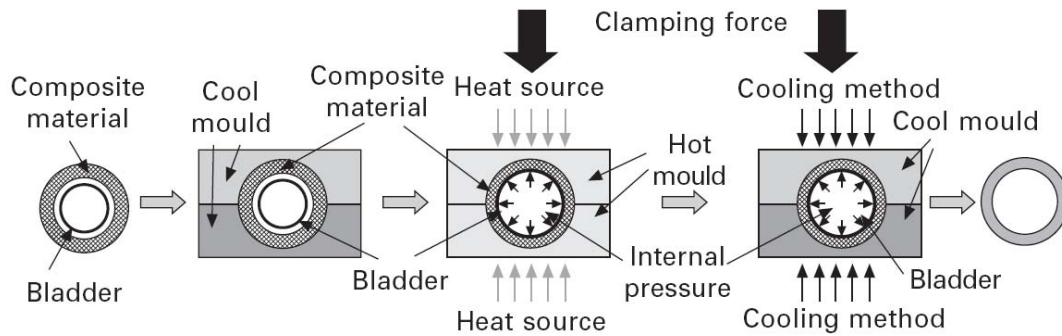


Figure 3.8: Isothermal bladder forming sequence [4].

In non-isothermal processing (see Figure 3.9), as with the other non-isothermal processes reviewed above, the bladder and material assembly is first pre-heated. It is then quickly transferred to a cool clamshell mold and internal bladder pressure is applied after closure. After a short consolidation period, the mold is opened so the part can be released.

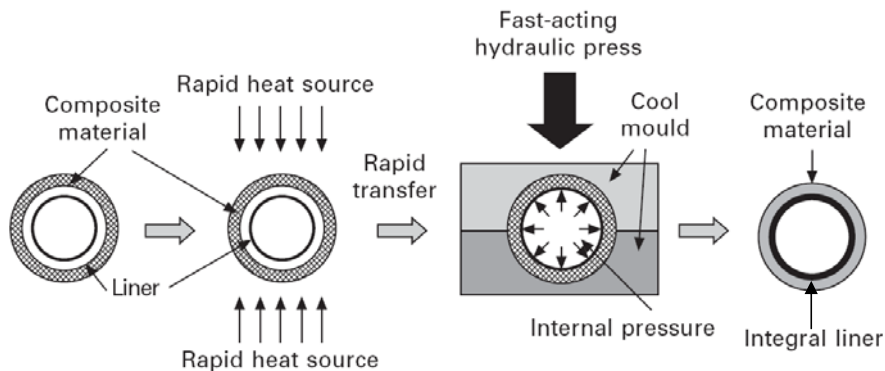


Figure 3.9: Non-isothermal bladder forming. In this example, the bladder is not removed and is kept as an integral liner in the final product [4].

3.3.3 Automated fiber placement processes

Filament winding and tape winding techniques were first developed for thermoset composites with resin baths used to impregnate dry fibers before being laid on rotating mandrels. With the advent of thermoset prepregs, these machines were modified to incorporate a pressure roll or shoe to tack the material in place on the mandrel. Based on

the same concept, gantry type machines equipped with multi-axis robots were also developed to place fibers on non-rotating surfaces.

The past decade saw automated fiber placement (AFP) and automated tape laying (ATL) technology reach a level of maturity sufficient to gain the trust of most major aircraft companies. Today, at least a dozen companies (MAG Cincinnati, Ingersoll, Automated Dynamics, and others) offer turnkey machines able to lay material as wide as 30cm at rates of up to 60m/min [10, 11]. A large number of these machines are now used to produce thermoset parts for Boeing and Airbus. These new AFP methods helped reduce part cost significantly by cutting down on lay-up time. However, for all thermoset prepreg-based fiber placement methods, intermediate de-bulking steps are still necessary to compact the material after a few plies are laid. Also, a final autoclave cure is necessary to complete the part.

With regard to this challenge, very promising thermoplastic composite ATL/AFP methods have been developed over the past 15-20 years, in which these de-bulking and curing steps can be omitted since thermoplastic fiber placement machines can melt and consolidate the material as it is being laid [12]. This *in-situ* consolidation technique is performed with systems similar to the one shown in Figure 3.10, in which material is heated above T_m just as it is about to reach the consolidation roller. Although fiber placement speeds are significantly slower for thermoplastics (3-15m/min) compared to thermosets, part processing is believed to be faster and cheaper due to the de-bulking and curing steps saved [13].

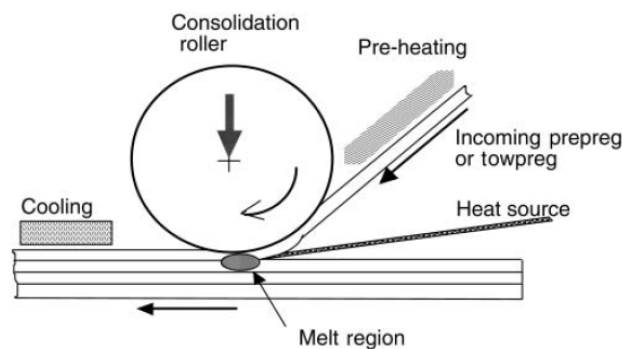


Figure 3.10: Melt and consolidation system for thermoplastic composite fiber placement techniques [12].

In terms of performance, the consolidation process still needs refinement before thermoplastic composites can compete with thermoset parts. Relatively high void contents are still observed when compared to autoclave-cured parts [14, 15]. Nevertheless, once thermoplastic composite ATL/AFP methods have reached maturity,

the fact that no intermediate de-bulking and curing steps will be necessary will clearly give an edge to thermoplastic composites when benchmarked against thermosets [13].

One of the main advantages of ATL/AFP methods over other thermoplastic composite manufacturing techniques is that they offer the possibility of manufacturing large parts with very complex reinforcement lay-ups without the use of large ovens or autoclaves. On the other hand, tooling and capital investment is very high, making the process justifiable only for large-scale production.

3.3.4 In-situ polymerization processes

3.3.4.1 Resin transfert molding

Resin-transfer molding processing for thermoplastic composites is based on thermoset resin-transfer molding technology. As shown in Figure 3.11, the production cycle process starts by placing a dry fiber pre-form inside a closed rigid mold. With the mold clamped securely and heated to the required polymerization temperature (T_{pol}), the reactive components of the polymer system are mixed and injected in the mold cavity at pressures generally between 5 to 10 bars. Depending on the resin system, polymerization can be performed below the melting temperature ($T_{pol} < T_m$) or above the polymer melting temperature ($T_{pol} > T_m$). In the latter processing scheme, the part needs to be cooled sufficiently below T_m prior to release from the mold.

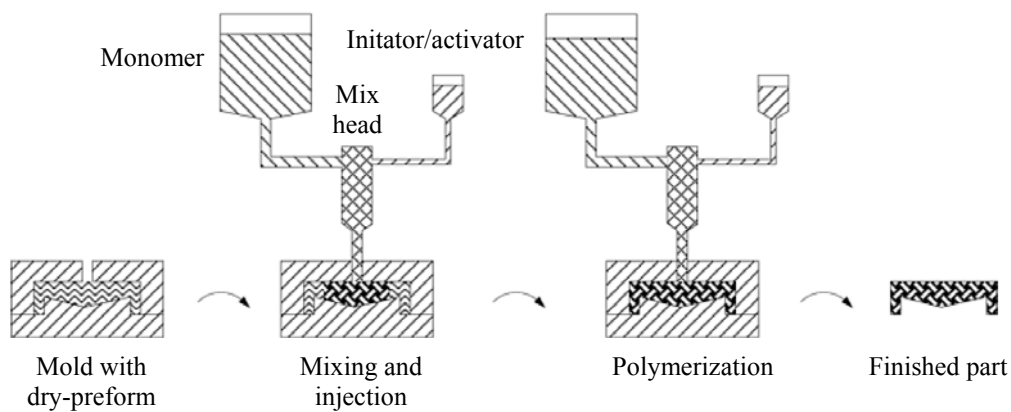


Figure 3.11: Resin transfer molding process for thermoplastic composites (adapted from [17]).

Up to now, thermoplastic RTM has aroused limited interest in the industry, with only a few demonstrator projects showing the feasibility of the process. In a project conducted at École Polytechnique Fédérale de Lausanne (EPFL), APLC12 panels were

injected by RTM and then press-formed [18]. In another project, Cyclics® PBT parts were produced by RTM at Leuven University [19].

3.3.4.2 Vacuum infusion

Based on RTM manufacturing principles, the vacuum infusion technique uses a solid mold half and a flexible mold half (usually a plastic film) instead of a set of two solid mold halves. Due to the flexible mold half, processing pressure is limited to atmospheric pressure.

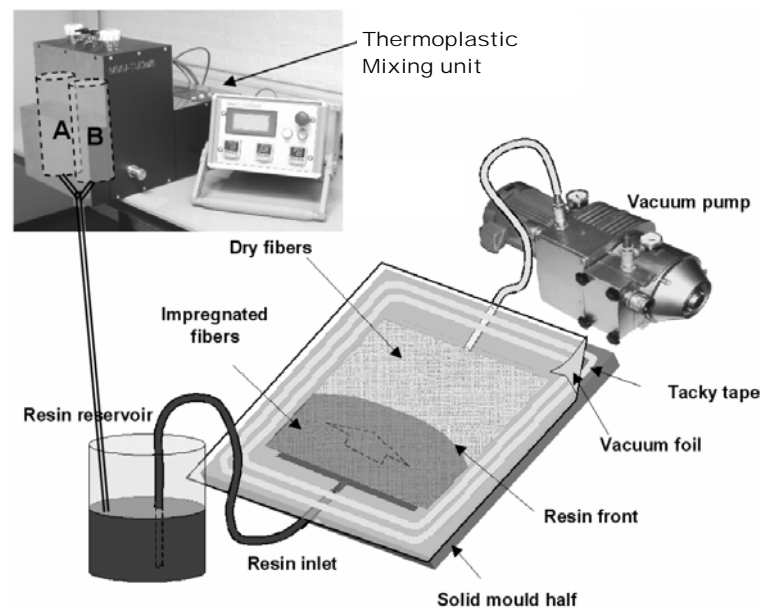


Figure 3.12: Typical resin infusion process for thermoplastic composites (adapted from [20]).

As with RTM, the first step of the process involves placing a dry fiber pre-form on the surface of the solid mold half (see Figure 3.12). The second step consists of covering the mold with a flexible medium, in this case, either a vacuum bag or a semi-rigid mold half (also known as light RTM). Once the vacuum is pulled between the flexible and the solid mold halves, the resin system can be introduced by opening an inlet valve. Resin is then forced to flow toward the outlet port connected to the vacuum pump. Once the pre-form is fully impregnated, the inlet port is closed and the part is left to polymerize before being released from the mold. As with RTM, isothermal or non-isothermal processing is possible depending on the resin system. In all cases, the resin reservoirs must be kept above the melting temperature of the different components of the polymer reactive system and the mold must be kept at the polymerization temperature.

Compared to RTM, vacuum infusion has the advantage of being low-cost and allows the manufacture of significantly larger parts. However, infusion time is longer due to low processing pressure and poor surface finish will always be obtained on the flexible mold side. Also, since vacuum bags and other consumables are generally not reusable, the process should be considered less sustainable.

Vacuum infusion of thermoplastic composites has also not yet been used on an industrial scale, but different systems and manufacturing techniques were investigated over the past decade. Significant progress in process development for anionic polyamide-6/glass composites was achieved at Delft Technical University [21] and infusion of APA-6 on carbon fibers was investigated at the University of Alabama [22].

3.3.4.3 Pultrusion

Thermoplastic and thermoset composites are pultruded in a similar manner, in which continuous fibers drawn from reels are wetted with resin and pulled through a die to form constant-cross-section profiles. For thermoplastic composites, fiber wet-out can be done with an extrusion screw that feeds molten thermoplastic as the fibers are pulled through. As mentioned earlier, fiber impregnation with molten thermoplastic can be somewhat troublesome, but since pressure close to the die is relatively high, fibers usually can be properly impregnated if the pulling rate is relatively low. To increase pulling speed, another way of impregnating the fibers was developed, using a reactively processed thermoplastic system. In this case, as the fibers are pulled through the die, a reactive mixture is injected and cured before the material is pulled out of the die. One of the most successful resin systems used for reactive pultrusion is the previously discussed Fulcrum® system (polyurethane). Using this system, production rates of 10m/minute have been reported [5].

3.3.5 *Joining techniques*

As mentioned in the introductory chapter, thermoplastic composite can be assembled with mechanical fasteners or bonded with adhesives like thermoset composites but they can also be welded. Welding (or fusion bonding) has the advantage over the other methods of not requiring extensive surface preparation and is fully reversible for end-of-life disassembly, repairs or production errors.

Three methods of welding have been extensively researched and are up to now the most common methods known to be used: resistance welding, ultra-sonic welding and induction welding [23-25]. Resistance welding has reached a level of maturity yet to be attained by induction or ultra-sonic welding and has been used successfully in numerous industrial projects, with welding of the A-320 J-nose ribs certainly being the most publicized. The technique consists of local melting and re-solidifying of the material where a joint needs to be formed. As shown in Figure 3.13, the heat source generally comes from an electrically resistive implant (usually a metal mesh) sandwiched between the bonding surfaces of the laminates. With current flowing in the resistive implant, the thermoplastic reaches its melting temperature while laminates are kept firmly in contact. Once the melting temperature has been reached, the current is switched off and the joint is cooled down while pressure is maintained. As mentioned earlier, the embedded resistive implant can be reused to disassemble the part.

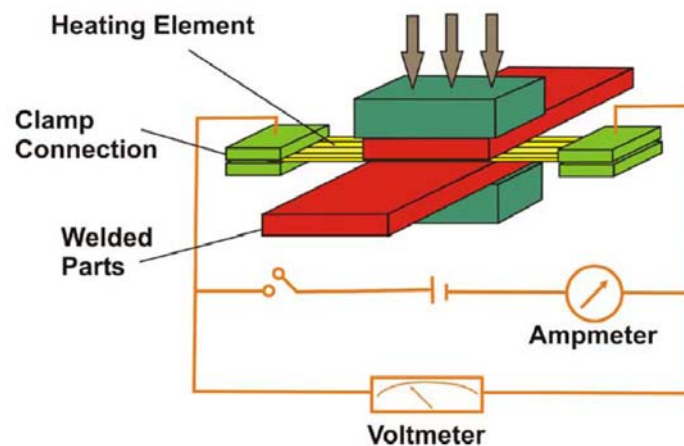


Figure 3.13: Typical resistance welding set-up for thermoplastic composite assembly [26].

3.4 Thermoplastic composite wind turbine blades

3.4.1 *Physical and mechanical property issues*

High stiffness, low weight, high fatigue resistance and of course low cost are the four most desired characteristics for wind turbine blade materials. Based on stiffness, weight and cost, there is so reason why thermoplastic materials could not be used as a matrix system for wind turbine blade materials. As mentioned in Chapter 2, today's matrix systems for wind turbine blades are polyester, vinylester or epoxy-based systems.

Their moduli are in the range of 2-4 GPa and their tensile strengths average around 50-60 MPa. Comparing the materials in Table 3.2, a number of engineering thermoplastics show similar or better stiffness and strength properties for an equivalent density. In terms of material costs, some thermoplastic matrix systems are also quite competitive with currently used matrix systems.

In general, thermoplastic matrices are preferred over thermosets because of their greater toughness, faster processing, unlimited shelf life and specific physical properties such as low flammability. These characteristics have well served the high-performance thermoplastic composites generally used in the aerospace industry, but the use of thermoplastic composites in general for structural applications for which high mechanical performance is necessary remains limited. Consequently, issues related to fatigue performance, such as fiber-to-matrix adhesion, have received less attention in recent R&D efforts. Successful use of these materials for wind turbine blade structures will therefore require better understanding of their fatigue behavior. As was the case for the early development of thermoset composites, dedicated sizing and coupling agents will likely need to be developed for thermoplastics to ensure an optimum fiber-to-matrix adhesion and provide satisfactory fatigue properties [21]. Some of these issues will be discussed in Chapter 4.

3.4.2 Sustainability issues

It is likely that due to the impressive growth rate of the wind energy industry and due to limited blade life, recyclability will soon join stiffness, low weight, fatigue resistance and low cost as key design requirements for wind turbine blade materials. Indeed, the wind energy composite market has witnessed an impressive steady growth rate of 20% over the past few years and is expected to consume more than 600,000 tons of composite materials by 2013 [27]. As a consequence of blade life being limited to 20 years, blade scrap tonnage should be comparable by 2025 and rise every year by 20%. Judging from these numbers, it is obvious that the industry will have to take their responsibilities regarding recycling.

Recent life-cycle analysis (LCA) by turbine manufacturers has demonstrated that scrap blades are usually sent to landfill due to their incapacity to be recycled [28]. When compared to the rest of the turbine (mostly steel), blades are the components contributing the most to the environmental impact as “bulk waste” (26.1% of the turbine material sent to landfill comes from blade waste). Similar conclusions were drawn at the

38th International Energy Agency Topical Expert meeting on material recycling and life cycle analysis of wind turbines in 2003, where blades were identified as problematic components to manage from a LCA perspective (see Figure 3.14) [29].

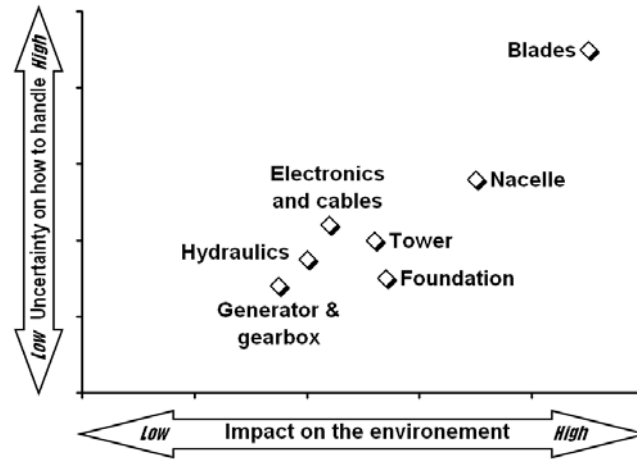


Figure 3.14: Key issues related to dismantling and recycling of wind turbines (adapted from [29]).

Due to the physical properties of the thermoset matrices used today in wind turbine blade structures, two options are currently available for blade recycling: Mechanical recycling (shredding) and reuse as filler for other materials, or incineration with energy and fiber recovery (best case scenario). LM Glasfiber has recently demonstrated recycling in a project in which shredded blades were used as filler for fiber-reinforced concrete [30]. In a different project, Vestas showed the potential of incineration without material recovery. In this case, energy recovery was made possible since blade particles were incinerated in power stations but 20% of the blade material still had to be sent to landfill in the form of ash [31]. Although these recent efforts yielded interesting solutions for today's end-of-life management of wind turbine blades, it is likely that within a few years, incinerating such high-value materials in power plants will make no sense. According to the European Association of Plastics Manufacturers (Plastic-Europe), plastic materials are already starting to follow a more sustainable end-of-life route by being recycled more often than they are being incinerated [32]. This can be explained by the expanding gap between new raw material prices and recycled material prices. Judging from this trend, material recycling will probably become the norm in the near future with incineration being used only for extreme cases when recycling is not possible.

In this context, thermoplastic composites could provide significantly more sustainable solutions than would today's thermoset composites. Since they can be melted without material degradation, full material recovery is a possibility. Chapter 4 will present some of these benefits by comparing cradle-to-gate life cycle analysis of epoxies against Nylon-6.

3.4.3 *Manufacturing issues*

As mentioned in Chapter 2, today's large wind turbine blades are generally manufactured using resin infusion or low temperature prepregs cured under vacuum. These two processes enable manufacturers to produce parts of up to 60m in length in one shot with laminate thicknesses often exceeding 10cm. Due the size of the parts involved, only two processes among those reviewed in this chapter have been identified as possible candidates for the production of TPC blades using today's structural blade design: resin infusion or ATL/AFP processing.

Today's state-of-the-art in reactive resin infusion of TPC is limited to the production of small and relatively thin laminates. Nevertheless, due to the very low viscosity of the resin system and controllable reaction rate, virtually any part length and thickness could technically be achieved. On the other hand, one of the most significant drawbacks of this manufacturing technique is its curing temperature. With processing temperatures ranging from 150°C to 220°C, reactive processing of engineering plastics is expected to show an increase energy consumption cost and an increase in tooling cost (significantly higher thermal cycling) when compared to thermoset composites. Still, this increase in cost is expected to be counter-balanced by the significantly shorter infusion time that could be achieved and the potentially lower cost of the resin systems.

Concerning the potential of ATL/AFP processes for wind turbine blade manufacturing, two main problems are expected to limit their usage: the very high initial investment for the machine and their ability to produce thick parts in short periods of time. With regard to the first problem, today's blade production rate is definitely not high enough to justify such a high initial investment. Although ATL/AFP thermoplastic composite blade production methods do not make sense today, it does not mean that they could not be part of the solution in the future if blade production is increased significantly. As for the second problem, the current state of the art in thermoplastic composite ATL/AFP is limited to relatively low material-laying rates. With today's 10-15 kg/hour material laying rate, it would be unthinkable to produce 50-

60-meter blades weighing 15-20 tons each with these machines (even when using multiple consolidation heads).

On a more general note, when compared to thermoset composite blades, thermoplastic composite production scrap could be recycled more easily. This can be considered as a significant advantage, knowing that 10-15% of the material is generally scrapped during blade manufacturing [33].

Finally, as seen throughout this chapter, the strength of thermoplastic composite manufacturing is its very short cycle time. In order to maximize the potential of thermoplastic composites for wind turbine blades, it is therefore essential to redesign blade structures with respect to thermoplastic composite manufacturing capabilities. In this respect, blade designs using ribs, multiple skin panels or stringers, which would be extremely expensive to produce using thermoset composites, could yield very cost-effective blades when built with thermoplastic composites.

3.4.4 Demonstrator projects

A few demonstrator projects for thermoplastic composite wind turbine blades have been reported since the mid 1990s.

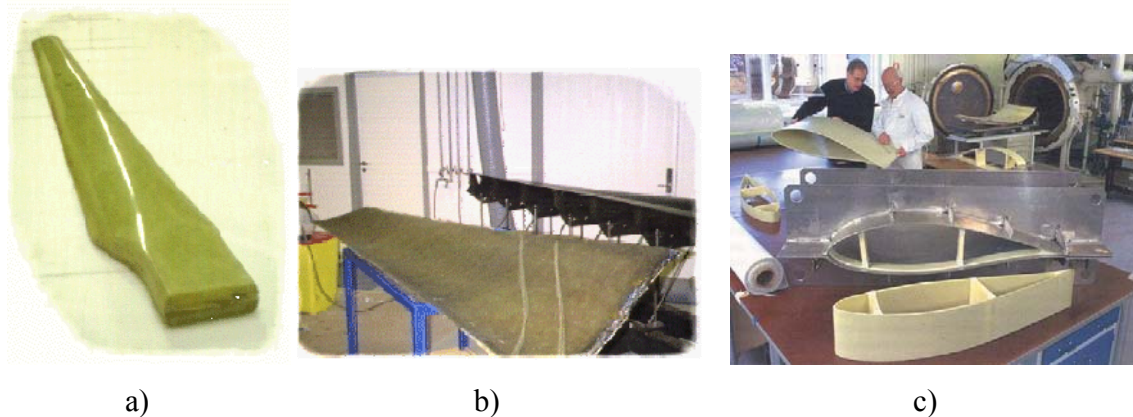


Figure 3.15: Thermoplastic blade demonstrator projects performed at Risø National Laboratories (Denmark). a) 1.5m glass/PET blade [34], b) 3.2m glass/PET blade section [34], c) 0.5m glass/PP blade section [35].

In 1996, a demonstrator blade was built at the Risø National Laboratory (Denmark) using Comfil glass/PET commingled fabrics [34]. Using vacuum to consolidate the laminate, isothermal melt processing of a 3.2m-long airfoil section was performed at 225°C (see Figure 3.15b). A couple of years later, Bonus (now Siemens) used the expertise of Risø to develop a glass/PP composite blade [35]. The concept was validated

with the fabrication of a 0.5m-long blade section melt processed under vacuum at 180°C (see Figure 3.15c).

Interest in TPC for wind turbine blades was recently revived through the concerted effort of ÉireComposites (formelly Gaoth Tec), Cyclics Corporation and Mitsubishi [36]. ÉireComposites, who already produces small glass/PP (Twintex) blades for 6kW and 15 kW machines, plans to build a 12.5-m demonstrator blade using glass/PBT (Cyclics). Some of the advantages that ÉireComposites expects from this new concept are as follows:

- Manufacturing time decreased by two thirds for large blades compared to existing thermoset composites technology.
- Significant reduction in the cost of manufacturing blades.
- A recyclable wind turbine blade at its end-of-life.
- Recycling possible for manufacturing waste / cut-offs.
- Zero emission of volatile organic compounds in the workplace.

Ultimately, ÉireComposites wants go through the certification process of their blade (blade testing and material characterization) to be able to commercialize the concept.

3.5 Conclusions

With respect to the different issues concerning material properties and manufacturing capabilities discussed in this chapter, the following conclusions are drawn:

Material properties:

- Because of their low cost, engineering polymers have been identified as the only matrix system possible for wind turbine blade thermoplastic composite materials. Advanced thermoplastic composites based on PEI, PPS or PEEK cannot be used, due to their prohibitive cost.
- Due to their recyclable nature, thermoplastic composites will offer the possibility of full material recovery at the product end-of-life.
- With some engineering polymers being cheaper than conventional thermoset resin systems, blade material cost could potentially be reduced when using thermoplastic composites.

- With polymer weight, strength and stiffness being comparable to conventional thermoset resin systems, no significant reduction in static mechanical performance is to be expected when using thermoplastic composite for wind turbine blade structures. This holds true if the matrix behaves similarly hygrothermally and can ensure equivalent fiber/matrix adhesion.
- Fatigue performance of thermoplastic composites will need to be investigated before being considered for wind turbine blade structures.

Manufacturing issues:

- Thermoplastic composite manufacturing processes in use today are mostly melt processes dedicated to the production of relatively small parts (up to 1-2m in length and 1-5mm thick) which are not suitable for the production of the thick and large composite shells found in today's wind turbine blade structures.
- Reactive processing techniques based on vacuum infusion were identified as the most promising manufacturing method for the production of large wind turbine blade structures.
- High processing temperatures for thermoplastic composites will result in higher manufacturing energy consumption costs but the reduction in processing time and matrix cost is expected to compensate for this.
- Due to the recyclable nature of thermoplastic composites, it is expected that blade production scrap will be largely recovered and reused.
- To maximize the potential of thermoplastic composites when used for wind turbine blade structures, it is essential to redesign the structure with respect to existing manufacturing strong points, e.g. fast non-isothermal melt processing of relatively small parts.

3.6 References

- [1] Strong, B., *Fundamentals of Composite Manufacturing: Materials, Methods and Applications*, second edition, Society of Manufacturing Engineers, 2008.
- [2] Mazumbar, S.K., *Composite Manufacturing: Materials, Product and Process Engineering*, CRC Press, London, 2002.
- [3] Gardiner, G., *Thermoplastic Composites: Inside Story*, High-Performance Composites, Gardner Publications, March, 2009.
- [4] Wakeman, M.D., Manson, J-AE, *Design and Manufacture of Textile Composites, Chapter 6: Composite Manufacturing -Thermoplastics*, Long, A., Editor, Woodhead Publishing Limited, Cambridge, England, 2005.
- [5] d'Hooghe, E.L., Edwards, C.M., *Thermoplastic Composites Technology; Tougher Than you Think*, Advanced Materials, Vol. 12, issue 23, December 2000, p.1865-1868.
- [6] Rijswijk, K, Bersee, H.E.N., *Reactive processing of textile fiber-reinforced thermoplastic composites – An overview*, Composite Part A: applied science and manufacturing, vol.38, issue 3, March 2007, p. 666-691.
- [7] Robroek, L. *The development of Rubber Forming as a Rapid Thermoforming Technique for Continuous fiber reinforced Thermoplastic Composites*, PhD Thesis, Delft University of Technology, 1994.
- [8] Bersee, H.E.N. *Diaphragm Forming of Continuous Fibre Reinforced Thermoplastics – Process Analysis and Development*, PhD Thesis, Delft University of Technology, 1996.
- [9] Monaghan, M.R., Mallon, P.J., O'Bradaigh C.M., Pipes R.B., *The Effect of Diaphragm Stiffness on the Quality of Diaphragm Formed Thermoplastic Composite Components*, Journal of Thermoplastic Composite Materials, Volume 3, July 1990.
- [10] Sloan, J., *ATL and AFP: Defining the megatrends in composite aerostructures*, High-Performance Composites, Gardner Publications, June, 2008.
- [11] Grant, C., *Speaking Out: Composite Structural Design and Manufacturing... the Times are Changing*, High-Performance Composites, Gardner Publications, July, 2007.
- [12] Sharp, R., Holmes, S., Woodall, C., *Material Selection/Fabrication Issues for Thermoplastic Fiber Placement*, Journal of Thermoplastic Composite Materials, Volume 8, January 1995.

- [13] Schlimbach, J., Mitschang, P., *Process-based Cycle Time Estimation for Thermoplastic Tape Placement*, Journal of Thermoplastic Composites materials, 19: 507, 2006.
- [14] Tierney, J., Gillespie, J.W., *Modeling of in-situ Strength Development for the Thermoplastic Composite Tow Placement Process*, Journal of Reinforced Plastics and Composites, 40:16, 2006.
- [15] Tierney, J., Gillespie, J.W., *Modeling of Heat Transfer and Void Dynamics for Thermoplastic Composite Tow Placement Process*, Journal of Reinforced Plastics and Composites, 40:16, 2006.
- [16] Hassan, N., Thompson, J.E., Batra, A., Hulcher, B., Song, X., Loos, A.C., *A heat transfer Analysis of the Fiber Placement Composite Manufacturing Process*, Journal of Reinforced Plastics and Composites, 24: 869, 2005.
- [17] Åström, Tomas, *Thermoplastic Composite Manufacturing*, ASM International Hanbook, Vol 21, Composites, 2001.
- [18] Wakeman, M.D., Zingraff, L., Bourban, P.-E, Månson, J.-A.E., Blanchard, P., *Stamp Forming of Carbon fibre/PA12 Composites – A Comparison of a Reactive Impregnation Process and a Commingled Yarn System*, Journal of Composites Science and Technology, 66; 19, 2006.
- [19] Parton, H., Verpoest, I., *In-situ Polymerisation of Thermoplastic Composites Based on Cyclic Oligomers*, Polymers, 26:60, 2005.
- [20] Joncas, S., van Rijswijk, K., Charron, J-F, Bersee, H.E.N., Beukers, A., *Interfacial Shear Strength Properties of Vacuum-infused Anionic Polyamide-6 Glass-fiber Composites*. 47th AIAA/ASME/ASCE/AHS/ASC Structures, Structural Dynamics, and Materials Conference, Newport, Rhode Island, USA, 1-4 May 2006.
- [21] van Rijswijk, K., *Thermoplastic Composite Wind Turbine Blades – Vacuum Infusion Technology for Anionic Polyamide-6 Composites*, PhD Thesis, Delft University of Technology, 2006.
- [22] Pillay, S., Vaidya, U.K., Janowski, G.M. *Liquid Molding of Carbon Fabric-reinforced Nylon Matrix Composite Laminates*, Journal of Thermoplastic Composites Materials, Vol. 18, November 2005.
- [23] Ageorges, J., Ye, L., Hou, M., *Advances in Fusion Bonding Techniques for Joining Thermoplastic Matrix Composites: a Review*, Composites Part A: Applied Sciences and Manufacturing, 32:839, 2001.
- [24] Stavrov, D., Bersee, H.E.N., *Resistance Welding of Thermoplastic Composites: an Overview*, Composites Part A: Applied Sciences and Manufacturing, 36:39, 2005.
- [25] Ahmed, T.J., Stavrov, D, Bersee, H.E.N., Beukers, A., *Induction Welding of Thermoplastic Composites: an Overview*, Composites Part A: Applied Sciences and Manufacturing, 37:1638, 2006.

- [26] Stavrov, D., Bersee, H.E.N., *Thermal Aspects in Resistance Welding of Thermoplastic Composites*. Proceedings of ASME Summer Heat Transfer Conference, Las Vegas, USA, July 2003.
- [27] JEC Composites, *Global Market Scenario Dynamic of the Composites Industry – 2009 Release. Strategic Studies*, 2009.
- [28] Vestas Wind Systems A/S, *Life cycle assessment of offshore and onshore sited wind power plants based on Vestas V90-3.0 MW turbines*.
- [29] Thor Sven-Erik, *Proceedings of the 38th IEA Topical Expert Meeting – Material Recycling and Life Cycle Analysis of Wind Turbine*. Roskilde, Denmark, March 2002.
- [30] LMGlasfiber Newsletter, *From waste problem to raw material in cement*, September 2004.
- [31] Advanced Materials & Composites News. *New Use Found for Old FRP Wind Turbine Blades*. Advanced Materials & Composites News, Composite Worldwide Inc., March issue, 2004.
- [32] European Association of Plastic Manufacturers, *The Compelling Facts about Plastics 2007*, Plastic-Europe, October 2008.
- [33] Vestas Wind Systems A/S, *Environment statement 2004 – Company site: Vestas Blades, Lem, Denmark, 2004*.
- [34] Lystrup, Aa., *Hybrid yarn for thermoplastic fibre composites*. Final report for MUP2 framework program no. 1994-503/0926-50, Summary of technical results, Risø-R-1034, 1998.
- [35] Lystrup, Aa., *Vacuum consolidation of thermoplastic composites for wind turbine rotor blades*. Proceedings of the 27th Risø international symposium on materials science, Risø (DK), 4-7 Sep 2006. p. 231-238.
- [36] <http://www.eirecomposites.com/> (wind energy brochure)

CHAPTER 4

ANIONIC POLYAMIDE-6 COMPOSITES FOR WIND TURBINE BLADES *MATERIAL PROPERTIES*

The objective of this chapter is to benchmark anionic polyamide-6 composites against conventional melt-processed polyamide-6 composites and epoxy-based composites commonly used for wind turbine blade structures. Physical properties such as moisture absorption, void content, crystallinity and degree of conversion will be used to compare matrix systems while tensile, compressive and shear moduli and strengths will be used to provide an overall comparison. The recycling potential of polyamide-6 composites will also be examined by comparing some of its mechanical properties against commercial-grade short-fiber composite materials.

4.1 Introduction

The polyamide-6 (PA-6) commonly used as a matrix in the composites industry is hydrolytically polymerized. The hydrolytic polymerization of ϵ -caprolactam monomer is done in the presence of a small amount of water at around 260°C for 10 to 20 hours. After purification, the obtained PA-6 granules can be further processed into composites through a variety of melt processes such as those reviewed in Chapter 3. Unfortunately, as seen in Chapter 3, melt processes are not well suited for the production of large parts. Thermoplastic reactive processing techniques based on vacuum infusion were thus identified as the most promising manufacturing method to produce large thermoplastic composite parts such as wind turbine blades.

An alternative way to obtain PA-6 is through anionic polymerization, which is suitable for reactive processing. The anionic polymerization of caprolactam can be performed between 130°C and 180°C and is completed within 3 to 60 minutes depending on the resin formulation. Since polymerization takes place below the polymer melting point (see Table 3.2), solid, highly crystalline anionic polyamide-6 (APA-6) is

formed. From a processing perspective, the water-like viscosity of caprolactam makes it ideally suited for vacuum infusion. Moreover, following a thorough review of potential reactive polymer systems, conclusions drawn from van Rijswijk [1] clearly identify APA-6 as the most promising resin system for wind turbine blade structures based on material performance, cost and processing temperature.

In reactive processes of this type, numerous parameters (process and material related) can significantly affect the resulting properties of the thermoplastic composites manufactured. In previous work by van Rijswijk et al [2-5], the influence of parameters such as processing temperature, infusion pressure and polymer formulation was extensively investigated, which provided the basis for the selection of a processing window suitable for the APA-6 system under study.

Based on the work of van Rijswijk et al, in an effort towards developing a suitable APA-6 composite for wind turbine blade structures, a first study will be presented in this chapter to target the best resin formulation and evaluate different fiber surface treatments and their effect on matrix-driven properties.

Using the results of this study, a second study will be presented in section 4.4 to compare vacuum-infused APA-6 composites to a conventional hot-pressed hydrolytically polymerized polyamide-6 (HPA-6) composite and a typical wind turbine epoxy-based composite. Static properties in tension, compression and shear will be found and preliminary fatigue performance will be assessed. To address the well-known vulnerability of PA-6 to water absorption, dry-as-molded (DAM) and moisture-conditioned samples were included in the test program. Based on neat matrix properties, composite mechanical properties, moisture absorption and fracture analysis, composites will be compared and a discussion of the results will be given.

Finally, a third study will propose a recycling strategy in which APA-6 composite recycled material will be injection molded and compared against a commercial-grade short-fiber injection molding compound.

4.2 Experimental procedures

For the first two studies mentioned above, different experimental procedures were used either to produce the laminates or characterize the materials. This section presents the procedures followed for both studies.

4.2.1 *Laminate description*

A balanced and symmetric cross-ply laminate composed of 12 plies of TenCate's (The Netherlands) S303 satin weave glass-fiber fabric was chosen for specimens to be manufactured. Matrix systems of Prime 20LV from SP Systems (UK) and AP Nylon from Brüggemann Chemical (Germany) were used respectively for the epoxy-based and APA-6-based composites. Akulon Nylon film from DSM (The Netherlands) was used for the melt-processed HPA-6 composite plates (film stacking).

4.2.2 *Processing of epoxy and HPA-6 composite plates*

Epoxy laminated plates were produced using a conventional vacuum infusion process. Laminates were cured at room temperature for 16 hours and then post-cured at 65°C for 7 hours. HPA-6 composite plates were produced by film stacking and melt-impregnated in a hot press following a temperature increase of 9°C/min from room temperature to 275°C before being pressed for 10 minutes and cooled down at a rate of -20°C/min.

4.2.3 *Processing of Anionic Polyamide-6 composites*

As with thermoset infused composites, the first step of the process involves laying up dry fiber textiles in a mold at room temperature. After bagging the lay-up with a heat-resistant and anionic-PA-6-compatible bagging film, tacky tape and transport tubes, the mold temperature is increased to the desired curing temperature prior to infusion.

The resin is usually prepared while the mold is being heated, with the proper amounts of monomer (AP Nylon), activator (caprolactam magnesium bromide (Bruggolen C1)) and initiator (difunctional hexamethylene-1, 6-dicarbamoylcaprolactam (Bruggolen C20)) being loaded into the tanks of a mixing/dosing unit such as the one shown in Figure 3.12. The activator is loaded into tank A, together with half of the monomer while the rest of the monomer, together with the initiator, is loaded tank B. The tanks are heated and once the components are molten, the content is degassed and kept at 110°C under a protective nitrogen environment to prevent oxidation and initiator deactivation due to reaction with moisture. The contents of tanks A and B are then mixed and infused into the mold at a pressure of 250 mbar. Once infused, the resin is allowed enough time to polymerize before the part can be released.

The properties of APA-6 depend strongly on the reaction temperature, which is determined by both external (mold) and internal (exotherm) heat sources. It is therefore expected that because the addition of fibers affects the internally generated heat, the APA-6 composite matrix will have properties differing from those of neat APA-6 processed at an identical mold temperature. Previous work led to the conclusion that the best neat matrix properties were obtained when processed at 150°C and that a significant drop in properties occurred when processed at lower temperature [2]. For composites, in order to obtain optimum matrix properties in between the fibers and to avoid a drop in matrix properties due to a too low reaction temperature, the composite optimum processing temperature was found to be 170°C to compensate for the loss in exothermal heat generated by the thermally insulating glass fiber bed.

4.2.3.1 Ring-opening polymerization

To understand some of the polymerization and crystallization phenomena discussed later in this chapter, a brief description of the ring-opening polymerization process will be given here. Once the different components are fully mixed and the temperature is sufficiently increased, the reaction starts with the dissociation of the initiator in negatively charged caprolactam anions and positively charged magnesium bromide cations (see Figure 4.1). Now negatively charged, the initiator will have the ability to open one of the rings of the activator and form what is called an acyllactam molecule. This molecule having lost a positive charge to the initiator upon formation will be negatively charged at one of its ends. Consequently, a caprolactam ring will be forced to open and mate its positively charged end with the negatively charged end of the acryllactam molecule. Once open, the caprolactam ring being also negatively charged at its free end will force a neighboring caprolactam ring to open and lengthen the polymer chain. Following the same principle, other polymer chains will grow from new initiator molecules being dissociated until most of the caprolactam is consumed.

Unfortunately, it is technically impossible to convert 100% of the caprolactam into polyamide-6 since any positively charged molecules present in the environment surrounding the caprolactam can potentially interfere with the reaction. Due to the nature of the initiator used, the positively charged magnesium bromide released when the initiator molecule starts the reaction will inevitably annihilate a certain amount of caprolactam. Moreover, any positively charged molecules within the fiber bed can also

contribute to increasing residual monomer content. This aspect will be discussed further in later sections of this chapter.

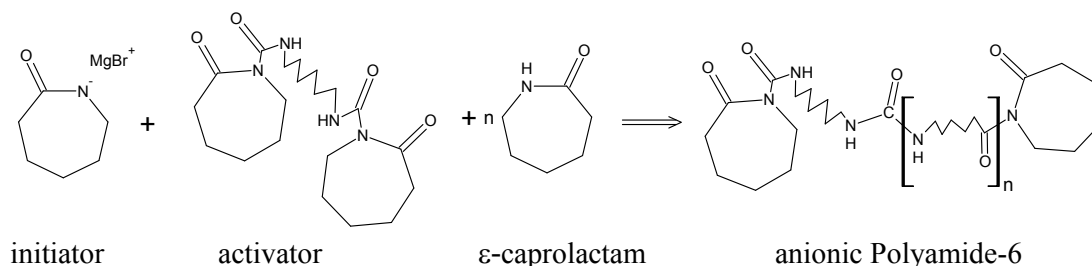


Figure 4.1: Anionic polymerization of ϵ -caprolactam into polyamide-6, using a hexamethylene-1,6-dicarbamoylcaprolactam activator and a caprolactam magnesiumbromide initiator.

4.2.4 Physical property measurements

4.2.4.1 Moisture absorption

The hygroscopic properties of each laminate were evaluated by producing water uptake curves according to the ASTM D5229 norm (*Standard test method for moisture absorption properties and equilibrium conditioning of polymer matrix composite materials*) for two different temperature and moisture conditions, namely 70°C and 100% relative humidity (RH), and 70°C and 62% RH. The latter temperature and moisture condition was used to recreate a 23°C and 50% RH moisture saturation level but in a shorter time period as suggested by the ISO 1110 norm (*Plastics - Polyamides - Accelerated conditioning of test specimens*). Both conditioning schemes were performed simultaneously in a climate chamber set at 70°C in which specimens were either fully immersed in water or exposed to a 62% RH environment. Prior to conditioning, all specimens were oven-dried and weighed to record their moisture-free mass.

4.2.4.2 Material constituents

Laminates were characterized physically to determine their fiber, matrix and void content. PA-6 laminates were also tested for degree of conversion (DOC) and crystallinity (X_c) levels (discussed in the next section).

Fiber and matrix contents were determined through ignition loss of the matrix according to ASTM D2584 (*Standard test method for ignition loss of cured reinforced resins*). After measuring the composite sample weight (W_{comp}), residue fibers left after

pyrolysis were weighed (W_f) and mass fiber percentage (m_f) and fiber volume content (v_f) were calculated using equation 4.1.

$$v_f = m_f \times \frac{\rho_{M-comp}}{\rho_f}, \text{ where } m_f = \frac{W_f}{W_{comp}} \quad (4.1)$$

Composite densities (ρ_{M-comp}) were found experimentally using the displacement method (ASTM D792 - *Standard test methods for density and specific gravity of plastics by displacement*) and the fiber density (ρ_f) was obtained from the manufacturer.

Composite void content measurement was done in accordance with norm ASTM 2734 (*Standard test methods for void content of reinforced plastics*) but had to be adjusted in the case of reactively processed APA-6 composites, for which the matrix density (ρ_{APA-6}) is influenced by the mass percentage of three constitutive elements: The mass percentage of the amorphous phase ($m_{amorphous}$), the mass percentage of the crystalline phase ($m_{crystal}$) and the mass percentage of the residual monomer (un-reacted) ($m_{monomer}$). These three constituents being process dependant (processing temperature, fiber sizing interaction, etc.), the theoretical densities used in ASTM 2734 for APA-6 composites were derived using equation 4.2, where the mass percentages of the three APA-6 matrix constituents were deduced from the crystallinity level and residual monomer content (RMC) of the matrix evaluated respectively by differential scanning calorimetry (DSC) and DOC tests. Monomer density ($\rho_{monomer}$), crystalline phase density ($\rho_{crystal}$) and amorphous phase density ($\rho_{amorphous}$) were obtained from data sheets.

$$\rho_{APA-6} = \frac{1}{\frac{m_{monomer}}{\rho_{monomer}} + \frac{m_{crystal}}{\rho_{crystal}} + \frac{m_{amorphous}}{\rho_{amorphous}}} \quad (4.2)$$

$$v_v = \frac{(\rho_{T-comp} - \rho_{M-comp})}{\rho_{T-comp}} \times 100 \quad (4.3)$$

$$\rho_{T-comp} = \frac{1}{\frac{m_f}{\rho_f} + \frac{m_r}{\rho_r}} \quad (4.4)$$

Finally, with some of the results of the pyrolysis, equation 4.3 was used to determine void content, in which the theoretical composite density (ρ_{T-comp}) was found using the mass percentages and densities of the fiber (ρ_f and m_f) and resin (ρ_r and m_r) according to equation 4.4.

4.2.4.3 Degree of conversion

Samples of APA-6 composites were taken from the laminates and ground into small particles (~1mm). Once weighed, they were refluxed for 8-10 hours in de-mineralized water. Caprolactam being water soluble, the difference in weight of the particles after being refluxed ($W_{monomer}$) can be attributed to the un-reacted monomer content. To evaluate the degree of conversion (DOC) of the polymer, the un-reacted monomer weight needs to be compared to the matrix weight of the composite. In this case, matrix weight is found by ignition loss (ASTM D2584) where the matrix weight is simply the composite weight (W_{comp}) subtracted from the fiber weight (W_f). Finally, with the weights of the constituents known, the DOC can be evaluated with equation 4.5.

$$DOC(\%) = 100 - \left[\frac{W_{mon}}{W_{comp} - W_f} \times 100 \right] \quad (4.5)$$

4.2.4.4 Cristallinity

The degree of crystallinity was determined using differential scanning calorimetry (DSC) by comparing the matrix melting enthalpy of the composite specimens (ΔH_m) to the enthalpy of fully crystalline PA-6 ($\Delta H_{100}=190J/g$) [6]. After drying overnight, small circular samples of weight W_{disc} were first held at 25°C for two minutes and then brought at a rate of 10°C/min up to 240°C in a Perkin-Elmer DSC-7 calorimeter. After the fiber weight (W_f) was measured using a Perkin-Elmer thermal gravimetric analyzer (TGA-7), the degree of crystallinity (X_c) was calculated using equation 4.6. Note that the crystallinity was corrected for the presence of residual monomer.

$$X_c(\%) = \frac{\Delta H_m}{\Delta H_{100}} \cdot \frac{W_{disc}}{W_{disc} - W_f} \cdot \frac{1}{DOC/100} \cdot 100 \quad (4.6)$$

4.2.5 Mechanical property measurements

4.2.5.1 Tensile, compressive and shear properties

Following the manufacturing of plates for all three composite types, test specimens were prepared and tested in tension, compression and shear in accordance respectively with the ISO 527-4 norm (*Test conditions for isotropic and orthotropic fiber-reinforced plastic composites*), the ISO 14126 norm (*Fiber-reinforced plastic composites – Determination of compressive properties in the in-plane direction*) and the ISO 14129 norm (*Fiber-reinforced plastic composite – Determination of the in-plane shear stress/shear strain response, including the in-plane shear modulus and strength, by the $\pm 45^\circ$ tension test method*).

4.2.5.2 Inter-laminar shear strength properties

Inter-laminar shear strength (ILSS) tests were performed at room temperature and relative humidity (23°C and 65% RH) according to the ASTM method D-2344 (*Standard test method for short-beam strength of polymer matrix composite materials and their laminates*). Beams 2-3 mm thick were cut as shown in Figure 4.2 using a wet diamond saw. A three-point bending jig equipped with 3-mm-diameter supports and a 6-mm-diameter loading nose was adjusted to a span of 11 mm to perform all ILSS tests.

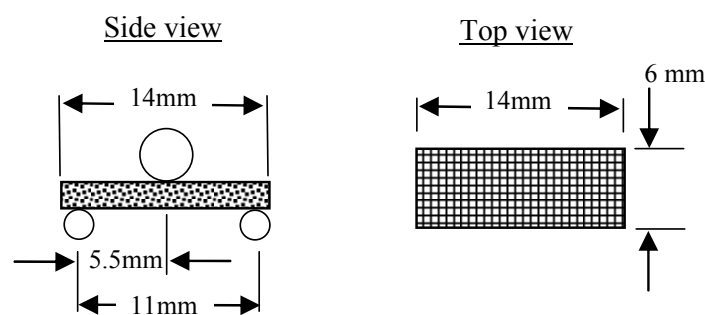


Figure 4.2: Geometry, dimensions and test conditions of the ILSS specimens.

4.3 Resin formulation and fiber surface treatment

Targeting mostly matrix-dominated material properties, the aim of this first study was to compare a series of APA-6-infused thermoplastic composites manufactured

using different resin formulations to epoxy-based composites commonly used for large wind turbine blade structures. Two series of test specimens were prepared either dry-as-molded (DAM) or conditioned at 70°C and 100%RH for 72 hours to capture the effect of material degradation due to moisture absorption. To assess the effect of fiber surface treatment for these two environmental conditions, both un-sized fibers and fibers coated with an aminosilane-based sizing widely recognized as compatible with both epoxy and PA-6 matrices were included in the test program.

In order to identify the best resin formulation for the APA-6 system, three types of activator and initiator ratios were used to produce six different composites when used with either sized or un-sized fibers (see Table 4.1). Epoxy-based composites were produced only with sized fibers. Seven different types of composites were thus manufactured to enable comparison with respect to matrix type and fiber surface treatment (see specimen description in Table 4.2).

Based on matrix properties, water uptake curves, void content and interlaminar shear strength (ILSS), composite types were compared to identify the best resin formulation for APA-6 composites, to evaluate the influence of moisture and to compare the performance of the different fiber surface treatments used. The following sections will present the results of this first study.

Table 4.1: APA-6 matrix formulation.

Matrix Type	Ratios with respect to monomer content (%mol)	
	Initiator*	Activator**
APA-6 (<i>formulation A</i>)	1.2	0.6
APA-6 (<i>formulation B</i>)	1.2	1.2
APA-6 (<i>formulation C</i>)	0.6	1.2

* Caprolactam magnesium bromide (Bruggolen C1)

** Difunctional hexamethylene-1,6-dicarbamoylcaprolactam (Bruggolen C20)

4.3.1 Fiber volume fraction and void content

Fiber volume fraction (v_f) and void content (v_v) were determined for all laminates, while the degree of conversion (DOC) and crystallinity level (X_C) was only found for the APA-6 laminates. Results are summarized in Table 4.2.

Table 4.2: Laminate physical properties.

Specimen description	Fiber surface treatment	v_f %	v_v %	DOC %	X_c %
APA-6	Sized	50.3	2.8	96.5	36.3
(formulation A)	Unsize	48.7	2.5	92.5	35.2
APA-6	Sized	49.9	3.6	96.8	36.1
(formulation B)	Unsize	48.7	1.8	94.1	37.8
APA-6	Sized	50.9	11.1	96.2	36.8
(formulation C)	Unsize	50.6	7.6	92.0	35.0
Epoxy	Sized	50.2	0.8	-	-

In order not to bias the ILSS results, special care was taken to match the fiber volume content of all composites by tuning some of the processing parameters. The difference in fiber volume content between all laminates was thus kept within 1%. Concerning void content, higher values were found for APA-6 laminates than for epoxy laminates. The APA-6 laminate produced with formulation C even peaked at an unusually large value of 11.1%. It is worth mentioning that the void content results shown in Table 4.2 are average values and that they could vary as much as 2% over the surface of some APA-6 panels (5 to 8 samples were usually taken over the surface of the plates).

Since the type of formulation cannot significantly affect the void content, these rather high void contents were most likely caused by poorly degassed resin. The fact that both sized and un-sized APA-6 (formulation C) laminates showed high void content reinforces this hypothesis since they were produced one after the other from the same resin batch.

4.3.2 Degree of conversion

The degree of polymerization has a profound influence on polymer properties since un-reacted residual monomer acts as a plasticizer. To investigate whether the selected fiber sizing has a negative effect on polymerization, the DOC of the various APA-6 composites presented in Table 4.2 were compared with DOC values for the neat resin (polymerized without fibers [1], see Figure 4.3).

It can be seen that formulations A and B lead to sized fiber composites with conversions that are similar to the neat polymer and that these conversion levels also correlate well with the theoretical values [1]. However, sized fiber composites using formulation C show conversion levels that are clearly below the theoretical value. The

explanation for this is that a temperature increase during polymerization (the exotherm) is necessary for continued polymerization up to high degrees of conversion. Formulation C has the lowest amount of initiator and therefore the lowest reaction rate. The resulting exothermic peak, mitigated by the presence of the fibers, is believed insufficient for this formulation to achieve high degrees of conversion.

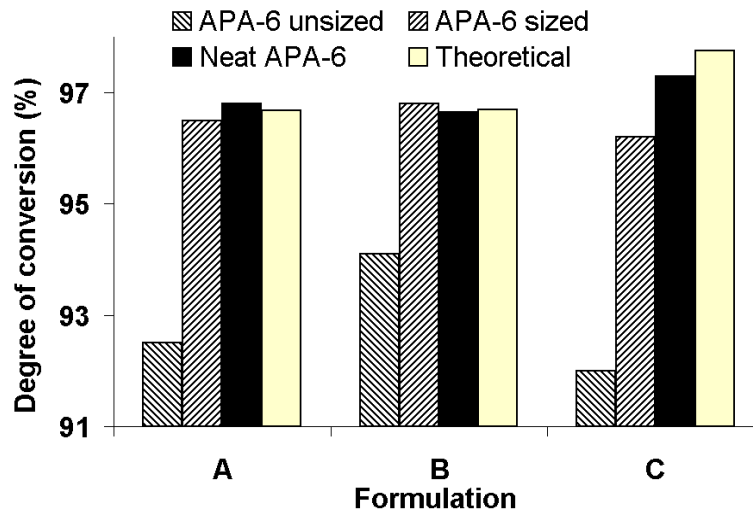


Figure 4.3: Degree of conversion of the three APA-6 composite formulations processed with sized and un-sized fibers compared to the maximum theoretical degree of conversion and experimental degree of conversion of neat APA-6.

Finally, when comparing DOC of sized fiber composites against un-sized fiber composites, it was noted that un-sized fibers adversely affected polymerization while the aminosilane-sized fibers appeared not to have disturbed the polymerization process. Since the initiator is very inclined to react with OH-groups (hydroxyl groups) present on the surface of bare fibers, the ~3-4% decrease in DOC for un-sized fiber composites compared to sized fiber composites could be due to local deactivation of the initiator in the interphase region. Also, since bare fibers are very vulnerable to moisture absorption, the initiator could also be deactivated when entering into contact with moisture-rich fibers. These results show the importance of moisture control during reactive anionic polyamide-6 processing of composites. In later studies by van Rijswijk, this hypothesis was validated with results showing that laminates flushed with dry nitrogen prior to infusion had a residual monomer content reduced by 8% compared to laminates that were flushed dry [7].

4.3.3 Moisture uptake

Depending on the specimen type and moisture condition, specimens usually reached moisture equilibrium within 20 days. Water absorption curves were made for the two temperatures and moisture conditions discussed in section 4.2.4.1. It can be seen clearly from Figures 4.4a and 4.4b that the epoxy composites absorb less water than APA-6-based composites. This larger water absorption level for APA-6 composites is considered attributable to the higher intrinsic diffusion properties of their matrix, combined with the fact that they show larger void contents compared to the epoxy specimens (2-3% higher).

When looking at the effect of fiber surface treatment on water absorption, results show that using a sizing significantly reduces the absorption rate. This phenomenon is observed in Figure 4.4a, in which the water absorption curves of sized and un-sized APA-6 laminates (formulation B) can be compared. Interestingly, although they have very different absorption rates early in their conditioning, both laminates yield similar saturation levels once at equilibrium. The large absorption rate of un-sized fiber laminates can be attributed to the presence of unreacted monomer in their interphase region. Caprolactam being water soluble, the absorption rate can be increased greatly since water can enter the laminate rapidly through the caprolactam-filled interphase region. Finally, not using a sizing apparently did not compromise fiber wettability when infusing APA-6, otherwise laminates with dry fibers would have shown higher water absorption levels. Proper wetting was to be expected no matter what fiber treatment was used since the viscosity of APA-6 resin is very low ($\sim 1 \text{ mPa}\cdot\text{s}$).

Three main factors could influence moisture saturation levels of the three different APA-6 composite formulations: Crystallinity level, RMC (or un-reacted monomer content) and void content. Since the crystalline phase absorbs significantly less moisture than the amorphous phase, laminates with different degrees of crystallinity are expected to yield different moisture saturation levels. For the laminates under study, crystallinity is not believed to be a key factor when comparing moisture saturation levels since all crystallinity levels are similar (see Table 4.2). Laminates with significantly different RMC could also yield different moisture contents since leaching out of un-reacted monomer can leave the composite with new voids filled with water. For sized fiber composites, since RMC is quasi-equal for all laminates (see Table 4.2, where $\text{RMC} = (100 - \text{DOC})$), RMC is not believed to be responsible for the observed differences in

moisture saturation levels. By ruling out these first two factors, void content is considered the most influential factor to explain moisture saturation level differences among sized APA-6 laminates. In agreement with this hypothesis, comparing void contents in Table 4.2 to the results of Figure 4.4a indicates that the three different formulations for sized APA-6 composites have moisture saturation levels proportional to their void content, suggesting that voids most probably act as small reservoirs when conditioned fully immersed in water. Similar trends can also be observed in Figure 4b, which shows that water absorption in the first days of conditioning is proportional to void content. It can be seen that moisture saturation was reached very early in the case of formulation C. The most probable explanation for this behavior is that compared to the other composites, its moisture diffusivity was increased significantly due to its large void content.

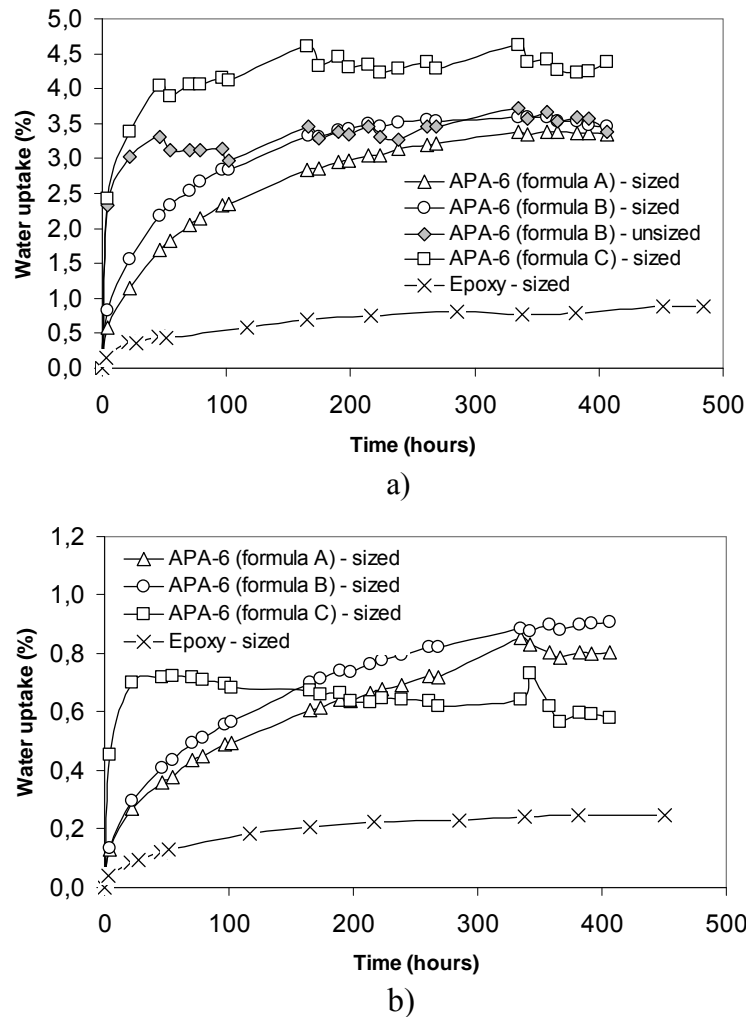


Figure 4.4: Water uptake curves for APA-6 and epoxy based composites. a) 70°C, 100%RH condition, b) 70°C, 62%RH condition.

4.3.4 Interlaminar shear strength

Figure 4.5 shows the results of ILSS tests performed on the different specimens. When first comparing the overall performance of sized and un-sized APA-6 composites, the beneficial effect of using a coupling agent between the fibers and the matrix can be seen clearly in both dry-as-molded (DAM) and wet conditions. In DAM conditions, ILSS of un-sized fiber laminates is considered to have been compromised by the earlier discussed presence of un-reacted monomer at the interphase. On the other hand, sized fiber APA-6 laminates performed relatively well in DAM conditions, yielding ILSS between 50-70 MPa. This significant increase in ILSS compared to un-sized fiber laminates shows that APA-6 can interact positively with the sizing and not be hindered by a layer of un-reacted caprolactam. It is suggested that for the sized fiber laminates, the RMC is well dispersed in the matrix rather than concentrated in the interphase region. Also, when referring to the DOC of the three formulations of Table 4.2, the amount of RMC seems to be affecting ILSS directly, since the higher the RMC, the lower the ILSS.

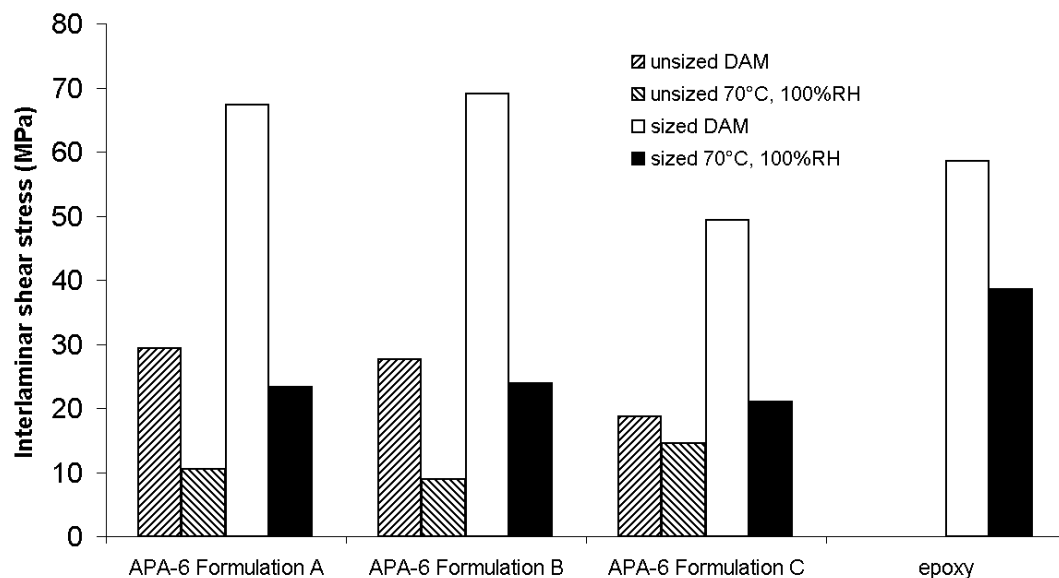


Figure 4.5: ILSS results of sized and un-sized APA-6 composites shown against epoxy-based composites.

In moist conditions, sized APA-6 laminates suffered from a significant drop in ILSS, showing retention levels between 35% and 40%. This adverse effect of moisture

conditioning on ILSS can be attributed to the following aspects either related to matrix shear property reduction or fiber-to-matrix bond degradation:

- The significant associated reduction of modulus for polyamides due to moisture absorption.
- Matrix swelling due to water uptake can reduce the beneficial effects of crystallization-induced mechanical locking around the fibers and consequently reduce fiber-to-matrix adhesion.
- Interaction between the matrix and the sizing can also be reduced by the presence of moisture at the interphase, due to hydrolysis of siloxane bonds or breaking of hydrogen bonds [7].

Although it was not possible to determine whether interlaminar failure of moisture conditioned APA-6 composite samples was caused by fiber-to-matrix de-bonding or matrix shear failure, the excessive deformation of the sample suggests that the matrix sheared significantly before the failure load was attained.

Finally, comparison of APA-6 composites to epoxybased composites shows that well-formulated APA-6 composites can yield 15% higher ILSS in DAM conditions. In moist conditions, retention levels of 40% and 64% were obtained respectively for APA-6 and epoxy-based composites.

4.3.5 Discussion

As shown in other studies, moisture absorption rate and saturation level can be influenced by various parameters, including the quality of the interfacial bond, the matrix type and its diffusion properties or the void content of the laminate [8-10]. In our case, results showed that using a sizing for APA-6 composites could significantly reduce the moisture absorption rate but did not affect saturation levels. Results also showed that the APA-6 composites were noticeably more vulnerable to moisture absorption than were epoxy-based composites. This vulnerability can be attributed to the larger intrinsic diffusion properties of their matrix but could also be influenced by the higher void content compared to their epoxy counterpart.

Figures 4.3 and 4.5 show a clear link between the degree of conversion and the ILSS of APA-6 specimens in the case of sized fiber composites. As expected, since un-reacted monomer acts as a plasticizer, when a low degree of conversion is attained

compared to that of neat matrix conversion, ILSS is adversely affected. This result underscores the importance of achieving a high degree of conversion to ensure the quality of APA-6 laminates.

It was somewhat surprising that in DAM conditions, well-formulated APA-6 composites can yield 15% higher ILSS than their epoxy-based counterpart. This result is believed attributable to the capability of APA-6-based composites to use a combination of chemical adhesion and strong mechanical locking caused by crystallinity-induced shrinkage around the fibres to improve ILSS. This explanation would also be in agreement with the significant drop in ILSS when specimens are conditioned since the large water absorption level observed for APA-6 composites generates excessive matrix swelling, which significantly reduces the contribution of mechanical locking to ILSS. Conversely, epoxy specimens showing a lower moisture absorption level could have a higher percentage of ILSS retention in “wet” conditions than APA-6 composites due to their associated reduced swelling.

As mentioned earlier, void content is expected to play an important role in ILSS degradation in “wet” conditions since it is linked directly to moisture uptake. Since the APA-6 specimens manufactured for this test program contained a higher void content than their epoxy counterparts, significant improvements in ILSS retention in humid conditions are expected for APA-6 composites if void content can be reduced. Results for laminates of lower void content could also help determine whether the greater influence on moisture saturation level is due to void content or intrinsic material diffusion properties.

Finally, based on the results of this study, formulation B was selected as best suited for APA-6 infused composites and was used for the benchmarking study to be presented in the next section.

4.4 Benchmarking anionic polyamide-6

In this section, based on the best initiator/activator formulation identified in the previous section, APA-6 composites will be benchmarked against a conventional hot-pressed hydrolytically polymerized polyamide-6 (HPA-6) composite and a typical wind turbine epoxy-based composite. To address the vulnerability of polyamide-6 (PA-6) to water absorption, dry-as-molded (DAM) and moisture-conditioned samples were again included in the test program. Based on neat matrix properties, composite mechanical

properties, moisture absorption and fracture characterization, composites were compared and a discussion of the results is given.

4.4.1 Basic laminate properties

To help interpret the results later, some key neat matrix material properties are shown in Table 4.3 for both DAM and moist conditions. Epoxy properties were obtained from the manufacturers while HPA-6 and APA-6 properties were obtained experimentally with the procedures described earlier.

After manufacturing the different composite panels, systematic testing was performed to find some of their basic characteristics. Density, fiber volume contents (v_f) and void contents (v_v) were determined for all three composites while degree of conversion (DOC) and degree of crystallinity (X_c) tests were performed for both thermoplastic composites. Results are shown in Table 4.4.

Table 4.3: APA-6, HPA-6 and epoxy matrix physical and mechanical properties.

Matrix material	Density (g/cm ³)	DOC (%)	X_c (%)	DAM, [Conditioned at 70°C-62%RH]			
				Tensile Mod. (GPa)	Tensile Str. (MPa)	Elong. at break (%)	Moisture content (wt%)
Epoxy	1.14	-	-	3.3 [-]	66 [-]	3.2 [-]	1.2
HPA-6	1.13	99.8	37	3.0 [1.3]	84 [59]	>50 [>50]	3.0
APA-6	1.164	97.3	41	4.2 [2.1]	96 [61]	8.5 [28]	2.4

Table 4.4: APA-6, HPA-6 and epoxy composites physical and mechanical properties.

	Matrix		
	Epoxy	HPA-6	APA-6
Dens. (g/cm ³)	1.82	1.88	1.83
v_v (%)	2.1	1.3	3.0
v_f (%)	47.5	51.2	49.5
DOC (%)	-	99.8	95.0
X_c (%)	-	33	35
Matrix moisture content (wt%)	0.8	2.5	2.7

4.4.2 Static properties

Tensile, compressive and shear moduli and strengths are the main properties used to compare material performance in dry-as-molded and humid conditions.

As in the previous study, in order not to bias the comparison between composites, special care was taken to match the fiber volume contents of all three composite types by tuning some of the processing parameters. This effort resulted in specimens showing a fiber volume content of $49.4 \pm 1.8\%$ for all three composites. Following the manufacturing of plates with all three composites, samples were prepared and tested in tension, compression and shear on a Zwick-Roell Z250 25-ton test machine. For these tests, groups of 8 to 12 samples were either moisture-conditioned at 70°C and 62% RH for two weeks (equivalent to 23°C/50% RH saturation – ISO 1110 standard) or dried for a week under vacuum at 60°C for the DAM condition. Finally, to compare the composites, apart from the physical properties discussed in the previous section (DOC, X_C , v_v , etc...), scanning electron microscopy (SEM) was used on selected samples.

4.4.2.1 Dry-as-molded

Figure 4.6 shows that in DAM conditions, APA-6 composites nearly outperformed epoxy and HPA-6-based composites for all loading conditions. While the modulus can be considered similar for all three composites, APA-6 composites showed a 20% increase in compressive strength and a slight improvement in tensile and shear strengths.

4.4.2.2 Moisture-conditioned

Figure 4.7 shows the properties of the composites in wet conditions. As expected, both thermoplastic composites were significantly more affected by moisture than were epoxy-based composites. Retention levels were found to average 79%, 82% and 94% respectively for the APA-6, HPA-6 and epoxy based composites. The tensile and compressive moduli of PA-6 composites were affected moderately by moisture while their shear modulus was degraded down to close to 50% of their DAM value. APA-6 composites suffered a larger loss of strength than their hydrolytic counterpart, showing retention levels in compression and tension of 62% and 87%, compared to 80% and 98%. APA-6 composites performed better in shear strength, with a retention level of 88% compared to 85% for HPA-6 composites.

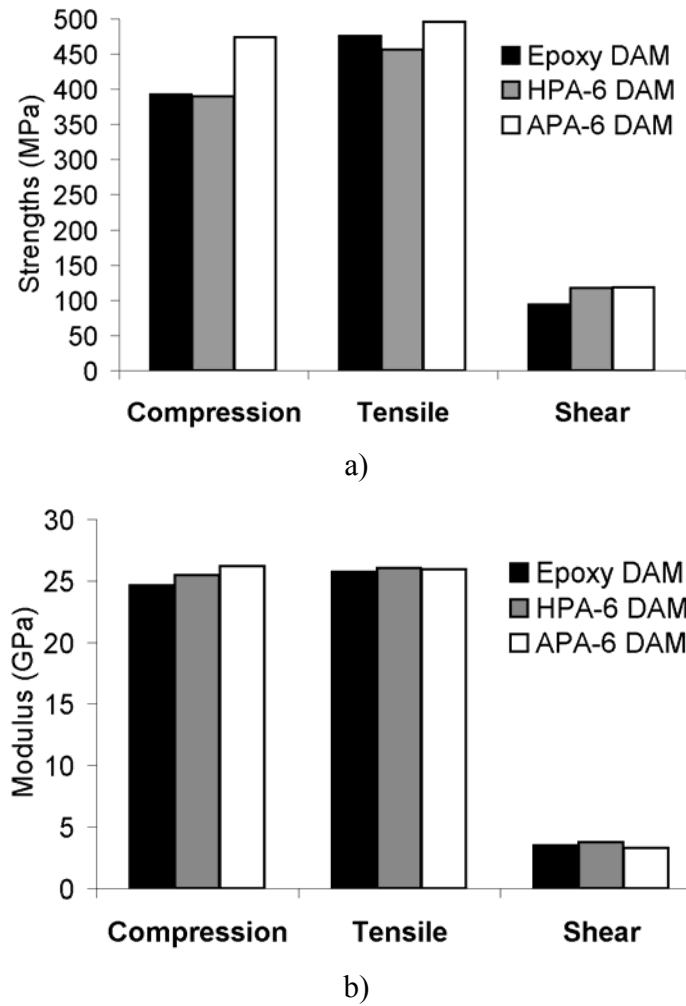


Figure 4.6: Epoxy, HPA-6 and APA-6 dry-as-molded composite properties. a) Compressive, tensile and shear strengths. b) Compressive, tensile and shear moduli.

4.4.2.3 Discussion

The high modulus and strength of the dry APA-6 neat matrix shown in Table 4.3 seems to translate directly into superior APA-6 composite in DAM conditions. The drop in performance of both polyamide composites due to moisture absorption is substantial compared to the seemingly unaffected epoxy composites and is more significant for APA-6 composites. In addition to its higher void content, the interface is suspected of being a weak point. In dry conditions, crystallization-induced shrinkage leads to strong mechanical locking of the fibers and the existence of a chemical interface is only of minor importance. However, moisture adsorption causes the matrix to swell and the chemical nature of the fiber-to-matrix bond becomes increasingly important for maintaining mechanical properties.

Figure 4.8 shows that whereas the HPA-6 matrix still seems to adhere to the fibers in wet conditions, the APA-6 matrix is completely peeled off. The fact that the HPA-6 composite has a better interface with the same sizing could be explained by the fact that at higher processing temperatures (275°C vs. 170°C) the aminosilanes are more reactive.

Besides the obvious improvements to be made regarding the void content and the fiber-to-matrix bond, the matrix itself also appears to have room for improvement. The fact that the crystallinity and conversion levels of APA-6 when used as a matrix are both lower than those of neat APA-6 indicates that the performance of the APA-6 composites still can be significantly improved.

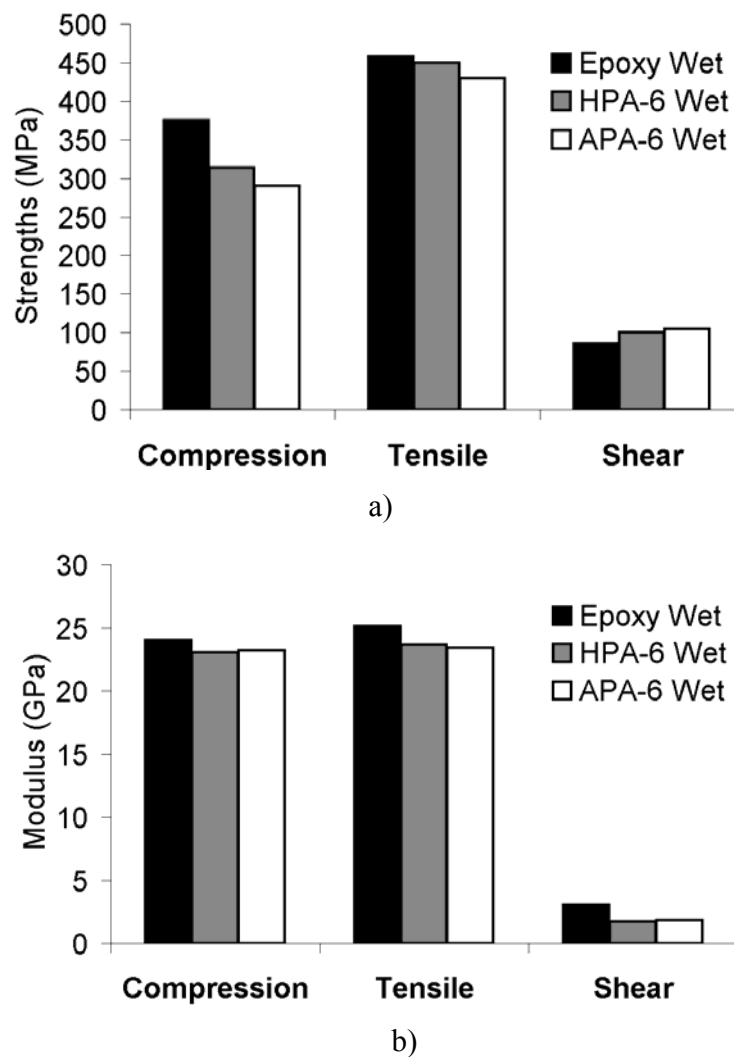


Figure 4.7: Epoxy, HPA-6 and APA-6 moisture conditioned (70°C-62%RH) composite properties (WET). a) Compressive, tensile and shear strengths. b) Compressive, tensile and shear modulus.

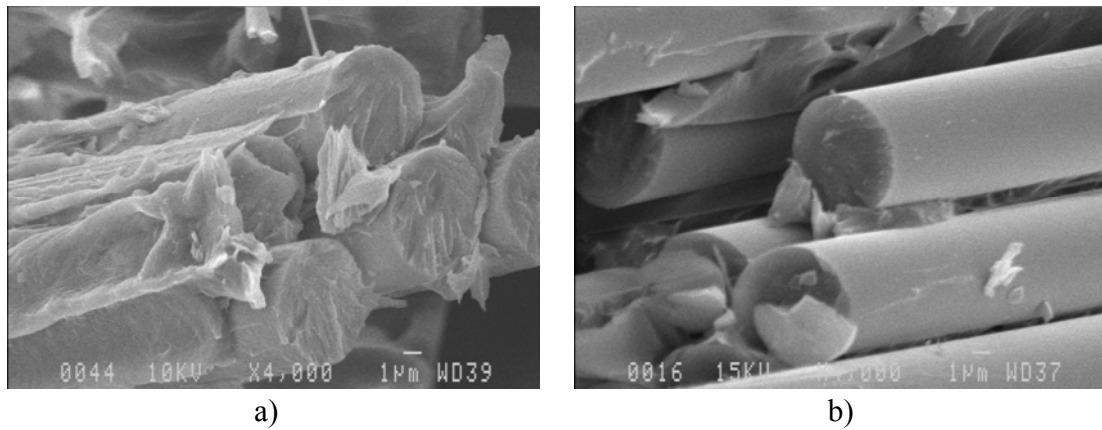


Figure 4.8: Scanning Electron Micrographs of the fracture surface after shear testing in wet conditions. a) HPA-6 composite. b) APA-6 composite.

4.4.3 Fatigue properties

In this section, the fatigue performance of the same three different composite laminates used for the static performance benchmark study just presented will be investigated. Since this study was not meant as a full fatigue characterization program, only dry-as-molded samples were tested in tension-tension fatigue ($R = 0.1$). As before, to help understand the response of the different composites to fatigue loading, basic physical properties were measured for all composites (see Table 4.5).

Fatigue testing was conducted on a MTS 831 Elastomer Test System with 647 Hydraulic Wedge Gips (1 MPa clamping force). At least five samples (75 x 10 x 2.9 mm, with end tabs, gauge length: 10 mm) were tested per load amplitude at a frequency of 10 Hz (sinusoidal). At that frequency, the temperature of the samples reached a maximum of 31°C. Since this temperature is well below the glass transition temperature of PA-6 (50-80°C), the results are believed to be unaffected by this slight increase in temperature. To help interpret the results, prior to presenting the benchmarking results, a short discussion of certain fatigue issues will be given.

4.4.3.1 Fatigue mechanisms

Fatigue damage usually starts with micro-cracks appearing in the matrix. Since crack initiation is favored by any impurities and defects present in the laminate, void reduction is of course crucial to increase damage tolerance in composites [11]. With increasing cycles, these micro-cracks grow to form larger cracks that eventually reach neighboring fibers. At this critical stage in damage accumulation, depending on the

quality of the fiber-to-matrix bond and the nature of the matrix, the crack can either progress along the interface or bridge across the fiber to continue growing in the same direction. Cracks in brittle matrices like epoxies will usually have a tendency to bridge fibers if the interface is of good quality while cracks in tougher matrix systems (typically thermoplastics) will progress instead along the interface [12]. Depending on the ongoing crack growth mechanism and type of loading applied, different types of fiber fracture will eventually occur (fiber breakage, micro-buckling, etc.). In general, interface crack propagation leads to more fiber breakage for an equivalent number of cycles compared to fiber bridging cracks, consequently leading to a shorter fatigue life [12].

4.4.3.2 The effect of void content

Based on the discussions in previous sections, APA-6 composites would be expected to have an improved fatigue resistance in DAM conditions when compared to HPA-6 composites since their interface can benefit from both mechanical locking of the matrix around the fibers and a stronger chemical bond of the fibers to their matrix. On the other hand, due to their high void content, damage tolerance in early cycles is expected to be very low. Since initial damage strongly influences fatigue life, the large void content of APA-6 composites in comparison with epoxy and HPA-6 composites could potentially adversely affect their fatigue life.

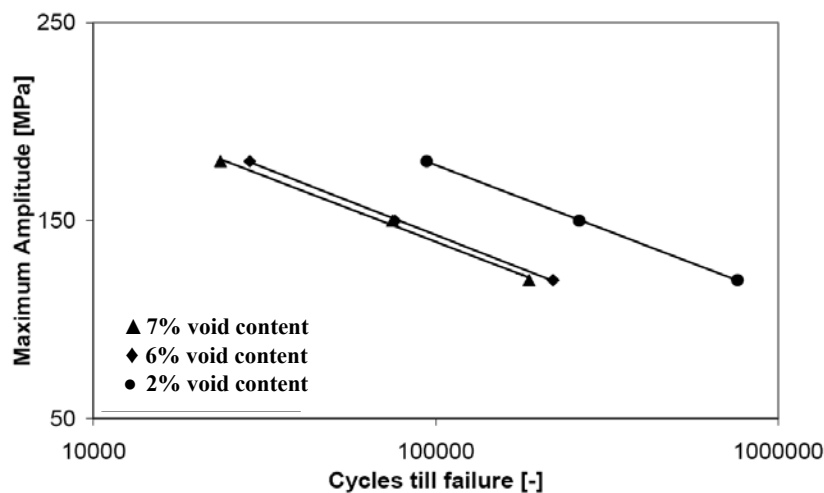


Figure 4.9: Influence of void content on fatigue properties of APA-6 composites (adapted from [13]).

To validate the hypothesis just put forward, APA-6 composites with significantly different void contents were tested in fatigue and compared. Figure 4.9 shows that a composite with a void content of 2% can in fact have a fatigue life almost twice that of composites having void contents of 6-7%.

4.4.3.3 Results and discussion

Figure 4.10 shows the S-N curves of the three composites benchmarked in this chapter. It can first be observed that APA-6 composites have a higher fatigue resistance than the melt-processed PA-6 composites. This is believed to be most likely caused by the stronger fiber-to-matrix interface of the APA-6 composite.

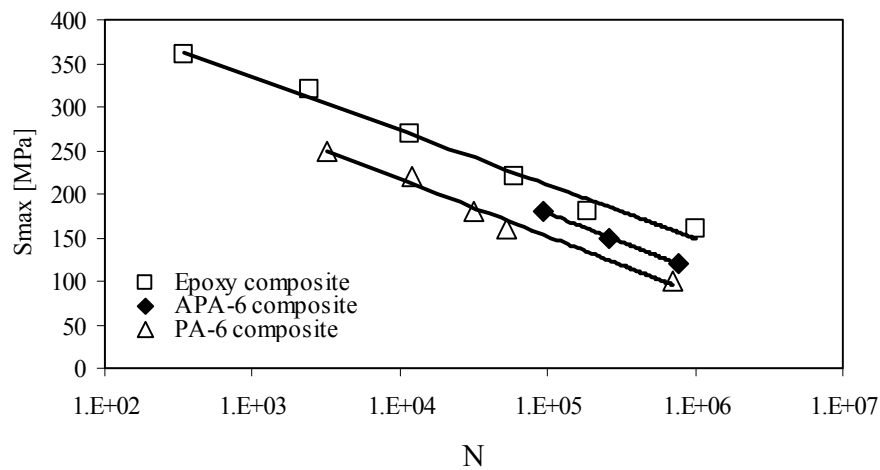


Figure 4.10: Tension-tension S-N curve of low void APA-6/glass composite compared against HPA-6 composites and epoxy-based composites.

As explained earlier, since APA-6 composites can benefit from mechanical locking of the matrix around the fibers as well as chemical bonding, their interface is superior to that of HPA-6 composites. The ILSS results of the APA-6 composites tested in fatigue shown in Table 4.5 being higher than HPA-6 composites also suggest that the interface of APA-6 composites is superior. Conversely, the higher crystallinity of the HPA-6 composites suggests that their matrix has higher shear strength and that stronger mechanical locking exists due to a higher level of crystallization-induced shrinkage. Nevertheless, their lower crystallinity notwithstanding, the APA-6 composites have a higher ILSS, which indicates that a stronger chemical bond exists between the fibers and the APA-6 matrix. The existence of a stronger fiber-to-matrix bond in the APA-6 composite is also confirmed by the SEM micrographs shown in Figure 4.11. Whereas the bare fibers of the PA-6 composite show detachment of the matrix, the strong

interfacial bond and stiffer nature of the APA-6 matrix has prevented crack growth along the fiber surface consequently leaving the matrix attached to it.

Table 4.5: Physical and mechanical properties of composites tested in fatigue.

	APA-6 composite	HPA-6 composite	Epoxy composite
Crystallinity [%]	29	37	-
Degree of conversion [%]	93	100	100
Void content [%]	3	1.3	2.1
ILSS [MPa]	72	64	59

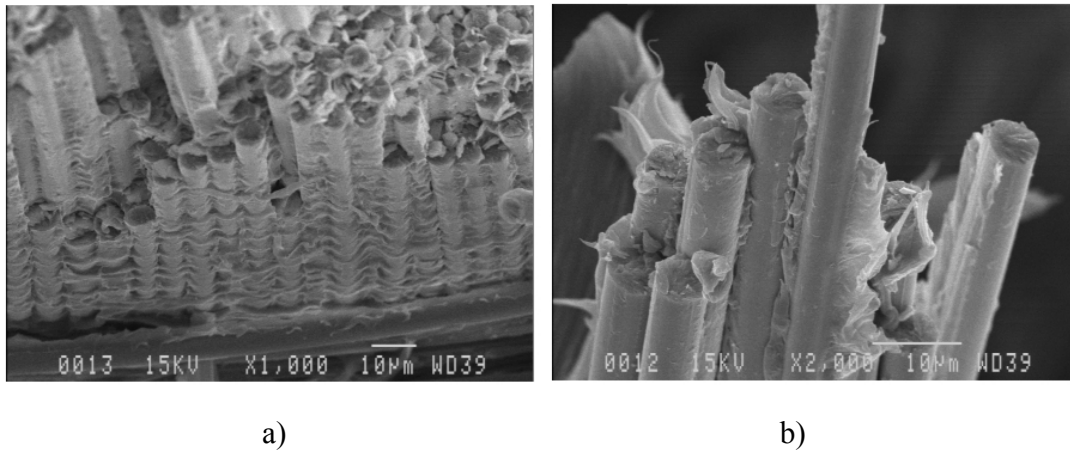


Figure 4.11: SEM micrographs (Jeol JSM-840) of the two thermoplastic composites. a) APA-6 composite. b) HPA-6 composite.

Referring again to Figure 4.10, it is obvious that epoxy composite outperforms both thermoplastic composites in fatigue. This improvement in fatigue properties can be attributed to the strong fiber-to-matrix bond typical of epoxy composites. This not being reflected in the ILSS results shown in Table 4.5 can be attributed to the lower degree of shrinkage of epoxies, which compromises mechanical locking of the matrix around the fibers. Knowing that 50-60 MPa is the typical range of shear strengths of epoxies, it is most likely that the matrix rather than the interface failed in shear during the ILSS test.

A last interesting observation regarding the differences in the fatigue behavior of the three benchmarked composites is worth mentioning. As shown in Figure 4.12, the standard deviation of samples tested at the same load was found to be significantly smaller for both thermoplastic composites. This is very beneficial for making accurate fatigue life predictions. Since scatter in strength and fatigue life is inherent to brittle matrix composite materials, it was to be expected that epoxy composites show larger

scatter bands when plotted in S-N curves. Due to their higher toughness, PA-6 composites are more resistant to crack growth perpendicular to the loading direction. In that sense, APA-6 composites are expected to offer better fatigue predictions than their epoxy-based counterpart if their fatigue resistance can be raised to a similar level.

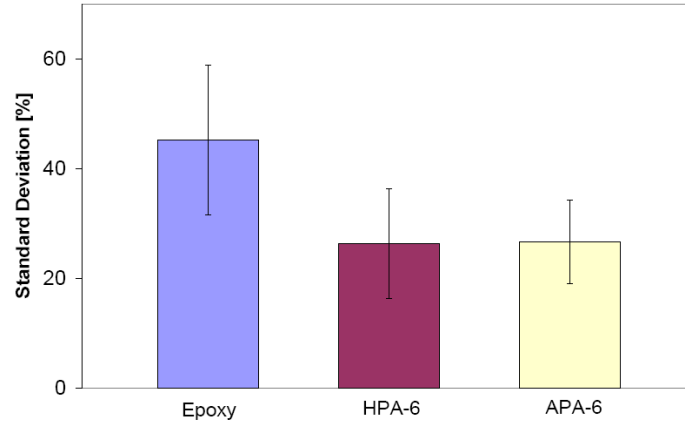


Figure 4.12: Fatigue data scatter represented as standard deviations on the different test load applied [13].

4.5 Development of a recycling strategy

The main objective of the work presented in this section was to evaluate the potential of APA-6 composites for recycling into short-fiber composite injection-molded parts. The potential of the recycled injection-molded material was evaluated on the basis of the strength and stiffness performance of ASTM type I test specimens.

4.5.1 Methodology

Short-fiber reinforced injection-molded parts typically have fiber weight contents (w_f) of 30 to 50%, which is significantly lower than continuous fiber composites ($\sim 70\%$). The shredded APA-6/glass composite laminates (often referred here as the “recyclate”) earlier described were therefore mixed with virgin resin prior to injection. When diluting recycled material with virgin resin, two options are available. If the virgin plastic pellets are of size similar to the recyclate, one can attempt simply to feed the pellets and raw material directly to the injection screw. The other option is to compound the materials (shredded laminates + dilution resin) first in order to produce plastic pellets with the desired fiber content by weight prior to injection. For this study, the first option was retained to see if a one-step recycling strategy was feasible.

The influence of the type of resin used for dilution, the influence of the size of the recycle particles (or length of the short-fibers) and the degradation of the short-fiber composite when recycled more than once was studied. To cover these three aspects, the laminates were first ground and separated in two different groups of different particle sizes (0.6-2mm and >2mm). APA-6 virgin plastic and hydrolytically polymerized polyamide-6 virgin plastic (HPA-6) were mixed with the two different groups of recycle to form four different families of material each showing a fiber content of 30% by weight (see Table 4.6).

In order to measure the effect of multiple regrinds and injections, parts obtained from a first injection using material from each of the four families were reground and injected a second time.

Table 4.6.: Recycled material description with respect to recycle particle size and dilution resin type.

Dilution Resin Type	Ground Particle Size	
	Mesh 30 $0.6 < l < 2 \text{ mm}$	Mesh 10 $l > 2 \text{ mm}$
APA-6	mesh 30 ground APA-6/glass laminates	mesh 10 ground APA-6/glass laminates
	mesh 30 ground APA-6 virgin plastic $w_f = 30\%$	mesh 10 ground APA-6 virgin plastic $w_f = 30\%$
HPA-6	mesh 30 ground APA-6/glass laminates	mesh 10 ground APA-6/glass laminates
	HPA-6 pellets (<i>Capron B135WP</i>) $w_f = 30\%$	HPA-6 pellets (<i>Capron B135WP</i>) $w_f = 30\%$

4.5.2 Material processing

4.5.2.1 Grinding of laminates

The laminates were first trimmed and cut into 25-mm-wide strips using a water-cooled diamond saw. The laminate strips were then cut into 50-mm-long pieces that were cleaned and de-burred (as shown on Figure 4.13a) before being granulated with a S-10-9 granulator manufactured by *C.W. Brabender Instruments*. The granulator was equipped with tungsten carbide rotating blades and a primary sieve that let only granules less than 6 mm long pass through. Final sifting was done using a model RX-29 *W.S. Tyler* Ro-tap testing sieve shaker with a stacking of 2.00-mm (mesh 10), 0.595-mm (mesh 30) and 0.250-mm (mesh 60) sieves. Material found above the 2-mm sieve was kept to form the first family of material to be injected ($l > 2 \text{ mm}$) while the material

left between the 2.00-mm and 0.595-mm sieves was kept to form the second family of material ($0.6 < l < 2$ mm). The rest of the sifted material was discarded.



Figure 4.13: Raw material shredding. a) Trimmed and cut laminate to be fed to the granulator. b) Recyclate being oven dried prior to injection.

4.5.2.2 Dilution resins

The APA-6 virgin plastic used for dilution was obtained from castings of the same resin used to manufacture the APA-6/glass laminates. The polymer blocks were first cut using a vertical band saw and then granulated and sifted with the same equipment and procedure as described above.

The second family of material with respect to dilution resin type was made by means of diluting commercial-grade HPA-6 pellets (*Capron B 135 WP*). The dilution resins were added to the recyclate to obtain short-fiber reinforced composite with a fiber content of 30% by weight.

4.5.2.3 Injection Molding

Injection molding of the ASTM type I test specimens was done with a BOY35A reciprocating screw injection machine set with a 35-ton clamp force. The recyclate and dilution resins were oven-dried under vacuum at 74°C for 48 hours prior to injection (see Figure 4.13b). The injection screw temperature profile increased from 260°C to 290°C from the hopper to the nozzle and the mold temperature was kept at 80°C. Mold filling was done at a rate of 100 mm/s and backpressure was held at 50 bars after the

injection. Runners and sprue were kept and reground for a second injection (see methodology for details).

4.5.3 Mechanical properties

The strength, modulus and elongation at break of the different material families were determined according to the ASTM Test Method for Tensile Properties of Plastics (ASTM D-638-03) using an *MTS Insight 200* mechanical testing machine equipped with a 10-kN load cell. The crosshead speed was set at 5 mm/min and a 50 mm span extensometer was clamped to the specimens until break. Prior to testing, the test specimens were dried under vacuum for at least 48h to obtain dry-as-molded (DAM) properties.

Table 4.7: Tensile properties of injected short-fibre glass reinforced specimens - 1st injection cycle.

	Tensile strength (MPa)	Standard deviation (MPa)	Tensile modulus (GPa)	Standard deviation (GPa)	Elong. at break (%)	Standard deviation (%)
APA-6 ($0.6 < l < 2$ mm)	143.8	3.9	9.19	0.35	2.53	0.20
APA-6 ($l > 2$ mm)	147.8	4.8	9.39	0.63	2.46	0.12
HPA-6 ($0.6 < l < 2$ mm)	179.9	7.0	9.93	0.63	2.66	0.10
HPA-6 ($l > 2$ mm)	182.5	7.7	10.29	0.59	2.48	0.07

Table 4.8: Tensile properties of injected short-fibre glass reinforced specimens - 2nd injection cycle.

	Tensile strength (MPa)	Standard deviation (MPa)	Tensile modulus (GPa)	Standard deviation (GPa)	Elong. at break (%)	Standard deviation (%)
APA-6 ($0.6 < l < 2$ mm)	138.7	2.0	9.12	0.20	2.74	0.12
APA-6 ($l > 2$ mm)	147.6	3.2	8.73	0.09	2.82	0.07
HPA-6 ($0.6 < l < 2$ mm)	167.8	3.3	9.51	0.46	3.29	0.03
HPA-6 ($l > 2$ mm)	172.2	1.4	9.44	0.16	3.28	0.10

Results for these tensile properties after the first and second injections are presented respectively in Tables 4.7 and 4.8. It is noted first that the influence of the type of dilution resin used is significant in the sense that all samples using HPA-6 as the dilution resin yielded higher tensile strength and modulus than APA-6-resin-diluted samples, even after two injection cycles. Comparison of the effect of fiber length on mechanical properties shows that longer fibers generally give slightly superior

mechanical properties. When observing the results to see if the material degrades after multiple regrinds and injections, results show that after two cycles of regrinding and injection molding was a 1-8% decrease in tensile strengths and moduli for all types of material studied. It is also noted that the standard deviations for both strength and modulus are much larger for the first injection cycle. This is likely due to the first cycle being done with a non homogeneous mix of ground recyclate and neat polymer pellets while the second injection cycle was done with a more homogenous regrind of the first cycle containing 30% fiber. This characteristic is also reflected by the difference in elongation at break percentages between the first and second injection recycled material. Elongations at break for the material of the second injection are significantly larger than those of the first injection.

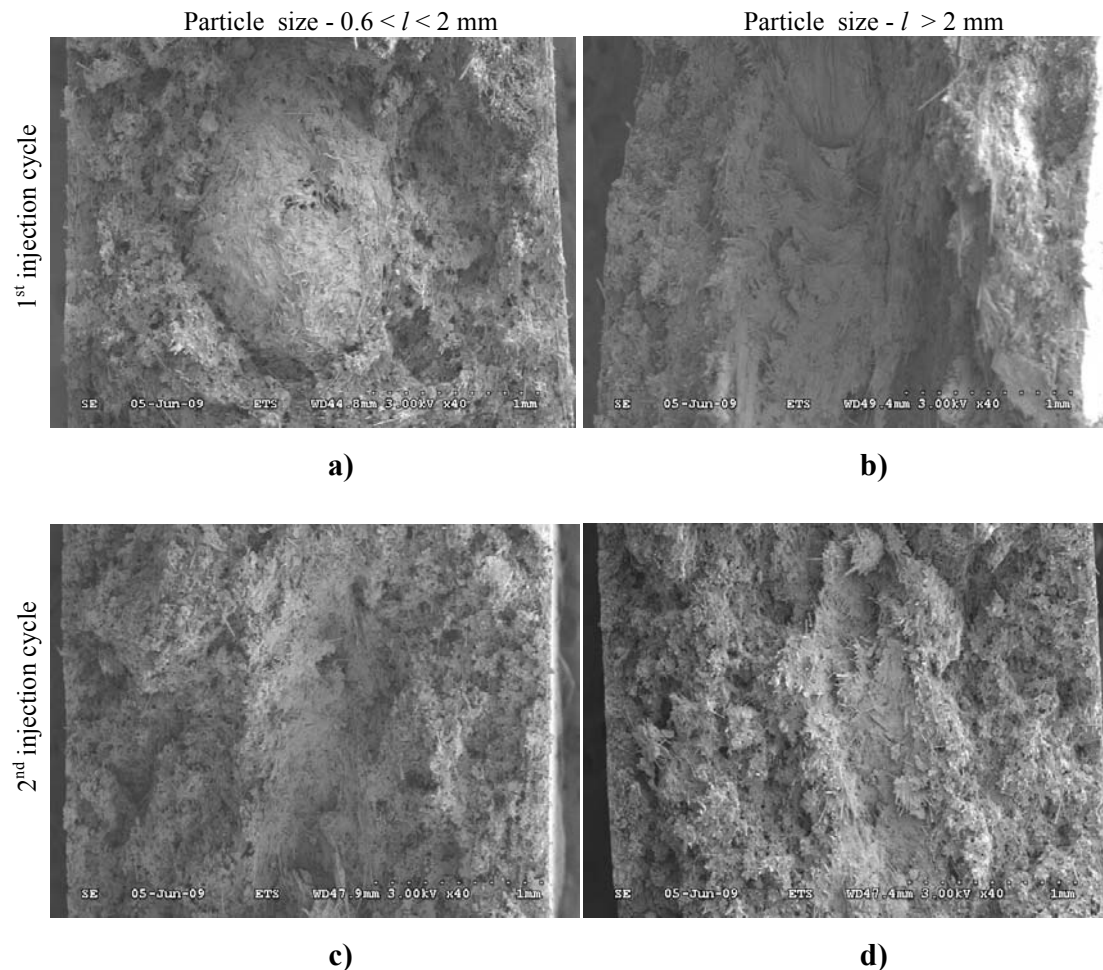


Figure 4.14: SEM micrographs of fractured surfaces of HPA-6 diluted recycled material specimens.

4.5.4 SEM micrographs of fractured surfaces

SEM micrographs of HPA-6-based and APA-6-based recycled specimens were first taken to show the full thickness of the fractured surfaces. These images can be seen respectively in Figures 4.14 and 4.15. Generally speaking, these SEM micrographs show evidence that the material is not homogeneously distributed throughout the specimens upon first injection. Large particles or cavities left after tensile testing having approximate dimensions of 1 to 2 mm can be seen on the surfaces of broken specimens (see Figures 4.14a and 4.15a).

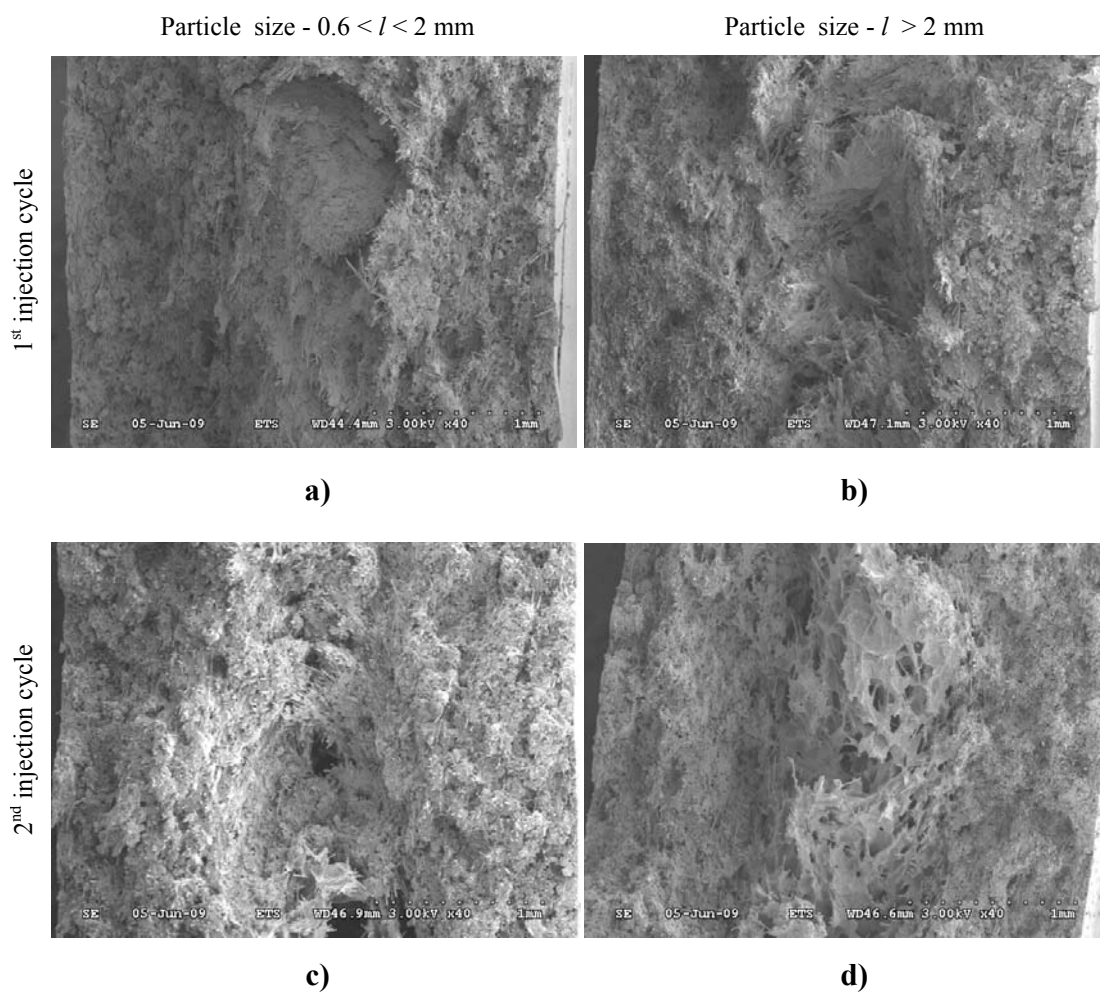


Figure 4.15: SEM micrographs of fractured surfaces of APA-6 diluted recycled specimens

It can also be observed on all first injection images of Figures 4.14 and 4.15 that smaller, more fluid particles appear to stick to the surface of the mold during the injection process while larger particles remain in the center of the channel, creating

“plug flow”. For HPA-6-diluted recycled material (Figure 4.14), this phenomenon appears to be more pronounced for the first injection while material distribution seems more uniform in samples of the second injection.

Large voids are visible at the center of specimens of APA-6-diluted recycled material fractured surfaces after the second injection (Figures 4.15c and 4.15d). Knowing that the APA-6 material used for dilution came from cast polymer blocks not specifically dedicated to injection processes, it is possible that these voids were generated due to a lack of viscosity or because of the presence of un-reacted monomer present in the APA-6 casted block.

4.5.5 Discussion

The results presented above showed that the longer the fiber length, the stiffer and more resistant the short-fiber composite could be. A similar trend in mechanical property degradation with respect to fiber length has been reported in other papers [14-15]. Since fiber length was reduced when the material was reground and injected, reductions of up to 8% in strength and stiffness were observed for specimens tested after a second regrind/injection cycle. In that context, processing directly by injection molding without prior compounding of the recyclate helps keep longer fibers in the reinforced plastic and consequently maximizes mechanical properties.

Table 4.9: Tensile properties of short-fiber reinforced polyamide-6 and PBT composites.

Short-fibre reinforced composite type	Fibre Weight Content (%)	Tensile Strength (MPa)	Tensile Modulus (GPa)
HPA-6 diluted recycled APA-6 material ($l > 2$ mm) 1 st injection cycle	30	182.5	10.29
Glass fibre reinforced polyamide-6 (DAM) [16]	30-35	165	8.6-10.0
PBT (Valox 420®) [17]	30	127.6	9.93
Recycled glass/PBT [17]	28	120.9	9.72

As shown in Table 4.9, the mechanical properties of the recycled short-fiber-reinforced composite are comparable or superior to those of commercial-grade short-fiber-reinforced polyamide-6 and other engineering plastic short-fiber reinforced composites of comparable fiber content. All materials shown in Table 4.9 were tested according to ASTM D638 standard and show lower stiffness and strength than HPA-6-

diluted APA-6-based composite recyclates. Compared to the commercial polyamide-6 short-fiber-reinforced composites shown in Table 4.9, the short-fiber-reinforced composite tested in this study had 10.6% greater strength and stiffness. It is noted with interest that although virgin PBT has a lower stiffness and a better strength than polyamide-6 (2.5 GPa vs. 3 GPa (modulus), 56 MPa vs. 35 MPa (strength)), its fiber-reinforced composite shows a similar stiffness but significantly lower strength than its polyamide-6-based counterpart.

4.6 Conclusions

In order to evaluate the potential of polyamide-6 composites for wind turbine blades, this chapter benchmarked vacuum-infused anionic polyamide-6 composites against conventional melt-processed polyamide-6 composites and epoxy-based composites. Basic static properties such as tensile, compressive and shear moduli and strengths were compared and preliminary fatigue life was evaluated for tension-tension loading conditions ($R = 0.1$). Also, the potential of APA-6 composite laminates to be recycled into short-fiber-reinforced composites was evaluated. Based on the results obtained and the different metrics used for comparison and analysis, the following conclusions may be drawn:

Manufacturing issues:

- Because of the very low viscosity of the anionic polyamide-6 resin system (10mPa·s, 35 times lower than epoxy) fiber wettability is excellent and infusion times are short. Conversely, the low viscosity offers little resistance to gas dissolution in the resin. Since the different resin components need to be kept in a protective environment under nitrogen prior to infusion, it is easy to generate a large quantity of voids in the composites if the resin is not properly degassed prior to infusion.
- Since most components of the anionic polyamide-6 resin system are very sensitive to moisture, special care must be taken to keep the raw materials as dry as possible prior to infusion. Moisture-rich fiber surfaces were found to deactivate the initiator and consequently reduce the interface quality significantly. In that sense, un-sized fibers are not to be used for APA-6-infused composites.
- Processing temperatures of 170-180°C are higher than what is usually used for thermosetting infusion resin systems, which are cured and/or post-cure at lower

temperatures. Although standard high-temperature epoxy tooling could still be used up to these temperatures, an increase in tooling cost is to be expected due to the reduced life of the molds (aggressive thermal cycling) and the more expensive heating system to be used. Nevertheless, this increase in cost is expected to be compensated by a faster cycle time (faster infusion and polymerization) and significantly lower cost of the resin (20% cheaper than epoxy).

Static mechanical properties:

- Crystallinity-induced shrinkage in APA-6 composites helps the matrix to form a firm mechanical lock around the fibers, which led these composites to perform better than epoxy-based composites in dry conditions. Interactions between the APA-6 matrix and the sizing helped form chemical adhesion at the interface. Because of the combination of mechanical locking and chemical adhesion, the APA-6 composites surpassed their thermoplastic counterparts in all mechanical properties tested in dry conditions.
- Under moist conditions, mechanical properties of PA-6 composites were degraded due to matrix swelling. This was expected due to the hydrophilic nature of PA-6. Nevertheless, using a sizing for APA-6 composites showed that it could help significantly to reduce the moisture absorption rate. All mechanical properties of both polyamides were affected significantly by moisture, with APA-6 composites being the most degraded composite because of their higher void content.
- Residual monomer content (RMC) acts as a plasticizer in APA-6 composites. Minimizing RMC helps improve matrix-driven mechanical properties such as ILSS.

Fatigue life:

- In dry-as-molded conditions, the reactively processed APA-6 composites outperformed the conventional melt-processed PA-6 in terms of fatigue because of its superior chemically bonded interface. Approximately 25% more load could be applied for an equivalent fatigue life.
- Although reactively processed APA-6 composites are significantly more fatigue resistant than their melt-processed counterpart in dry-as-molded conditions, their fatigue resistance is far from matching that of epoxy-based composites. On the other hand, it was demonstrated that due to the brittle nature of epoxy-based composites,

their fatigue data exhibits notably larger scatter than thermoplastic composites. Therefore, fatigue life predictions for PA-6 composites should be more accurate than for the epoxy-based equivalent. For fatigue driven structures such as wind turbine blades, this will help reduce material safety/knockdown factors and consequently increase design allowables.

Sustainability:

Long-fiber APA-6/glass composite laminates were mechanically recycled into APA-6 short-fiber-reinforced composites by regrinding and injection molding of ASTM type I test specimens. Tensile tests showed that the strength and modulus of the recycled material could be up to 10% higher than those of commercial short-fiber glass-reinforced polyamide-6 composites at equivalent fiber content. It is therefore plausible to see these materials used by the automotive industry where a large quantity of short-fiber-reinforced polyamides is being consumed for under-the-hood applications. Other processes not studied in this chapter could also be interesting for recycling, namely compression molding or extrusion. For example, compression molding could help produce parts having longer fibers since no dilution resin is needed for the process and larger granules with higher fiber content could be used directly. If so, given a big enough market to absorb end-of-life materials, the development of recyclable wind turbine blades could help diminish the uncertainties and environmental impact related to the dismantling and recovery of composite wastes in the wind energy sector.

4.7 References

- [1] Rijswijk, K., Bersee, H.E.N., *Reactive processing of textile fiber-reinforced thermoplastic composites – An overview*, Composite Part A: applied science and manufacturing, vol.38, issue 3, March 2007, p. 666-691.
- [2] Van Rijswijk, K., Bersee, H.E.N., Beukers, A., Picken, S.J. and Van Geenen, A.A. (2006), *Optimisation of anionic polyamide-6 for vacuum infusion of thermoplastic composites: Influence of polymerisation temperature on matrix properties*, Polymer Testing, 25:875-887.
- [3] Van Rijswijk, K., Koppes, K., Bersee, H.E.N., Beukers, (2004), *Processing Window for Vacuum Infused Fiber Reinforced Anionic Polyamide-6*, 7th International Conference on Flow Processes in Composite Materials (FPCM-7), Newark, Delaware, USA, 1-3 July.
- [4] Van Rijswijk, K., Valsveld, D.P.N., van Rhijn, P., Bersee, H.E.N., Beukers, and Picken, S.J., (2003), *Process Considerations for Liquid Moulding of Composites Based on Anionic Polyamide-6*, 14th International Conference on Composite Materials (ICCM-14), San Diego, California, USA, 14-18 July.
- [5] Van Rijswijk, Bersee, H.E.N., Beukers, Jager, W.F. and Picken, S.J., (2005), *Choice of Activator and Initiator for Vacuum Infusion of Anionic Polyamide-6 Composites*, 15th International Conference on Composite Materials (ICCM-15), Durban, South Africa, 27 June - 1 July.
- [6] Cartledge, H. C. Y., Baillie, C. A., *Studies of microstructural and mechanical properties of nylon/glass composite- Part I :The effect of thermal processing on crystallinity, transcrystallinity and crystal phases*, Journal of Materials Science, Volume 34, Number 20, Octobre 1999.
- [7] van Rijswijk, K., *Thermoplastic Composite Wind Turbine Blades – Vacuum Infusion Technology for Anionic Polyamide-6 Composites*, PhD Thesis, Delft University of Technology, 2006.
- [8] Clark, R.L., Kander, R. G. and Sauer, B. B., *Nylon 66/poly(vinyl pyrrolidone) reinforced composites: 1.Interface microstructure and evaluation of fiber-matrix adhesion*, Composites partA: applied science and manufacturing, Vol. 30, 1999, pp. 27-36.
- [9] Clark, R.L., Kander, R. G. and Sauer, B. B., *Nylon 66/poly(vinyl pyrrolidone) reinforced composites: 2.Bulk mechanical properties and moisture effects*, Composites part A: applied science and manufacturing, Vol. 30, 1999, pp. 37-48.
- [10] Thomason, J. L., *The interface region in glass fibre-reinforced epoxy resin composites: 2 Water absorption, voids and the interface*, Composites, Vol. 26, No. 7, 1995, pp. 477-485.

- [11] Reifnider, K., *Handbook of Composites – Chapter 35 - Durability and damage tolerance of fibrous composite systems, voids and the interface*, Second edition, Chapman and Hall, 1998, pp. 795-809.
- [12] Gamstedt, E.K., Talreja, R., *Fatigue Damage Mechanisms in Unidirectional Carbon-fiber-reinforced Plastics*, Journal of Materials Science, 34 (1999): 2535-2546.
- [13] Malek, O., *Preliminary Fatigue Analysis of Anionic Polyamide-6 Composites*, Master's Thesis, Delft University of Technology, 2007.
- [14] Denault, J., Robert, C., Michaud, J. & Bureau, M.N., *Recycling Technology for Continuous Glass Fibre/Polypropylene Composites*, In ACUN-2: International Conference on Composites in the Transportation Industry, Sydney (Australia), February 14-18 (2000):410-414.
- [15] Licea-Claverie A., Valdez, J.O., García-Hernández, E., Zizumbo, A., Álvarez-Castillo, A. & Castaño, V.M., *Reprocessing Effects on the properties of a Hybrid Nylon 6,6-Composite Reinforced with Short Glass and Carbon Fibers*, Journal of Reinforced Plastics and Composites, 21(9)(2002):847-856.
- [16] Harper, C.A., *Handbook of Plastics, Elastomers and Composites*, McGraw-Hill, Second Edition, 1992.
- [17] Steenkamer D.A. & Sullivan J., *On the recyclability of a cyclic thermoplastic composite material*, Composites Part B, 29(1998):745-752.

CHAPTER 5

AERODYNAMIC AND STRUCTURAL MODELLING *DESIGN AND ANALYSIS TOOLS*

Wind turbine blade aerodynamic and structural analytical design tools were created as a starting point for the different preliminary structural design studies presented in later chapters. The tools presented in this chapter will be used to set the baseline blade design used throughout the remaining chapters of this thesis, to generate different load cases and to estimate blade structural performance.

5.1 Introduction

Loading on wind turbines blades is stochastic in nature and comes from four different sources: aerodynamic loads, gravitational loads, inertia loads (centrifugal and gyroscopic) and operational loads (grid failure, braking, yawing etc.) [1]. Although significant advancements in 3D CFD-based design codes for wind turbine rotor design have been achieved in recent years, today's commercially available wind turbine aerodynamic codes (Aerodyn®, Bladed®, etc.) are all based on 2D blade element momentum (BEM) theory. Generally, these aerodynamic codes can be coupled to structural dynamics codes (Yawdyn®, Fast®, etc.) or structural blade design codes (FAROB®, NUMAD®, etc.) to respectively evaluate the dynamic response of the turbine or to perform stress analysis on blade structures subjected to different load cases. These load cases, formulated in different national or international standards such as the International Electrotechnical Commission *61400-1*, the Danish Standard *DS 472* or the Germanischer Lloyd's *Guideline for the Certification of Wind Turbine*, are used by manufacturers to guide their designs and to certify their wind turbine for operation.

Blade design involves a series of technical disciplines such as aerodynamic design, structural design and dynamic analysis, but also involves non-technical issues like material cost, manufacturing cost or transportation logistics. Since a wind turbine is designed to minimize the energy production cost (turbine cost + energy production

cost), wind turbine manufacturers need to keep the cost of their machine as low as possible [2, 3]. Rotor blades are of course not excluded from the overall optimization scheme when designing wind turbines and need to produce the maximum power possible for the lowest cost possible.

Since the goal of this thesis is not to design a blade for a specific wind turbine but rather to evaluate the potential of thermoplastic composite blade designs, blade design will not be performed based on a large optimization routine taking into account the multiple parameters just mentioned. Blades will instead be designed solely with respect to aerodynamic, structural and dynamic issues. Nevertheless, as will be discussed in the next chapter, other issues such as cost and transport will be considered to adapt the design to current trends in the industry.

Although some aspects of blade design and analysis presented in the next chapter were performed with commercial software (Yawdyn), aerodynamic blade loading was in the end determined using a self-written Matlab based code. This decision was motivated because of the following considerations:

- Although some design software was available for free, obtaining a software package (or a combination of different packages) that could perform aerodynamic, dynamic and blade structural analysis was difficult.
- The tools developed for this thesis are meant to be used for preliminary design purposes and do not require all the features offered in commercial packages.
- Apart from setting blade geometry and calculating blade loading, the design and analysis tools must be able to generate specific input files (IGES, FEM load files, etc) for the CAD and FEM software used for structural design. These features were not possible with commercial packages but could be easily implemented with Matlab.

This chapter will present the different tools developed for blade design and analysis. The first section of this chapter will present the aerodynamic design and analysis tool. Based on classical blade element momentum theory equations, the key elements coded, the assumptions made and limitations involved will be presented. In a second section, the structural design and analysis tool will be presented. Again, the theory behind the code will be presented and its limitations will be exposed. This chapter focuses purely on presenting the different tools used in later chapters. Their interaction, validation and specific purpose within the design and analysis process will be dealt with in chapter 6.

5.2 Aerodynamic design and analysis: Theory

The aerodynamic design and analysis tool coded to compute loads throughout this thesis is based on the blade element momentum theory (BEM). It is well known that when used for design and analysis purposes the most critical deficiency of this theory is that it treats the concentric annular rings it uses to solve induced velocities (or induction factors) independently from the remaining annuli of the rotor area, which means, flow interactions between the different annuli are not taken into account^[2,3]. When referring to Figure 5.1, this means that a blade element of width δr positioned at a chord station r is not affected aerodynamically by its neighboring blade elements. This limitation makes the momentum theory inaccurate when computing induced velocities if a significantly non-uniform rotor loading is expected. Nevertheless, it is generally accepted that on variable-speed pitch-regulated machines (our case), rotor loading is uniform enough to consider the momentum theory sufficiently accurate for performance calculations [4].

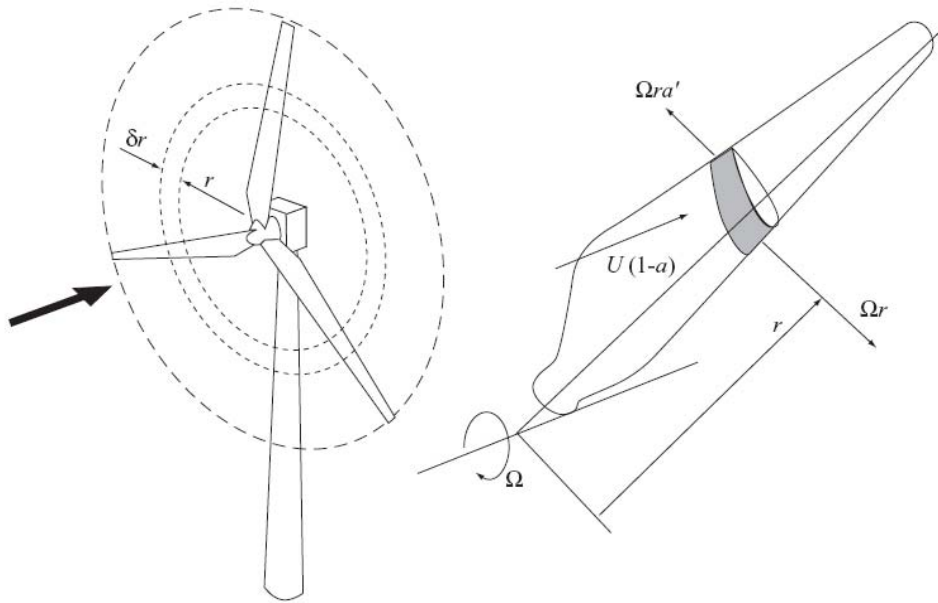


Figure 5.1: Upwind three bladed wind turbine showing a blade element of width δr positioned at station r . (adapted from [1])

Elements of the blade element theory and momentum theory were coded in the MATLAB environment. For completeness, the key elements of the blade element theory will first be presented to familiarize the reader with the different velocity components affecting a rotor blade element. The momentum theory will then be outlined briefly and

the algorithm chosen to solve for induced velocities will be described. Although flow calculation is considered 2D, some 3D corrections will be included through the introduction of a tip loss factor and a root loss factor. Finally, to facilitate off-design calculations, a turbulent wake state model was included in the code to deal with cases for which the Betz limit is not respected. These two aspects will be discussed at the end of this section.

Since the following sections provide only a synthesis of the theory used in this thesis, the reader interested in further detail is referred to classical wind turbine aerodynamic textbooks [1,5,6] in which the pioneering work of Betz, Prandl and others is described [7,8].

5.2.1 Blade Element Theory

Blade element theory is used to describe the basic relationships existing between the velocities and forces acting on a blade element. Figure 5.2 presents the blade element model used in this thesis along with the nomenclature of the different velocity and force vectors. Not included in the nomenclature are the so-called axial and angular induction factors (a and a').

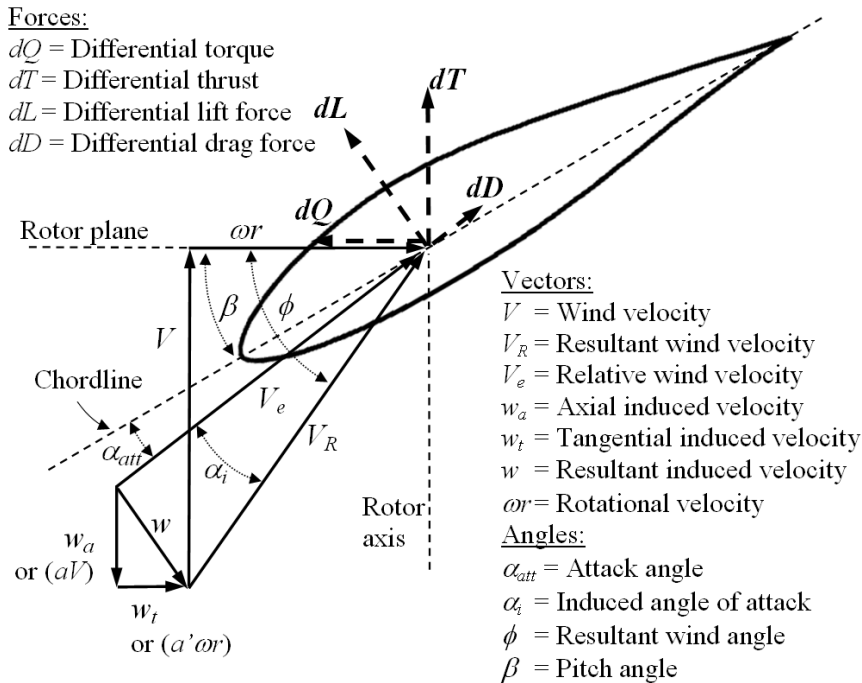


Figure 5.2: Velocity and force diagram of a blade element as seen looking along the blade axis.

To harness energy from the wind, the wind turbine changes the momentum of the wind as it strikes the rotor plane. As can be seen in Figure 5.2, the linear momentum of the wind is reduced as the wind velocity (V) is slowed down by a value of w_a (or $a*V$ using the concept of induction factor a) when it reaches the rotor plane. This change in linear momentum translates directly into thrust on the rotor axis. Unfortunately, thrust does not generate electrical power and is just a consequence of producing torque, which in this case is created because of a change in the rotational momentum of the wind. Assuming that the wind has no rotational momentum as it strikes the rotor plane, an increase in rotational momentum is imparted to the flow trailing downstream because of the tangential velocity (w_t) induced at the rotor plane. Again, this velocity can be expressed using an induction factor (a') where $w_t = a' * \omega r$.

Referring again to Figure 5.2, the specific contribution to thrust (dT) and torque (dQ) of a blade element situated at a local chord station (r) can be calculated as follows:

$$dT = dL \cos(\phi - \alpha_i) + dD \sin(\phi - \alpha_i) \quad (5.1)$$

$$dQ = r[dL \sin(\phi - \alpha_i) - dD \cos(\phi - \alpha_i)] \quad (5.2)$$

where the local differential lift and drag forces at that element can be calculated as follows:

$$dL = \frac{1}{2} \rho V_e^2 c C_l dr \quad (5.3)$$

$$dD = \frac{1}{2} \rho V_e^2 c C_d dr \quad (5.4)$$

where ρ , c , dr , C_l and C_d are respectively the air density, the blade element average chord length, the blade element radial length, and finally the local lift and drag coefficients at that blade element. In order to solve Equations 5.1 and 5.2, one must determine the induced angle of attack (α_i), which is a function of the axial and tangential induced velocities (w_a) and (w_t) just discussed. The momentum theory briefly presented in the next section will be used to solve these induced velocities.

5.2.2 Momentum Theory

Also referred to as actuator disk theory, momentum theory is the most widely used theory to solve axial induced velocities.

Referring to Figure 5.3, based on the continuity and conservation of linear momentum principles, the theory states that the velocity passing through the rotor (V_1) will be the average of the velocities far in front of the rotor (V) and far behind the rotor (V_2). The velocity decrement when approaching the rotor, $(V-V_2)/2$, is designated as the rotor axial induced velocity (w_a) and can be related to the rotor disk area (A) and thrust (T) using the following expression:

$$T = \rho A(V - w_a)2w_a \quad (5.5)$$

As shown in Figure 5.3, when applying this important finding to a stream tube of thickness dr positioned at a local chord station (r) instead of on the full rotor area, a differential version of Equation 5.5 can be expressed in the form of Equation 5.6.

$$T_{streamtube} = dT = \rho 2\pi r dr (V - w_a)2w_a \quad (5.6)$$

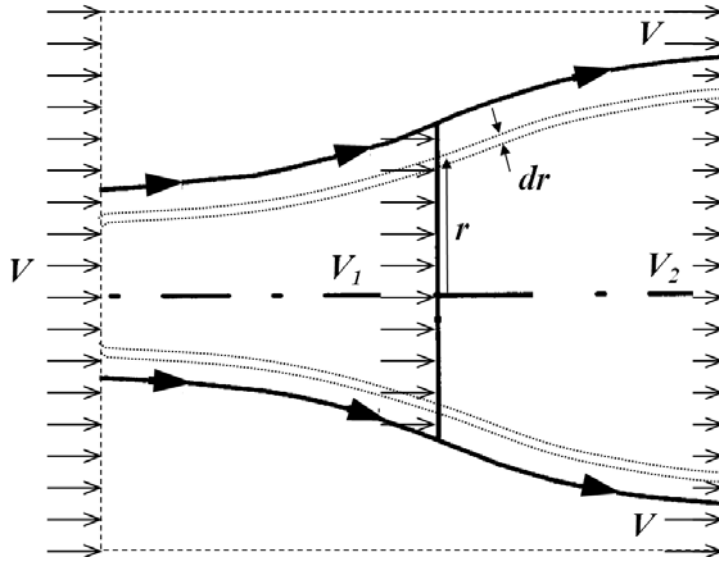


Figure 5.3: Actuator disk model of a wind turbine rotor with illustrated streamtube of thickness dr .

In this latter equation, thrust is again related to the axial induced velocity, as was the case in the section on blade element theory. The combination of linear momentum theory and blade element theory will be used to solve for axial induced velocities.

To compute the tangential induced velocities (w_t), the conservation of momentum principle is used as well. In this case, the change in angular momentum of the flow is

linked to the torque absorbed by the rotor in the same way the linear momentum was linked to thrust in the expression just presented [7]. In reaction to the torque generated at the rotor shaft, the flow behind the rotor is forced to rotate in the opposite rotational direction. Assuming that the fluid enters the rotor with no angular velocity, an angular velocity of $2w_t$ is imparted to the flow as torque is generated. The angular momentum is changed therefore from 0 (since it is assumed that there is no tangential component to the incoming flow) to a non-zero angular momentum equal to the mass flow rate times the angular speed at which it is rotated, times the radius at which this mass rotates. In terms of annual rings, this change in angular momentum can be expressed as follows:

$$\text{Angular momentum} = \underbrace{2\pi r dr \rho (V - w_a)}_{\text{mass flow rate}} * \underbrace{2w_t r}_{\text{angular velocity}} * \underbrace{r}_{\text{radius}} \quad (5.7)$$

Knowing that the torque generated is equal to the change in angular momentum, Equation 5.8 can be used to find the differential torque received at a blade element of length dr situated at a chord station r .

$$Q_{\text{streamtube}} = dQ = 4\pi r^3 dr \rho (V - w_a) w_t \quad (5.8)$$

In this latter equation, torque is related to the tangential induced velocity. As was also mentioned in the section on blade element theory, rotor torque is directly proportional to the rotational speed imparted to the incoming flow by the rotor (w_t).

5.2.3 Blade element momentum theory

Combining Equation 5.1, 5.3 and 5.4 of the blade element theory, the contribution of a stream tube of thickness dr to thrust can be expressed as follows:

$$dT = \frac{1}{2} B \rho V_e^2 c dr [Cl \cos(\phi - \alpha_i) + Cd \sin(\phi - \alpha_i)] \quad (5.9)$$

where B is the number of blades, which needs to be incorporated to include the contribution of all blade elements acting on the stream tube. When equated, Equation 5.9 and Equation 5.6 can be rewritten as Equation 5.10, which links linear momentum theory to blade element theory.

$$8\pi r(V - w_a)w_a = BV_e^2 c [C_l \cos(\phi - \alpha_i) + C_d \sin(\phi - \alpha_i)] \quad (5.10)$$

Combining expressions of blade element theory but this time with respect to torque (Equations 5.2, 5.3 and 5.4), Equation 5.11 is obtained.

$$dQ = \frac{1}{2} B \rho V_e^2 c r dr [C_l \sin(\phi - \alpha_i) + C_d \cos(\phi - \alpha_i)] \quad (5.11)$$

Based on the angular momentum theory just presented and on blade element theory, an expression based on torque can be derived. In this case, Equation 5.11 is merged with Equation 5.8 to give:

$$8\pi r^2(V - w_a)w_t = BV_e^2 c [C_l \sin(\phi - \alpha_i) + C_d \cos(\phi - \alpha_i)] \quad (5.12)$$

As presented in a later section, Equations 5.10 and 5.12 are part of the set of equations coded to solve for induced velocities.

5.2.4 Tip and root loss factors

Tip and root loss factors are included in the wind turbine design and analysis code to take into account the lift loss at blade sections near the tip or the root. This reduction of lift is due to the inevitable tendency of air to flow from the high-pressure side of the blade to the low-pressure side of the blade in the tip region or the root region. The pressure difference in front and behind the rotor being dramatically reduced at these areas, lift is significantly reduced, and in turn, torque and power are reduced. A number of methods have been developed to take into account tip and root losses. One of the most common methods and also the most widely accepted is the so-called Prandtl tip loss factor. Although it was found to lose accuracy at low tip speed ratio ($\lambda = \omega R/V$), the Prandtl tip loss factor yields fairly accurate results for tip speed ratios above five [9,10]. Since the blade designs generated in this thesis are all above this range of tip speed ratios, the Prandtl loss factors were used in the calculations. Equations 5.13 and 5.14 were used to obtain respectively tip and root loss factors (F_{tip} and F_{root}) in which ϕ is the resultant wind angle at station r and R_{hub} is the wind turbine's hub radius.

$$F_{tip} = \frac{2}{\pi} \cos^{-1} \exp \left[-\frac{B(R-r)}{2r \sin \phi} \right] \text{ where, } \phi = \tan^{-1} \left(\frac{V}{\omega r} \right) \quad (5.13)$$

$$F_{root} = \frac{2}{\pi} \cos^{-1} \exp \left[-\frac{B(r - R_{hub})}{2r \sin \phi} \right] \quad (5.14)$$

5.2.5 Turbulent wake state

As seen in Figure 5.2, as a consequence of thrust being absorbed by a wind turbine rotor, wind speed is reduced downstream. Since the velocity passing through the rotor (V_1) is the average of the velocities far in front of the rotor (V) and far behind the rotor (V_2), when the rotor reduces the wind velocity by half as the wind strikes the rotor, the velocity downstream in theory should drop to zero. For axial induced velocities greater than half the incoming wind speed, the momentum theory predicts a reversed flow. Since this situation is a physical impossibility, the wake behind the rotor plane in fact starts to absorb air from outside the wake and become highly turbulent (known as the turbulent wake state). Pioneering work performed by Glauert showed that a significant increase in thrust occurs when the rotor falls in the turbulent wake state [11]. This effect is illustrated in Figure 5.4, which shows his experimental data points plotted in terms of thrust coefficient (C_T), which is simply the ratio between the thrust produced (dT) and the dynamic force of the wind (see Equation 5.15).

Various approaches can be followed to match Glauert's empirical data to different thrust coefficient formulations (linear, parabolic, etc.). As shown in Figure 5.4, one technique is simply to use a straight line. Taking a value of $C_{T1} = 1.8$ for $a = 1$, yields the linear interpolated expression of C_T shown in Equation 5.16. For this value of C_{T1} , the line becomes tangent to the parabola (the momentum theory) at a value of $a_T = 0.33$, making the turbulent wake state calculation valid only for induction factors above that value. Because of its simplicity, this formulation was retained for turbulent wake state calculations in this thesis.

$$C_T = \frac{dT}{1/2 \rho V^2 2\pi r dr} \quad (5.15)$$

$$C_T = C_{T1} - 4(\sqrt{C_{T1}} - 1)(1 - a) \text{ where the transition point is, } a_T = 1 - \frac{1}{2}\sqrt{C_{T1}} \quad (5.16)$$

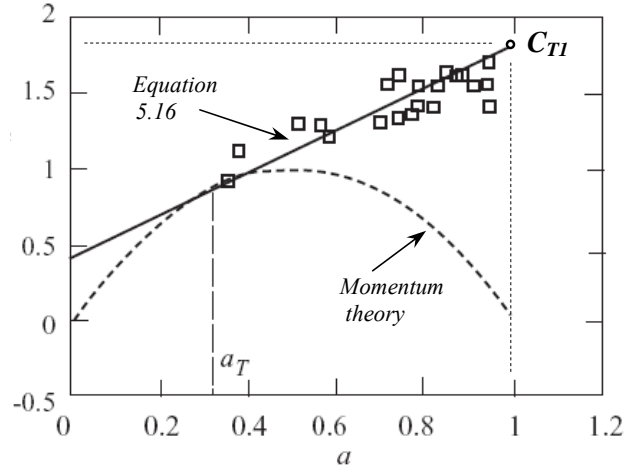


Figure 5.4: Thrust coefficient experimental values plotted against the momentum theory and a linear interpolated function (adapted from [1])

5.3 Design and Analysis Tool: Iteration procedure

When including the tip and root loss factors just discussed, a total loss factor ($F = F_{tip} * F_{root}$) can be incorporated into Equations 5.10 and 5.12 to give Equations 5.10a and 5.12a. To solve for induced velocities, one needs to solve these two equations. Since V_e and $\phi - \alpha_i$ are also functions of the axial and tangential induced velocities, trigonometric expressions derived from blade element theory (Equations 5.17 to 5.19) are used to complete the pair of equations to be solved.

$$8\pi r(V - w_a)w_a F = BV_e^2 c [C_l \cos(\phi - \alpha_i) + C_d \sin(\phi - \alpha_i)] \quad (5.10a)$$

$$8\pi r^2(V - w_a)w_t F = BV_e^2 c [C_l \sin(\phi - \alpha_i) + C_d \cos(\phi - \alpha_i)] \quad (5.12a)$$

$$V_e = [(V - w_a)^2 + (\omega r + w_t)^2]^{1/2} \quad (5.17)$$

$$\sin(\phi - \alpha_i) = (V - w_a)/V_e \quad (5.18)$$

$$\cos(\phi - \alpha_i) = (\omega r + w_t)/V_e \quad (5.19)$$

Due to the non-linearity of the equations, the axial and tangential induced velocities are usually found by iteration. Of course when starting a new blade design, some of the variables embedded in Equations 5.10a and 5.12a need to be defined as input variables while others can be obtained as output variables according to specific aerodynamic optimality criteria such as maximum power coefficient, maximum torque and so on.

Chapter 6 will deal specifically with the choices made to describe certain variables. The following section will therefore present only the iteration procedure used to solve for induced velocities regardless of the design strategy followed.

5.3.1 Algorithm

Referring to Figure 5.5, assuming that the blade geometry is known (chord distribution, twist, etc.), a pitch angle at a specific blade element is calculated including the pitch offset if the blade is pitched (step 1). With an attack angle of zero ($\alpha_{att}=0$) chosen as a first guess when entering the iteration loop, the corresponding C_l and C_d for that attack angle are found by table look-up. With these C_l and C_d values in hand, Equations 5.10a and 5.12a are solved to find the induced velocities and associated induced angle of attack. With this calculated induced angle of attack, a pitch angle can be calculated and compared to the real pitch angle at that blade station (step 1). If the pitch angles are different, calculations are redone with a different attack angle and corresponding C_l and C_d . As depicted in Figure 5.5, convergence is obtained and the loop is exited when the correct C_l , C_d and matching angle of attack are found to satisfy the pitch angle calculated in step 1.

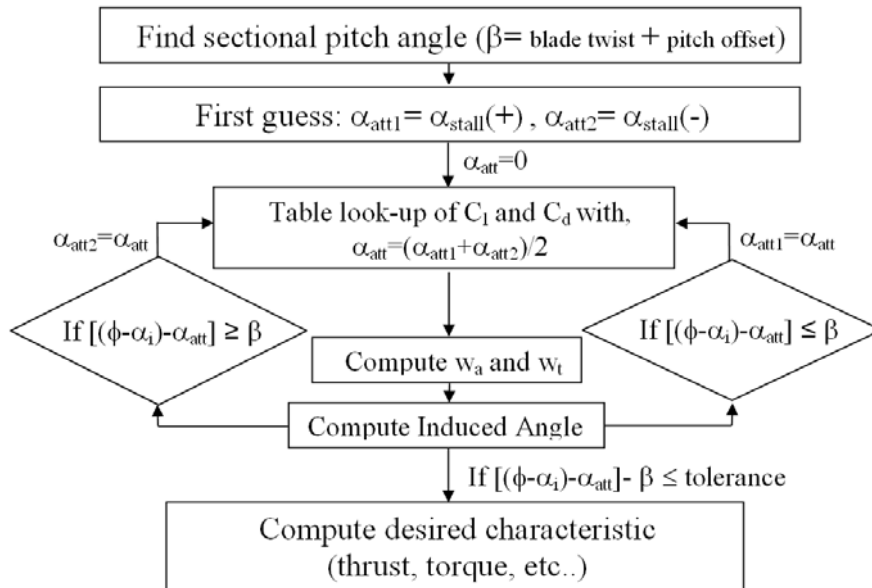


Figure 5.5: Convergence algorithm to solve for induced velocities at a specific blade element.

Of course, at each iteration step, after calculating w_a and w_t with the momentum theory (Equations 5.10a and 5.12a), a check is made to verify that the axial induction (a) does not exceed $1/3$, in which case the axial induced velocity would be derived instead from Equation 5.16.

5.3.2 Airfoil characteristics

To ensure convergence for all possible attack angles between -90° and $+90^\circ$, the algorithm was allowed to select values of C_l and C_d from three different regions: the negative stall region, the airfoil data region or the positive stall region (see Figure 5.6).

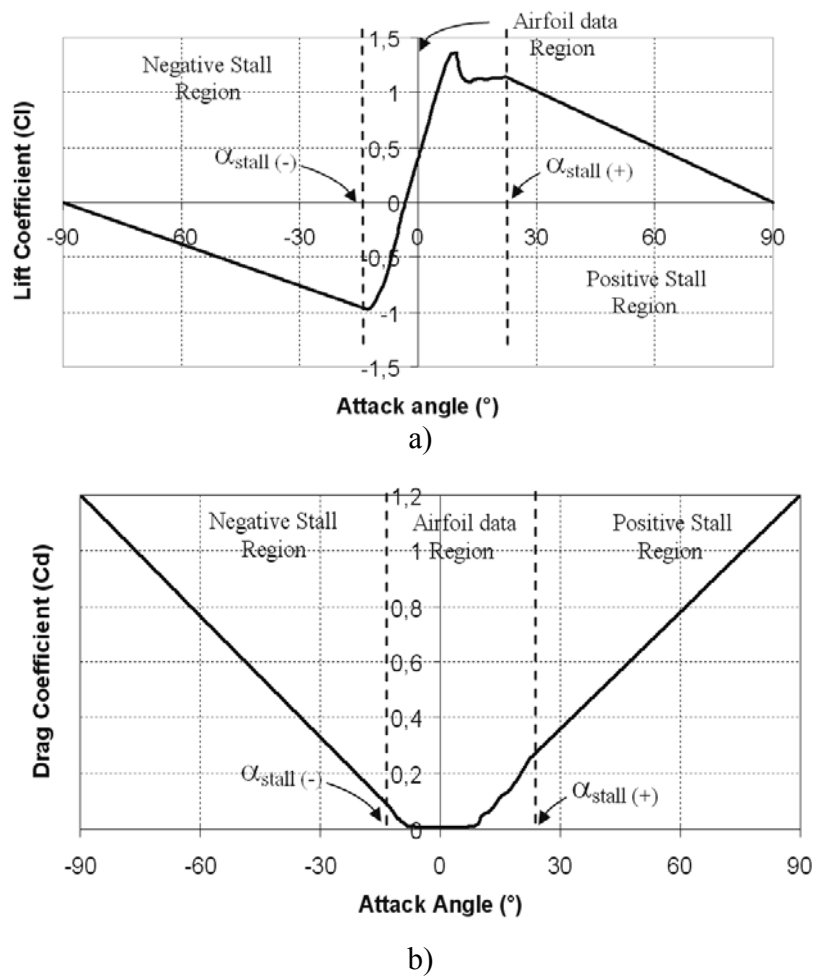


Figure 5.6: Typical lift and drag coefficient distributions used for off-design analysis, a) C_l -Alpha curve b) C_d -Alpha curve

For attack angles exceeding the first and last airfoil data points available, the true non-linear behavior of lift and drag was replaced by a simpler linear approximation for which the C_l and C_d values at $+90^\circ$ and -90° were estimated to be those of a flat plate

positioned perpendicular to the flow ($C_l = 0$ and $C_d = 1.2$). This last approximation could be considered rather coarse especially since an increase in lift is expected after stall to form a post-stall lift peak. Since modern variable-pitch wind turbine blades are not expected to operate outside of the airfoil data region, this coarse linearization should not influence the results and was used only to allow the algorithm to operate freely within wider attack angle bounds.

5.4 Structural design and analysis tools

The structural design and analysis tools are based on a parametric cross-section configuration representative of current commercial blade structural designs. The structural layout consists of a load-bearing box spar section, covered by two thin skins (see Figure 5.7). Spar size and position with respect to the leading edge is user defined as well as all specific section properties.

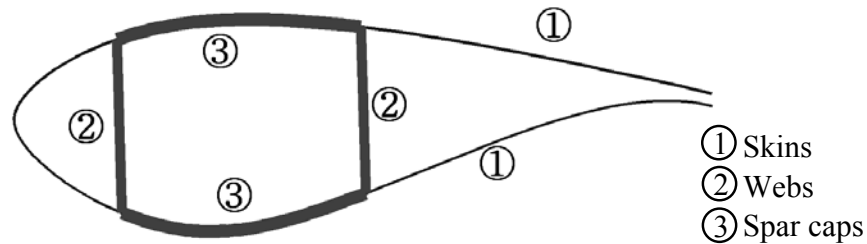


Figure 5.7: Parametric description of cross-section showing skins, webs and spar caps.

Since typical large wind turbine blade laminate stacking sequences and thicknesses are different for all three components (spar caps, webs and skins), user-defined material longitudinal moduli, strengths and thicknesses can also be given as input to the structural design and analysis module.

The next sections will discuss the approach followed to evaluate stress, tip deflection and natural frequencies using the cross-sectional description.

5.4.1 Stress Analysis

Since the tools developed for this thesis are used for comparison purposes and not detailed design, simplifications were made to reduce the complexity of the structural analysis. From a material point of view, the true anisotropic behavior of composite

laminates was reduced to isotropic properties. Nevertheless, since the different components of the blade (spar caps, webs and skins) have different longitudinal stiffness, blade cross-section is considered non-homogeneous. The contribution to load bearing of the webs, skins and spar caps, will thus be proportional to the value of their respective stiffness moduli. Furthermore, blade cross-section being non-symmetric, the neutral axis cannot be determined intuitively like in symmetric beams.

These characteristics force the classical mechanics of material equations to be adjusted for non-homogeneous, non-symmetrical beams. To compute the flexural stresses (σ_f) at a specific blade station, the following flexure formula for beams with an arbitrary cross-section shape and an arbitrary orientation of the resultant bending moment ($M_R = (M_x + M_y)^{1/2}$) vector was used:

$$\sigma_f = \frac{M_x y}{I_x} - \frac{M_y x}{I_y} \quad (5.20)$$

As with symmetric and homogeneous beam cross-sections, this bending stress equation is referenced to the principal axis coordinate system, that is, the coordinate system having its origin at the centroid of a homogeneous cross-section and having its axis oriented with respect to the strongest and weakest cross-sectional area moment of inertia axis.

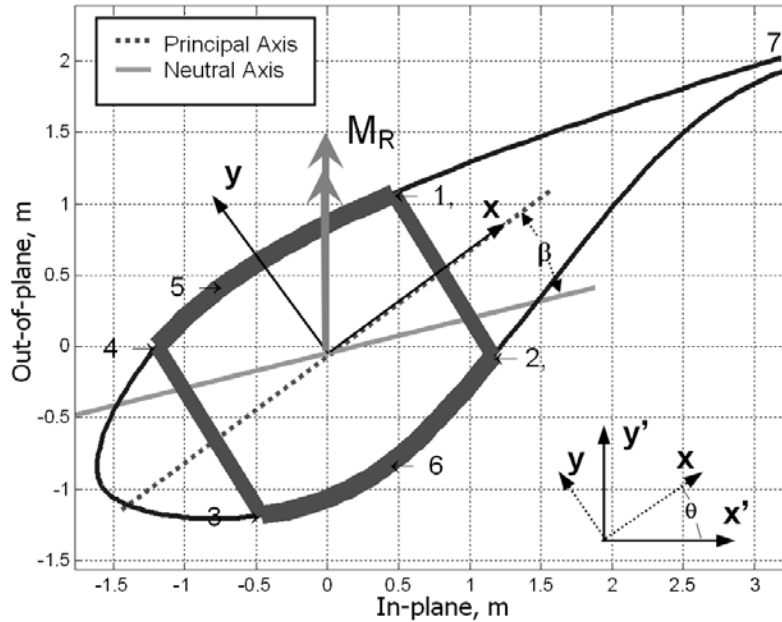


Figure 5.8: Cross-section model used to compute stresses in non-homogeneous and non-symmetrical beams.

As depicted in Figure 5.8, the difficulty in applying this equation for non-symmetrical and non-homogeneous beams lies in finding the centroid position and principal area moment of inertia (I_x and I_y) of the cross-section. This was solved by means of a weighted sum method used to determine the centroid position and area moment of inertia of an equivalent homogeneous cross-section representative of the true non-homogeneous cross-section. Details on how this approach was applied are presented in the next section.

5.4.2 Weighted area moment of inertia

To apply the weighted sum method to non-homogeneous blade cross-sections, webs, spar caps, and skins were all described as a series of small segments each having a specific area (dA) and position in the $x'y'$ rotor plane reference system depicted in Figure 5.8. In our case, the origin of this reference system is at the leading edge of the airfoil.

From this data, the centroid position (\bar{X}, \bar{Y}) was determined from Equations 5.21 and 5.22, in which subscripts s , w and Sc are used respectively for spar, web and spar cap and superscript t stands for “transformed” (or normalized in stiffness with respect to the spar cap stiffness):

$$\bar{X} = \frac{\int_{A_s} x' dA_s^t + \int_{A_w} x' dA_w^t + \int_{A_{Sc}} x' dA_{Sc}^t}{\int_{A_s} dA_s^t + \int_{A_w} dA_w^t + \int_{A_{Sc}} dA_{Sc}^t} \quad (5.21)$$

and

$$\bar{Y} = \frac{\int_{A_s} y' dA_s^t + \int_{A_w} y' dA_w^t + \int_{A_{Sc}} y' dA_{Sc}^t}{\int_{A_s} dA_s^t + \int_{A_w} dA_w^t + \int_{A_{Sc}} dA_{Sc}^t} \quad (5.22)$$

where,

$$dA_s^t = dA_s \frac{E_s}{E_{Sc}}, \quad dA_w^t = dA_w \frac{E_w}{E_{Sc}} \quad (5.23)$$

and

$$dA_{Sc}^t = dA_{Sc} \frac{E_{Sc}}{E_{Sc}} = dA_{Sc} \quad (5.24)$$

Once the centroid position of the cross-section is known, the cross-sectional area moments of inertia ($I_{x'}$, $I_{y'}$) and cross-sectional product of inertia ($I_{x'y'}$) with respect to the $x'y'$ coordinate system centered at centroid can be calculated as follows:

$$I_{x'} = I_{x'(s)}^t + I_{x'(w)}^t + I_{x'(Sc)}^t = \int_{A_s} (x')^2 dA_s^t + \int_{A_w} (x')^2 dA_w^t + \int_{A_{Sc}} (x')^2 dA_{Sc}^t \quad (5.25)$$

$$I_{y'} = I_{y'(s)}^t + I_{y'(w)}^t + I_{y'(Sc)}^t = \int_{A_s} (y')^2 dA_s^t + \int_{A_w} (y')^2 dA_w^t + \int_{A_{Sc}} (y')^2 dA_{Sc}^t \quad (5.26)$$

$$I_{x'y'} = I_{x'y'(s)}^t + I_{x'y'(w)}^t + I_{x'y'(Sc)}^t = \int_{A_s} x'y' dA_s^t + \int_{A_w} x'y' dA_w^t + \int_{A_{Sc}} x'y' dA_{Sc}^t \quad (5.27)$$

Knowing that the angle between the $x'y'$ and the xy coordinate systems (θ) can be determined using the following relationship:

$$\tan 2\theta = \frac{-2I_{x'y'}}{I_{y'} - I_{x'}} \quad (5.28)$$

The principal area moments of inertia I_x and I_y can finally be calculated with Equations 5.25 and 5.26 now referenced to the principal axis coordinate system (xy). With the coordinates of the centroid and angular position of principal coordinate system (θ) now known, the x and y coordinates of the different possible local maximum stress points depicted in Figure 5.8 (points 1 to 7) can be found and stresses can be evaluated for each of them with Equation 5.20. Finally, for visualization purposes, the angular position of the neutral axis (β) can be determined using the following relationship:

$$\tan \beta = \frac{I_y}{I_x} \tan \theta \quad (5.29)$$

This angle is plotted on the cross-section as shown on Figure 5.8.

5.4.3 Tip Deflection Analysis

As with the flexural stress calculations, deflection equations must take into account the non-homogeneity and asymmetric nature of the blade cross-section. This was achieved using the weighted flexural rigidity (\overline{EI}) of the blade sections in the classical deflection and slope equations of cantilever beams. If the blade is composed of a series of span-wise elements of length dr , a distinct local flexural rigidity can be determined for each element using the following relationship:

$$\overline{EI} = E_s I_s^t + E_w I_w^t + E_{Sc} I_{Sc}^t \quad (5.30)$$

For this purpose, the moment area of inertia can again be calculated using Equation 5.25 or Equation 5.26. With these local flexural rigidities, the local deflection (v) and local slope of the deflection curve (α) (see Figure 5.9) can be computed for each blade element using Equation 5.31, knowing the local blade element transverse shear force (P) and bending moment (M).

$$v = \frac{Pdr^3}{3\overline{EI}} + \frac{Mdr^2}{2\overline{EI}}, \quad \alpha = \frac{Pdr^2}{2\overline{EI}} + \frac{Mdr}{\overline{EI}} \quad (5.31)$$

Finally, to determine the blade deflection (δ_i) at any given chord station, a deflection sum of each local blade section, including the effect of the summed slopes of the deflection curve (θ_i) of the preceding blade sections, can be obtained using the following equations:

$$\delta(i) = \delta(i-1) + (dr \sin(\theta(i-1))) + v(i) \quad (5.32)$$

where,

$$\theta(i) = \alpha(i-1) + \alpha(i) \quad (5.33)$$

When solving for the blade section situated at the root ($i = 1$), the two first terms of Equation 5.32 and first term of Equation 5.33 vanish and the deflection (δ_i) and slope (θ_i) at the first chord station ($r = dr$) can be found with Equation 5.31. For the remaining blade sections up to the blade section at the tip (where $i = n$), all the terms of Equation 5.32 will exist. By solving Equation 5.32 sequentially from element 1 at the root up to element n at the tip, the tip deflection (δ_n) can be determined.

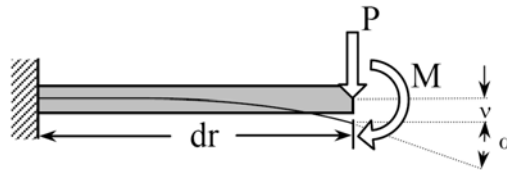


Figure 5.8: Cantilever beam model used to compute the local blade element deflection (v) and slope of the deflection curve (α).

5.4.4 Natural Frequency Analysis

A matrix form of the Myklestad method, the Thompson method was used to evaluate blade natural frequencies [12, 13]. This method involves modeling the blade as a series of lumped masses individually connected by mass-less beam elements having a specific flexural rigidity (EI). This is depicted schematically in Figure 5.10. In the present case, the flexural rigidity is the weighted flexural rigidity obtained from Equation 5.30.

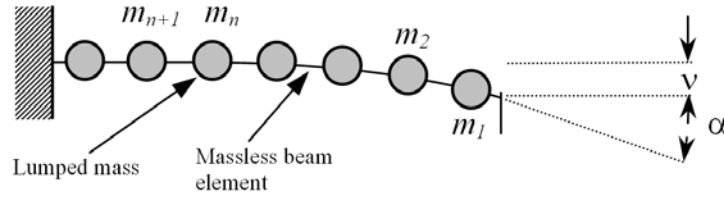


Figure 5.10: Lumped-mass model used to evaluate blade natural frequency.

The method involves solving a set of sequence equations based on classical beam theory. The equations are developed by considering all forces and moments acting on a mass “ $n+1$ ” and associated mass-less beam element connected to it. Figure 5.11 depicts the free body diagram with respect the radial forces (F), shear forces (S), moments (M), deflection (z), and angle of deflection (α) used to solve for natural frequencies.

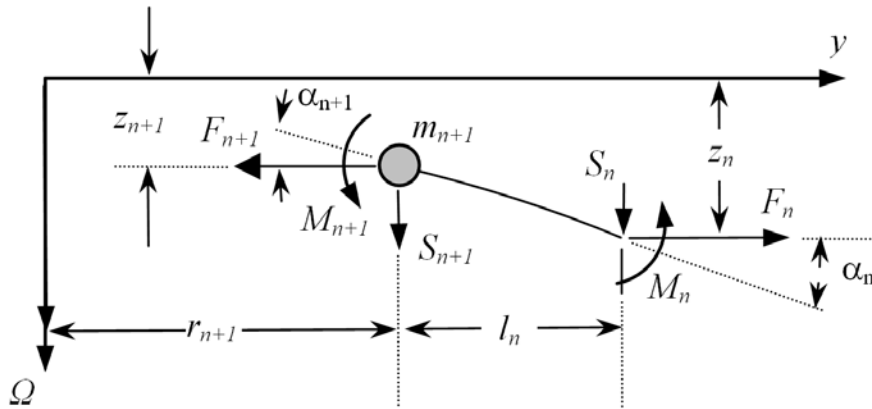


Figure 5.11: Free-body diagram of mass $n+1$ with massless beam element of length l_n connected to it (adapted from [12]).

From Figure 5.11, the five governing equations can be written in which ω is the flapping frequency of the blade and Ω is rotor rotational speed:

$$F_{n+1} = F_n + m_{n+1}\Omega^2 r_{n+1}, \text{ from a sum of forces on the y axis} \quad (5.31)$$

$$S_{n+1} = S_n + m_{n+1}\omega^2 z_{n+1}, \text{ from a sum of forces on the } \Omega \text{ axis} \quad (5.32)$$

$$M_{n+1} = M_n + S_n l_n - F_n(z_n - z_{n+1}), \text{ from a sum of moment at node } n+1 \quad (5.33)$$

$$\alpha_{n+1} = \alpha_n(1 + F_n v_{Fn}) - S_n v_{Fn} - M_n v_{Mn}, \text{ where } \alpha = \int M/\overline{EI} \quad (5.34)$$

$$z_{n+1} = z_n - \alpha_n(l_n + u_{Fn}F_n) + u_{Fn}S_n + u_{Mn}M_n, \text{ where } z = \iint M/\overline{EI} \quad (5.35)$$

Replacing 5.35 in 5.33 as well as in 5.32, Equations 5.32 and 5.33 can be rewritten as follows:

$$S_{n+1} = S_n(1 + u_{Fn}m_{n+1}\omega^2) + M_n u_{Mn}\omega^2 m_{n+1} - \alpha_n(l_n + u_{Fn}F_n)\omega^2 m_{n+1} + z_n\omega^2 m_{n+1} \quad (5.36)$$

$$M_{n+1} = M_n(1 + u_{Mn}F_n) + S_n(l_n + F_n u_{Fn}) - \alpha_n(l_n + u_{Fn}F_n)F_n \quad (5.37)$$

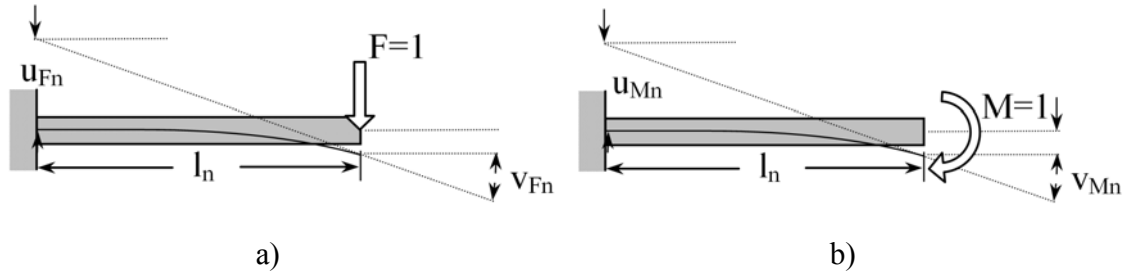


Figure 5.12: Unit local slope of the deflection curve (u) and deflection (v) of the mass-less beam element of length l_n , a) when submitted to a shear force, b) when submitted to a bending moment.

Knowing that the radial force is generated by the centrifugal force, F_{n+1} can be calculated using Equation 5.38. In addition, from classical beam theory, the local unit slope of the deflection curve (u) and deflection (v) when submitted to a shear force or a bending moment as shown in Figure 5.12 can be calculated using Equations 5.39 through 5.43.

$$F_{n+1} = \sum_{i=1}^{n+1} m_i \Omega^2 r_i \quad (5.38)$$

$$u_{Fn} = \frac{l_n^3}{6(EI)_n} \quad (5.39)$$

$$v_{Fn} = \frac{l_n^2}{2(EI)_n} \quad (5.40)$$

$$u_{Mn} = \frac{l_n^2}{2(EI)_n} \quad (5.41)$$

$$v_{Mn} = \frac{l_n}{(EI)_n} \quad (5.42)$$

To solve for natural frequencies, these equations must be solved starting from the tip of the blade ($n = 1$) to the root where n is the total number of lumped masses. In the matrix form, Equations 5.32 to 5.35 can be expressed as Equation 5.43.

$$\begin{bmatrix} S \\ M \\ \alpha \\ z \end{bmatrix}_{n+1} = \overline{\overline{D}}_n \begin{bmatrix} S \\ M \\ \alpha \\ z \end{bmatrix}_n \quad \text{where, } \overline{\overline{D}}_n = \begin{bmatrix} 1 + u_{Fn} m_{n+1} \omega^2 & u_{Mn} \omega^2 m_{n+1} & -(l_n + u_{Fn} F_n) \omega^2 m_{n+1} & \omega^2 m_{n+1} \\ l_n + u_{Fn} F_n & 1 + F_n u_{Mn} & -(l_n + u_{Fn} F_n) F_n & 0 \\ -v_{Fn} & -v_{Mn} & 1 + F_n v_{Fn} & 0 \\ u_{Fn} & u_{Mn} & -(l_n + u_{Fn} F) & 1 \end{bmatrix} \quad (5.43)$$

To find the natural frequency in the rotational state or not, the following boundary conditions must be respected: S_I , M_I , α_R and $z_R = 0$. These conditions are used to simulate a clamped blade root (α_R and $z_R = 0$) and a free blade tip (no shear nor bending moment at tip ($S_I = 0$ and $M_I = 0$)). To evaluate z_R , a summation of the different D matrixes must be performed since:

$$z_R = \overline{\overline{A}}^* z_1 \quad \text{where } \overline{\overline{A}} = \prod_{i=1}^n \overline{\overline{D}}_i \quad (5.44)$$

For the boundary conditions to be respected, the following residue (T) must be equal to zero:

$$T = A_{34} - \frac{A_{33} A_{44}}{A_{43}} \quad (5.45)$$

For every zero value of the residue obtained when flapping frequencies (ω) are scanned, the boundary conditions at the root are satisfied and the flapping frequency corresponds to a natural frequency. This is illustrated in Figure 5.13, which shows the plot of flapping frequency (abscissa) against their calculated residue (ordinate) in a so-called residue plot. Both non-rotational frequency (ω_{nr}) and rotational frequency (ω_r) plots are shown. Compared to an analytical solution [14], Figure 5.13 shows an error of less than one percent for the first and second modes while an error of around 5% can be found when evaluating the third mode. These results were obtained using ten lumped masses to represent the 9m-long beam.

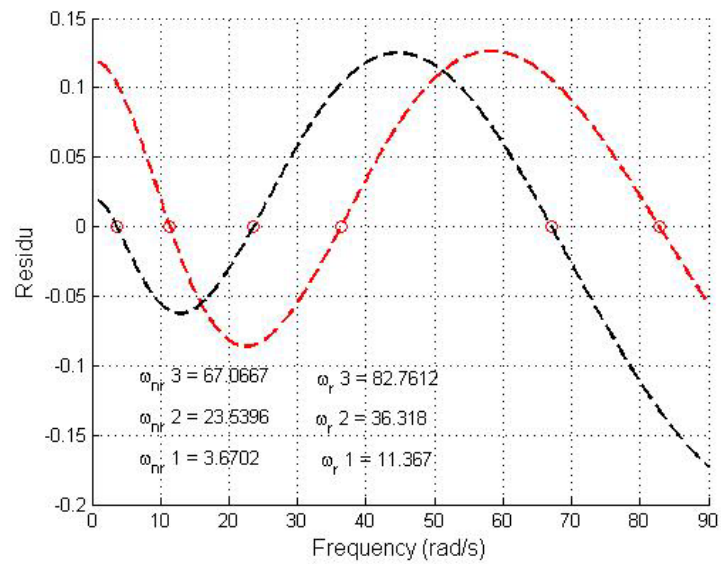


Figure 5.13: Residue plot showing the first three non-rotating and rotating natural frequencies of a 9m-long beam of bending stiffness $EI = 4 \times 10^5 \text{ Nm}^2$ rotating at $\Omega = 30 \text{ rad/s}$.

5.5 References

- [1] Burton, T., Sharpe, D., Jenkins, N., Bossanyi, E., *Wind Energy Handbook*, John Wiley and Sons, 2001
- [2] Snel, H., *Review of the Present Status of Rotor Aerodynamics*. Wind Energy, vol 1, pp. 46-69, 1998.
- [3] Snel, H., *Review of Aerodynamics for Wind Turbines*, Wind Energy, vol 6, pp.203-211, 2003.
- [4] Madsen, H. Aa., Mikkelsen, R., Øye, S., Bak, C., Johansen, J., *A detailed investigation of the blade element momentum (BEM) model based on analytical and numerical results and proposal for modifications of the BEM model*, Journal of Physics: Conference Series – The science of Making Torque from Wind, (75), 2007.
- [5] Manwell, J.F., McGowan, J.G., Rogers, A. L., *Wind Energy Explained – Theory, Design and Application*, John Wiley and Sons, 2002
- [6] Hau, E. *Wind turbines: Fundamentals, Technologies, Application and Economics*. second edition, Springer-Verlag, Berlin Heidelberg, 2006.
- [7] Prandtl, L., and Betz, A., *Vier Abhandlungen zur Hydrodynamik und Aerodynamik*, Gottingen Nachr., Gottingen, Selbstverlag des Kaiser Wilhelminstituts für Stromungsforschung.
- [8] Goldstein, S., “*On the Vortex Theory of Screw Propellers*”, Proceedings of the Royal Society”, London, vol. 123, no. 792, pp. 440-465, 1929.
- [9] Shen, W., Z., Mikkelsen, R., Sørensen, J., N., Bak, C., *Tip loss corrections for wind turbine computations*, Wind Energy, Volume 8, Issue 4, pp 457-475, 2005.
- [10] Guanpeng, X., and Lakshmi, S.N., *Application of a Viscous Flow Methodology to the NREL Phase VI Rotor*. Proceedings of the ASME Wind Energy Symposium, Reno, Nevada, 2002.
- [11] Glauert, H., ‘*The analysis of experimental results in the windmill brake and vortex ring states of an airscrew*’. ARCR R&M No. 1026, 1926.
- [12] Joosse, P.A., *Frequenties en Doorbuiging van een Balk Bepaald met de Methods van Mykeltstad en Thomson*, Technical Report No. IW-88021R, Technische Universiteit Delft Delft, The Netherlands, 1988.
- [13] Thomson W.T., Dahleh, M.D., *Theory of Vibration with Applications*, 5th Edition, Prentice-Hall, Upper Saddle River, NJ., 1998.
- [14] A.D.Wright, C.E. Smith, R.W. Thresher, and J.L.C.Wang, *Vibration Modes of Centrifugally Stiffened Beams*, Journal of Applied Mechanics, Volume 49, pp. 197–202, 1982.

CHAPTER 6

GENERIC BLADE MODEL AND DESIGN LOADS

In preparation for the next two chapters focused on structural optimization, this chapter aims at defining critical load cases for preliminary blade design. These load cases being influenced by aerodynamic loads, inertial loads and gravity loads, a generic blade geometry is first described. In accordance with the IEC-61400-1 standard, different load cases are then evaluated from which four critical load cases are identified.

6.1 Introduction

As mentioned in the introductory chapter, the research effort presented in this thesis aims at developing new structural designs dedicated to large thermoplastic composite wind turbine blades. This will be achieved in the next two chapters by systematically searching for new structural layouts by means of topology and size optimization techniques.

Before being able to use these techniques, design loads will have to be determined. This chapter will therefore focus on identifying the reference load cases to be used for the different optimization runs presented in the remaining chapters of this thesis. The aerodynamic, inertial and gravity loads will thus be solved for the two IEC-61400-1¹ design conditions considered most relevant to large wind turbine blade preliminary design (power production condition, parked design condition). Within these two design conditions, the most critical load cases will be identified and quantified. To judge if a load case is more critical than another for power production load cases, root-bending moments determined using Yawdyn will be compared. For parked design conditions, a simple Matlab script will be used to compare root-bending moments.

¹ International Electrotechnical Commission (IEC) -61400-1 Wind turbines generator systems - Part 1: Design requirements

As a first step towards identifying design load cases, a generic blade will be designed using the aerodynamic design tools presented in the previous chapter. Since some load case evaluations require dynamic analysis (power production load cases), it will be necessary to estimate blade stiffness characteristics using the structural design and analysis tools developed in the previous chapter.

Finally, to circumvent some of the difficulties associated with transposing Yawdyn-determined root-bending moments into readable files for input to the finite element models presented later in this thesis, the aerodynamic design and analysis tool presented in chapter 5 will be used to generate the associated distinct span-wise aerodynamic loads and format them in the appropriate FEM file format.

6.2 Generic blade design

6.2.1 Blade geometry

It is well known that modern wind turbine blades are now designed with very complex optimality criteria involving more than aerodynamic efficiency. For example, to the detriment of aerodynamic performance, thrust loads can be tailored to reduce adverse effects on other turbine components and ultimately extend the wind turbine's life and reliability [1]. For the purposes of this thesis, instead of using a generic blade design based on classical textbook optimality criteria (Glauert, max. torque, max. C_p , etc.), the current trends in MW-size wind turbine blades design (rated wind speed, tip speed ratio, chord distribution, etc...), which are specific to sites and manufacturers, were surveyed and the most important trends were used as guidelines to design the generic blade [2-5]. Figure 6.1 presents these trends with respect to rotor radius (R).

Since the main interest of this research project is to find design solutions for blades to be installed on very large wind turbines (5MW and over) and knowing at what pace wind turbine blade size has evolved over the past few years, it was decided to base the study on a 75m-long blade. Based on the current state of the art, this blade would be intended for an 8MW three-bladed up-wind variable-speed-and-pitch-regulated wind turbine having a hub height of 150m.

Following the design trends shown in Figure 6.1, the generic blade geometry chosen for this thesis has a maximum chord length (C_{max}) of 7.5% R and is situated at 20% of the rotor radius. The chord at tip was set at 20% of the maximum chord length and the

chord distribution was considered linear from the maximum chord position to the blade tip. Finally, a hub radius of 5%R was chosen and the blade root diameter was fixed at 70% of C_{max} .

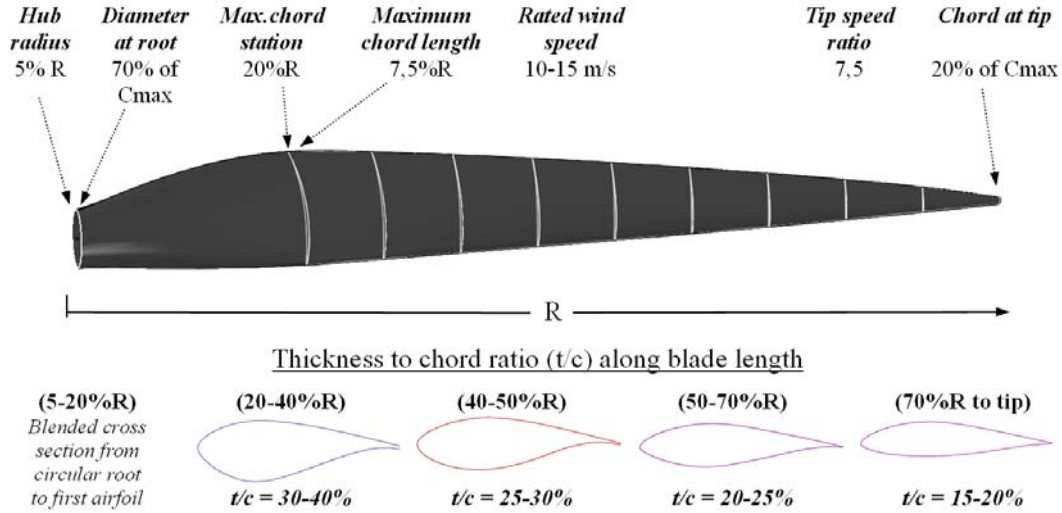


Figure 6.1: Trends in MW-size blade design expressed in function of blade length (R) – Main parameters and types of airfoil used.

Table 6.1: 75-meter-long generic blade geometry with corresponding airfoils

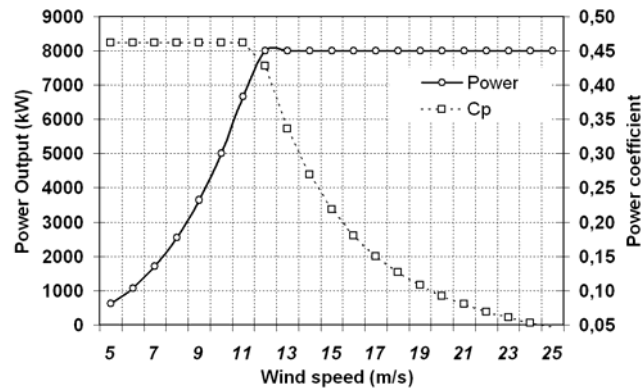
Chord station (r) [m]	Chord (c) [m]	Twist (θ_T) [°]	Airfoil	Thickness to chord ratio (t/c)
3.75	3.938	-	Circular	-
15	5.625	21.2	DU-97-W-300	0.30
21.67	5.125	13.1	DU-97-W-300	0.30
28.33	4.625	8.2	DU-97-W-300	0.30
35	4.125	4.3	DU-91-W2-250	0.25
41.67	3.625	3.3	DU-00-W-212	0.212
48.33	3.125	2.1	DU-00-W-212	0.212
55	2.625	1.3	DU-96-W-180	0.18
61.67	2.125	0.7	DU-96-W-180	0.18
68.33	1.625	0.1	DU-96-W-180	0.18
75	1.125	0	DU-96-W-180	0.18

Airfoils used for the aerodynamic part of the blade (from maximum chord position to tip) are DU series (developed at Delft University of Technology) [6]. Four different airfoils were selected to allow a higher thickness-to-chord ratio in the highly loaded region near the root of the blade and a lower ratio near the tip. The region between the

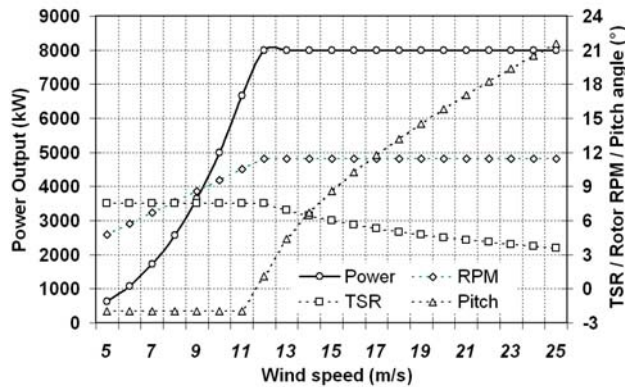
root and the maximum chord position evolves from a circular section to the airfoil shape used at C_{max} . Based on the above mentioned blade characteristics, Table 6.1 shows the generic blade geometry, for which r is the radial position of the section relative to the rotor's axis of rotation, c is the chord length and θ_T is the twist angle at each station. The distribution of twist is non-linear and was set to yield the desired design angle of attack at each blade element (6°).

6.2.2 Rotor performance

As shown in Figure 6.2a and 6.2b, from a rotor performance evaluation performed with the aerodynamic analysis tools presented in chapter 5, the nominal power (P) of the turbine is attained at a rated wind speed (V_r) of 12 m/s. The blade tip speed ratio (λ) is kept constant at 7.5 up to rated wind speed. Between this wind speed and the cut-out wind speed (V_{out}) of 25 m/s, the rotational speed is fixed at $\omega = 11.5$ rpm with C_p and λ decreasing as load is shed by the pitch system.



a)



b)

Figure 6.2: Generic blade rotor performance characteristics with respect to wind speed, a) power curve and corresponding power coefficient, b) power curve, TSR, rotor RPM and pitch angle.

To validate the aerodynamic analysis tool coded for the purposes of this thesis, Aerodyn was used to compare the induction factors, in-plane forces and out-of-plane forces at each blade element. The interested reader is referred to Appendix A for the complete data set of this validation study.

6.2.3 Blade mass, mass moment of inertia and natural frequency

When performing structural dynamic analysis, specific physical and structural blade characteristics must be known. In our case, YawDyn (v12.16) [7] was used to evaluate the blade dynamic response, which calls upon the AeroDyn (v12.58) [8] software to compute the aerodynamic loads on the blades at each time step. When modeled as cantilever blades, YawDyn requires blade stiffness data in order to evaluate the dynamic response of the rotor. In our case, since span-wise blade stiffness distribution is unknown (the blade is not structurally designed yet!), blade stiffness must be projected. This was done using the analytical structural analysis tools presented in the previous chapter and is presented in the next section.

6.2.3.1 Estimated blade stiffness and natural frequency

To run an analysis with cantilevered blades, YawDyn uses the hinge-spring concept to evaluate the blade out-of-plane root bending moments. This concept, based on classical helicopter theory and first adapted to wind turbines by Eggleston and Stoddard [9], considers the blade to be infinitely rigid and connected to the hub by a torsion spring able to simulate the blade out-of-plane bending stiffness.

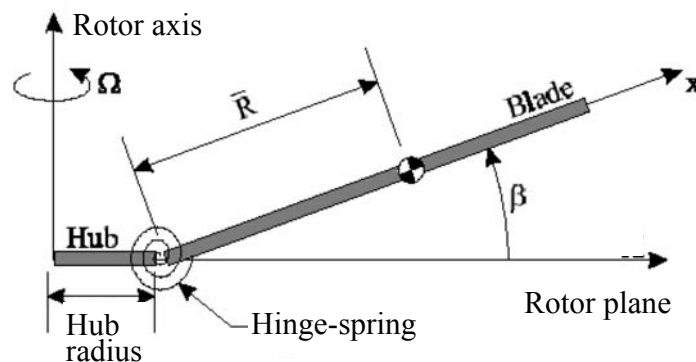


Figure 6.3. The equivalent hinge-spring model for the blade flap degree of freedom (adapted from [8]).

As shown in Figure 6.3, apart from the hinge-spring constant (κ_β), YawDyn requires the position of the blade's center of gravity (\bar{R}), the blade mass and the blade mass moment of inertia in the out-of-plane direction (I_b). The hinge-spring constant can be calculated as shown in Equation 6.1 if the out-of-plane blade mass moment of inertia and non-rotating natural frequency (ω_{NR}) are known.

$$\kappa_\beta = \omega_{NR}^2 I_b \quad (6.1)$$

where,

$$I_b = \int_{R_{hub}}^R r^2 dm \quad (6.2)$$

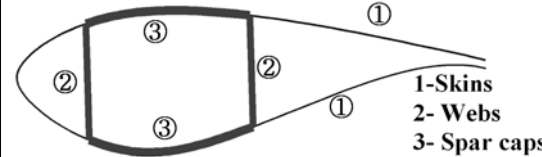
Again, at the preliminary design stage, blade mass moment of inertia and blade natural frequency can be only estimated. To do so, the first step was to determine a blade mass representative of a 75m-long blade dedicated to an 8MW turbine. This was done with Figure 1.7 in the introductory chapter, in which a 75m-long blade mass was estimated at 35,000 kg.

To estimate the blade's center of gravity and mass moment of inertia, a baseline cross-section configuration representative of current commercial blade structural designs was used. The structural layout consists of a load-bearing box spar section with webs positioned at 15% and 50% of chord length, covered by two thin skins (see the illustration in Table 6.3). Typical large wind turbine blade laminate stacking sequences were used for all three components (spar caps, webs and skins). For the webs and skins, a laminate of $50\% \pm 0^\circ$ and $50\% \pm 45^\circ$ fibers was used. In the spar cap, the laminate was composed of 0° and $\pm 45^\circ$ fibers, occupying respectively 70% and 30% of the volume [10]. Using the material lamina properties presented in Table 6.2, the different laminate properties presented in Table 6.3 were computed using classical lamination theory (CLT). When compared to experimental results, especially in compression, this analytical method will overestimate the strength values since failure mechanisms like fiber microbuckling or fiber-to-matrix interface failure are not taken into account in CLT. Nevertheless, since the stiffness modules are not affected significantly by these phenomena, mass moment of inertia and blade natural frequency can be estimated using these approximated values.

Table 6.2: Unidirectional material properties of glass/PA-6 composite (Source: Bond Laminates)

UD lamina material	PA-6/Glass
Density [kg/m^3]	1.77
Fibre volume [%]	46
Elastic modulus (E_1), [GPa]	38
Elastic Modulus (E_2), [GPa]	8.24
Tensile strength (S_1^T), [MPa]	869
Tensile strength (S_2^T), [MPa]	32.03
Shear modulus (G_{12}), [GPa]	1.80
Shear strength, (τ_{12}), [MPa]	65.47
Compressive strength (S_1^C), [MPa]	634
Compressive strength (S_2^C), [MPa]	72.94
Poisson's ratio (ν_{12})	0.28

Table 6.3: Blade cross-section properties of the different components used to estimate blade mass moment of inertia, center of gravity and natural frequency.

		Longitudinal Modulus	Tensile Strength*	Compressive strength*
Material	Components	(GPa)	(MPa)	(MPa)
PA-6/ Glass	Skins & webs	6,0	32.1	54.1
	Spar cap	29,5	166.8	204.6

*including a safety factor of 1.82 (most severe IEC material safety factor)

Table 6.4: Blade cross-section component thicknesses with respect to blade length

Chord station [m]	Spar thickness [mm]	Web thickness [mm]	Skin thickness [mm]	Linear blade weight distribution [kg/m]
3.75-15	92,4	-	-	1855,7
15-21.67	55,6	10,6	16,7	559,3
21.67-28.33	49,0	9,3	14,7	435,2
28.33-35	44,4	8,4	13,3	342,1
35-41.67	43,5	8,2	13,1	287,7
41.67-48.33	42,5	8,1	12,7	234,1
48.33-55	32,8	6,2	9,8	147,4
55-61.67	25,0	4,7	7,5	88,8
61.67-68.33	14,9	5,3	5,3	34,9
68.33-75	5,0	5,0	5,0	7,4

Cross-section component thicknesses were determined in order to respect the material strength limits when subjected to a simple parked design situation. The 50-year extreme wind speed model (discussed later in the parked design situations section) was used in combination with maximum lift coefficients being applied at every chord station. As shown in Equation 5.20, bending stresses are determined using effective area moments of inertia that take into account the non-symmetric and non-homogeneous nature of the cross-section. Since the contribution of the double-bias $\pm 45^\circ$ plies to blade stiffness is very low compared to UD plies, Equation 5.20 yields very low stresses in areas where this material is predominant. This is quite normal since the role of the cross-ply material is not to provide blade bending stiffness and strength but rather prevent splaying of 0° fibers and contribute to blade torsional stiffness [11-12].

Because blade strength and stiffness is due mostly to the presence of unidirectional material, the first step in finding cross-section thicknesses involves evaluating the spar cap thickness along blade length. With these span-wise thicknesses, double-bias material thicknesses are deducted in order to respect the material thickness ratio earlier discussed. In doing so, a representative lengthwise blade linear weight distribution can be identified from the first blade station where an airfoil is used up to the blade tip. It is worth noting that a minimum ply thickness of 5mm was imposed for the lightly loaded tip area in order to keep thicknesses as realistic as possible.

Due to the complex stress state present in the blade section extending from blade root to maximum chord (root carrot connections, large curvatures, etc.), instead of estimating material thicknesses with Equation 5.20, an empirical relationship based on commercial blade root designs was used. As suggested by Bir [11-12], who surveyed different blade manufacturers to develop his expression, blade root thickness can be estimated using Equation 6.3.

$$t_{root} = 0.08 \sqrt{\frac{R}{40}} (meters) \quad (6.3)$$

For $R = 75m$, a root thickness of 109.5mm is obtained. For the material between the root and the first airfoil section, the thickness simply tapers off from the thickness at the root to the thickness at the first airfoil section.

Since material strength limits are optimistic theoretical values, the total blade mass computed with this approach will be inevitably somewhat less than the expected

35,000kg (~28,000kg in this case). Nevertheless, since the lengthwise sectional blade weight distribution can be considered representative of commercial blades, the material density was scaled to a value yielding the desired total blade mass of 35,000kg. These thicknesses are presented in Table 6.4, which also lists the lengthwise linear blade weight distribution. To validate the analytical method used to estimate these cross-section thicknesses, a FE model was built and used to compare results. The interested reader is referred to Appendix B for the benchmark study comparing the analytical method used and a FE-based linear analysis.

Using these values, a first non-rotating blade natural frequency of 0.97Hz was found, the blade mass center of gravity was positioned at $R = 14.6\text{m}$ and a blade mass moment of inertia $I_b = 1.46\text{e7 kgm}^2$ was determined with respect to blade root. The calculations leading to these results were done using the method described in section 5.4.4 and Equation 6.2.

6.3 Design loads

For simplicity, aerodynamic, gravitational and inertial loads are expressed throughout this thesis in a coordinate system referenced to the rotor plane as seen in Figure 6.4.

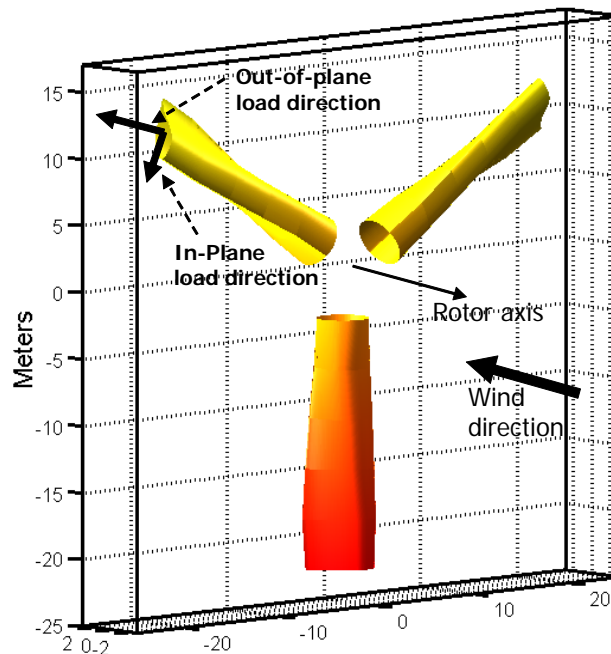


Figure 6.4: Rotor plane reference system showing out-of-plane and in-plane loads.

The rotor plane is considered perpendicular to the ground. Gravity loads thus have no component in the out-of-plane direction and can act only in the in-plane direction. Conversely, aerodynamic loads have components both in the in-plane and out-of-plane directions. As seen in chapter 5, in wind turbine terms, the out-of-plane components of the aerodynamic loads are often referred to as thrust loads whereas the aerodynamic in-plane components are referred to as torque loads. These in-plane and out-of-plane loads will later be used to compute the bending moments and shear forces acting on the blade with reference to the same rotor plane reference system. As for inertial loads, they act in a radial direction with respect to the rotor axis. Depending on the finite element model presented in chapter 7 and 8, gravitational and inertial loads will either be taken into account directly in the finite element environment using material density and rotational speed or simulated with force vectors or pressure applied respectively to nodes or element surfaces.

6.3.1 IEC-61400-1 design situations

Loads on the wind turbine blade were determined according to the IA Wind turbine generator system (WTGS) class of the International Electrotechnical Commission 61400-1 standard [13]. This standard defines eight different design situations for which the integrity of the turbine has to be validated:

- Power production;
- Power production plus occurrence of fault;
- Start-up;
- Normal shut-down;
- Emergency shut-down;
- Parked (stand still or idling);
- Parked and fault condition;
- Transport, assembly, maintenance and repair.

Since this thesis only deals with preliminary blade design, a large number of these design situations are impossible to evaluate since they require complete knowledge of wind turbine characteristics (control systems, tower/foundation design, transport and

assembly, etc.). For this reason, this study will only consider specific power production design situations and parked design situations in which the blade characteristics presented earlier are alone sufficient to evaluate the design situation. The following two sections will present these design situations and corresponding load cases.

6.3.2 Power production design situation load cases

For the power production design situation, the IEC 61400-1 standard defines nine load cases ranging from normal wind-profile-driven load cases to extreme wind-shear-driven load cases. Again, as was the case for the multiple design situations listed earlier, a large number of these load cases require wind turbine design characteristics not available during the preliminary stage of blade design. Therefore, out of the nine load cases described in the IEC 61400-1 standard, only the load cases using the following three wind conditions can be evaluated at a preliminary blade design stage:

- Normal wind profile model:
 - At 0° yaw angle (NWP(0))
 - At -15° yaw angle (NWP(-15))
 - At 15° yaw angle (NWP(+15))
- Extreme wind shear:
 - Horizontal negative extreme wind shear (EWS(HN))
 - Horizontal positive extreme wind shear (EWS(HP))
 - Vertical extreme wind shear (EWS(V))
- 50-year recurrence extreme direction change:
 - Negative direction change (EOG50(N))
 - Positive direction change (EOG50(P))

Since the wind turbine studied here is a pitch-regulated machine, the maximum load is reached at the rated wind speed. Loads were therefore evaluated only at this wind speed. All wind conditions listed above have been evaluated using AeroDyn and YawDyn to find the most critical load case. The “IEC wind” package included in Yawdyn was used to simulate the different wind conditions stated above.

6.3.2.1 In-plane and out-of-plane bending moments

To compare loads, the bending moments at blade root evaluated by YawDyn were used. Results for all load cases studied are shown in Table 6.5. These bending moments take into account aerodynamics, gravitational, inertial and dynamic loads.

The critical load cases were those subjected to extreme wind shear (EWS). The vertical extreme wind shear produces the maximum out-of-plane bending moment when the blade is in the vertical position and pointing upward ($\psi=187.2^\circ$), that is, when the blade is subjected to the highest wind speed due to wind shear. The maximum in-plane load is found with a horizontal negative extreme wind shear, when the blade is at the horizontal position on the side where the aerodynamic forces are in the same direction as the gravity load ($\psi=270.2^\circ$) and when the wind shear generates the highest wind speed.

Table 6.5: Out-of-plane and in-plane bending moments computed using YawDyn for the different power production load cases.

Design load case	Out-of-plane				In-plane			
	M_{\max} [$\times 10^6$ Nm]	Time step [s]	Power [kW]	Azimuth [$^\circ$]	M_{\max} [$\times 10^6$ Nm]	Time step [s]	Power [kW]	Azimuth [$^\circ$]
NWP(0)	12.26	2.20	7899	189.3	7.85	1.70	7888	266.1
NWP(-15)	11.19	2.51	6773	216.0	7.72	0.34	6772	268.8
NWP(+15)	11.69	1.99	6876	171.7	7.54	0.29	6874	264.7
EWS(HN)	20.24	10.13	9462	270.2	10.74	10.13	9462	270.2
EWS(HP)	20.12	9.70	9400	113.1	7.85	1.70	7888	266.1
EWS(V)	21.62	10.56	9916	187.2	8.98	9.82	9936	243.4
EOG ₅₀ (N)	12.26	2.20	7899	189.3	7.85	4.50	7885	266.7
EOG ₅₀ (P)	12.28	4.98	7887	187.9	7.85	1.7	7888	266.1

6.3.3 Parked design situations

The parked design situation load cases were computed using a MATLAB program. Two situations were simulated: one with the blade in the vertical position (pointing upward) and the other in the horizontal position for which the gravity load is in the same direction as the aerodynamic load. Both situations were computed with the 50-year extreme wind speed model (EWM). For the vertical blade case, wind coming from all directions was considered since the nacelle and pitch angle are considered fixed. The

fact that a wind turbine fault can occur when the blades are not in the fully feathering position suggests that wind may strike the blade at any pitch angle. Thus, for the horizontal blade case, any blade pitch angle between 0° and 80° (angle corresponding to a fully feathered position) were considered. In all cases, lift and drag coefficients along blade length were calculated according to the method presented in section 5.3.2.

As with the power situation load cases, the blade root bending moments were used to compare blade loading. In order to compare loads with the power production situation, a flapwise/edgewise coordinate system was used with the flapwise and edgewise directions being equivalent to the out-of-plane and in-plane directions used when calculating power production load cases. When studying the different parked design situation load cases, a maximum flapwise bending load of 28.94×10^6 Nm was found when the blade was at the vertical position and the wind direction was at -9° from the tip chord line. In this case, when considering blade twist, the different blade sections were almost perpendicular to the incoming flow. A maximum edgewise load of 29.96×10^6 Nm occurred when the blade was in the horizontal position and the pitch angle was 30° .

6.4 Load cases for the optimization problems

For the optimization problems, the four most important load cases presented in the two previous sections were retained:

- Load case 1: Maximum power production out-of-plane loads produced by the vertical EWS wind condition with the blade pointing in the upward direction;
- Load case 2: Maximum power production in-plane loads produced by the horizontal EWS wind condition with the blade positioned horizontally;
- Load case 3: Maximum parked flapwise loads produced by the EWM with the blade pointing upward and positioned perpendicular to the wind;
- Load case 4: Maximum parked edgewise loads produced by the EWM with the blade positioned horizontally and pitched at an angle of 30° ;

It is important to note that although the root-bending moments produced by these load cases can be considered as similar, these load cases are actually very different from each other. In power production load cases, most of the aerodynamic load comes from the outer part of the blade while in the parked situations most of the aerodynamic load

comes from the inner part of the blade. This creates very different bending moment and shear force distributions along blade length. Also, the parked design load case with the blade positioned vertically produces loads that are larger in the flapwise direction than in the edgewise direction while the load case with the blade positioned horizontally produces loads that are in the same order of magnitude (including gravity) in both directions. Because these load cases are very different in nature, they will not affect specific chord stations in the same manner. For this reason, all load cases were used in the optimization process to ensure that the optimized design would perform well under all loading conditions.

To retrace the aerodynamic loads along blade length that contribute to the four load cases mentioned above, the contribution of the inertial and gravity loads was first subtracted from the maximum root-bending moments calculated for these load cases. The aerodynamic design and analysis tools developed in chapter 5 were then used to match the corresponding aerodynamic solicitation with the resultant root-bending moment required. Accordingly, it was possible to determine lengthwise bending moment and shear force distributions generated for each load case. Figures 6.5 to 6.8 show these aerodynamic loads expressed as discrete lengthwise loads (dF), shear force (V) and bending moment (M) diagrams for the four critical load cases mentioned earlier. According to the IEC 61400-1 standard, loads presented in these figures have been increased by a safety factor of 1.35 when transferred in the form of applied pressure to the finite element model. In addition, again according to the IEC 61400-1 standard, safety factors of 1.35 and 1.25 were applied respectively to gravity loads and inertial loads.

6.5 Conclusions

In preparation to perform structural topology and size optimization on large thermoplastic wind turbine blades based finite element modeling, a generic blade geometry and associated main physical and structural characteristics was developed.

Using this blade, specific design situations described in the IEC-61400-1 standard were studied and four critical load cases were identified. Two of these load cases came from power production design situations for which aerodynamic loading is mainly concentrated at the most outboard section of the blade. Maximum out-of-plane and in-

plane bending moments found for this particular design situation are respectively 21.62×10^6 Nm and 10.74×10^6 Nm.

The other design situation studied was the parked design situation. This design situation is generally used to simulate storm-like situations in which the turbine is at a standstill. After studying different azimuth and pitch angles for the turbine subjected to the IEC 50-year extreme wind speed model (EWM), the maximum flapwise and edgewise bending moments for this particular design situation were found to be 29.96×10^6 Nm and 28.94×10^6 Nm respectively.

In order to apply the proper loads in the finite element models presented in chapters 7 and 8, the contributions of inertial, gravity and aerodynamic loads to these root-bending moments were extracted. Using the aerodynamic design and analysis tools developed in chapter 5, span-wise in-plane and out-of-plane aerodynamic forces were identified for all four critical load cases.

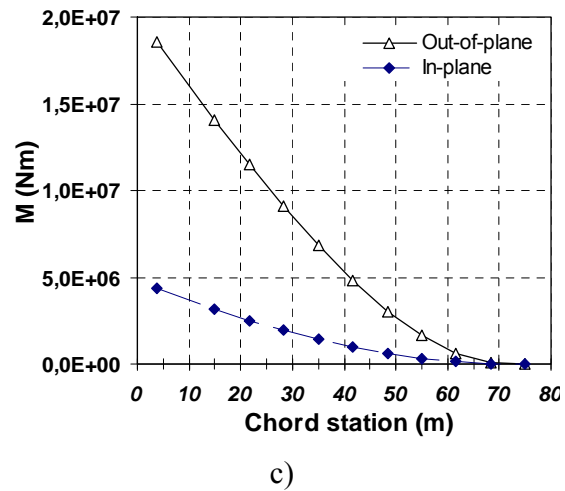
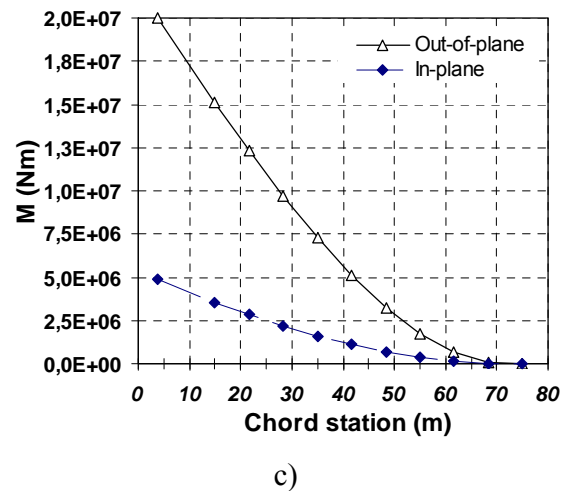
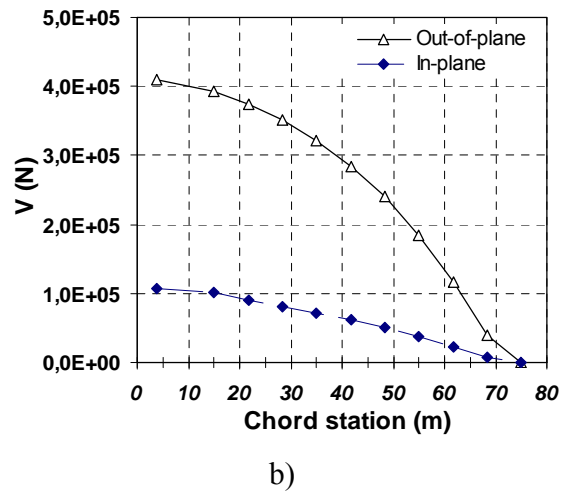
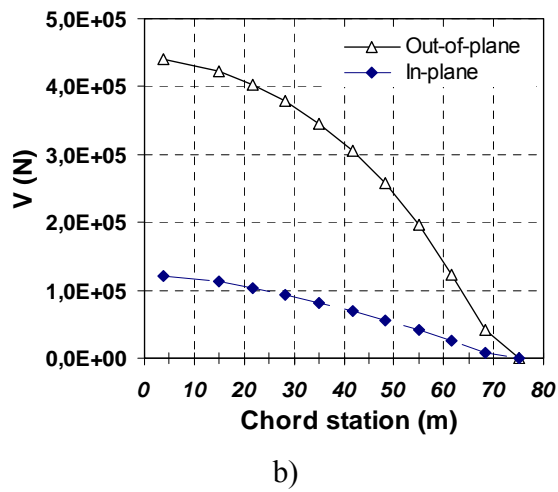
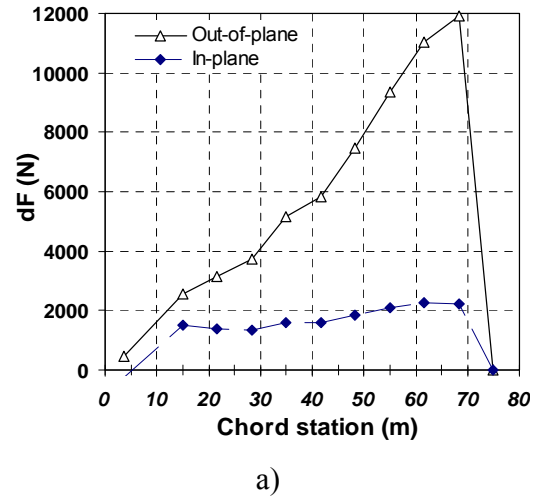
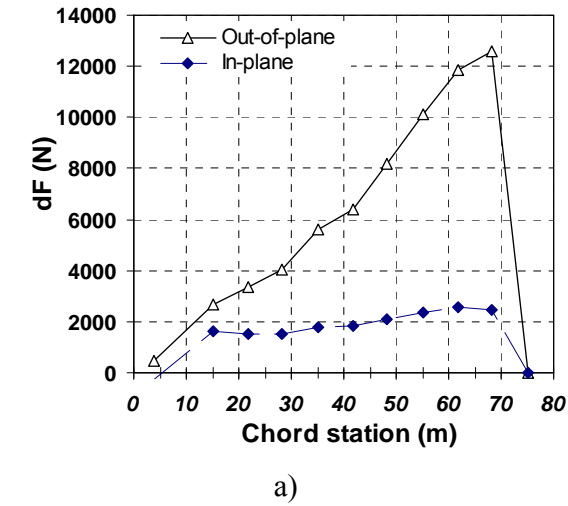
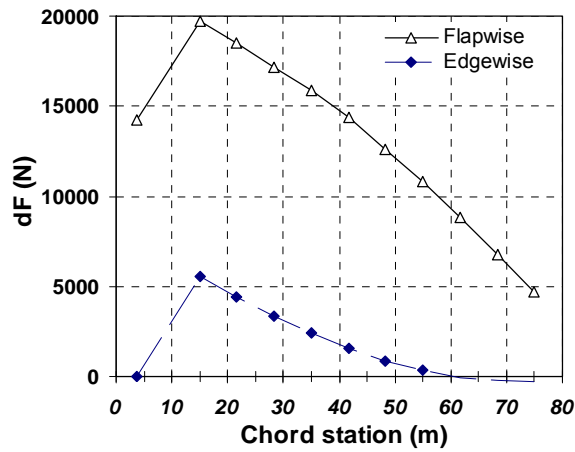
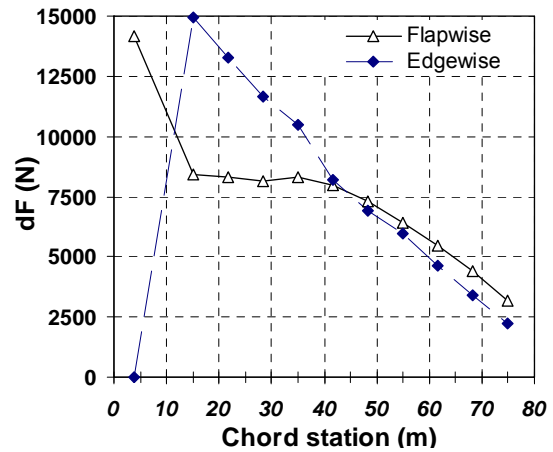


Figure 6.5: Aerodynamic load case 1,
a) Applied load (dF), b) Shear forces
V), c) Bending moments (M).

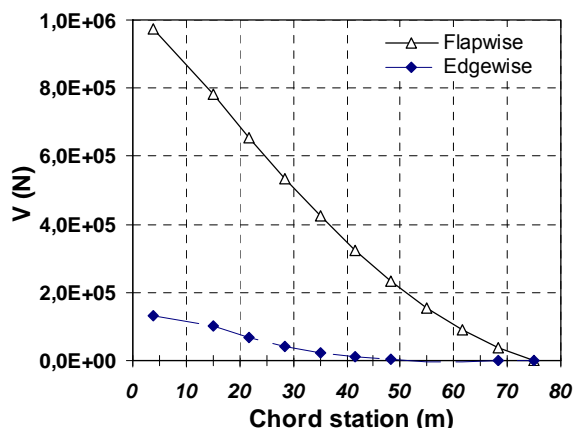
Figure 6.6: Aerodynamic load case 2,
a) Applied load (dF), b) Shear forces
(V), c) Bending moments (M).



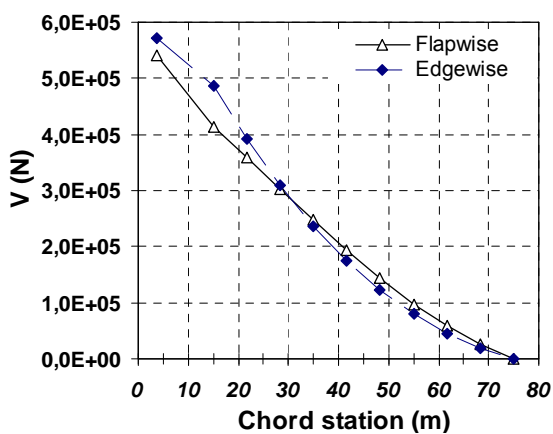
a)



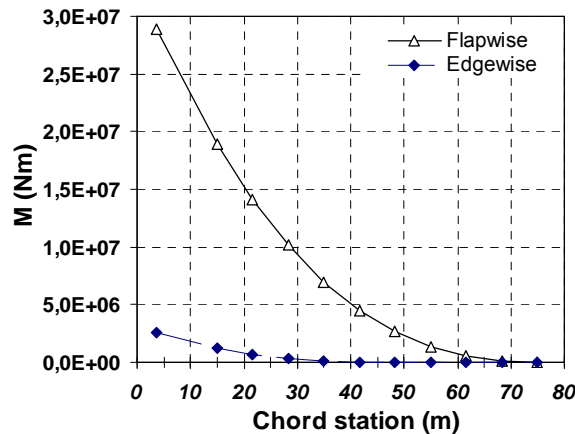
a)



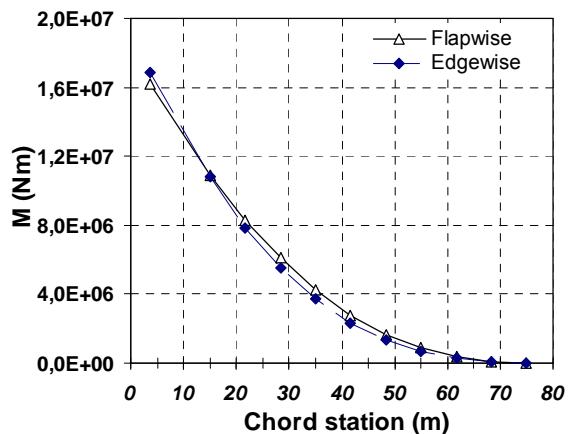
b)



b)



c)



c)

Figure 6.7: Aerodynamic load case 3, a) Applied load (dF), b) Shear forces (V), c) Bending moments (M).

Figure 6.8: Aerodynamic load case 4, a) Applied load (dF), b) Shear forces (V), c) Bending moments (M).

6.6 References

- [1] Snel, H., *Review of Aerodynamics for Wind Turbines*, Wind Energy, vol 6, pp.203-211, 2003.
- [2] Malcolm, D.J., Hansen A.C, *WindPACT Turbine Rotor Design Study*, Technical Report No. NREL/SR-500-32495, National Renewable Energy Laboratory, Golden, CO, 2002
- [3] Griffin, D.A., *WindPACT Turbine Design Scaling Study Technical Area 1 – Composite Blades for 80 to 120 meter Rotor*, Technical Report No. NREL/SR-500-29492, National Renewable Energy Laboratory, Golden, CO, 2001.
- [4] Griffin, D.A., *Blade System Design Studies Volume 1: Composite Technologies for Large Wind Turbine Blades*, Technical Report No. SAND2002-1879, Sandia National Laboratories, Albuquerque, NM, 2002
- [5] Berggreen, C., Branner, K., Jensen, J. F., and Schultz, J. P., *Application and Analysis of Sandwich Elements in the Primary Structure of Large Wind Turbine Blades*, Journal of Sandwich Structures and Materials, Vol. 9, 2007, pp. 525–551.
- [6] Timmer, N., van Rooij, R.P.J.O.M., *Summary of the Delft University Wind Turbine Dedicated Airfoils*, Journal of solar energy engineering, Vol. 125, November 2003, pp. 488–496.
- [7] Laino, D. J. and Hansen, A. C., *User's Guide to the Wind Turbine Aerodynamics Computer Software AeroDyn*, Windward engineering LC, 2002.
- [8] Laino, D. J. and Hansen, A. C., *User's Guide to the Wind Turbine Dynamics Computer Program YawDyn*, Windward engineering LC, 2003.
- [9] Eggleston, D. M. and Stoddard, F., S., *Wind Turbine Engineering Design*, Van Nostrand Reinhold, New York, 1987.
- [10] Veers, P.S. and al., *Trends in the Design, Manufacture and Evaluation of Wind Turbine Blades*, Wind Energy, vol 6, pp.245-259, 2003.
- [11] Bir, G.S. *A Computerized Method for Preliminary Structural Design of Composite Wind Turbine Blades*, Special Issue of the Journal of Solar Engineering, Volume 123, Number 4, November 2001.
- [12] Bir, G. S., Migliore P., *Preliminary Structural Design of Composite Blades for Two- and Three- Blade Rotors*, NREL/TP-500-31486, Golden, CO: National Renewable Energy Laboratory, September 2004.
- [13] International Electrotechnical Commission, *61400-1 Wind turbines generator systems - Part 1: Design requirements*, Geneva (Switzerland), 2nd ed., 1999.

CHAPTER 7

PRELIMINARY DESIGN OF LARGE THERMOPLASTIC COMPOSITE BLADES *A TOPOLOGY OPTIMISATION APPROACH*

In this chapter, a new structural topology for large thermoplastic composite (TPC) wind turbine blades is presented. Since thermoplastic composites are processed differently than their thermosetting counterpart, the design proposed in this chapter was not based on existing thermoset composite blade designs but rather developed using structural topology optimization techniques. Keeping in mind the strengths and limitations of TPC manufacturing, the different design solutions found through this optimization process were interpreted and a final design was proposed.

7.1 Introduction

The structural design used today for large wind turbine blades relies on a box spar as the main load-bearing element. Two general philosophies may be applied to yield such a design. As shown in Figure 7.1a, the box spar can be formed from two C-shaped webs bonded to an upper surface and lower surface blade skin bonded at the leading edge and trailing edge. In this case, the blade skins are heavily reinforced in the area comprised between the two webs (often called the spar caps) to close the box spar and provide an adequate load path. Instead of using two C-shaped webs, some manufacturers prefer producing the box spar individually on a dedicated mandrel (approach preferred by Vestas, Gamesa and others). This seamless box spar is later bonded to non-structural upper and lower surface skins to give the blade its final shape. This design philosophy is illustrated in Figure 7.1b. As mentioned in the introductory chapter, experts in the wind energy business [1-6] believe that the design just described might not be ideal for larger blades. Their conclusion suggests that the current design might have reached its maturity and that without major design changes to materials and structure, no significant weight and cost reduction will be possible.

As mentioned in chapter 3, although a reactive processing technique based on vacuum infusion was identified as one of the most promising manufacturing methods for the

production of large thermoplastic composite (TPC) parts, TPC manufacturing processes in use today are mostly melt processes dedicated to the production of relatively small parts (up to 1-2m in length and 1-5mm thick). To maximize the potential of thermoplastic composites when used for wind turbine blade structures, it is essential to redesign the structure with respect to existing TPC material and manufacturing strong points. Based on the conclusions of chapter 3, blade designs using ribs, multiple skin panels or stringers produced with fast non-isothermal melt processes could help significantly to maximize the potential of TPC in this context.

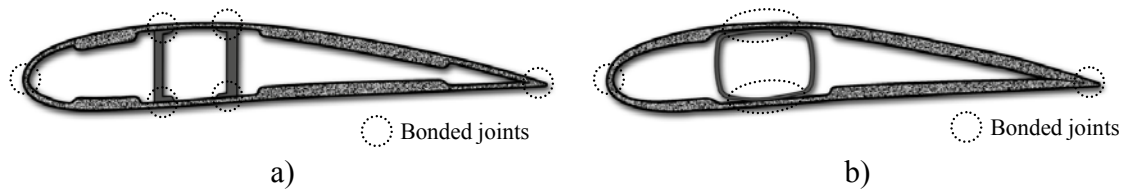


Figure 7.1: Modern FRP wind turbine blade structural designs. a) four-part C-shaped web and skin design, b) three part box-spar and non-structural skin design.

Because of the issues stated above, the designs developed in this chapter are not based on existing thermoset composite blade designs. Instead, the work presented in this chapter concentrates on exploring new blade structures more compatible with current TPC manufacturing techniques through a systematic search for optimized structural layouts using topology optimization techniques. After first presenting the methodology used to guide the design process, the topology optimization results of two different finite element (FE) models will be presented and conclusions will be drawn to serve as guidelines for the blade preliminary design work presented in chapter 8.

7.2 Methodology

7.2.1 *Finite-element-based structural optimization tools*

In recent years, a substantial research effort has been deployed to develop different structural design optimization tools. Building on the pioneering work of Anthony E. G. Michell on trusses back in 1904 [7], renewed interest in structural engineering optimization in the mid 1970s and early 1980s led to the development of different computer-aided structural optimization techniques. Numerous review papers trace this

technology back to its early development and explain the most the important techniques for structural design optimization (evolutionary algorithms, density methods, genetic algorithms, etc.). Since a thorough review of these techniques is beyond the scope of this thesis, the interested reader is referred to the works Rozvany, Sigmund, Bendsøe, Steven and others to know more on the subject [8-10]. Nevertheless, for completeness, the basic principles of the Solid Isotropic Material with Penalization method (SIMP) will be reviewed later in this chapter since it is the method favored for the work performed in this thesis.

In computer-aided structural design, three different tools are generally used to bring a design from its preliminary stage to its detailed stage: topology optimization tools, shape optimization tools and sizing optimization tools. As shown in Figure 7.2, topology optimization tools are used first to help designers determine the overall material layout that best sustains the loads within a large design domain. In other words, this optimization step helps determine where material is needed and where it is not with respect to a specific objective function (minimize weight, minimized compliance, etc.) bounded by certain constraints (limitations on volume fraction used, deflection, stress, etc.). Based on this rough material layout, the second optimization step searches for an optimum contour by allowing nodes to be displaced to maximize the performance of the structure with respect to its main function. Again, the formulation of this optimization problem is based on an objective function bounded by a series of constraints. Finally, once this shape optimization step is completed, the design can be refined further by subjecting the structure to a sizing optimization routine in which the best material thicknesses can be determined.

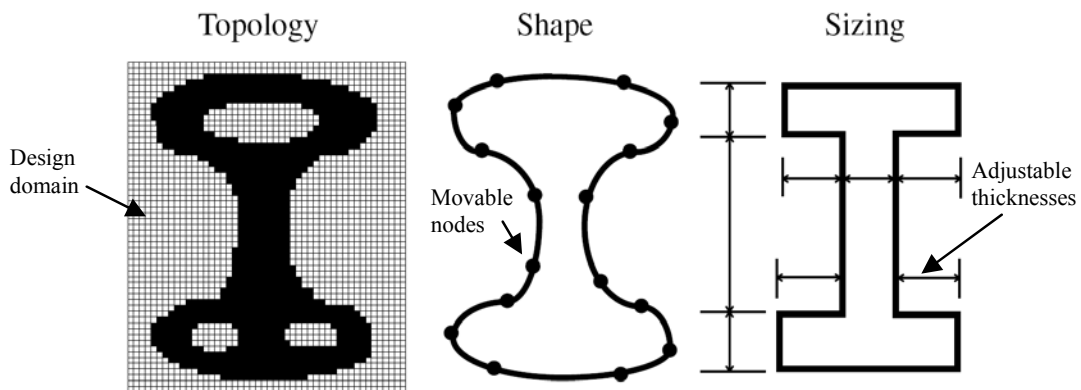


Figure 7.2: Classic three-step computer-aided structural optimization process (topology, shape and size optimization) used to bring a design from the preliminary design stage to the detailed design stage (adapted from [9]).

Nowadays, since some of the techniques just discussed are integrated into commercial FE codes, designers can rely more and more on different optimization tools to assist them during the design process. Size and shape optimization tools are the most common commercial tools available. Such software is not intended for preliminary design purposes but rather to help designers evaluate quickly the impact of a change (loads, materials, shape, etc.) to an existing design. The ANSYS® *DesignXplorer*® package and Catia's *Product Engineering Optimizer 2*® package are good examples of software offering the above-mentioned capabilities based on design of experiments techniques combined with response surfaces.

Commercially available topology optimization packages are less common than shape and size optimization packages. Software providers adopted two different approaches when the time came to incorporate topology optimization tools into FE software environments. They either developed their own topology optimization tools or partnered with smaller companies able to interface their software with their solver and post-processor. MSC-Nastran and Altair are companies that chose the first approach and developed their own packages (MSC-Nastran Topology® and Optistruct®). On the other hand, ANSYS, ABAQUS and others have partnered with companies like FE-Design (Tosca packages) to give users the ability to perform topology optimization.

Already, since topology, shape and size optimization tools have been integrated into well-established FE-based structural analysis software, different applied engineering design problems have been solved with these tools. Various design cases from the automotive industry have been reported [11-12] and more recently, interesting weight-saving design studies have been performed for structural aerospace parts [13-14].

7.2.2 Topology optimization method

For structures involving multiple load cases and asymmetric design domains such as wind turbine blades, topology optimization tools can offer designers the possibility of investigating design solutions that would have been difficult to discover intuitively.

To find optimum preliminary blade designs, the OptiStruct® optimization software packaged in Altair's HyperWorks® FE-element software was used throughout the next two chapters. The topology optimization technique coded in Optistruct® used to converge to optimum solutions is called the “*density method*” method (also known as the “Solid Isotropic Material with Penalization” (SIMP)) and was developed by Bendsoe and Sigmund [15]. As with most other topology optimization techniques, this

method converges to optimum solutions by using user-defined objective functions and constraints to alter the different design variables.

The design variables for the optimization problems presented in this chapter are the densities of each solid element contained in the design domain. These densities (ρ_e) (which should not be confused with the material density), can vary from 0 to 1 to modify element stiffness as follows:

$$\tilde{K}_e = \rho_e^p K_e \quad (7.1)$$

where K_e and \tilde{K}_e are respectively the real and modified stiffness matrices of the element and p is a penalty factor that helps avoid intermediate values of ρ_e (forces values to 0 or 1). Thus, when the density of an element is 0, its stiffness is nil (equivalent to absence of material). When the density is 1, the real material properties are applied to the element. As the optimization process progresses, the elements that are not beneficial to the objective function or to respect certain constraints will decrease in density and useful elements will increase in density so that the distribution of densities at the end of the computation will show where material is most needed and where it is not. Unfortunately, even when using a penalty factor (with common values varying from 2 to 4), intermediate values of density can subsist. Nevertheless, when post-processing the results, clear structural layouts can be identified when varying the threshold value used to display the element densities.

More details on this method can be found in the book by Bendsøe and Sigmund [15] and details on the implementation of this method in Altair's OptiStruct solver can be found in articles by Zhou et al. [16], Thomas et al. [17] and in the OptiStruct documentation [18].

7.2.3 Problem formulation

The objective function of both optimization problems presented later in this chapter is set to minimize the sum of the structure's compliance for each load case when subjected to a volume fraction constraint of 0.2 applied to the design domain (meaning that only 20% of the original design volume can be used). Since compliance is the opposite of stiffness, this problem formulation is equivalent to maximizing the stiffness of the structure.

The compliance for a certain load case is computed as the compliance of the full structure (design and non-design domains) and is equal to the strain energy of the structure. In a FE model, the compliance (c) is computed as follows:

$$c = \frac{1}{2} f^T u \quad (7.2)$$

where f is the load vector and u is the nodal displacement vector [18]. Note that some authors define the compliance as twice the value of the strain energy ($c=f^T u$) [19].

Using the compliance and the volume fraction of the design domain as variables, the optimization problem can be formulated as shown in Equation 7.3.

$$\min C_w = \sum w_i C_i = \sum \frac{1}{2} w_i f_i^T u_i \quad (7.3)$$

subjected to:

$$Vol.Frac. = \frac{V_i}{V_{ini.design}} \leq 0.2$$

As stated in Equation 7.3, only 20% of the volume of the initial design domain ($V_{ini.design}$) is used (V_i), forcing strategic placement of material to maximize structure stiffness. A different weighting factor (w_i) can be applied to the different load cases applied (f_i) to sum the weighted compliance (C_w) and give each load case more or less impact on the final design. It is worth noting that this type of optimization generally does not take into account constraints such as buckling, stress or strain limits. Its purpose is to identify load paths and help the designer determine an ideal structural layout. Specific material and structural constraints are usually dealt with at a later stage in the optimization process with models having discrete geometries.

7.2.4 Preliminary design development strategy

As depicted in Figure 7.3, the preliminary blade structural design optimization strategy proposed in this thesis involves three steps: two initial topology optimization steps and a final sizing optimization step. It can be noticed that when compared to the classical structural design optimization strategy proposed in Figure 7.2, the shape

optimization step was omitted since the exterior shape of the blade is also the exterior boundary of the design domain. In other words, the outside surface of the design domain needs to be kept intact for aerodynamic purposes and cannot be modified in shape as is done in a classical shape optimization process. Omitting this important optimization step diminishes the amount of information gathered to build the FE model used for the final sizing optimization step. To compensate for this loss, the topology optimization step was done using two different FE models and the sizing optimization step was performed with a generic FE model able to simulate different configurations. This approach is believed to have sufficiently broadened the range of design solutions explored to compensate for the absence of the shape optimization step.

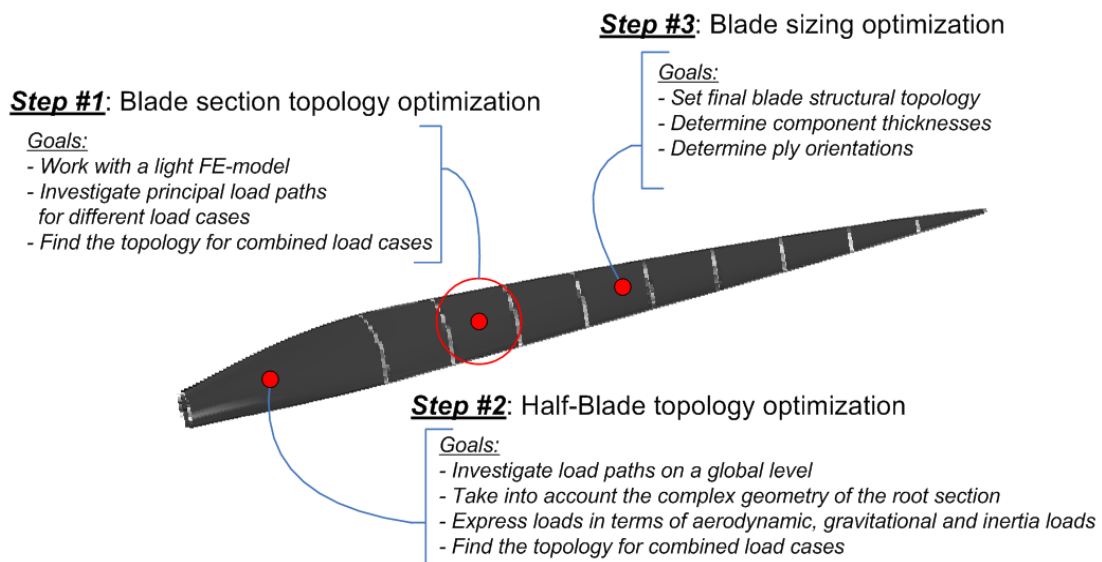


Figure 7.3: Proposed three-step structural optimization design process with associated goals.

As shown in Figure 7.3, step 1 involves performing different topology optimization runs on a short, non-twisted and non-tapered airfoil-shaped blade section. By first running the optimization process with individual loads applied separately, preferred load paths will be identified with respect to the type of load applied. Extending the study to combined load cases, a more general structural topology capable of withstanding multiple loads will be identified. Based on these results, a larger, half-blade model (root-to-blade mid-span) will be used to explore structural topologies in the transition area between the first airfoil-shaped blade section and the circular root blade section. This will be done in step 2 of the optimization strategy (see Figure 7.3). As explained in the previous section, buckling and material stress limits are not used as constraints in steps

1 and 2. Nevertheless, as has been shown in numerous other design studies, simply maximizing stiffness while constraining the design volume fraction yields efficient designs for most classical load cases [12-14]. Since bending is the main solicitation in our case, it is believed that topology optimization can be used with confidence.

Finally, using the results of steps 1 and 2, a third study will be performed to set specific blade dimensions. This last step, based on a shell element blade model, will use sizing optimization tools to determine shell thicknesses, laminate lay-ups and ply orientations for a blade designed for minimum weight subjected to tip deflection, stress and buckling constraints. The results of this sizing optimization procedure will be dealt with in the next chapter while the results of the two first topology optimization steps will be presented in the following sections.

7.3 STEP 1: Topology optimization of a blade section

Due to their asymmetric nature, wind turbine blades unfortunately do not lend themselves to easy partial modeling, unlike some symmetric structures. Therefore, at the cost of dealing with large FE models, only full-blade models can truly represent reality. On the other hand, as noted earlier, due to seriously restrictive manufacturing and cost constraints, wind turbine blade structures must remain simple. It therefore seems obvious that a blade structure should show some repetitive patterns along its length. Because of these two important aspects, it was decided to first work on a blade section to explore the different results obtained with topology optimization before extending the work to larger FE models.

7.3.1 *Finite element model*

For the selection of the blade section to be modeled, the closest inboard section not situated in the blended root section (in which the cross-sectional variation is too large) was considered. With reference to the blade geometry described in chapter 6, this corresponds to sections that would be situated at chord stations beyond 15m. The airfoil chord length and thickness at that station being respectively 5.625m and 1.69m, a 6.66m-long blade section starting from 15m of blade length and extending outboard to 21.66m (the third chord station used to describe the blade in chapter 6) was chosen for

modeling. To simplify the model further, the local blade section twist and taper were not considered.

After testing different methods to model the blade section, a simplified cantilever beam model was favored to run the topology optimization. To recreate blade loading with accuracy in the chosen section for the different load cases developed in chapter 6, a rigid body element (RBE) fixed at the outboard end of the section was used. As shown in Figure 7.4, the use of an RBE provided the possibility of recreating the loading generated by the blade's outboard forces by applying an equivalent resultant shear force (F_R) and bending moment (M_R) at the far end of the blade section. For clarity, only flapwise loads are presented in Figure 7.4 but edgewise loads are modeled in a similar fashion. Although the bending moments (M_1 and M_2) and shear forces (V_1 and V_2) can be reproduced precisely with this technique according to the diagrams presented in chapter 6, small load differences may exist within the blade section since simplified constant load distributions were used over the blade section both in the flapwise and edgewise directions instead of the exact non-linear aerodynamic pressure and weight distributions. Since these differences are small and also because the contribution of the distributed loads over the blade's surface is relatively small compared to the contribution of F_R and M_R , it is believed that this simplification will not have a significant influence on the topology optimization results.

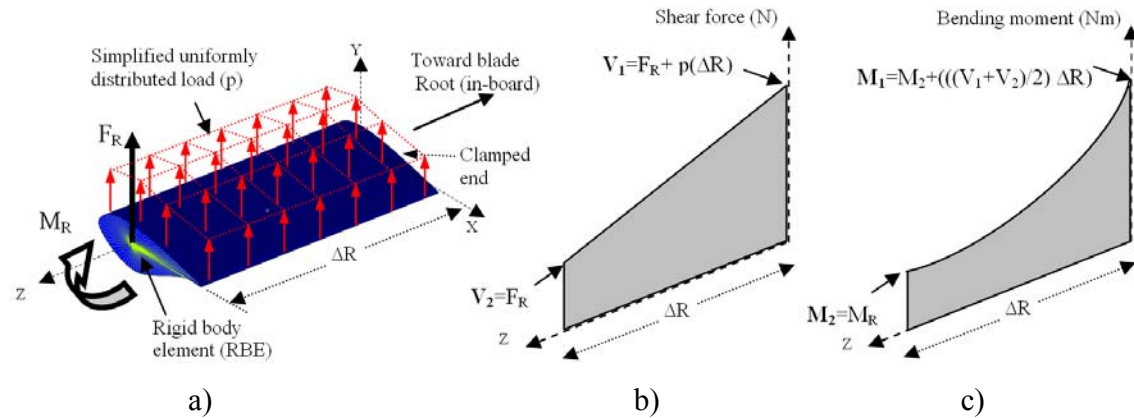


Figure 7.4: Generalized FE model of blade section (ΔR) with corresponding flapwise shear force and bending moment diagrams. a) Cantilever beam concept illustration with tip RBE to apply the equivalent load M_R and F_R , b) Corresponding shear force diagram, c) Corresponding bending moment diagram.

7.3.2 Model loading

From chapter 6, four critical load cases were retained for design. Since these are somewhat different in nature (in terms of bending moment and shear force distribution along blade length), it was suggested that they be studied simultaneously to yield a blade design capable of withstanding all load cases. Nevertheless, when studying a short blade section, the load cases of chapter 6 can be analyzed to target the single most critical load case. It was thus determined that when applying gravity loads and expressing all load cases with respect to a flapwise and edgewise reference system, the worst loading conditions for the blade section chosen for this study were due to load case #4 for the edgewise direction and to load case #3 for the flapwise direction.

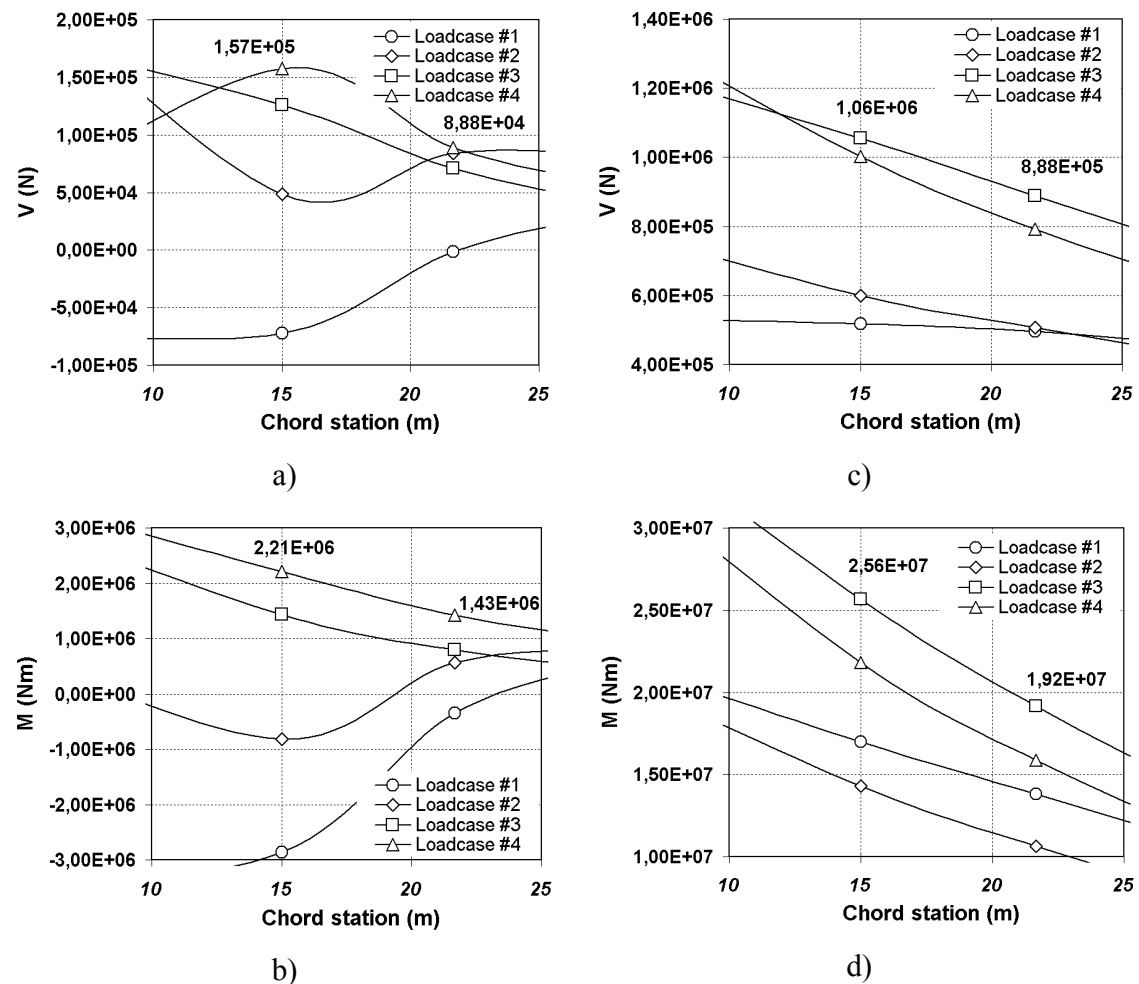


Figure 7.5: 15 m to 21.66 m blade section (ΔR) flapwise shear force and bending moment diagrams for all load cases*. a) Edgewise shear force diagram b) Edgewise bending moment diagram, c) Flapwise shear force diagram, d) Flapwise bending moment diagram. (* gravity loads were included)

The values of bending moments and shear forces present at the 15m and 21.66m blade stations for these load cases are presented in Figure 7.5 and will need to be reproduced in the blade section FE model.

Using the values shown in Figure 7.5, the equivalent resultant shear forces, bending moments and pressure distributions to be applied to the RBE to reproduce loading in the 6.66m-long blade section were derived. Figure 7.6 shows these loads applied using the FE model with the corresponding shear force and bending moment diagrams for the flapwise and edgewise directions. It is worth noting that in the FE model the edgewise uniformly distributed loads was reproduced by tailoring the element density of non-design elements to match the loading (10,250 N/m) and that the weight of the elements part of the design domain was set to zero for them not to influence loading during the optimization process.

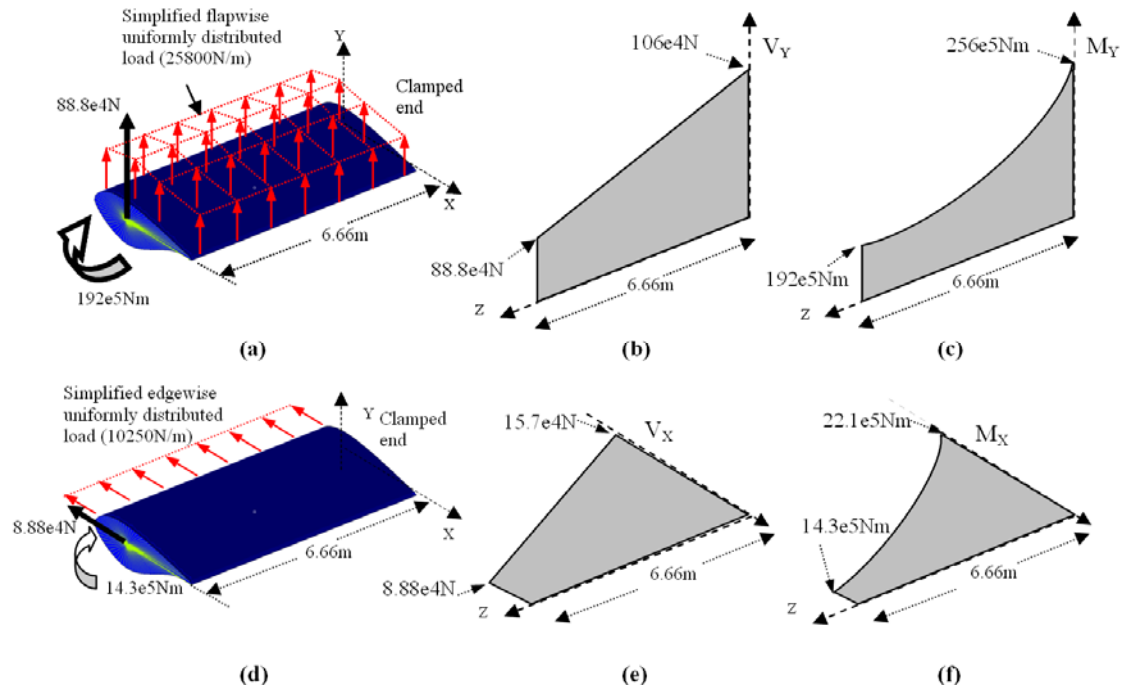


Figure 7.6: 15 to 21.66 m blade section FE model with corresponding shear force and bending moment diagrams. a) Flapwise loading on blade section, b) Flapwise shear force (V_Y) diagram, c) Flapwise bending moment (M_Y) diagram, d) Edgewise loading on blade section, e) Edgewise shear force (V_X) diagram, f) Edgewise bending moment (M_X) diagram.

7.3.3 Optimization variables, objective function and constraints

As discussed earlier, since wind turbine blades must retain their exterior shape intact for aerodynamic purposes, the topology environment had to be described in such a way that the exterior surface of the blade section is kept intact while allowing the interior volume to be used as the design domain. This was accomplished using shell elements on the surface of the blade section and filling the inner volume of these shells with tetrahedral elements. In the Optistruct® environment, the shell elements were labeled as part of a non-design domain whereas the tetrahedral elements were labeled as part of the design domain. About 40,000 elements were used in the design domain whereas approximately 10,000 shell elements composed the non-design domain. Different material labels were used for the two different domains and a very low stiffness and thickness was given to the shell elements to minimize their contribution to the structure's compliance. To perform the optimization, two types of response were used: the compliance of the structure and the volume fraction of the design domain. The objective function was set as specified in Equation 7.3.

As discussed earlier, to keep the design as simple as possible for cost and manufacturing reasons, an extra constraint should be included in the topology environment to force repetitive patterns along blade length. To take this into account, the symmetry function of Optistruct® was used and a symmetry plane perpendicular to the blade section Z axis was described at mid span of the model.

7.3.4 Results

7.3.4.1 Edgewise individual load case solutions

In order first to see the influence of the different loads applied to the model, optimized solutions for each individual load case were found. Performing these singular load case studies provided the opportunity to test the influence of some of the different topology parameters offered in Optistruct® and also helped to identify trends in structural layout configurations for simple load cases before attacking multiple load cases.

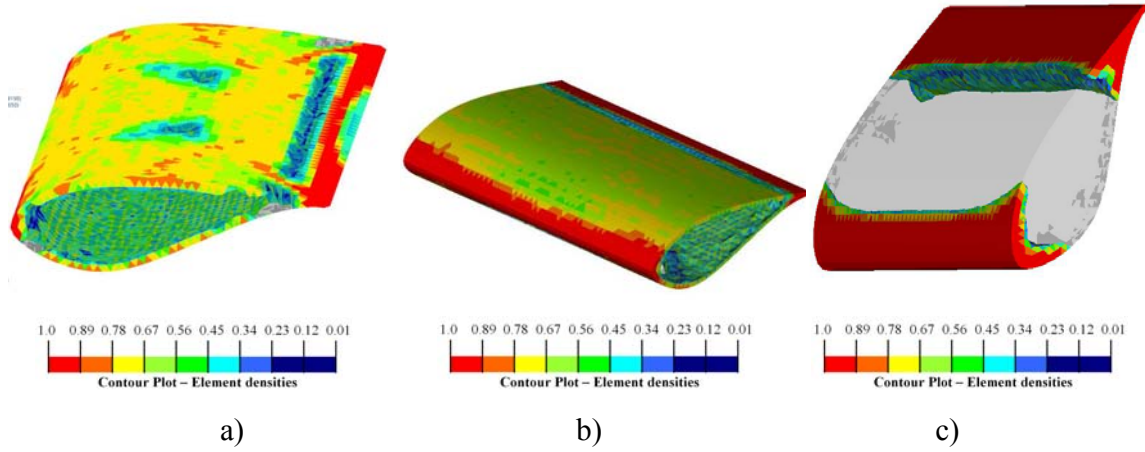


Figure 7.7: Topology optimization results for individual edgewise load cases. a) simplified edgewise uniformly distributed load case, b) equivalent resultant shear force load case, c) equivalent resultant bending moment load case.

Figure 7.7 shows the results obtained for each of the individual load cases studied in the edgewise direction (some weighting factors (w_i) in Equation 7.3 were set to zero to exclude unwanted load cases). From Figure 7.7a and Figure 7.7b it can be deduced that when subjected to the simplified edgewise uniformly distributed load or the equivalent shear force applied at the RBE, the optimum topology converges to a structural skin concept.

When subjecting the blade section to the equivalent edgewise bending moment (see Figure 7.7c), material was kept only at the leading edge and trailing edge. Since it is known that no shear is generated in a beam subjected only to a pure bending moment, this result is quite logical.

7.3.4.2 Flapwise individual load case solutions

As with the edgewise load cases, the different flapwise loads were run separately to find optimal structural layouts for each. Figure 7.8 presents the results obtained for the flapwise uniformly distributed pressure load case, flapwise equivalent resultant shear force load case and flapwise equivalent resultant bending moment load case.

From Figure 7.8a, it was discovered that when subjected to the simplified flapwise uniformly distributed load case, the optimum topology tends to converge to a rib/spar solution. It seems that in order to attain an optimal structure, two simultaneous strategies are adopted: the first being to generate an “I-beam” spar structure in the thickest region

of the blade section to try to minimize overall compliance and the second being to generate a few ribs to minimize the local compliance of the leading and trailing edges.

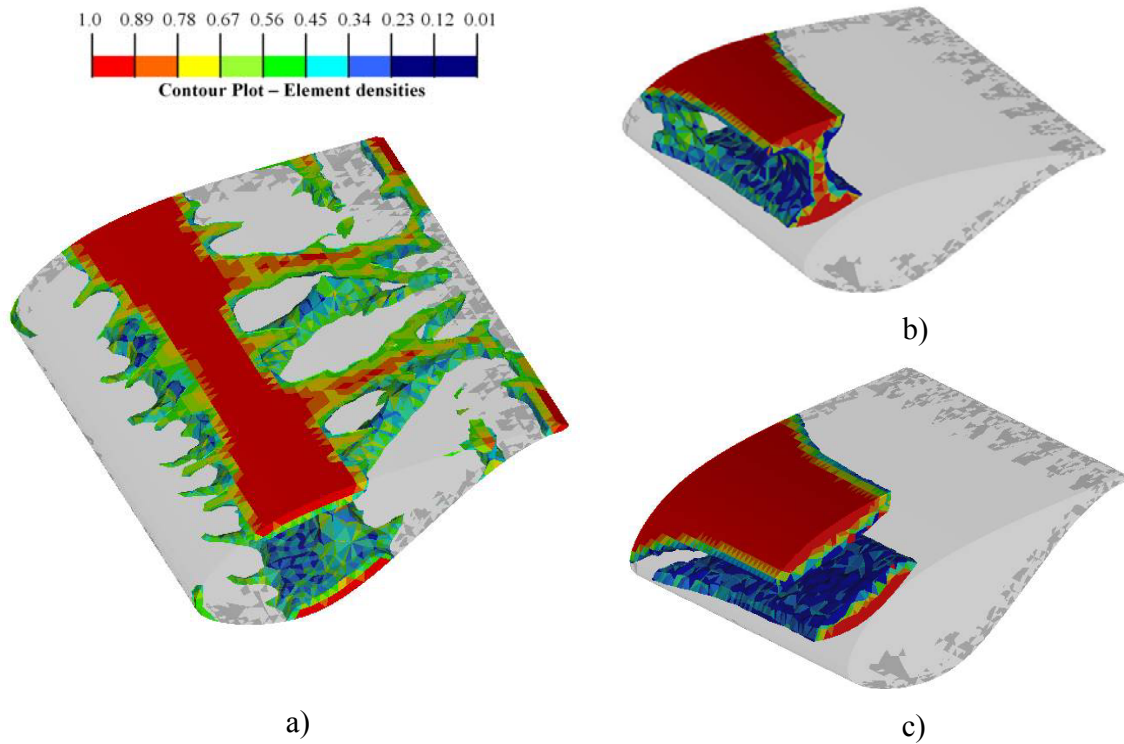


Figure 7.8: Topology optimization results for individual flapwise load cases. a) simplified flapwise uniformly distributed pressure load case, b) equivalent resultant shear force load case, c) equivalent resultant bending moment load case.

In contrast with the results in Figure 7.8a, when loaded only by the equivalent flapwise shear force, an “I-beam” solution is created without any ribs (see Figure 7.8b). This seems logical since the shell elements bounding the design domain no longer bear pressure loads individually as they do in Figure 7.8a. Finally, Figure 7.8c shows the optimized solution for the equivalent resultant bending moment. As in the edgewise case, a structural layout deprived of a shear web well represents what should be the ideal configuration for a pure bending moment load case.

7.3.4.3 Multiple Load Case Solutions

With simultaneous application of the individual load cases of the previous sections, now using the weighted compliance of each individual load case as a response, optimal structural layouts were found. Figure 7.9 presents these results for the edgewise

combined load case, the flapwise combined load case and finally a multiple load case in which all loads (edgewise and flapwise) are applied.

Figure 7.9a shows that when the three different flapwise loads are combined, the optimum solution still resembles a rib/spar configuration but the number of ribs is increased in the middle section of the blade section in comparison to Figure 7.8a. It is also noted that more material is concentrated in the spar region in comparison with Figure 7.8a, possibly to compensate the presence of the loads applied to the RBE. Although it is difficult to identify the reason for the increased number of ribs, the topology thus obtained can be considered a well-balanced mix of all three previously discovered optimal solutions for individual load cases.

For the edgewise combined load case, a similar mix of previously found individual load case solutions can also be found in the optimal topology solution (Figure 7.9b). It can be observed that strong leading and trailing edge sections are still part of the topology but certainly the most unexpected feature of this structural layout is the very distinct “truss like” web configuration that was not present in any of the individual edgewise load case solutions. An explanation for this result could be that the structural skin configuration earlier discovered for edgewise singular load cases may be optimal to a certain extent, but if the bending moment load becomes significant (which is true in this case) more material needs to be kept at the leading and trailing edges, forcing the preference of a “truss like” structure.

The topology optimization solution when all loads are applied (Figure 7.9c) is similar to the topology found for the multiple flapwise load case. It is clear that the solution is designed mainly to hold flapwise loads due to its heavily reinforced upper and lower surfaces. This is understandable since the flapwise bending loads are five to six times larger than the edgewise bending loads. The solution also correlates well with the fact that the area moment of inertia in the flapwise direction of the blade section is much smaller than in the edgewise direction, therefore making the structure much weaker in the flapwise direction. On the other hand, it is more difficult to explain why three distinct small web sections now support the shear loads (shown on XY plane views). One hypothesis is that the previously needed “X shape” truss structure for the combined edgewise load case (Figure 7.9b) and solid vertical web for the combined flapwise load case (Figure 7.9a) were replaced by three distinct vertical shear webs better suited to support combined shear loads simultaneously in the flapwise and edgewise directions.

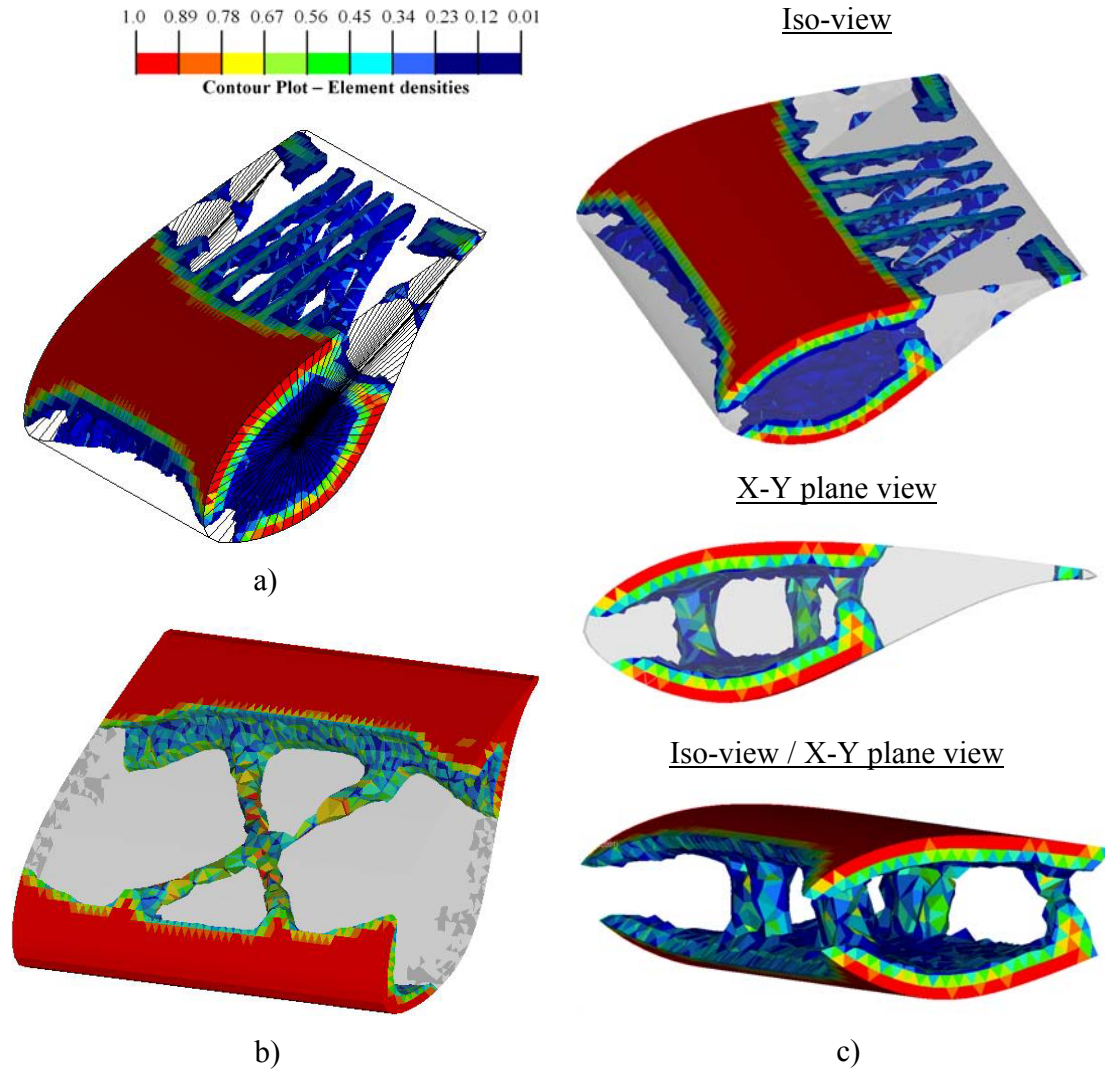


Figure 7.9: Topology optimization results for multiple load cases. a) Multiple flapwise load case, b) Multiple edgewise load case, c) Multiple load case with all loads included (edgewise + flapwise loads).

7.3.5 Discussion

Although the results presented in Figures 7.7, 7.8 and 7.9 are interesting, some parameters and intrinsic characteristics of the FE model used were identified as having significant influence on the topology optimization solutions.

First of all, the boundary conditions set on the blade section to be optimized inevitably created highly stressed areas that can act as starting points to generate discrete structural layouts during the topology optimization process. These boundary conditions have an adverse effect on topology optimization solutions since wind turbine

blade loading by its nature is never concentrated on a single point except in the case of the root attachment. Also, when modeling just a short blade section, the optimized structural layout obtained should normally be considered optimal for that specific blade section only. Nevertheless, since blade loading and design domains are relatively similar from one blade section to another along blade length, it is expected that the solutions shown in Figure 7.9 could also be considered optimal for other airfoil-shaped blade sections. On the other hand, this is most certainly not true for blade sections near the root, where the design domain changes from an airfoil shape to a circular cross-section.

Of course the best way to confirm or disprove the hypotheses just mentioned would be to model the full blade with aerodynamic, inertial and gravity loads, but this approach has the unfortunate drawback of the extremely long computational time required to process a much larger model. To make this approach feasible and keep computational time within acceptable limits, a half-blade model was used. The topology optimization result obtained with this model will be presented in the next section.

7.4 STEP 2: Topology optimization using a half-blade model

7.4.1 *Finite element model*

The half-blade FE model used for topology optimization is shown on Figure 7.10. To lighten the model when compared to a full blade model, only the section from the root to the 35-m chord station (47% of blade length) was considered. The upper and lower surfaces of the blade were meshed with four-node quadrilateral shell elements and the surfaces at both ends were meshed with three-node triangular shell elements.

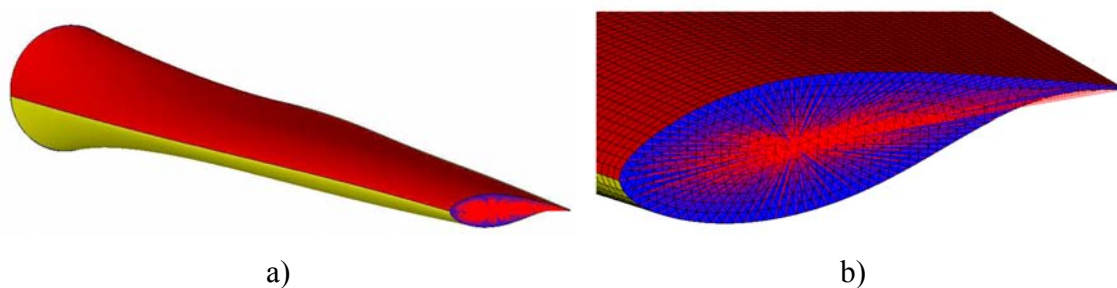


Figure 7.10: Half-blade finite element model used for topology optimization. (a) blade without mesh, (b) zoom at the 35 m radial position (where the blade is cut-off).

As with the previous model, the closed volume formed by these shell elements was filled with four-node tetrahedral solid elements to compose the design domain for the topology optimization problem.

As was done in step 1, the shell elements were assigned very low stiffness ($E = 1 \times 10^{-6}$ GPa) and thickness (1 mm). This is done so the shells do not contribute to the structure's stiffness and are used only to apply the aerodynamic loads. The design domain (solid elements) uses isotropic material with a Young's modulus of 10 GPa (corresponding approximately to the longitudinal modulus of a 50% unidirectional and 50% $\pm 45^\circ$ polymer matrix/glass composite) and a Poisson's ratio of 0.3. Shell elements have no mass whereas the solid element density was adjusted to yield a total blade mass of 35,000 kg to respect the blade design proposed in chapter 6. This allows direct modeling of gravitational and centrifugal forces using gravity and a rotational force in the FE model.

7.4.2 Model Loading

The blade was clamped at its root contour and a rigid body element was created at the 35-m chord station to apply loads equivalent to those applied by the outboard blade section (35m to tip). All nodes on the 35-m chord station were connected to a master node (with all degrees of freedom constrained) to which equivalent shear forces, bending moments and normal force were applied to simulate the aerodynamic, gravitational and inertial loads of the outboard section of the blade. Table 7.1 summarizes the applied loads, which were simply extracted from load cases calculated in chapter 6.

Table 7.1: Equivalent 35-m chord station shear forces, bending moments and normal force applied to simulate the aerodynamic, gravitational and inertial loads generated by the outboard section of the blade.

Design load case	Flapwise		Edgewise		Lengthwise
	Bending moment [$\times 10^5$ Nm]	Shear force [$\times 10^5$ N]	Bending moment [$\times 10^5$ Nm]	Shear force [$\times 10^4$ Nm]	Normal force [$\times 10^4$ N]
#1	99.93	4.741	14.33	7.536	66.36
#2	94.86	4.637	15.21	3.617	66.36
#3	94.30	5.733	1.440	3.160	-
#4	64.68	3.968	45.98	28.34	-

Aerodynamic loads were applied to the FE model in accordance with the blade element momentum theory presented in chapter 5. Using a Matlab routine, the computed aerodynamic loads were then linked to the connectivity tables (position of nodes and connectivity of elements) of the FE model to apply the proper pressure to each shell element of the upper and lower surfaces of the blade. It is worth noting that for a given radial position, the pressure was simplified to a constant linear pressure distribution over the chord length.

7.4.3 Optimization variables, objective function and constraints

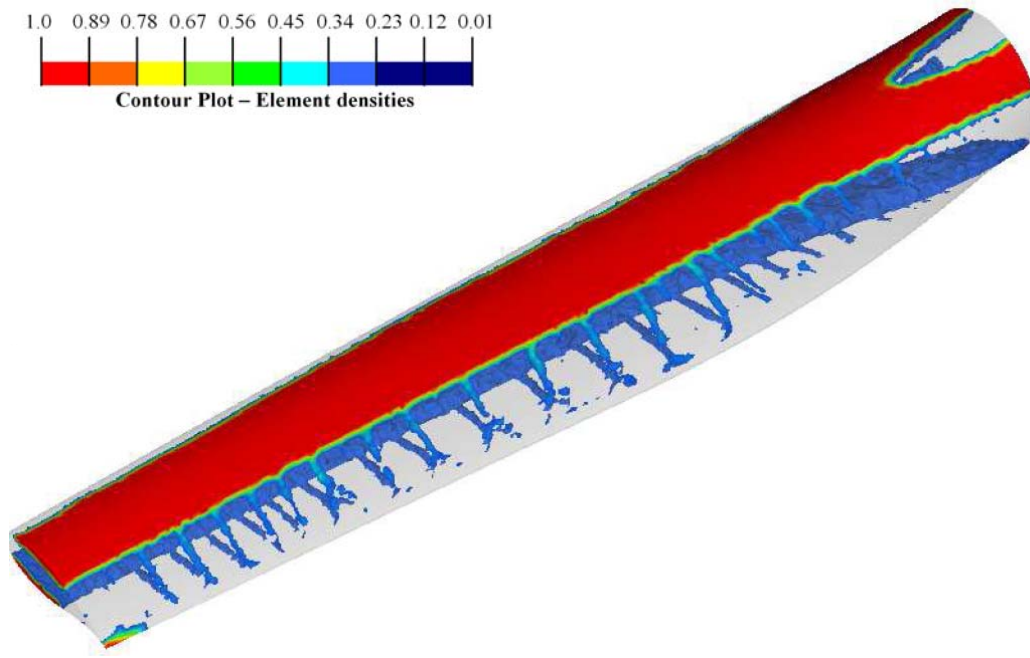
To perform the optimization, the same types of response variables were again used: the compliance of the structure and the volume fraction of the design domain. The objective function was set as specified in Equation 7.3 in which all four critical load cases identified in chapter 6 were applied using the method described in the previous section.

As opposed to the short-blade-section model presented earlier, a symmetry plane was not forced on the model, leaving the optimization routine totally free of constraints (apart from the volume fraction constraint of Equation 7.3).

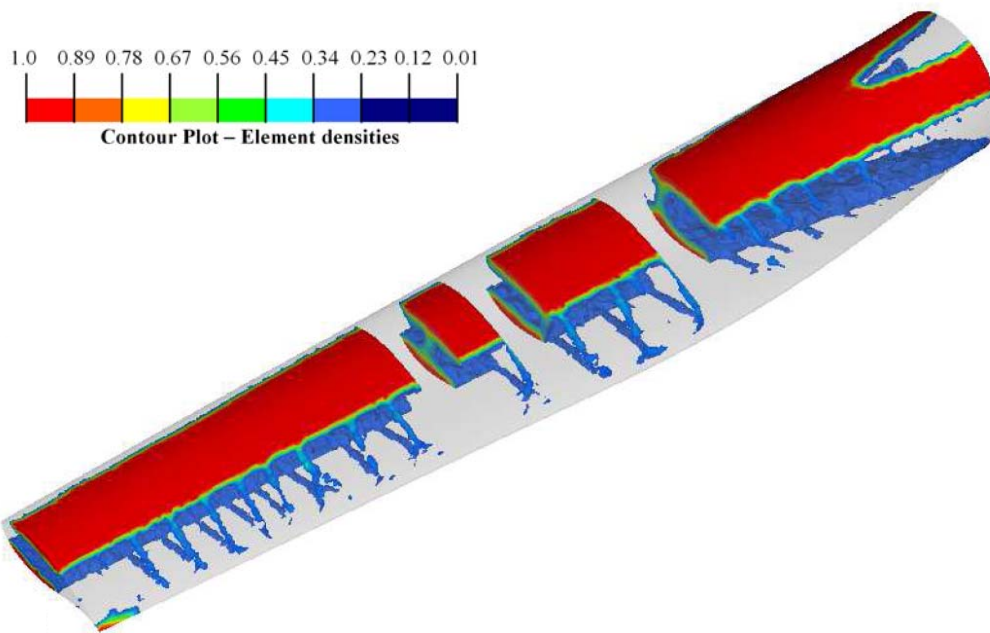
7.4.4 Results

The results of the optimization problem are shown in Figure 7.11 as a contour plot of the element densities at the last iteration. As with the previous figures, high-density regions show places where material is needed and low density regions show places where material is less necessary. As expected, it can be seen clearly in Figure 7.11a that a structure with two spar caps emerges to support the load, which is predominantly in the out-of-plane direction. These spar caps are situated in the thickest part of each cross section to maximize sectional inertia.

The location of the shear webs is a bit harder to interpret. As can be seen in Figure 7.11b, in some sections, a single web is situated at 1/3 of the chord length (typical for small and medium-sized blades) while for other sections, webs are visible at about 15 or 50% of the chord length (typical of large blades) [2-4, 20]. However, a clear closed spar structure could not be identified.



a)



b)

Figure 7.11: Half-blade topology optimization results shown as contour plot of the element densities (design domain elements) - only elements with a density higher than 0.1 are shown. (a) Full model, (b) Full model with sectional cuts to show the presence of webs.

Also visible in Figures 7.11a and 7.11b, at the root of the blade, it can be noticed that each spar cap splits in two sections. The blade is thus attached at its root by means of four symmetrically arranged members. This topology offers a higher edgewise section modulus than if the two spar caps simply continued until they reached the root. This root attachment gives approximately the same section modulus in the edge-wise direction as in the flapwise direction.

Another interesting structural element seen in Figure 7.11 is the distinctive presence of ribs in the trailing edge section. A distance of 1 to 2 meters separates these ribs, of which the density varies from about 0.1 to 0.3. Although their density might be considered low, they appear in a region of near-zero density and help support the pressure loads applied in the trailing edge region to reduce the distortion of aerodynamic profiles.

7.5 Conclusions

In this chapter, the first two steps of a three-step preliminary design development strategy based on topology and size optimization techniques were completed (see Figure 7.3). In step 1, to keep computational time short, topology optimization was performed on a small airfoil-shaped blade section. With this model, the study of all individual load cases identified in chapter 6 as critical was made possible. Also, when subjected to all load cases, an optimized blade section structural topology was determined (see Figure 7.9c). In step 2, to reduce the adverse effect of having boundary conditions prone to structural growth and also to study the root transition area of the blade, a half-blade was modeled. The optimized structure subjected to all critical load cases is presented in Figure 7.11. For both studies, because of the presence of the heavily reinforced upper and lower surfaces and the vertical connecting members (webs) observed in the designs, it can be concluded that the structural topologies obtained are similar overall to the structural topologies in use today for MW-size wind turbine blades. However, ribs were obtained in both steps 1 and 2, which are never present in today's designs.

Based on these results, the third step of the optimization process to be presented in the next chapter will focus on refining the rough design solution established in this chapter. For this third and last step of the preliminary design process, the structural topology identified in steps 1 and 2 will be transposed to a generic shell element model on which size optimization (thickness and ply orientation) will be performed. To serve

as guidelines to build this shell model, the following two sections will conclude on some of the important design features found in this chapter. Encompassing all these design features, the generic shell element model built will give the designer the possibility of validating or invalidating the usefulness of the each of these design features.

7.5.1 Spar cap and webs

When subjected to all load cases, both FE element models studied in this chapter yielded spar caps (upper and lower surface) extending from approximately 15% to 50% of the chord length. In the root transition area, both spar caps separated into two to form four members symmetrically arranged around the root circumference and giving approximately the same section modulus in the edge-wise and flapwise directions.

Concerning webs, as can be seen in Figure 7.11b, in chord stations closer to the tip, a single web positioned at 1/3 of the chord length seems to be the ideal configuration. On the other hand, near the root transition area, because edgewise bending moments become significant with respect to flapwise bending moments, the single web configuration observed further down the blade span is left aside for a two-web configuration closing both ends of the spar caps (15 or 50% of the chord length). However, the exact position at which the transition from single to double shear web occurs could not be clearly identified.

7.5.2 Presence of ribs

As seen in Figure 7.11, the topology-optimized structure subjected to all critical load cases shows the distinctive presence of ribs in the trailing-edge section. These ribs, separated by a distance of 1 to 2m, significantly contribute to reducing the overall compliance of the structure; otherwise they would not be visible in the contour plot of the element densities. Structural growth thus shows that ribs are preferred over simply thickening the skins when trying to minimize the compliance of the structure. When compared to today's blade constructions, this design feature can be considered unusual since sandwich constructions rather than ribs are generally used to impart the desired stiffness to the leading and trailing edge sections.

7.6 References

- [1] Griffin, D.A.. *Alternative materials, manufacturing processes and structural designs for large wind turbine blade*, 40th AIAA Aerospace Sciences Meeting and Exhibit, AIAA, Washington, DC, 2002, pp. 27-39.
- [2] Malcolm, D.J., Hansen A.C.. *WindPACT Turbine Rotor Design Study*. NREL/SR-500-32495. National Renewable Energy Laboratory. Golden, CO, 2002.
- [3] Griffin, D. A., *Blade system design studies volume 1 : composite technologies for large wind turbine blades*. SAND2002-1879. Sandia National Laboratories, Albuquerque, NM, 2002.
- [4] Griffin, D.A., *WindPACT Turbine Design Scaling study technical area 1 – Composite blades for 80 to 120 meter rotor*. NREL/SR-500-29492. National Renewable Energy Laboratory. Golden, CO, 2001.
- [5] Brondsted, P., Lilholt, H., Aage, L. *Composite Materials for Wind Power Turbine Blades*, Annual review of Materials Research, 2005, 35:505-538.
- [6] Hillmer, B., Borstelmann, T., Schaffarczyk, P.A., Dannenberg, L., Aerodynamic and Structural Design of MultiMW Wind Turbine Blades beyond 5MW, Journal of Physics: Conference Series, The Science of Making Torque from Wind, (75), 2007
- [7] Michell, A. G. M., *The limit of economy of material in frame structures*, Philosophical Magazine, 8(6), 1904, pp. 589-597.
- [8] Rozvani, G.I.N., *Aims, scope, methods, history and unified terminology of computer-aided topology optimization in structural mechanics*, Structural and Multidisciplinary Optimization, Vol. 21, 2001, pp. 90–108.
- [9] Kincinger, R., Arciszewski, T., De Jong, K., *Evolutionary computation and structural design: A survey of the state-of-the-art*, Computers and Structures, Vol. 3, 2005, pp. 1943-1978.
- [10] Kim, H., Querin, O.M., Steven, G.P., *On the development of structural optimization and its relevance in engineering design*, Design Studies, Vol 23 No. 1 January 2002, pp. 85-102.
- [11] Fuchs., H. P., *The optimal structural design of a composite automotive front structure*, proceedings of the 8th Symposium on Multidisciplinary Analysis and Optimization, AIAA 2000-4708, Long Beach, California, 2000.
- [12] Chen, C., J., Young, C., *Integrate Topology/Shape/Size Optimization into Upfront Automotive Component Design*, 10th AIAA/ISSMO Multidisciplinary Analysis and Optimization Conference, AIAA-2004-4594, Albany, New York, 2004.

- [13] Krog, L., Tucker, A., Kemp, M., Boyd, R. *Topology optimization of aircraft wing box ribs*, proceedings of the 10th AIAA/ISSMO Multidisciplinary Analysis and Optimization Conference, AIAA 2004-4481, Albany, New-York, 2004.
- [14] Amorosi, S., *Application of topology, size and shape optimization on the 787 wing leading edge structure*, proceedings of the Hyperworks Technology Conference (HTC), Troy, Michigan, September, 2006
- [15] Bendsøe, M. and Sigmund, O., *Topology Optimization: Theory, Methods and Applications*, Springer-Verlag, Berlin, Heidelberg (Germany), 2003.
- [16] Zhou, M., Pagaldipti, N., Thomas, H., and Shyy, Y., *An Integrated Approach to Topology, Sizing and Shape Optimization*, Structural and Multidisciplinary Optimization, Vol. 26, 2004, pp. 308–317.
- [17] Thomas, H., Zhou, M., and Schramm, U., *Issues of Commercial Optimization Software Development*, Structural and Multidisciplinary Optimization, Vol. 23, 2002, pp. 97–110.
- [18] *Optistruct User Manual*, Altair Engineering, inc., Troy (United States), 1999.
- [19] de Ruiter, M. J., *Topology Optimization Using a Topology Description Function Approach*, Ph.D. thesis, Delft University of Technology, Delft (The Netherlands), 2005.
- [20] Berggreen, C., Branner, K., Jensen, J. F., and Schultz, J. P., *Application and Analysis of Sandwich Elements in the Primary Structure of Large Wind Turbine Blades*, Journal of Sandwich Structures and Materials, Vol. 9, 2007, pp. 525–55.

CHAPTER 8

PRELIMINARY DESIGN OF LARGE THERMOPLASTIC COMPOSITE BLADES *STRUCTURAL ELEMENT SIZING OPTIMIZATION*

Based on the general structural topology determined in the previous chapter, this chapter presents the results of different composite sizing optimization studies performed on six distinct blade structural designs. While being constrained on stress, tip deflection and buckling, blade section thicknesses and fiber orientations were found to minimize the different design blade masses. Based on a comparison study with conventional epoxy-based blade designs, results are analyzed and a final thermoplastic composite blade design is proposed.

8.1 Introduction

In chapter 7, although topology optimization results roughly revealed what could be an ideal blade structural design, many questions remain unanswered. Since the models used were purely isotropic and simply minimized blade compliance, no details could be obtained concerning laminate lay-up. While ribs appeared in the structure, their necessity was not validated in a more realistic modeling context including buckling and strength criteria. Furthermore, shear web number and position could not be identified clearly from topology optimization results alone. The goal of this chapter is to address these unresolved issues and ultimately to propose a final TPC-oriented wind turbine blade design. This will be achieved upon completing step 3 of the optimization process presented in Figure 7.3.

Based on a generic blade FE model, shell thicknesses, laminate lay-ups and ply orientations will be determined for blades designed for minimum weight under tip deflection, stress and buckling constraints. To set up this material sizing optimization problem, the first section of this chapter will present the generic blade FE model used for all sizing optimization studies performed in this chapter, discuss blade loading and explains the objective function and constraints formulated to guide the optimization

process. Epoxy-based and TPC-based blade designs will then be optimized and compared which will lead to a final TPC blade design to be proposed.

8.2 Blade model and formulation of the optimization problem

8.2.1 Generic shell element model

Guided by the results obtained from the topology optimization study, a generic shell element model with three webs situated at 15%, 33% and 50% of the chord length was built in Altair's Hypermesh® environment (see Figure 8.1b). To simulate different web configurations, the model offers the possibilities of removing the central web to analyze a blade with two shear webs positioned at 15% and 50% of the chord length or of removing the leading and trailing edge webs to analyze a model with only one shear web positioned at 33% of the chord length. Also based on the results obtained in chapter 7, ribs were placed at intervals of one meter. Again, it is also possible to remove some ribs from the finite element model in order to compare different combinations of rib number and spacing.

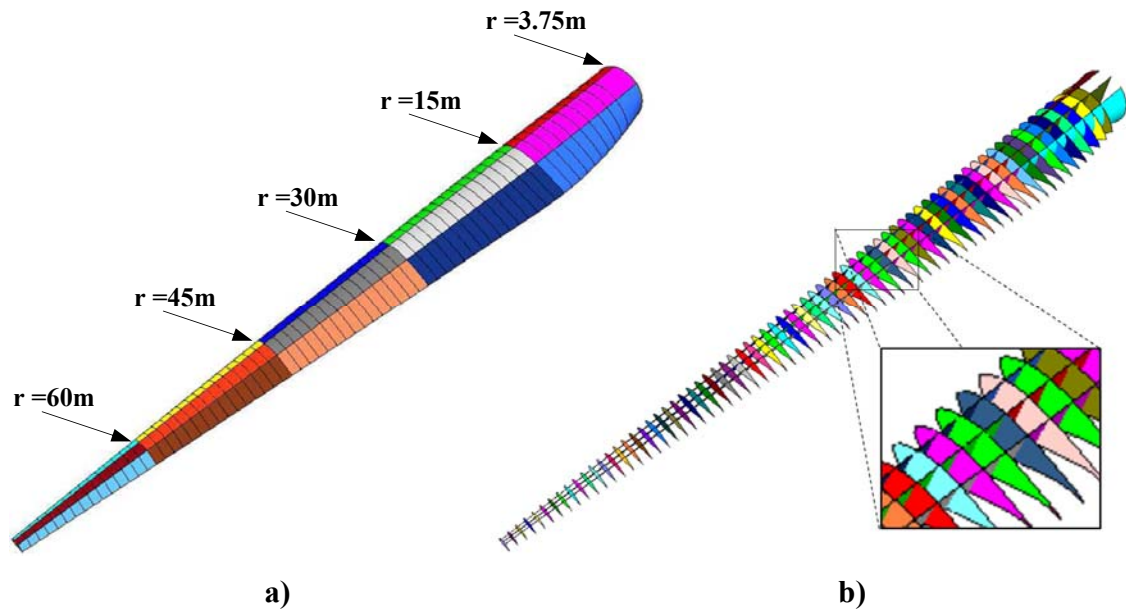


Figure 8.1: Generic shell finite element model of the blade. (a) External shape; (b) Inner structure.

To keep computational time within acceptable limits, only three different rib configurations (0 rib, 35 ribs and 70 ribs) were investigated. Since the goal is to

determine whether or not ribs are useful, using these three distinct rib configurations is believed sufficient to draw conclusions.

8.2.2 *Model loading and material property description*

In chapter 6, four critical load cases were identified. Since full blade length is now modeled, blade loads can simply be obtained from these load cases. With the blade fixed at its root contour, aerodynamic loads were applied individually to the FE model in accordance with Figures 6.5, 6.6, 6.7 and 6.8 to create four separate load cases. As was done in chapter 7 using a Matlab routine, the aerodynamic loads were linked to the connectivity tables (position of nodes and connectivity of elements) of the FE model by applying the proper pressure to each shell element of the upper and lower surfaces of the blade. It is worth noting that for a given blade radial position, aerodynamic loads were modeled using a constant linear pressure distributed across chord length. To simulate gravitational and inertial loads, gravity and the corresponding rotational forces were simply applied to the FE model for each load case.

Concerning materials, the blade geometry described in the previous section was separated into several areas for which specific laminate descriptions can be assigned (different colors in Figures 8.1a and 8.1b). The upper and lower surfaces of the blade are each composed of five leading edge sections, five spar cap sections and five trailing edge sections. The leading edge web, middle web and trailing edge web were likewise described in five lengthwise sections. Finally, with 70 ribs included in the structure, a maximum of 115 different sections can be found along the blade length (for a blade configuration with three webs and 70 ribs).

For every section, a composite shell laminate made from a 0° unidirectional layer (0° being the blade's longitudinal direction), a $\pm 45^\circ$ biaxial layer and a layer of core material can be defined. For ribs, an extra 90° layer can be added to the laminate. The options used to solve the composite laminate properties in Optistruct® (Altair's linear solver) were set to homogenize the properties of the composite layers, which allows the overall laminate properties to be independent of the stacking sequence (smear option). Once determined with the optimization technique described in the next section, at a later detailed design phase, the thickness of the different layers can be used to evaluate the number of plies needed at each section if the thickness of each individual ply is known.

For all blade models studied later in this chapter, material strength values were divided by a safety factor of 1.82, the most severe material safety factor according to the IEC 61400-1 standard, to take into account the inherent variability of material strength.

8.2.3 Design variables, objective function and constraints

The optimization problem is formulated as a composite material sizing optimization problem. The design variables in this optimization problem are the thicknesses of the composite shell element layers of the different blade sections just discussed. The lower and upper thickness boundaries of these layers are set respectively to a near zero value (1×10^{-3} mm) and to 100 mm. Depending on the blade configuration studied (number of webs and ribs), the number of design variables can vary from 105 to 400 as shown in Table 8.1. For example, a blade using two webs and 35 ribs contains 30 skin sections each having three layers (0° , $\pm 45^\circ$ and core), 10 web sections also having three layers, and 35 ribs each having four layers (0° , $\pm 45^\circ$, 90° and core). This yields 90 design variables for the skins, 30 design variables for the webs and 140 design variables for the ribs (260 in total).

Table 8.1: Number of elements and design variables for the different blade model studied.

Models	Number of nodes	Number of elements (n_e)	Number of design variables (n)
2 webs, 0 rib	48 196	49 486	120
2 webs, 35 ribs	52 308	55 227	260
2 webs, 70 ribs	56 463	61 070	400
1 web, 0 rib	43 409	44 028	105
1 web, 35 ribs	47 769	49 769	245
1 web, 70 ribs	52 185	55 612	385

As formulated in Equation 8.1, to find the thickness of each layer (x_i) of each blade section (equal to the number of design variables (n) shown in Table 8.1), the objective function is set to minimize blade mass (m) while being constrained by three fundamental blade design criteria. The composite failure index (F) must stay below a value of 1.0 in every element (e) when subjected to j individual load cases ($n_j = 4$ in our case). The blade tip deflection (δ) is limited to 10 m (13% of blade length) and the buckling factor (λ) of the first k buckling mode ($n_k = 5$ in our case) must also stay below 1.0 (no buckling allowed) when subjected to the same j individual load cases.

Objective function:

$$\min_x m$$

Constraints: (8.1)

$$\begin{aligned} \delta_j &\leq 10.0m, & j &= 1, \dots, n_j \\ \lambda_{jk} &\leq 1.0, & j &= 1, \dots, n_j, \quad k = 1, \dots, n_k \\ F_{je} &\leq 1.0, & j &= 1, \dots, n_j, \quad e = 1, \dots, n_e \\ 0.001 &\leq x_i \leq 100mm & i &= 1, \dots, n \end{aligned}$$

To find a solution to Equation 8.1, the objective function is evaluated through an iterative process. This is performed with Altair's Optistruct® solver, which uses a gradient-based optimization approach first to evaluate the different responses for all four individual load cases with a set of user-specified design variables (first guess) [1-3]. Since cross-section material thicknesses were evaluated in chapter 6 in order to estimate the blade natural frequencies (see Table 6.4), these values were averaged over the blade sections described earlier to serve as the set of variables used to run the first iteration (see Table 8.2). To complete the data set, an initial-guess layer thickness of 3mm (1mm of 0°, 1mm of ±45° and 1mm of 90°) was used for the rib skins and 10mm was used for all core layers.

Table 8.2: Layer thicknesses used as the first-guess data set - Extrapolated from stress-based analytically found blade cross-section properties when subjected to a 50-year extreme gust load case.

Blade section (m)	Spar caps			Webs			Leading and trailing edge skins		
	UD (mm)	Biaxial (mm)	Total (mm)	UD (mm)	Biaxial (mm)	Total (mm)	UD (mm)	Biaxial (mm)	Total (mm)
3.75-15	64.68	27.72	92.40	5.30	5.30	10.60	8.35	8.35	16.70
15-30	38.92	16.68	55.60	5.30	5.30	10.60	8.35	8.35	16.70
30-45	31.08	13.32	44.40	4.20	4.20	8.40	6.65	6.65	13.30
45-60	22.96	9.84	32.80	3.10	3.10	6.20	4.90	4.90	9.80
60-75	10.43	4.47	14.90	2.65	2.65	5.30	2.65	2.65	5.30

After the first iteration, based on the different responses, the solver then performs a convergence test to see if the set of design variables satisfies the convergence criteria. In this case, convergence is achieved if the change in the objective function is less than the objective tolerance (0.5%) and if constraint violations are less than 1%.

If convergence is not obtained, sensitivity analysis is then performed to select a new set of design variables for a second iteration. Since the composite failure index constraint considers the response of all blade elements, performing sensitivity analysis on each of them is computationally prohibitive. The Optistruct® solver therefore uses constraint screening to retain responses that capture the essence of the original design problem while keeping the optimization problem at an acceptable size. Since not performing a sensitivity analysis on elements far from violating the constraint does not affect the direction of the optimization problem, they can be removed from the sensitivity analysis for the on-going design iteration. The settings used in Optistruct® considered only the 20 most critical constraints that came within 50% of their bound value (on the satisfactory side) for each response type, for each section and for each load case.

Based on the results of this targeted sensitivity analysis, a new set of design variables is chosen, the FE model is reanalyzed, the different responses are again calculated and a new convergence test is performed. This iteration process is continued until convergence is achieved or until a maximum number of iteration is reached (80 in this case).

8.3 Baseline epoxy/glass wind turbine blades

For later benchmarking of thermoplastic-based composite wind turbine blade designs against conventional epoxy-based composite blade designs, a glass/epoxy composite blade was first designed using the optimization process just described. This allowed a fair blade design comparison based solely on material properties and structural topology, which would have not been possible if TPC blades had been compared to epoxy-based blade designs found in the literature.

Since ribs are never used in epoxy-based wind turbine blade designs, they were removed from the FE model presented in Figure 8.1b. Because TPC blades using one shear web and two shear webs will be studied later in this chapter, epoxy-based blades using identical web configurations were designed. An FE model with the leading-edge and trailing-edge webs removed was thus used to set the structural characteristics of a single-shear web design while an FE model with the middle shear web removed was used for the double-shear web design.

8.3.1 Material properties

As mentioned in section 8.2.2, the composite shell elements are composed of a 0° layer, a $\pm 45^\circ$ layer, a 90° layer (only for ribs) and a core material layer. The basic properties of these layers are described in Table 8.3. Unidirectional composite properties were obtained from the OPTIDAT material database [4-5] while biaxial properties are those presented in chapter 4 (see Figure 4.6). Since ply orientation is user-defined when describing an element, experimental $\pm 45^\circ$ and 90° material properties are not necessary. Biaxial and unidirectional properties can be used respectively with rotated of 45° and 90° . For core material properties, typical medium density closed-cell core material properties were used [6]. As stated earlier, when inputted in the FE models, the material strength values shown in Table 8.3 were divided by a safety factor of 1.82 to comply with the IEC 61400-1 standard.

Table 8.3: Properties of Epoxy/Glass fibre composites and core material.

			Laminate		Core material
Material properties			Unidirectional	Biaxial ($0/90^\circ$)	
Density	ρ	kg/m ³	1880	1820	100
Longitudinal elastic modulus	E_1	GPa	39.20	27.05	125×10^{-3}
Transverse elastic modulus	E_2	GPa	14.50	27.05	125×10^{-3}
In-plane shear modulus	G_{12}	GPa	4.83	3.48	47.25×10^{-3}
Longitudinal tensile strength	S_1^T	MPa	830.00	476.00	
Transverse tensile strength	S_2^T	MPa	53.90	476.00	
Longitudinal compressive strength	S_1^C	MPa	523.00	392.00	
Transverse compressive strength	S_2^C	MPa	165.00	392.00	
In-plane shear strength	S_{12}	MPa	78.10	93.15	

8.3.2 Design solutions based on stiffness and strength

To exclude the influence of buckling on the final design, a first study using only the composite failure index and tip deflection constraints was conducted. To simplify further this first study and also because core material is used mainly to increase panel stability subjected to compressive loads (buckling), core thickness was set to zero in all sections.

The mass for each optimized design when solved with Equation 8.1 (excluding the buckling constraint) is presented in Table 8.4. For the two-blade model studied, the

critical optimization constraint was found to be the tip deflection of load case 3. The table also indicates that the blade with one shear web is slightly lighter.

Table 8.4: Masses of optimized epoxy-based blade designs with associated critical constraints – The objective function was subjected only to stiffness and strength constraints.

Model	Mass (kg)	Critical constraints	Max constraint viol. (%)
1 web	29 996	Tip def. (3), failure index (11 elements)	0.003
2 web	30 512	Tip def. (3), failure index (14 elements)	0.098

Table 8.5: Element total thickness and 0° fiber fraction for blade sections extending from 3.75 to 45m – Optimized epoxy-based one-web and two-web blade designs subjected to stiffness and strength constraints.

Blade section	Chord station of the 2 web blade design			Chord station of the 1 web blade design		
	3.75-15m	15-30m	30-45m	3.75-15m	15-30m	30-45m
Upper surface leading edge skin	4.5 mm 62.9%	4.4 mm 62.0%	5.6 mm 59.9%	5.0 mm 77.3%	4.4 mm 76.6%	4.6 mm 73.2%
Upper surface spar cap	62.4 mm 95.9%	67.7 mm 97.6%	80.6 mm 97.6%	53.6 mm 95.1 %	65.9 mm 97.7%	81.8 mm 97.8%
Upper surface trailing edge skin	9.5 mm 87.3%	7.9 mm 87.7%	6.9 mm 79.9%	8.6 mm 86.4%	8.2 mm 87.6%	5.7 mm 81.8%
Lower surface leading edge skin	9.0 mm 79.9%	4.0 mm 59.3%	4.7 mm 55.3%	15.2 mm 87.4%	4.2 mm 56.1%	5.3 mm 57.9%
Lower surface spar cap	51.0 mm 96.2%	70.5 mm 97.6%	81.5 mm 97.7%	51.0 mm 94.7%	69.9 mm 97.6%	83.4 mm 97.5%
Lower surface trailing edge skin	3.3 mm 76.9%	3.3 mm 70.0%	3.8 mm 78.3%	3.9 mm 77.8%	3.5 mm 74.1%	3.9 mm 78.9%
Trailing edge web	11.0 mm 66.2%	8.5 mm 79.9%	4.1 mm 57.3%	-	-	-
Leading edge web	14.0 mm 76.7%	7.3 mm 89.3%	4.4 mm 60.0%	-	-	-
Middle (single) web	-	-	-	18.3 mm 76.9%	17.2 mm 95.4%	6.7 mm 73.5%

To view panel thicknesses and laminate properties in the different sections of the blades, Table 8.5 shows the shell thicknesses and fraction of the unidirectional fiber layer present in the different sections of the blade extending from 3.75m to 45m. As with commercial blades, the objective function yielded spar cap sections composed mainly of 0° material that are significantly thicker than other sections of the blade. Skins and webs are relatively thin compared to the spar caps and use less UD material, which is also typical of current blade designs. The fraction of 0° fibers in the spar caps is around 95% to support the load that is predominantly bending. This value is a bit high compared to those found in the literature (70-80% is typical). This can be explained by

the fact that cross-plyies are generally used to control torsional dynamic effects, which were not taken into account in chapter 6 [6-8].

For both designs it can be seen that the thickness of the webs and the thickness of most aerodynamic skins has a tendency to decrease from root to tip, which is normal for constant cross-section cantilevered structures loaded mainly in bending. In contrast, the spar cap thickness increases from the root to the 45-m chord station. This can be explained by the fact that the blade section moment of inertia decreases rapidly from root to the 45m chord station forcing extra material to be needed to respect the constraints even if the bending moment diminishes rapidly when moving away from the root. Finally, as shown in Figure 8.2, excluding buckling from the set of constraints and not using core material yields blade designs that lack panel stiffness in the trailing edge sections. In both cases, aerodynamic profile distortion reaches a point at which blade performance would be drastically affected.

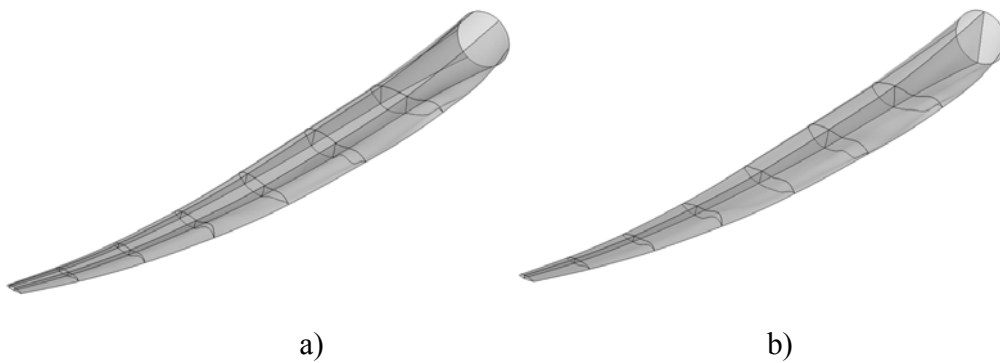


Figure 8.2: Shape of deformed aerodynamic profiles (for load case 3) of the epoxy-based blades designed for strength and stiffness. a) Two-web design. b) One-web design.

8.3.3 Design solutions based on stiffness, strength and buckling

To design blades that are more representative of today's blade construction, new optimization runs were performed using core material while being constrained by the composite failure index (strength), the tip deflection (stiffness) and the buckling factor as specified in Equation 8.1. The mass of each optimized blade design is presented in Table 8.6. For both web configurations studied, the critical optimization constraint was again the tip deflection for load case 3. Although the difference could be considered marginal, Table 8.6 also indicates that the lightest blade this time had two shear webs.

It is noted with interest that blade mass correlates relatively well with the current trend in the evolution of blade mass with respect to blade length. From Figure 1.8, based on commercial data, a blade 75m long should have a mass of about 32,900kg. Given that the preliminary designs suggested here do not include root studs, gel coat, adhesive joints and other important blade elements, it seems reasonable to say that the proposed designs represent relatively well the current design trends discussed in chapter 6.

Table 8.6: Masses of optimized epoxy-based blade designs with associated critical constraints – The objective function is subjected to stiffness, strength and buckling constraints.

Model	Mass (kg)	Critical constraints	Max constraint viol. (%)
1 web	30 756	Tip def. (3), failure index (41 el.), buck. (3,4)	0.024
2 web	30 070	Tip def. (3), failure index (26 el.), buck. (3)	0.208

Element thicknesses, 0° layer proportions and core thicknesses are presented in Table 8.7 for chord stations extending from 3.75m to 45m. For element thicknesses, the conclusions drawn based on the previous blade models are still applicable in the case of these two new designs: 1- thick spar caps take the majority of the load and are primarily composed of 0° fibers, 2- skin and web thicknesses have a tendency to taper off towards the tip.

When looking at core thickness distribution, it is interesting to see that core thickness is significantly greater in sections subjected to compressive loading. In fact, the core of the upper surface trailing edge section can be up to five times thicker than the lower surface trailing edge section. The comparison of the upper and lower spar cap sections close to the root shows a similar trend.

Another interesting phenomenon to observe is the reduction of most skin surface thicknesses in comparison with the previously shown designs. The introduction of core thus not only improves stability but can also help increase overall blade stiffness and reduce local stress. In addition, in buckling-prone sections such as the upper trailing edge section and trailing edge web section, a significant drop in 0° layer proportion is noted in comparison with the previous design. This has the effect of reducing local panel stiffness and thus reducing vulnerability to buckling.

Table 8.7: Element total thickness, 0° fiber fraction and core thickness for blade sections extending from 3.75 to 45m – Optimized epoxy-based one-web and two-web blade designs subjected to stiffness, strength and buckling constraints.

Blade section	Chord station of the 2 web blade design			Chord station of the 1 web blade design		
	3.75-15m	15-30m	30-45m	3.75-15m	15-30m	30-45m
Upper surface leading edge skin	5.2 mm	2.8 mm	2.4 mm	8.0 mm	6.6 mm	4.0 mm
	82.9%	68.7%	58.7%	81.0%	69.4%	57.3%
	10.3 mm	6.6 mm	6.1 mm	19.4 mm	18.0 mm	7.9 mm
Upper surface spar cap	61.6 mm	73.7 mm	83.5 mm	58.7 mm	73.2 mm	82.3 mm
	96.9%	98.0%	97.7%	94.7%	96.1%	97.3%
	27.4 mm	7.6 mm	5.6 mm	20.6 mm	15.8 mm	7.4 mm
Upper surface trailing edge skin	5.1 mm	4.1 mm	2.6 mm	9.2 mm	4.2 mm	3.1 mm
	73.1%	66.4%	49.6%	67.4%	51.9%	63.6%
	47.7 mm	48.5 mm	23.9 mm	56.0 mm	62.7 mm	25.5 mm
Lower surface leading edge skin	12.9 mm	5.2 mm	3.5 mm	17.7 mm	6.8 mm	4.4 mm
	91.3%	76.0%	68.1%	87.4%	68.3%	59.6%
	9.6 mm	8.7 mm	6.1 mm	37.3 mm	19.8 mm	7.7 mm
Lower surface spar cap	47.6 mm	69.7 mm	82.9 mm	46.8 mm	67.3 mm	80.7 mm
	96.2%	97.4%	97.0%	95.0%	96.9%	97.3%
	10.1 mm	5.4 mm	5.0 mm	18.0 mm	9.7 mm	7.1 mm
Lower surface trailing edge skin	2.7 mm	2.1 mm	2.5 mm	5.2 mm	2.4 mm	2.2 mm
	74.9%	73.5%	62.3%	71.3%	68.8%	61.5%
	12.2 mm	11.0 mm	7.6 mm	11.4 mm	16.0 mm	10.5 mm
Trailing edge web	7.1 mm	6.0 mm	3.4 mm	-	-	-
	58.0%	37.9%	49.6%	-	-	-
	18.5 mm	19.6 mm	7.2 mm	-	-	-
Leading edge web	11.3 mm	8.3 mm	2.0 mm	-	-	-
	72.0%	92.7%	54.9%	-	-	-
	7.9 mm	7.8 mm	7.0 mm	-	-	-
Middle (single) web	-	-	-	15.3 mm	18.3 mm	4.6 mm
	-	-	-	66.2%	92.7%	57.3%
	-	-	-	20.7 mm	4.7 mm	8.5 mm

Finally, Figure 8.3 shows the blade aerodynamic profile of the two designs when subjected to load case 3. It is obvious from comparison with Figure 8.2 that including the buckling constraint in the optimization process drastically reduces distortion.

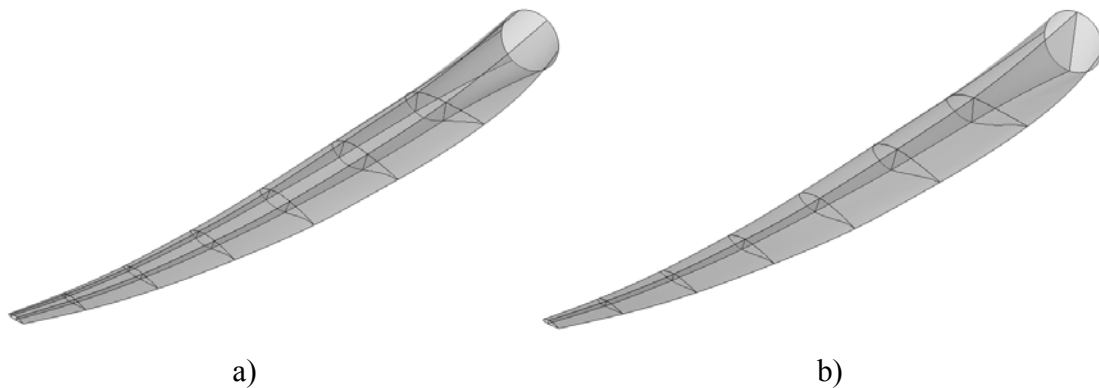


Figure 8.3: Shape of deformed aerodynamic profiles (for load case 3) of the epoxy-based blades designed with respect to strength, stiffness and buckling. a) Two-web design. b) One-web design.

8.4 Polyamide-6/glass composites wind turbine blades

Using the generic blade model described in section 8.2.1, different rib/web combinations can be investigated to further refine the structural topology discovered in chapter 7. In order to compare the performance of polyamide-6/glass (PA-6/glass) composite blades to epoxy-based composite blades based solely on material properties, PA-6/glass blades with no ribs were first dimensioned. Finally, to investigate the effect of ribs on blade structural response, blades with rib spacing of 1m and 2m were tested (see Table 8.1 for the list of models). As with the two epoxy-based designs just presented, a study excluding the buckling constraint and core material was first conducted.

8.4.1 Material properties

Basic biaxial PA-6 composite material properties were obtained from chapter 4 (see Figure 4.6). As with the epoxy-based biaxial properties earlier presented, dry-as-molded properties were retained and are summarized in Table 8.8. In the case of unidirectional composite properties, since this type of composite was not tested experimentally in chapter 4, typical unidirectional PA-6/glass composite properties were obtained from the literature [9]. As mentioned earlier, experimental $\pm 45^\circ$ and 90° ply properties are not necessary since these laminates are simply biaxial and unidirectional laminates rotated respectively of 45° and 90° .

Table 8.8: Properties of PA-6/glass fibre composites and core material.

			Laminate		Core material
Material properties			Unidirectional	Biaxial (0/90°)	
Density	ρ	kg/m ³	1770	1800	100
Longitudinal elastic modulus	E_1	GPa	38.00	26.00	125x10 ⁻³
Transverse elastic modulus	E_2	GPa	8.24	26.00	125x10 ⁻³
In-plane shear modulus	G_{12}	GPa	1.80	4.10	47.25x10 ⁻³
Longitudinal tensile strength	S_1^T	MPa	869.00	495.00	
Transverse tensile strength	S_2^T	MPa	32.00	495.00	
Longitudinal compressive strength	S_1^C	MPa	634.00	473.00	
Transverse compressive strength	S_2^C	MPa	72.90	473.00	
In-plane shear strength	S_{12}	MPa	65.50	127.00	

As seen in Table 8.8 when compared to Table 8.3, the same medium-density closed-cell core as for the epoxy-based blades was used. Finally, as it was done with the epoxy-based material properties, the material strength values inputted in the FE models were all divided by a safety factor of 1.82 to comply with the IEC 61400-1 standard.

8.4.2 Design solutions based on stiffness and strength

To compare the PA-6-based blade designs with the epoxy-based blades just presented, a first study using only the composite failure index and the tip deflection constraints was conducted. As for the previous epoxy-based blades, core thicknesses were set to zero in all sections.

The optimized masses for each blade design are presented in Table 8.9. For all blade models, the critical optimization constraint was again the tip deflection for load case 3. The table also indicates that the blade with the lightest topology has one shear web and 70 ribs. Comparing blade designs not using ribs, only a few hundred kilos distinguish the epoxy-based and PA-6-based blades.

Also noticeable in Table 8.9 is the fact that for both the single and double web designs, blade designs using ribs can be significantly lighter (up to 8.5% lighter). This suggests that the added weight due to the presence of ribs can be more than compensated by a larger reduction in the weight of the skins and webs, which now benefit from rib support.

Table 8.9: Masses of optimized PA-6-based blade designs with associated critical constraints – The objective function is subjected to stiffness and strength constraints.

Model	Mass (kg)	Critical constraints	Max constraint viol. (%)
2 webs, 0 rib	30 759	Tip def. (3), failure index (6 elements)	0.001
2 webs, 35 ribs	28 748	Tip def. (3), failure index (3 elements)	0.054
2 web, 70 ribs	28 131	Tip def. (3), failure index (8 elements)	0.013
1 web, 0 rib	29 557	Tip def. (3), failure index (10 elements)	0.017
1 web, 35 ribs	29 782	Tip def. (3), failure index (1 elements)	0.014
1 web, 70 ribs	27 934	Tip def. (3), failure index (11 elements)	No constraint viol.

Table 8.10 shows the shell thicknesses and fraction of the 0° fiber layer of all blade models for the sections of the blade extending from 30 to 45m. As was the case for epoxy-based blades, the objective function yielded thick spar caps with a high lengthwise UD material content to support most of the bending load. The upper and

lower surface spar cap thicknesses are almost the same for all blade models but show a slight tendency to increase with the number of ribs.

Table 8.10: Element total thickness and 0° fiber fraction for blade sections extending from 30 to 45 m – Optimized PA-6/glass one-web and two-web blade designs subjected to stiffness and strength constraints.

Blade section	PA-6/glass blades						Epoxy/glass blades	
	2 webs 0 rib	2 webs 35 ribs	2 webs 70 ribs	1 web 0 rib	1 web 35 ribs	1 web 70 ribs	2 webs 0 rib	1 web 0 rib
Upper surface	6.8 mm	3.9 mm	2.5 mm	4.8 mm	6.0 mm	2.8 mm	5.6 mm	4.6 mm
leading edge skin	61.7%	62.6%	62.6%	77.8%	59.9%	59.5%	59.9%	73.2%
Upper surface	81.2 mm	83.8 mm	87.2 mm	83.7 mm	84.5 mm	85.4 mm	80.6 mm	81.8 mm
spar cap	95.4%	97.2%	97.9%	97.4%	94.6%	98.0%	97.6%	97.8%
Upper surface	7.9 mm	4.5 mm	2.6 mm	6.9 mm	5.5 mm	2.8 mm	6.9 mm	5.7 mm
trailing edge skin	76.6%	81.7%	72.3%	82.6%	75.5%	80.7%	79.9%	81.8%
Lower surface	6.0 mm	3.6 mm	2.4 mm	4.7 mm	5.7 mm	2.6 mm	4.3 mm	5.3 mm
leading edge skin	58.9%	60.8%	61.2%	56.3%	58.7%	58.1%	53.8%	57.9%
Lower surface	81.3 mm	81.3 mm	86.7 mm	84.7 mm	85.5 mm	87.1 mm	81.4 mm	83.4 mm
spar cap	95.6%	97.1%	97.8%	97.5%	94.6%	98.0%	98.0%	97.5%
Lower surface	4.8 mm	2.9 mm	1.6 mm	4.2 mm	3.0 mm	1.6 mm	3.9 mm	3.9 mm
trailing edge skin	75.7%	76.9%	67.9%	76.9%	68.0%	71.4%	77.7%	78.9%
Trailing edge web	4.2 mm	2.7 mm	2.5 mm	-	-	-	4.1 mm	-
	62.4%	59.6%	46.3%	-	-	-	54.4%	-
Leading edge web	4.9 mm	2.7 mm	1.9 mm	-	-	-	4.1 mm	-
	60.2%	55.1%	52.6%	-	-	-	61.8%	-
Middle (single) web	-	-	-	5.2 mm	3.8 mm	3.9 mm	-	6.7 mm
	-	-	-	76.4%	67.2%	57.0%	-	73.5%

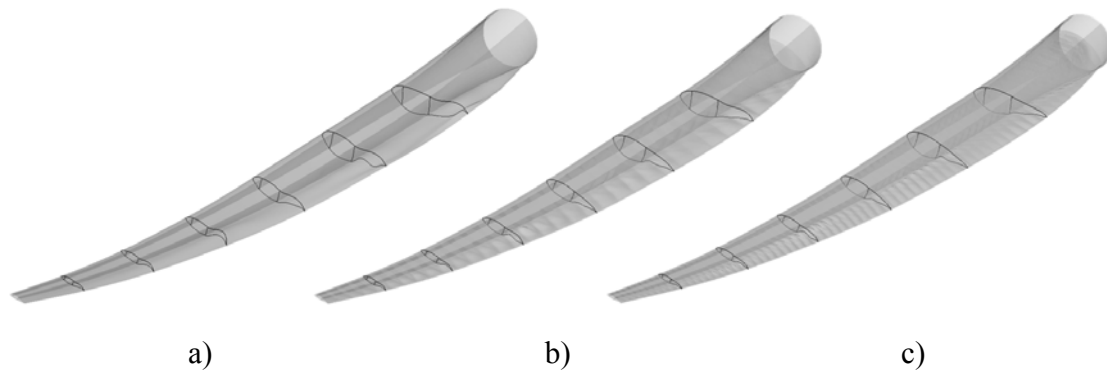


Figure 8.4: Shape of deformed aerodynamic profiles (for load case 3) of different blade models when subjected to stiffness and strength constraints. a) 2 webs and no rib. b) 2 webs and 35 ribs. c) 2 webs and 70 ribs.

For all blade topologies it can be seen that the thickness of the aerodynamic skins (leading edge and trailing edge sections) and webs generally decreases as the number of ribs increases. As suggested earlier, this means that the presence of ribs allowed thinner skins and webs, even if buckling was not included as a constraint in the objective

function. For models with two shear webs, since the thicknesses of the spar caps are very similar for all models, the mass saved by reducing the thickness of the skins and webs is directly transferred to the ribs. Interestingly, as it can be seen in Figure 8.4, even though models with ribs are lighter and have thin skins, they are much better at preventing aerodynamic profile distortion than thicker-skinned models.

Rib thickness (e) with respect to blade span (r) is plotted in Figure 8.5. As stated earlier, a total rib thickness of 3mm (1mm of 0° , 1mm of $\pm 45^\circ$ and 1mm of 90°) was used as the starting value during the optimization routine. Since the results showed that the 1/3 ratio between fiber layers remained relatively stable during the optimization process ($\pm 5\%$), only the total thickness is shown.

It can be observed that the starting thickness in the tip region was not altered significantly during the optimization. This is understandable since the effect of a rib thickness change in that area has very little influence on the objective function (the mass of tip ribs is insignificant with respect to blade mass). The fact that tip ribs are unaffected by the objective function also confirms that their stress level was maintained below the material failure index, otherwise their thickness would have increased.

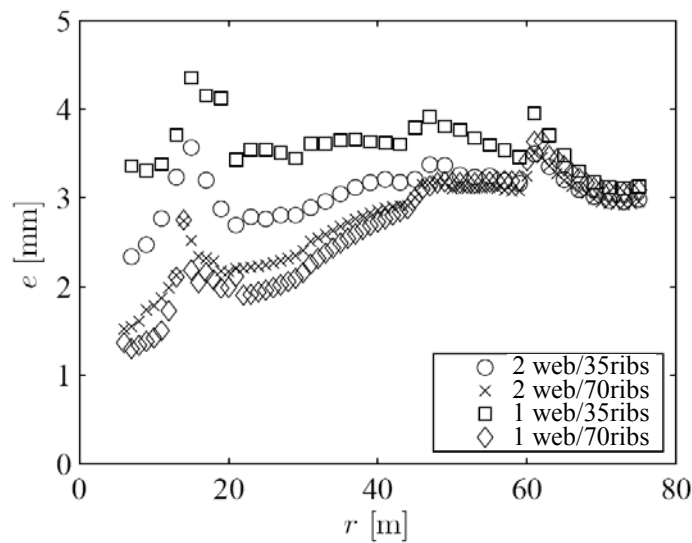


Figure 8.5: The evolution of rib thickness with respect to blade length for the different blade designs – Only the stiffness and strength constraints are applied (no buckling constraint).

Near the blade root, both the one-web and the two-web 35-rib designs show rib thicknesses that are approximately twice the thickness of those of the 70-rib designs. This suggests that doubling rib spacing forces rib thickness to double as well to maintain

equivalent structural performance. Comparing the rib thicknesses in the one-web and two-web 35-rib designs, it is clear that the one-web design requires thicker ribs. This makes sense since the panel surface area to support for the one-web design is larger than for the two web design. This phenomenon is slightly more difficult to perceive on the 70-rib designs, for which rib thicknesses are similar.

From a general perspective, one can also note localized rib thickening at the 15m, 45m and 65m blade stations. This corresponds to the areas where skin thickness changes from one section to the next (ply drop). Blade skin stability is therefore compromised by this sudden change in skin thickness, which translates into thicker ribs needed to compensate.

8.4.3 Design solutions based on stiffness, strength and buckling

The final study performed in this chapter concentrates on finding blade material thicknesses and composite layer proportions for the same blade designs presented in the previous section but when subjected to all three constraints in Equation 8.1 (i.e. including buckling). The mass of each optimized blade design is presented in Table 8.11. Again, the tip deflection for load case 3 was found to be the critical optimization constraint for all designs except the one-web/70-rib design, for which the tip deflection of load cases 3 and 4 were both judged critical.

Table 8.11: Masses of optimized PA-6-based blade designs with associated critical constraints – The objective function is subjected to stiffness, strength and buckling constraints.

Model	Mass (kg)	Critical constraints	Max constraint viol. (%)
2 webs, 0 rib	30 272	Tip def. (3), failure index (5 elements), buck. (3)	0.003
2 webs, 35 ribs	29 861	Tip def. (3), failure index (3 elements), buck. (3,4)	0.798
2 web, 70 ribs	29 922	Tip def. (3), failure index (2 elements), buck. (3,4)	No const. viol.
1 web, 0 rib	30 342	Tip def. (3), failure index (11 elements), buck. (3,4)	No const. viol.
1 web, 35 ribs	29 815	Tip def. (3), failure index (2 elements), buck. (3)	0.098
1 web, 70 ribs	31 241	Tip def. (3,4), failure index (1 elements), buck. (3)	No const. viol.

As was the case for blades designed only for strength and stiffness, only a few hundred kilos distinguish the epoxy-based blade designs from their thermoplastic composite counterparts (see Table 8.6 for comparison). Comparing the results of Table 8.9 with those of Table 8.11, it is apparent that when buckling is taken into account, the 35-rib design is favored with respect to blade mass. For both the one-web and two-web

concepts, using 35 ribs yielded the lightest blade design (3% lighter for the one-web configuration compared to the baseline rib-less epoxy-based design).

Table 8.12 shows the shell thicknesses, fractions of the 0° fiber layer and core material thicknesses of all blade models for the sections of the blade extending from 30 to 45m (all blade section results are presented in Appendix C). The rib-less PA-6 blade designs allow similar conclusions to those drawn in the case of epoxy regarding the buckling constraint: 1- the thickness of the aerodynamic skins and webs decreases significantly when core material is introduced into the structure, 2- in buckling-prone areas, thick core material is used and the proportion of the 0° layer decreases to bring about local unloading of the composite panels.

Table 8.12: Element total thickness, 0° fiber fraction and core thickness for blade sections extending from 30 to 45m – Optimized PA-6/glass one-web and two-web blade designs subjected to stiffness, strength and buckling constraints.

	PA-6/glass blades						Epoxy/glass blades	
Blade section	2 webs 0 rib	2 webs 35 ribs	2 webs 70 ribs	1 web 0 rib	1 web 35 ribs	1 web 70 ribs	2 webs 0 rib	1 web 0 rib
Upper surface	4.1 mm	2.6 mm	2.3 mm	3.3 mm	3.2 mm	4.2 mm	2.4 mm	4.0 mm
leading edge skin	55.6%	53.0%	55.4%	46.6%	54.1%	53.5%	58.7%	57.3%
	8.2 mm	7.1 mm	7.2 mm	9.6 mm	7.3 mm	8.1 mm	6.1 mm	7.9 mm
Upper surface	88.0 mm	88.0 mm	87.9 mm	87.7 mm	85.6 mm	89.6 mm	83.5 mm	82.3 mm
spar cap	96.9%	97.3%	96.9%	97.3%	97.8%	95.6%	97.7%	97.3%
	7.6 mm	6.6 mm	6.8 mm	10.3 mm	7.1 mm	8.1 mm	5.6 mm	7.4 mm
Upper surface	4.7 mm	2.4 mm	3.0 mm	3.6 mm	4.2 mm	5.3 mm	2.6 mm	3.1 mm
trailing edge skin	40.6%	22.7%	16.0%	37.3%	15.5%	26.8%	49.6%	63.6%
	20.4 mm	19.2 mm	15.4 mm	24.5 mm	14.5 mm	12.4 mm	23.9 mm	25.5 mm
Lower surface	5.7 mm	4.5 mm	5.5 mm	3.8 mm	5.1 mm	10.2 mm	3.5 mm	4.4 mm
leading edge skin	63.7%	62.9%	61.7%	61.1%	65.6%	71.8%	68.1%	59.6%
	8.2 mm	7.1 mm	7.3 mm	7.0 mm	7.4 mm	8.1 mm	6.1 mm	7.7 mm
Lower surface	84.8 mm	84.5 mm	83.9 mm	80.3 mm	82.8 mm	80.4 mm	82.9 mm	80.7 mm
spar cap	96.8%	97.3%	98.0%	98.1%	97.6%	95.5%	97.0%	97.3%
	7.5 mm	6.4 mm	6.7 mm	5.9 mm	6.9 mm	7.8 mm	5.0 mm	7.1 mm
Lower surface	2.4 mm	1.5 mm	0.8mm	2.1 mm	1.6 mm	1.5 mm	2.5 mm	2.2 mm
trailing edge skin	58.1%	60.8%	72.2%	75.5%	76.5%	68.2%	62.8%	61.5%
	8.0 mm	8.3 mm	7.5 mm	12.6 mm	13.3 mm	8.9 mm	7.6 mm	10.6 mm
Trailing edge web	3.1 mm	2.9 mm	3.3 mm				3.4 mm	
	62.9%	65.8%	68.1%	-	-	-	49.6%	-
	8.7 mm	8.8 mm	7.8 mm				7.2 mm	
Leading edge web	3.6 mm	2.6 mm	3.2mm				2.0 mm	
	55.2%	57.4%	51.9%				54.9%	-
	8.4 mm	6.9 mm	7.2 mm				7.0 mm	
Middle (single)				4.2 mm	3.9 mm	3.5 mm		4.6 mm
web	-	-	-	46.6%	66.6%	71.1%	-	57.3%
				9.0 mm	8.9 mm	7.8 mm		8.5 mm

Comparing blade designs that include ribs, it was observed previously (in the case where the buckling constraint was not active) that for all topologies the thickness of the

aerodynamic skins and webs generally decreased as the number of ribs increased. With the inclusion of the buckling constraint, this conclusion no longer holds since Table 8.12 shows that blade designs using 70 ribs generally have thicker skins and webs than their 35-rib counterpart. This leads to the conclusion that there should be an optimal rib number situated likely between 0 and 70. From a structural point of view, this also means that skin and web buckling can be controlled adequately with ribs and that an overall blade mass reduction can be obtained even if ribs are added to the structure.

The comparison of Figures 8.6 and 8.4 shows that as was the case with epoxy-based blades, including the buckling constraint in the objective function clearly reduces profile distortion.

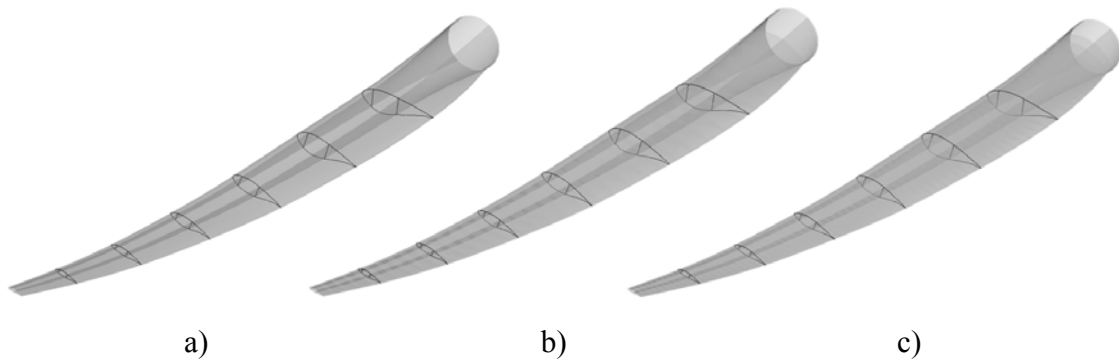


Figure 8.6: Shape of deformed aerodynamic profiles (for load case 3) of different blade models when subjected to stiffness, strength and buckling constraints. a) 2 webs and no ribs. b) 2 webs and 35 ribs. c) 2 webs and 70 ribs.

For comparison with the study without the buckling constraint, rib thickness (e) and core material thickness with respect to blade span (r) were plotted in Figure 8.7. A total rib thickness of 6mm (1mm of 0° , 1mm of $\pm 45^\circ$, 1mm of 90° and 3mm of core material) was used as the starting value during the optimization routine. Since the results showed again that the 1/3 ratio between fiber layers remained relatively stable during the optimization process, only the total skin thickness is shown in Figure 8.7a.

In the tip region, it can be observed that the starting thickness was not altered significantly during the optimization. Firstly, the fact that their thickness does not increase proves that they do not violate the failure index constraint. On the contrary, they seem to be slowly going thinner from tip to mid-span. As explained earlier, this is due to the fact that the mass of tip ribs is insignificant with respect to total blade mass which gives them very little power to influence the objective function if their thickness

is reduced. Ribs at mid-span having more mass can influence a bit more the objective function and are reduced in thickness accordingly.

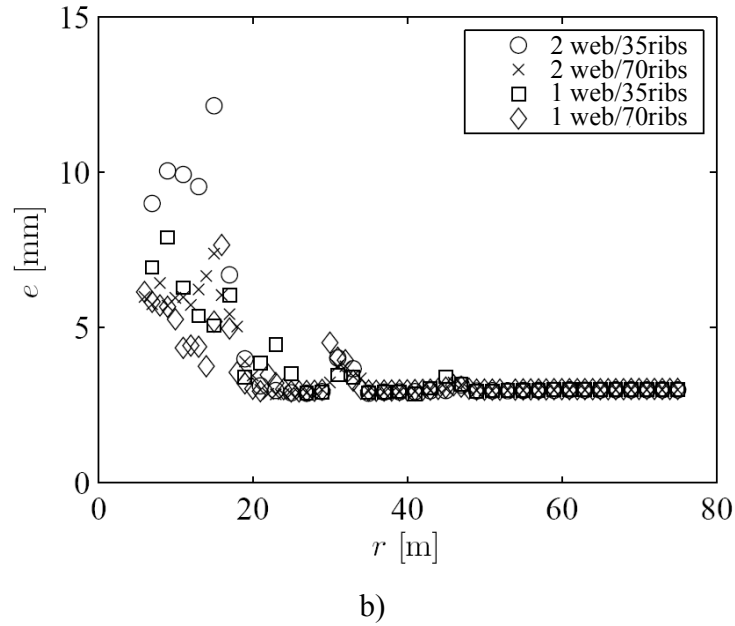
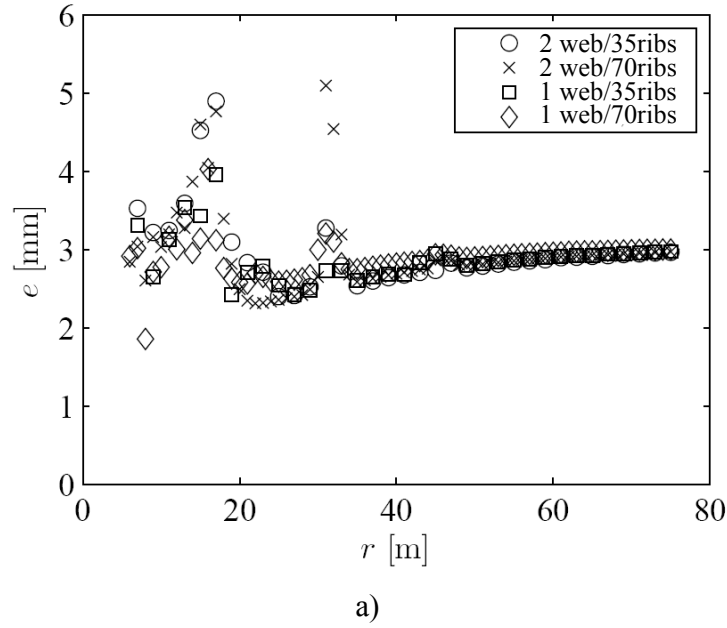


Figure 8.7: The evolution of rib thickness with respect to blade length for the different blade designs – Stiffness, strength and buckling constraints applied. a) Skin thickness evolution. b) Core material thickness evolution.

As shown in Figure 8.7a, near the root, ribs of all blade designs show skin thickening. A similar trend appears in Figure 8.7b, with core thickness increasing substantially near the root section. Data analysis showed that to maintain the buckling

factor below unity in ribs near the root where the blade cross-section thickness is quite large, skin thickness and core thickness were forced to increase.

From a general perspective, localized rib thickening is again apparent at the 15m, 30m and 45m blade stations. As explained earlier, this corresponds to the areas where skin thickness changes from one section to another (ply drop), forcing ribs to be slightly thicker to compensate local aerodynamic skin instability.

8.5 Discussions and Conclusions

It was argued earlier in this thesis that to maximize the potential of thermoplastic composites for use in wind turbine blade structures, it is essential to redesign the structure with respect to existing TPC material and manufacturing strong points. Based on the conclusions of chapter 3, blade designs using ribs, multiple skin panels and stringers produced with fast non-isothermal melt processes could significantly help maximize this potential. In parallel, results of chapter 7 proved that a blade structure using ribs could actually help increase its overall stiffness (minimize its compliance).

The work presented in this chapter consolidated these two previous findings and benchmarking different TPC oriented blade designs against classic thermoset composite blade designs. This was done as the third step of a three-step structural topology optimization process (see Figure 7.3). The different optimization runs performed on the various blade configurations described in Table 8.9 or Table 8.11 led to the following conclusions:

8.5.1 Preferred topology for TPC wind turbine blades

In light of the results presented in Tables 8.11 and 8.12, although its mass is a few hundred kilos higher than that of the one-web concept, the 35-rib configuration using two webs is the most promising concept for TPC wind turbine blades. Having three distinct sections (trailing edge, box spar and leading edge section) gives this configuration an advantage over its one-web counterpart. Working with a closed-cell main-load-carrying structural member helps in controlling load paths and minimizes the load transferred to the buckling prone trailing edge section. It also offers the possibility of easy manufacturing of the box-spar using a material different from that of the leading edge and trailing edge sections. As was the case in the aeronautic industry, TPC

composites could be used initially in wind turbine blade structure as secondary structure components (the box-spar still being made with thermoset composites). Gaining manufacturing experience with only these non-structural components could help manufacturers gain experience at minimal risk.

8.5.2 *The presence of ribs in wind turbine blade structures*

- With respect to the objective function used to perform the different optimization runs, it was shown that ribs are capable of reducing overall blade mass slightly by providing support to webs and aerodynamic skins.
- Ribs can also help significantly to reduce profile distortion, compared to rib-less designs. Recent work performed at Risø National Laboratory (Denmark) showed that skin de-bonding or web buckling due to large cross-sectional distortion is often the starting point for overall blade failure [10]. Since ribs help reduce local strain and reduce blade distortion, they could help delay delamination or de-bonding, which should increase blade ultimate strength. Jensen observed this phenomenon in a study showing that placing five ribs over a 17m span of a blade girder could increase failure load by 30% [11].
- In the linear analysis context in which the present study was performed, the ideal number of ribs for a 75m-long wind turbine blade appears to be situated between 0 and 70. However, since ribs are not bare-loading structural elements, they do not influence the objective function directly but rather help other structural elements perform better to minimize the objective function. Consequently, the objective function used throughout this chapter provided the opportunity to validate that ribs were useful but could not provide optimal design solutions for them. This could be achieved in a later detailed design phase by isolating the ribs from the structure with a free-body analysis. Krog et al, who applied this technique to the optimization of aircraft wing box ribs [12] provide details on how this could be done.
- On a more global level, ribs could provide support for the attachment of future load mitigation control surfaces such as flaps, tabs or other aerodynamic devices [13-15].

8.5.3 General considerations

- To limit computational time, the number of design variables had to be kept relatively small. As a consequence, the blade was divided into only five lengthwise sections. With this approach, as shown in Table 8.1, the number of variables for the optimization runs performed in this study varied between 105 and 400. Compared to other preliminary design studies, the amount of ply drops along blade length could be considered small. For example, Bir and Bergreen used respectively six and 10 ply drops over their blade lengths [16, 17]. Of course, at the expense of longer processing time, more refined designs could have been obtained. This can be understood by looking at Figure 8.8, in which blade failure indexes are plotted for the two-web/35-rib design. The large stress gradient perceived in constant thickness sections shows that thinning the composite shells more gradually from root to tip could help minimize blade mass even more.

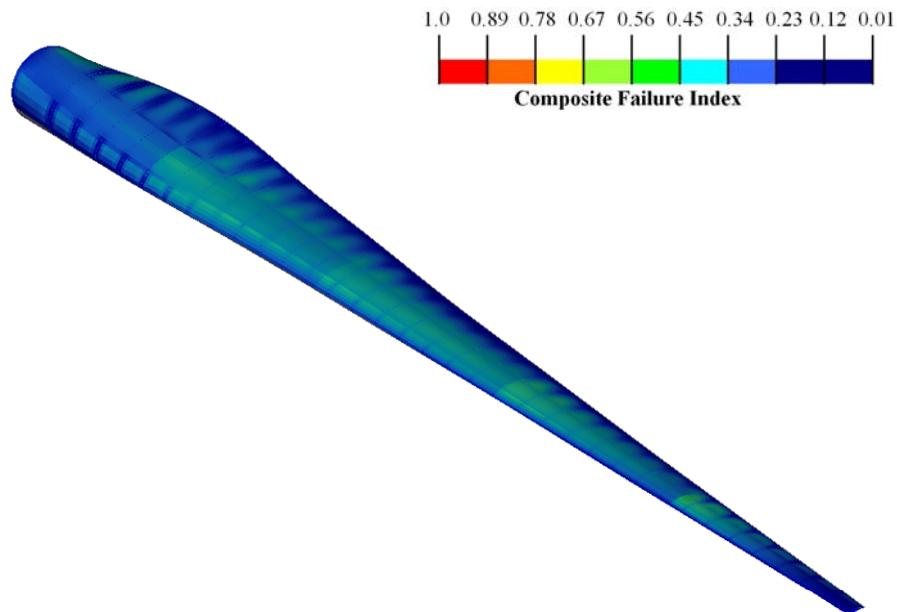


Figure 8.8: Composite failure index contour plot of the 2 web/35-rib blade design under load case 3.

- Convergence tolerances were set to relatively high values to limit computational time. As a consequence, elements close to the tip have

significantly less influence over the objective function (minimize mass) compared to thicker elements near the root. This phenomenon was observed on ribs and was reported in sections 8.4.2 and 8.4.3. Convergence tolerance should be therefore be decreased at the cost of significantly longer computational times in order to gain more confidence in results obtained for tip regions.

- For preliminary design purposes, linear analysis is generally accepted. In the course of this work, since the study was done on a comparison basis between designs, linear analysis is believed to have led to defensible conclusions, although measured deformations were large. Nevertheless, non-linear analysis is necessary to treat issues such as Brazier loads, delamination, post-buckling behavior, crack growth and other important local failure mechanisms that may lead to ultimate blade failure. Non-linear analysis will therefore be essential during the detailed design phase.
- Fatigue loads are of primary importance for wind turbine blade design. This was taken into account indirectly in the preliminary design process presented in this chapter by simply applying the most severe safety factor of the IEC-61400-1 standard. A more realistic way to take fatigue loads into account is to evaluate the mean and amplitude stresses in different fatigue critical zones of the blade. With these local fatigue stress spectra, specific fatigue limits can be evaluated using constant-life diagrams and incorporated into the FE model to calculate failure indexes. This approach should be followed for detailed design.
- Blade structural optimization was performed under combined loading (flapwise and edgewise) according to the critical load cases identified in chapter 6. Unfortunately, blades designed with respect to these specific load cases are not guaranteed to respect the failure index for other load cases that could be very different in nature. During the detailed design phase, other load cases should be checked and blade design should be adapted if some constraints are found to be violated.
- As mentioned in chapter 3, TPC are generally produced with fast non-isothermal melt processes. Up to now, using thick core material in TPC structures is not common practice. An alternative way possibly better suited to TPC processing would be to use stringers or corrugated panels to replace the

sandwich structures used for the designs suggested in this chapter. From a structural point of view, for equivalent mass, corrugated panels have been shown to hold 10-15% more compressive load than conventional constant thickness sandwich panel [18].

It was mentioned in chapter 4 that an increase in manufacturing cost is to be expected due to a reduced tooling life (aggressive thermal cycling) and the more elaborate mold-heating system needed to cure APA-6 resin. It was argued that this cost increase could be compensated by a faster cycle time (faster infusion, polymerization and assembly methods) and the significantly lower resin cost of the APA-6 resin system compared to epoxy systems. To validate this hypothesis and prove the cost effectiveness of the TPC blade design proposed in this thesis, a thorough cost analysis will be necessary. Ideally, cost issues should be taken into account early in the design process. In this context, the preliminary design objective function (Equation 8.1) could be modified to incorporate a cost function that would influence the outcome of the optimization process.

8.6 References

- [1] Zhou, M., Pagaldipti, N., Thomas, H., and Shyy, Y., *An Integrated Approach to Topology, Sizing and Shape Optimization*, Structural and Multidisciplinary Optimization, Vol. 26, 2004, pp. 308–317.
- [2] Thomas, H., Zhou, M., and Schramm, U., *Issues of Commercial Optimization Software Development*, Structural and Multidisciplinary Optimization, Vol. 23, 2002, pp. 97–110.
- [3] *Optistruct User Manual*, Altair Engineering, inc., Troy (United States), 1999.
- [4] Nijssen, R.P.L., OptiDAT – database reference document, OPTIMAT report: OB_TC_R018, doc. No. 10224, 2006.
- [5] Nijssen, R.P.L., OptiDAT – Fatigue of wind turbine material database, via www.kc-wmc.nl/optimat_blades
- [6] Berggreen, C., Branner, K., Jensen, J. F., and Schultz, J. P., *Application and Analysis of Sandwich Elements in the Primary Structure of Large Wind Turbine Blades*, Journal of Sandwich Structures and Materials, Vol. 9, 2007, pp. 525–551.
- [7] Griffin, D.A., *WindPACT Turbine Design Scaling study technical area 1 – Composite blades for 80 to 120 meter rotor*. NREL/SR-500-29492. National Renewable Energy Laboratory. Golden, CO, 2001.
- [8] Griffin, D. A. and Zuteck, M. D., *Scaling of Composite Wind Turbine Blades for Rotor of 80 to 120 Meter Diameter*, Journal of Solar Energy Engineering, Vol. 123, 2001, pp. 310–318.
- [9] van Rijswijk, K., Joncas, S., Bersee, H., Bergsma, O., and Beukers, A., *Sustainable Vacuum-Infused Thermoplastic Composites for MW-Size Wind Turbine Blades - Preliminary Design and Manufacturing Issues*, Journal of Solar Energy Engineering, Vol. 127, 2005, pp. 570–580.
- [10] Jensen, F.M., *Ultimate strength of a large wind turbine blade*, PhD dissertation, Risø National Laboratory for sustainable Energy – Technical University of Denmark, Roskilde, Denmark, 2008.
- [11] Jensen, F.M., Falzon, B.G., Ankersen, J., Stang, H., *Structural testing and numerical simulation of a 34m composite wind turbine blade*, Composite Structures, Vol. 76, 2006, pp. 52-61.
- [12] Krog, L. Tucker, A., Kemp, M., Boyd, R., *Topology optimization of aircraft wing box ribs*, proceedings of the 10th AIAA/ISSMO Multidisciplinary Analysis and Optimization Conference, Albany, New-York, August 2004..

- [13] van Wingerden, J. W., Hulskamp, A. W., Barlas, T., Marrant, B., van Kuik, G. A. M., Molenaar, D.-P., Verhaegen, M., *On the Proof of Concept of a 'Smart' Wind Turbine Rotor Blade for Load Alleviation*, Wind Energy, 2008; 11:265–280.
- [14] Buhl, T., Gaunaa, M., Bak, C., *Potential of load reduction using airfoils with variable trailing edge geometry*, Journal of Solar Energy Engineering 2005; 127: 503–516.
- [15] Yen Nakafuji, D. T. Van dam, C.P. Michel, J., Morrison, P., *Load Control for Turbine Blades: A Non-Traditional Microtab Approach*, ASME Wind Energy Symposium, Reno, Nevada, January 2002, AIAA 2002-0054
- [16] Bir, G. S., Migliore P., *Preliminary Structural Design of Composite Blades for Two- and Three- Blade Rotors*, NREL/TP-500-31486, Golden, CO: National Renewable Energy Laboratory, September 2004.
- [17] Berggreen, C., Branner, K., Jensen, J. F., and Schultz, J. P., *Application and Analysis of Sandwich Elements in the Primary Structure of Large Wind Turbine Blades*, Journal of Sandwich Structures and Materials, Vol. 9, 2007, pp. 525–551.
- [18] Joncas S., Lemay, J., Bergsma, O.K., Bersee, H.E.N., Beukers, A., *Topography Optimization for Maximum Buckling Loads of Wind Turbine Blade Sandwich Panels*, 15th International Conference on Composite Materials (ICCM-15), Durban, South Africa, June 2005.

CHAPTER 9

CONCLUSIONS AND RECOMMENDATIONS

The main objective of the work presented in this thesis was to propose design solutions for large thermoplastic composite (TPC) blades within the current context of the wind energy industry. In doing so, anionic polyamide-6 (APA-6) was first identified as the most promising thermoplastic polymer system for large wind turbine blades, based on material properties, cost and processing. After mechanically characterizing APA-6/glass composites, TPC-based blade designs were developed using a finite-element-based topology and size optimization approach and then benchmarked against conventional epoxy-based blade designs. This chapter recalls the most important findings of this thesis and formulates recommendations to guide future work.

9.1 Main conclusions on materials and manufacturing

9.1.1 *Manufacturing issues*

The largest wind turbine blades currently exceed 60m in length and use laminates more than 10cm thick. Given the size of the composite parts involved, chapter 3 identified only two thermoplastic composite manufacturing processes as possible candidates for the production of large thermoplastic composite blades: resin infusion and ATL/AFP processing. Two main problems are expected to limit the use of ATL/AFP processes: the very high capital cost for the machine and their limited material-laying rate. With current 10-15 kg/hour material-laying rates, it is unlikely that 50-60-meter blades weighing 15-20 tons will be produced with these machines in the near future (even when using multiple consolidation heads), especially knowing that blade manufacturing facilities typically produce a couple of blades per day.

On the other hand, apart from the tooling temperature required, which is a bit high compared to those used for thermoset-based composites, there is technically no limitation to APA-6-resin-infused part size. Furthermore, due to the very low resin viscosity of the APA-6 system (10 mPa·s, which is 35 times lower than epoxy) fiber

wettability should be improved and infusion times shortened. Also, the low viscosity of the APA-6 system is expected to reduce fiber washout during infusion, thereby reducing fiber waviness [1]. Finally, since resin counts for approximately 35% of blade mass, significant overall material cost savings are expected due to resin costs being approximately 20% less for APA-6 than for commonly used epoxy systems.

For the manufacturing of smaller parts (up to 1-2m) such as ribs or skin panels, elastomeric tool forming was identified as the most suitable process. Although diaphragm forming has not yet found commercial success, when simply used with vacuum, it could be used for larger parts.

9.1.2 APA-6 composite mechanical properties

In dry-as-molded conditions, results shown in chapter 4 demonstrated that APA-6/glass composites surpassed their epoxy-based counterpart in tensile, compressive and shear strengths and moduli. Conversely, under moist conditions, mechanical properties of APA-6 composites were significantly degraded due to matrix swelling and interface degradation. To a certain extent, this was to expect due the more hydrophilic nature of PA-6 when compared to epoxy. Nevertheless, excessive degradation was found to be caused by the higher void content found in APA-6 composites when compared to epoxy-based composites. Also, the inevitable water-soluble residual monomer present in the polymer is believed to have contributed to mechanical property degradation since it increases moisture absorption rate.

Concerning tension-tension fatigue properties, in dry-as-molded conditions, the reactively processed APA-6 composites showed fatigue resistance far from matching the fatigue resistance of epoxy-based composites. However, compared to conventionally processed HPA-6 composites, APA-6 composites were 25% more resistant. This is believed to be most likely caused by the stronger fiber-to-matrix interface of the reactively processed APA-6 composite. Through better control over moisture absorption and void content, a significant increase in the fatigue resistance of APA-6 composites is expected. Nonetheless, at this stage of material development, fatigue performance and poor mechanical performance under moist conditions are undoubtedly two key elements limiting the use of APA-6 composites for wind turbine blade structures.

9.1.3 *Material recycling*

Long-fiber-infused APA-6/glass composite laminates were recycled into APA-6 short-fiber reinforced composites by regrinding and injection molding of ASTM type I test specimens. Tensile tests showed that the strength and modulus of the recycled material could be up to 10% higher than those of commercial short-fiber glass reinforced polyamide-6 resins at equivalent fiber weight content (see Table 4.9). It therefore would not be surprising to see these materials used by the automotive industry, in which large quantities of virgin reinforced polyamides are being consumed for under-the-hood applications. If so, given a big enough market to absorb end-of-life materials, the development of recyclable wind turbine blades could diminish the uncertainties and environmental impact related to the dismantling and recovery of composite wastes in the wind energy sector.

9.2 Main conclusions regarding structural design

9.2.1 *Box-spar configuration*

The topology optimization results obtained in chapter 7 showed that at mid-span of the blade, shear webs positioned at approximately 15% to 50% of chord length were ideal for reducing blade compliance. With the blade heavily reinforced on the upper and lower surfaces comprised between these webs (spar caps), the structural topology found at mid-span is similar to the structural topologies used today for MW-size wind turbine blades. For chord stations closer to blade tip, where the gravity load is significantly reduced, a single web positioned at 1/3 of the chord length seems to be the ideal configuration. As was the case for the mid-span blade section, the upper and lower blade surfaces between 15% and 50% of chord length are again heavily reinforced to withstand the predominantly bending loads.

Near the root transition area, because edgewise bending moments become significant with respect to flapwise bending moments, the spar caps split into two sections. The blade is then attached to the root by means of four symmetrically arranged members. This topology yields similar in-plane and out-of-plane root stiffness, which is also typical of what is found in current MW-size wind turbine blades.

9.2.2 Rib reinforced aerodynamic surfaces

Results of chapter 7 demonstrated that the presence of trailing edge ribs separated by a distance of 1 to 2 m in the structure helped minimize blade compliance. This means that ribs were preferred over simply thickening the skins as is usually done in current blade constructions. The potential of ribs was validated in chapter 8 with a size optimization study based on stress, stiffness and buckling stability in which ribbed blade designs were found to be slightly lighter than conventional wind turbine blade constructions.

More importantly, ribs helped considerably to reduce profile distortion compared to rib-less designs. Recent work performed at the Risø National Laboratory (Denmark) showed that skin de-bonding or web buckling due to large cross-sectional distortion is often the starting point for global blade failure [2]. Since ribs help reduce local strain and reduce blade distortion, they can help delay delamination or de-bonding, which should increase blade ultimate strength. This phenomenon was observed by Jensen [3] who showed that placing 5 ribs over a 17m span of a blade girder could increase failure load by 30%.

9.2.3 Proposed designs

In chapter 8, the 35-rib configuration using two webs was identified as the most promising concept for TPC wind turbine blades. Compared to current epoxy-based blade design, the mass of the blade designed according to this concept could be reduced by 3% while retaining identical structural performance. Having three distinct sections (leading edge, box spar and trailing edge section) gives this configuration an advantage over the one-web design, which offered a very similar structural performance at equivalent blade mass. Working with a closed-cell main-load-carrying structural member helps in controlling load paths and minimizes the load transferred to the buckling-prone trailing edge section. It also offers the possibility of manufacturing the box-spar in a different material than the leading edge and trailing edge section. As was the case in the aeronautical industry, TPC composites could be used initially as secondary structures for wind turbine blades (while continuing to make the box-spar out of thermoset composites). Introducing these materials first as non-structural components in wind turbine blade structures could help manufacturers gain experience with them at minimal risk.

9.3 Research objective assessment

In the introduction chapter, different objectives were set to try and bridge the gap for thermoplastic composites to be successfully used in large wind turbine structures. In this section, with respect to the above-mentioned conclusions, the extent to which these research objectives were achieved will be assessed.

9.3.1 *Identifying a potential thermoplastic resin system*

The first objective of this project was to identify a potential thermoplastic resin system to be used as a matrix for large thermoplastic composite wind turbine blades. Following a broad review of thermoplastic polymers, engineering polymers were identified as having the greatest overall potential for use in thermoplastic composite wind turbine blades because of their excellent mechanical performance to cost ratio. With some engineering polymers being cheaper than conventional thermoset resin systems, blade material cost could potentially be reduced if thermoplastic composites would be used. Based on matrix performance, with engineering polymer weight, strength and stiffness being comparable to conventional thermoset resin systems, no significant reduction in static mechanical performance is to be expected when using thermoplastic composite for wind turbine blade structures owing a similar fiber-to-matrix adhesion.

From a manufacturing perspective, chapter 3 showed that thermoplastic composite manufacturing processes in use today are mostly melt processes dedicated to the production of relatively small parts and therefore are not suitable for the production of the thick and large composite shells found in current wind turbine blade structures. However, a new reactive processing technique based on vacuum infusion was identified as the most promising manufacturing method for fast production of large wind turbine blade parts.

Within the engineering polymer family, based on cost, performance and the fact that it can be reactively processed at significantly lower temperatures than other engineering polymers, polyamide-6 was identified as being the most promising resin system for large wind turbine blades.

9.3.2 *Benchmarking PA-6/glass against epoxy/glass composites*

The second objective formulated at the beginning of this thesis was twofold: 1- benchmark APA-6 composites against a typical epoxy-based composite used in the wind energy industry, 2- propose a sustainable solution for the end-of-life management of APA-6 composites.

Since the APA-6 reactively processed composite studied in this thesis was still at an early stage of material development, the main goal pursued in this benchmarking study was to identify the potential benefits and pitfalls of the material for preliminary design purposes and for further material development. In this context, the results presented for the laminate tested in chapter 4 fulfilled the research objective. It was shown that in dry conditions, static performance (strengths and moduli) of APA-6 composites was comparable or slightly better than conventional materials used for wind turbine blade structures. It was also demonstrated that moisture had a significant adverse effect on these performances due to matrix swelling of APA-6 composites. These results contributed to defining new avenues for further material development (ongoing research) to try to improve the manufacturing process (reduction of voids and RMC) and increase the quality of the laminates (fiber/matrix interface).

From a fatigue performance perspective, results showed that APA-6 composites in dry conditions outperformed the conventional melt-processed PA-6 composites because of its superior chemically bonded interface. Approximately 25% more load could be applied for an equivalent fatigue life. Although reactively processed APA-6 composites are significantly more fatigue resistant than their melt-processed counterpart, their fatigue resistance was shown to be far from matching the fatigue resistance of epoxy-based composites. These results helped identify the most important area for improvement for APA-6 composites to be used for wind turbine blades, which are fatigue-driven structures.

Finally, the potential benefit of recycling APA-6/glass composite laminates into APA-6 short-fiber reinforced composite injection-molded parts was demonstrated. According to conclusions presented earlier in chapter 4, the recycled material could be competitive with commercial short-fiber glass-reinforced polyamide-6 composites currently sold at equivalent fiber weight content.

9.3.3 *Proposal of an integrated TPC large wind turbine blade design*

The third objective of this thesis was to propose an integrated blade design concept that would maximize the potential of TPC for use in large wind turbine blade structures. It is worth noting that integrated design principles can be quite specific depending on the technical field (engineering, product development, architecture, etc...). They can also be quite broad and often incorporate aspects related to marketing, packaging, sales and other non-technical aspects. In the context of this thesis, the integrated design principle followed is illustrated in Figure 1.5 and does not take into consideration non-technical aspects. It simply aims at finding the best structure possible by maximizing material and processing capabilities.

In order to propose such an integrated design for large TPC wind turbine blades, a TPC material and process review was first carried out (chapter 3). As mentioned earlier, this study confirmed that up to now, TPC parts are generally small and are manufactured using fast non-isothermal processes. Nonetheless, novel manufacturing processes such vacuum-assisted reactive processing are currently being developed for the production of large and thick TPC parts.

As explained in section 1.3, designers usually develop their designs with knowledge of the manufacturing limits with which they have to contend. For example, it is well known that thermoset-based composite manufacturing is not well suited to rapid production of small parts at low cost. This forces thermoset-based blade designers to minimize the number of parts, which will not necessarily be the case for TPC-based blade designs. It thus became quite evident that the current structural design used for large wind turbine blades (three or four large parts) was probably not ideal from a TPC manufacturing perspective.

Consequently, in the case of this thesis, manufacturing limits constraining the design process were almost non-existing because:

- 1- Fast non-isothermal processes could be used to produce small/thin parts
- 2- Vacuum infusion reactive processing could (eventually) be used to produce large and thick APA-6 composite parts.

With the design process being virtually “unconstrained” (apart from material limits and functionality requirements), recently developed FE-based topology optimization

tools were favored to explore designs that would not necessarily have been discovered by intuitive processes. Moreover, because these tools are able to maximize the performance of a structure subjected to numerous load cases, they provided the opportunity to yield a blade design that performed well under different operational scenarios.

Ultimately, the combined topology/size optimization scheme followed in chapters 7 and 8 helped to propose an integrated design (the two-web/35-rib concept) that required both above-mentioned processes. Vacuum infusion reactive processing is necessary to produce the thick and large blade spar elements while fast non-isothermal processes are required to produce small parts such as ribs and skin panels.

9.3.4 Benchmarking TPC blades against a classic blade design

The final objective of this thesis was to benchmark the performance of the large TPC blade concept developed in this thesis (the two-web/35-rib concept) against a conventional epoxy-based blade design (two-web design).

In order not to bias this benchmark study, special care was taken to base the study purely on material and structural concept performance. This objective was reached by evaluating the mass and general structural behavior of both blade designs under the following conditions:

- Both blades use the same generic blade design developed in chapter 6,
- Both blades are subjected to the same load cases (as described in chapter 8)
- Laminate thicknesses of both blades are determined by means of a sizing optimization process that used the same objective function, which minimizes mass while being constrained by stress, stiffness and a stability criterion (as described in chapter 8).

Results showed that compared to current conventional epoxy-based blade design, the TPC blade design concept developed in this thesis could reduce blade mass by 3% for identical structural performance. Furthermore, due to the presence of ribs, aerodynamic profile and web distortion was significantly reduced in comparison with conventional epoxy-based blade design.

9.4 Potential benefits for the wind energy industry

As shown in chapter 2, materials used for wind turbine blade structures have covered a very large spectrum over the past 40 years with metals (steel and aluminum), wood, wood laminates and fiber-reinforced polymer (FRP) composites being used. Structural design being strongly influenced by the materials and processes used, current blade designs reflect the influence of the different industries involved in early composite wind turbine blade development. History recalls that the aeronautical and composite-boat-building industries were certainly the two most involved in early composite blade design and manufacturing. In the end, composite-boat-building technology won the battle against aeronautical-based designs, due primarily to cost issues.

Although today's market strictly uses thermoset-based double-shear-web or box spar blade designs, thermoplastic composite blade designs are expected to push their way through because: 1- they have the potential to reduce blade cost, 2- they will be easier to recycle than thermoset composite blades, 3- they will facilitate low-cost and effective integration of active control devices.

These potential benefits and the expected technology hurdles to overcome are discussed in the sections that follow.

9.4.1 *Potential blade cost reduction*

Thermoplastic composites can reduce production time, often cost less and have no shelf life limitation in comparison with thermoset composites. Due to these advantages, thermoplastic composites are slowly replacing thermoset composites in the automotive industry, the aeronautic industry, the sports and leisure industry and other important composite industries (see Figure 9.1).

This massive switch in technology in the automotive industry was triggered as a result of the EU vehicle end-of-life directive. Forced to replace most of their under-the-hood BMC/SMC thermoset parts by recyclable GMT parts, this industry simply had no other choice but to acquire thermoplastic-based technology quickly in order to comply with new vehicle end-of-life regulations. In the aeronautical industry, the technology switch was not motivated as much by recycling as by cost. Costly and labor intensive, autoclave-cured thermoset parts are slowly being replaced by low-cost fast-processed thermoplastic composites. Although both industries strongly benefited from this

technology S-curve jump, both initially had to invest significantly in material and process development. A similar effort will be required of the wind energy industry. The two key elements for successful usage of TPC in wind turbine blade structures will be: 1 – the development of reactively processed resin systems and associated manufacturing techniques, 2 – the development of material capable of withstanding the fatigue requirements of wind turbine blades. Research on these two elements was initiated in this thesis and in the sister thesis of K. van Rijswijk [5] but a significant effort is still required in order to transfer the technology to industry.

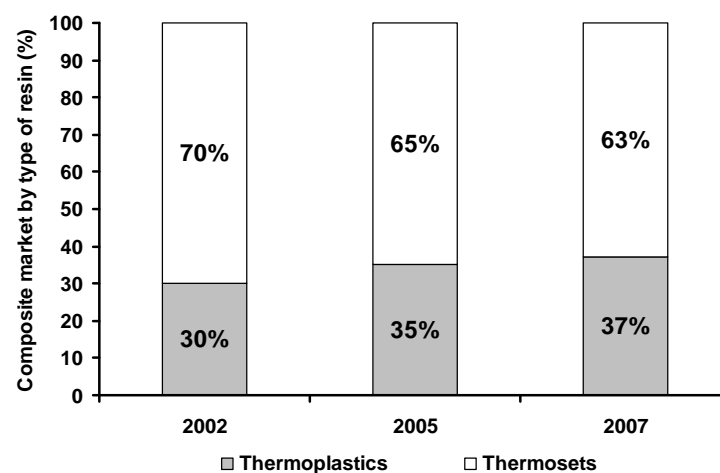


Figure 9.1: Global composite market share by type of resin (in volume) (adapted from [4]).

9.4.2 Blade recycling and the fear of legislation

Worldwide wind energy calls for tenders are starting to include strict measures regarding decommissioning, forcing turbine manufacturers to find sustainable ways to dispose of used turbines. Strict waste disposal policies could eventually limit the use of thermosetting resins in blade structures since they are more difficult to recycle than thermoplastic composites. If this happens (and it might be soon), a certain time frame is generally established for the technology switch to occur in order to allow the industry to absorb the shock. The chances of successful survival of these “forced” technology switches are usually directly proportional to the time previously spent by companies in developing the new technology. As mentioned earlier, one approach the wind energy

industry could use in order to prepare gradually for such a technology switch would be first to use thermoplastic composites for secondary structures (while continuing to make box spars out of thermoset composites). Introducing the new materials first as non-structural components (skins and ribs) in wind turbine blade structures could help manufacturers gain experience at minimal risk.

9.4.3 TPC structural design benefits

Research in load mitigation techniques through active control devices such as flaps, tabs or other aerodynamic surfaces is starting to show that wind turbine blade life could be extended significantly if blades were equipped with such devices [6-8]. Because small thermoplastic composite parts can be processed significantly faster than thermoset composite parts, and since thermoplastics are commonly used as flexure hinges, thermoplastic composites should facilitate easier low-cost integration of these devices compared to thermoset-based composites. Apart from minimizing airfoil distortion (earlier discussed), ribs could also serve as anchorage points for these devices.

Finally, as mentioned in chapter 3, TPC structures are generally welded. Since this joining method is generally reversible (depending on the welding technique used), blade disassembly for recycling could be facilitated when TPC composites are used.

9.5 Recommendations for future work

Due to the multidisciplinary nature of the work presented in this thesis, recommendations for future work are grouped with respect to manufacturing, material, design and cost issues.

9.5.1 Manufacturing issues

In order to use APA-6 infusion for parts larger than the 30 x 30 cm panels produced for this thesis, a significant research effort will be needed. Since the APA-6 composite properties are highly dependent on cure temperature, temperature control was identified as one of the key parameters to control in order to produce high quality laminates. Although laminates up to 2.5cm thick were cured successfully in the context of this work, due to the exothermic nature of the resin system, large variations in cure temperatures are expected when infusing parts with significant laminate thickness

variations, such as in wind turbine blade skins. Consequently, very versatile mold-heating systems will be needed when infusing large APA-6 composite parts.

Although part assembly was not examined in this thesis because blade design only reached the preliminary design stage, welding was identified as the most probable technique to be used for part assembly. While this process is well understood for relatively thin composite parts to be joined, welding of thick laminates remains scientifically unexplored. Welding lengths and part mismatch are expected to be the main aspects to investigate.

9.5.2 *Material issues*

As mentioned in chapter 4, moisture resistance and void reduction were identified as the two most important aspects with regard to improving the static and fatigue properties of APA-6 composites. Ongoing research at the Design and Production of Composite Structures group is focusing on these issues by increasing the crystallinity of APA-6 and improving the fiber/matrix interface. New resin formulations are currently being tested and infusion equipment has been upgraded to limit the presence of dissolved nitrogen (used to protect the resin system from the atmosphere), which contributes to void formation.

9.5.3 *Structural design issues*

For preliminary design purposes, linear analysis is commonly used. In the course of this work, since the study was done on a comparison basis between designs, linear analysis is believed to have led to defensible conclusions although measured deformations were large. Nevertheless, non-linear analysis will be necessary in order to treat issues such as Brazier loads, delamination, post-buckling behavior, crack growth and other important local failure mechanisms that may lead to ultimate blade failure.

Fatigue loads are of primary importance for wind turbine blade design. This was taken into account indirectly in the preliminary design process presented in this thesis by simply applying the most severe material safety factor of the IEC-61400-1 standard. A more realistic way to take fatigue loads into account could be to evaluate the mean and amplitude stresses in different fatigue critical zones of the blade. With these local fatigue stress spectra, specific fatigue limits could be evaluated using constant life diagrams and incorporated into the FE model to calculate failure indexes.

As mentioned in chapter 3, TPC are generally produced with fast non-isothermal melt processes. Up to now, using thick core material in TPC structures is not common practice. An alternative way possibly better suited for TPC processing would be to use stringers or corrugated panels instead of sandwich structures to control buckling. Based on the results of exploratory work performed in the course of this thesis [9] corrugated panels were shown to hold 10-15% more compressive load than conventional constant-thickness sandwich panels. Further investigation of TPC-oriented design solutions for controlling buckling on compression-loaded panels is therefore recommended for future work.

9.5.4 Cost analysis

Although standard high-temperature epoxy tooling could still be used to process APA-6 composites, an increase in tooling cost is to be expected due to the reduced life of the molds (aggressive thermal cycling) and the more elaborate heating system needed. It was argued in chapter 4 that this increase in cost could be compensated by a faster cycle time (faster infusion, polymerization and assembly methods) and significantly lower resin cost.

To validate the cost effectiveness of the TPC blade design proposed in this thesis, a thorough cost analysis will be required. Ideally, cost issues should be taken into account early in the design process. In this context, the preliminary design objective function (Equation 8.1) could be modified to incorporate a cost function that would influence the outcome of the optimization process.

9.6 References

- [1] Mandell, J., Samborsky, D.D., Cairns, D.S., *Fatigue of Composite Materials and Substructures for Wind Turbine Blades*, Technical Report No. SAND2002-0771, Sandia National Laboratories, Albuquerque, NM.
- [2] Jensen, F.M., *Ultimate strength of a large wind turbine blade*, PhD dissertation, Risø National Laboratory for sustainable Energy – Technical University of Denmark, Roskilde, Denmark, 2008.
- [3] Jensen, F.M., Falzon, B.G., Ankersen, J., Stang, H., *Structural testing and numerical simulation of a 34m composite wind turbine blade*, Composite Structures, Vol. 76, 2006, pp. 52-61.
- [4] JEC Composites, Global Market Scenario Dynamic of the Composites Industry – 2009 Release. Strategic Studies, 2009.
- [5] van Rijswijk, K., *Thermoplastic Composite Wind Turbine Blades – Vacuum Infusion Technology for Anionic Polyamide-6 Composites*. PhD dissertation, Delft University of Technology, Delft, 2007.
- [6] van Wingerden, J. W., Hulskamp, A. W., Barlas, T., Marrant, B., van Kuik, G. A. M., Molenaar, D.-P., Verhaegen, M., *On the Proof of Concept of a ‘Smart’ Wind Turbine Rotor Blade for Load Alleviation*, Wind Energy, 2008; 11:265–280.
- [7] Buhl, T., Gaunaa, M., Bak, C., *Potential of load reduction using airfoils with variable trailing edge geometry*, Journal of Solar Energy Engineering 2005; 127: 503–516.
- [8] Yen Nakafuji, D. T. Van dam, C.P. Michel, J., Morrison, P., *Load Control for Turbine Blades: A Non-Traditional Microtab Approach*, ASME Wind Energy Symposium, Reno, Nevada, January 2002, AIAA 2002-0054
- [9] Joncas S., Lemay, J., Bergsma, O.K., Bersee, H.E.N., Beukers, A., *Topography Optimization for Maximum Buckling Loads of Wind Turbine Blade Sandwich Panels*, 15th International Conference on Composite Materials (ICCM-15), Durban, South Africa, June 2005.

APPENDIX A

AERODYNAMIC ANALYSIS TOOLS COMPARISON AGAINST AERODYN RESULTS

This appendix presents the results of a comparison study done to validate the aerodynamic analysis tool coded for this thesis (see chapter 5). Based on the blade geometry presented in Table 6.1, induction factors, in-plane forces and out-of-plane forces were computed at each blade station and compared with results obtained from a well know commercial code (Aerodyn). Both codes used the same wind turbine condition: RPM=11.5, wind speed=12m/s (no wind shear), pitch angle= 0.919° . As seen on Figure A1 to Figure A4, results found with the method described in chapter 5 show good agreement with the results found with Aerodyn for chord stations between $r=15\text{m}$ and blade tip.

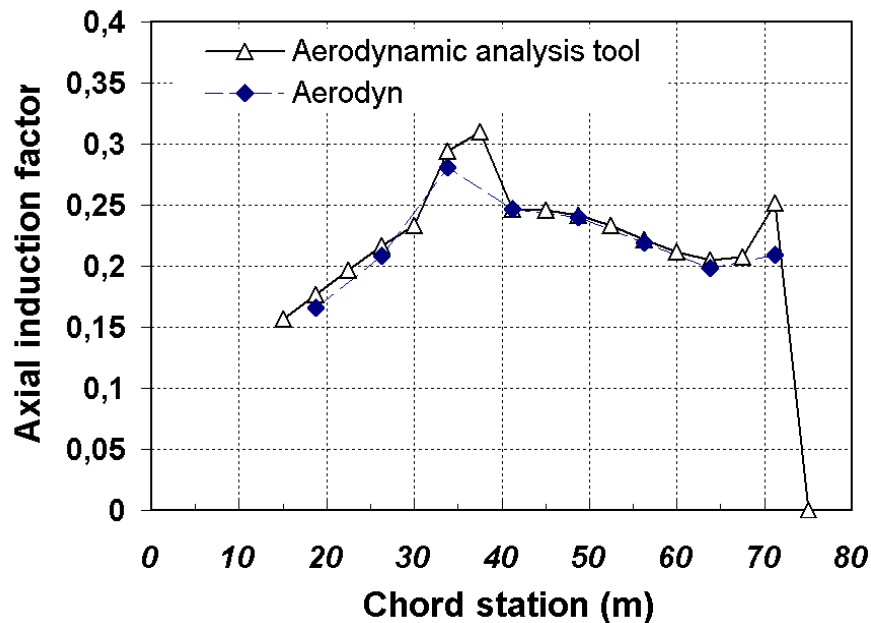


Figure A.1. Axial induction factors with respect to blade length – A comparison against Aerodyn.

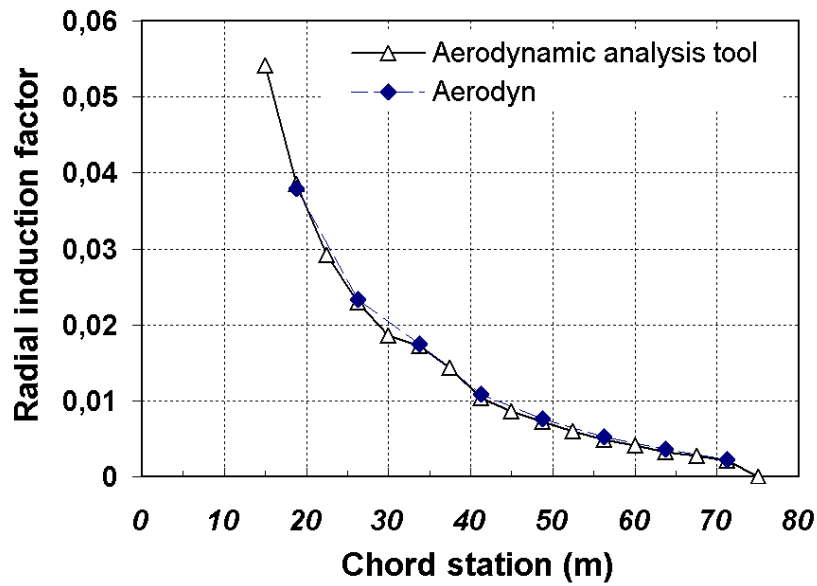


Figure A.2. Radial induction factors with respect to blade length – A comparison against Aerodyn.

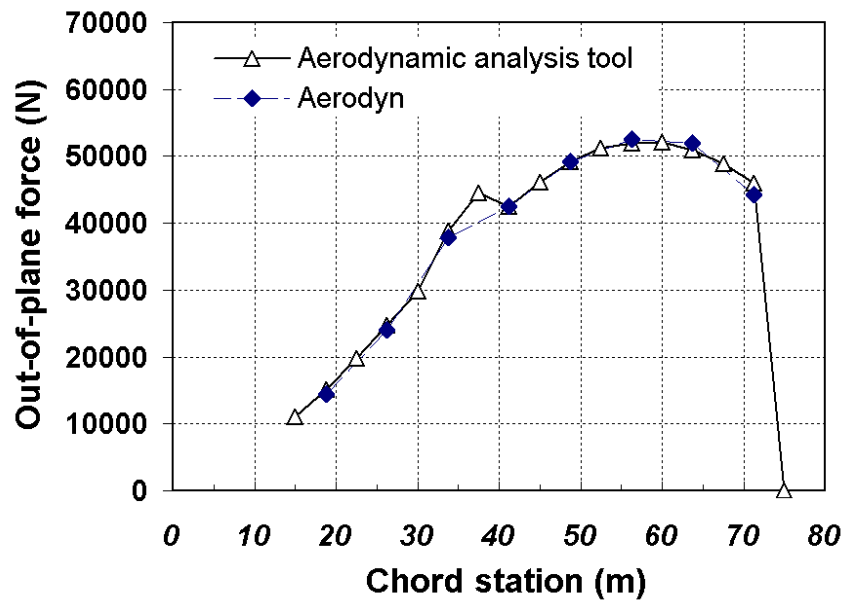


Figure A.3. Local out-of-plane force at each blade station ($dr=7.5m$) – A comparison against Aerodyn.

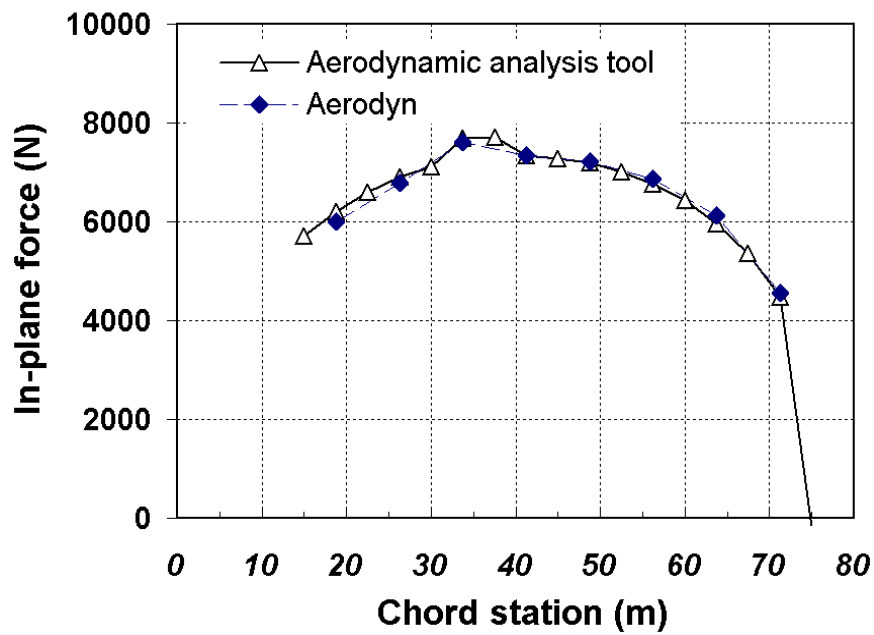


Figure A.4. Local in-plane force generated at each blade station (dr=7.5m) – A comparison against Aerodyn.

APPENDIX B

STRUCTURAL ANALYSIS TOOLS *COMPARISON AGAINST A FINITE ELEMENT MODEL*

This appendix presents the results of a comparison study done to validate some aspects of the structural analysis tool coded for this thesis (see chapter 5). The structural lay-out of the blade used for comparison consists of a load bearing box spar section with webs positioned at 15% and 50% of chord length, covered by two thin skins (see figure of Table 6.3). Typical large wind turbine blade laminate stacking sequences were used for all three components (spar caps, webs and skins). For both the webs and skins, a laminate of 50% 0° and 50% $\pm 45^\circ$ fibers was used. In the spar cap, the laminate was composed of 0° and $\pm 45^\circ$ fibers, occupying respectively 70% and 30% of the volume. Based on the blade geometry presented in Table 6.1, using the blade construction details presented in Table 6.4 and using the material properties shown in Table 6.2 and 6.3, a finite element model was built. The nodes at blade root contour were fixed to simulate the root connection and the same aerodynamic loading as the one used in the analytical tool coded for this thesis (50 year extreme gust) was applied to the FE model using pressure load.

As explained in chapter 6, laminate thicknesses were determined with the structural analytical tool presented in chapter 5 in order to limit stress to the values presented in Table 6.3. Therefore, when using the same blade construction details in a shell FE model, similar stress levels should be found. As shown in Figures B.1 and Figure B.2, the analysis demonstrated that similar stress levels can be found with a FE model. Of course, since constant thickness laminates are used for the different blade sections, maximum stress is always reached at the transition areas between sections. In the FE analysis, the sudden change in laminate thickness results in a local stress concentration. This phenomenon can of course not be modeled with the structural analysis tools presented in chapter 5. Nevertheless, the fact that the average stress levels are very similar to values presented in Table 6.3 proves that the analytical tool presented in chapter 5 is able to predict laminate thickness when constrained by stress limits.

When comparing blade deformation, tip deflection calculated with the analytical tools developed in chapter 5 correlates relatively well with the linear analysis performed on the FE model. Figure B.3 shows that blade tip deflection reaches 18.2m while the analytical tools coded for this thesis estimated a tip deflection of 16.4m.

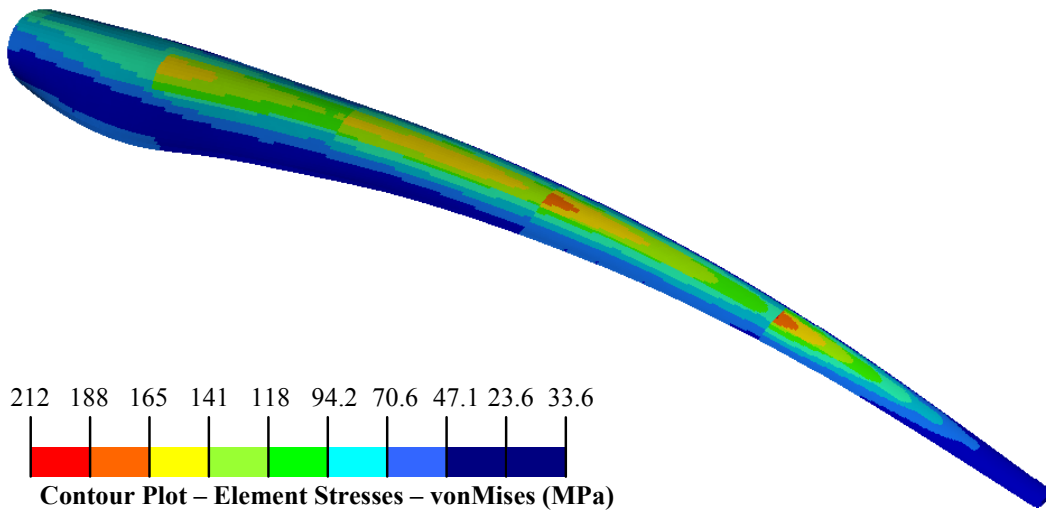


Figure B.1. Blade upper surface von Mises stresses contour plot

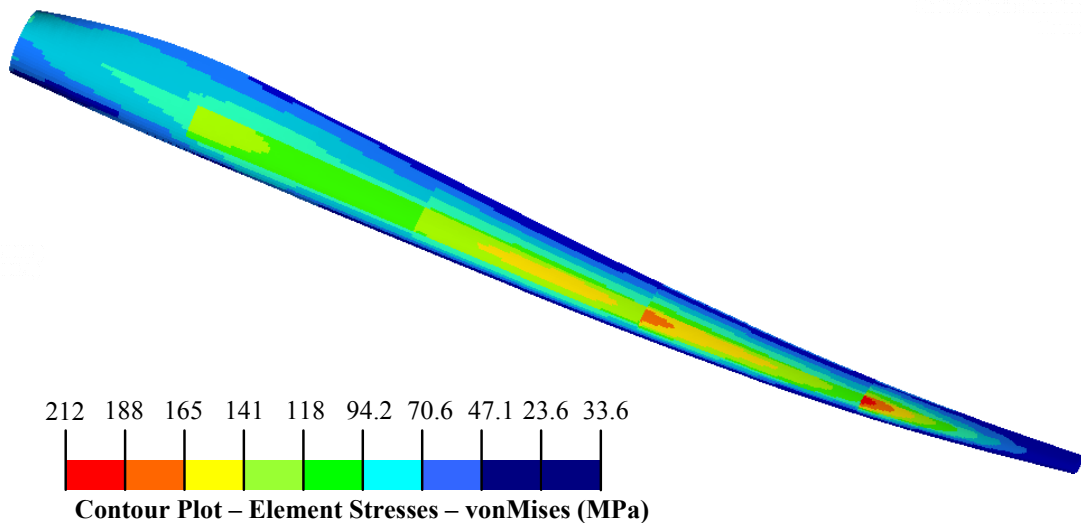


Figure B.2. Blade lower surface von Mises stresses contour plot

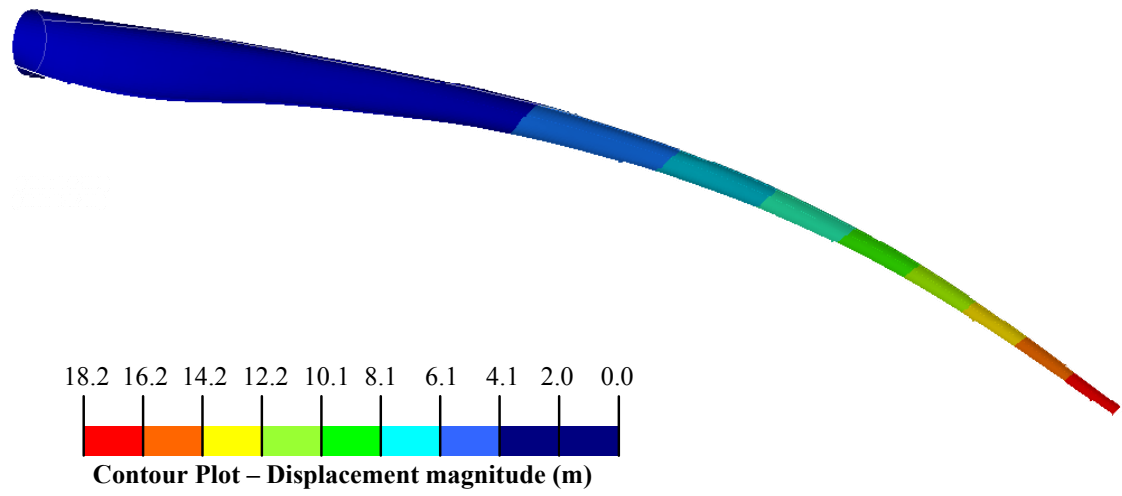


Figure B.3. Blade contour plot for element displacement (out-of-plane)

APPENDIX C

COMPOSITE SIZE OPTIMIZATION RESULTS

This appendix presents the complete laminate details for optimized PA-6/glass one web and two web blade designs subjected to stiffness, strength and buckling constraints. For comparison purposes, the baseline epoxy-based blades are also shown. The results are presented with respect to lengthwise blade sections (see Figure 8.1 for details).

Table C.1. Element total thickness, 0° fibre fraction and core thickness for blade sections extending from 3.75 to 15 m - Optimized PA-6/glass one web and two web blade designs subjected to stiffness, strength and buckling constraints.

Blade section	PA-6/glass blades						Epoxy/glass blades	
	2 webs 0 rib	2 webs 35 ribs	2 webs 70 ribs	1 web 0 rib	1 web 35 ribs	1 web 70 ribs	2 webs 0 rib	1 web 0 rib
Upper surface	6.0 mm	4.4 mm	4.9 mm	8.7 mm	5.8 mm	8.6 mm	5.2 mm	8.0 mm
leading edge	73.9 %	40.6 %	26.1 %	80.0 %	33.6 %	30.1 %	82.9 %	81.0 %
skin	7.9 mm	10.3 mm	12.2 mm	13.3 mm	14.0 mm	12.7 mm	10.3 mm	19.4 mm
Upper surface	63.2 mm	64.4 mm	59.2 mm	66.9 mm	63.1 mm	63.3 mm	61.6 mm	58.7 mm
spar cap	94.5 %	92.5 %	92.9 %	92.4 %	94.0 %	85.6 %	96.9 %	94.7 %
	37.7 mm	10.0 mm	8.2 mm	20.8 mm	13.6 mm	7.2 mm	27.4 mm	20.6 mm
Upper surface	6.2 mm	6.7 mm	10.1 mm	10.4 mm	10.8 mm	14.7 mm	5.1 mm	9.2 mm
trailing edge	66.2 %	47.0 %	68.7 %	52.9 %	68.9 %	57.6 %	73.1 %	67.4 %
skin	47.9 mm	39.6 mm	25.6 mm	60.4 mm	55.2 mm	19.7 mm	47.7 mm	56.0 mm
Lower surface	13.9 mm	21.3 mm	15.2 mm	24.9 mm	20.0 mm	16.5 mm	12.9 mm	17.7 mm
leading edge	86.8 %	90.7 %	91.5 %	94.5 %	89.3 %	81.8 %	91.3 %	87.4 %
skin	9.8 mm	3.3 mm	3.0 mm	20.9 mm	3.4 mm	3.2 mm	9.6 mm	37.3 mm
Lower surface	50.9 mm	43.7 mm	50.3 mm	42.2 mm	45.1 mm	49.1 mm	47.6 mm	46.8 mm
spar cap	94.7 %	96.4 %	98.7 %	96.1 %	96.7 %	94.6 %	96.2 %	95.0 %
	13.4 mm	5.2 mm	5.8 mm	29.2 mm	5.6 mm	6.8 mm	10.1 mm	18.0 mm
Lower surface	3.8 mm	2.8 mm	1.5 mm	4.0 mm	4.2 mm	3.2 mm	2.7 mm	5.2 mm
trailing edge	62.4 %	76.5 %	67.6 %	60.3 %	75.1 %	69.4 %	74.9 %	71.3 %
skin	11.4 mm	10.3 mm	8.5 mm	7.0 mm	7.6 mm	7.0 mm	12.2 mm	11.4 mm
Middle	0.0 mm	0.0 mm	0.0 mm	17.0 mm	9.2 mm	8.8 mm	0.0 mm	15.3 mm
(single) web	0.0 %	0.0 %	0.0 %	43.0 %	27.0 %	32.5 %	0.0 %	66.2 %
	0.0 mm	0.0 mm	0.0 mm	63.6 mm	20.3 mm	14.3 mm	0.0 mm	20.7 mm
Trailing edge	5.7 mm	6.1 mm	5.9 mm	0.0 mm	0.0 mm	0.0 mm	7.1 mm	0.0 mm
web	36.2 %	37.0 %	39.1 %	0.0 %	0.0 %	0.0 %	58.0 %	0.0 %
	14.8 mm	7.4 mm	6.8 mm	0.0 mm	0.0 mm	0.0 mm	18.5 mm	0.0 mm
Leading edge	13.6 mm	6.3 mm	7.4 mm	0.0 mm	0.0 mm	0.0 mm	11.3 mm	0.0 mm
web	66.2 %	46.7 %	36.8 %	0.0 %	0.0 %	0.0 %	72.0 %	0.0 %
	4.3 mm	8.9 mm	5.4 mm	0.0 mm	0.0 mm	0.0 mm	7.9 mm	0.0 mm

Table C.2. Element total thickness, 0° fibre fraction and core thickness for blade sections extending from 15 to 30 m - Optimized PA-6/glass one web and two web blade designs subjected to stiffness, strength and buckling constraints.

Blade section	PA-6/glass blades						Epoxy/glass blades	
	2 webs 0 rib	2 webs 35 ribs	2 webs 70 ribs	1 web 0 rib	1 web 35 ribs	1 web 70 ribs	2 webs 0 rib	1 web 0 rib
Upper surface	6.0 mm	3.2 mm	2.3 mm	8.2 mm	2.0 mm	3.8 mm	2.8 mm	6.6 mm
leading edge	72.7 %	48.7 %	27.1 %	66.6 %	49.5 %	42.1 %	68.7 %	69.4 %
skin	8.0 mm	7.8 mm	8.8 mm	13.3 mm	8.1 mm	7.8 mm	6.6 mm	18.0 mm
Upper surface	74.8 mm	77.1 mm	74.3 mm	82.0 mm	77.9 mm	76.2 mm	73.7 mm	73.2 mm
spar cap	96.6 %	95.0 %	95.8 %	93.9 %	94.3 %	86.6 %	98.0 %	96.1 %
	13.0 mm	7.2 mm	7.5 mm	15.7 mm	14.3 mm	7.7 mm	7.6 mm	15.8 mm
Upper surface	5.3 mm	11.1 mm	12.0 mm	6.8 mm	7.8 mm	13.0 mm	4.1 mm	4.2 mm
trailing edge	59.9 %	26.7 %	52.2 %	25.0 %	22.9 %	55.7 %	66.4 %	51.9 %
skin	48.1 mm	25.8 mm	17.8 mm	45.5 mm	33.5 mm	17.4 mm	48.5 mm	62.7 mm
Lower surface	7.7 mm	11.7 mm	7.5 mm	10.5 mm	9.7 mm	12.3 mm	5.2 mm	6.8 mm
leading edge	64.7 %	81.2 %	66.4 %	76.6 %	78.2 %	67.7 %	76.0 %	68.3 %
skin	16.2 mm	6.8 mm	6.6 mm	17.0 mm	6.2 mm	7.4 mm	8.7 mm	19.8 mm
Lower surface	72.8 mm	69.6 mm	66.9 mm	66.6 mm	68.3 mm	69.1 mm	69.7 mm	67.3 mm
spar cap	96.5 %	96.7 %	97.5 %	98.0 %	97.6 %	95.9 %	97.4 %	96.9 %
	10.4 mm	5.7 mm	5.3 mm	7.1 mm	5.3 mm	6.5 mm	5.4 mm	9.7 mm
Lower surface	2.9 mm	2.5 mm	1.6 mm	3.1 mm	3.2 mm	4.3 mm	2.1 mm	2.4 mm
trailing edge	68.6 %	73.0 %	58.0 %	82.6 %	62.3 %	55.0 %	73.5 %	68.8 %
skin	10.9 mm	9.1 mm	8.9 mm	13.1 mm	14.6 mm	6.3 mm	11.0 mm	16.0 mm
Middle	0.0 mm	0.0 mm	0.0 mm	13.0 mm	9.4 mm	5.3 mm	0.0 mm	18.3 mm
(single) web	0.0 %	0.0 %	0.0 %	51.0 %	74.5 %	55.5 %	0.0 %	92.7 %
	0.0 mm	0.0 mm	0.0 mm	29.3 mm	21.3 mm	11.0 mm	0.0 mm	4.7 mm
Trailing edge	5.4 mm	4.3 mm	3.9 mm	0.0 mm	0.0 mm	0.0 mm	6.0 mm	0.0 mm
web	35.7 %	46.3 %	63.5 %	0.0 %	0.0 %	0.0 %	37.9 %	0.0 %
	16.2 mm	13.8 mm	10.9 mm	0.0 mm	0.0 mm	0.0 mm	19.6 mm	0.0 mm
Leading edge	9.5 mm	4.4 mm	3.7 mm	0.0 mm	0.0 mm	0.0 mm	8.3 mm	0.0 mm
web	87.5 %	72.2 %	59.7 %	0.0 %	0.0 %	0.0 %	92.7 %	0.0 %
	8.3 mm	13.9 mm	10.7 mm	0.0 mm	0.0 mm	0.0 mm	7.8 mm	0.0 mm

Table C.3. Element total thickness, 0° fibre fraction and core thickness for blade sections extending from 30 to 45 m - Optimized PA-6/glass one web and two web blade designs subjected to stiffness, strength and buckling constraints.

Blade section	PA-6/glass blades						Epoxy/glass blades	
	2 webs 0 rib	2 webs 35 ribs	2 webs 70 ribs	1 web 0 rib	1 web 35 ribs	1 web 70 ribs	2 webs 0 rib	1 web 0 rib
Upper surface	4.1 mm	2.6 mm	2.3 mm	3.3 mm	3.2 mm	4.2 mm	2.4 mm	4.0 mm
leading edge	55.6 %	53.0 %	55.4 %	46.6 %	54.1 %	53.5 %	58.7 %	57.3 %
skin	8.2 mm	7.1 mm	7.2 mm	9.6 mm	7.3 mm	8.1 mm	6.1 mm	7.9 mm
Upper surface	88.0 mm	88.0 mm	87.9 mm	87.7 mm	85.6 mm	89.6 mm	83.5 mm	82.3 mm
spar cap	96.9 %	97.3 %	96.9 %	97.3 %	97.8 %	95.6 %	97.7 %	97.3 %
	7.6 mm	6.6 mm	6.8 mm	10.3 mm	7.1 mm	8.1 mm	5.6 mm	7.4 mm
Upper surface	4.7 mm	2.4 mm	3.0 mm	3.6 mm	4.2 mm	5.3 mm	2.6 mm	3.1 mm
trailing edge	40.6 %	22.7 %	16.0 %	37.3 %	15.5 %	26.8 %	49.6 %	63.6 %
skin	20.4 mm	19.2 mm	15.4 mm	24.5 mm	14.5 mm	12.4 mm	23.9 mm	25.5 mm
Lower surface	5.7 mm	4.5 mm	5.5 mm	3.8 mm	5.1 mm	10.2 mm	3.5 mm	4.4 mm
leading edge	63.7 %	62.9 %	61.7 %	61.1 %	65.6 %	71.8 %	68.1 %	59.6 %
skin	8.2 mm	7.1 mm	7.3 mm	7.0 mm	7.4 mm	8.1 mm	6.1 mm	7.7 mm
Lower surface	84.8 mm	84.5 mm	83.9 mm	80.3 mm	82.8 mm	80.4 mm	82.9 mm	80.7 mm
spar cap	96.8 %	97.3 %	98.0 %	98.1 %	97.6 %	95.5 %	97.0 %	97.3 %
	7.5 mm	6.4 mm	6.7 mm	5.9 mm	6.9 mm	7.8 mm	5.0 mm	7.1 mm
Lower surface	2.4 mm	1.5 mm	0.8 mm	2.1 mm	1.6 mm	1.5 mm	2.5 mm	2.2 mm
trailing edge	58.1 %	60.8 %	72.2 %	75.5 %	76.5 %	68.2 %	62.3 %	61.5 %
skin	8.0 mm	8.3 mm	7.5 mm	12.6 mm	13.3 mm	8.9 mm	7.6 mm	10.6 mm
Middle	0.0 mm	0.0 mm	0.0 mm	4.2 mm	3.9 mm	3.5 mm	0.0 mm	4.6 mm
(single) web	0.0 %	0.0 %	0.0 %	46.6 %	66.6 %	71.1 %	0.0 %	57.3 %
	0.0 mm	0.0 mm	0.0 mm	9.0 mm	8.9 mm	7.8 mm	0.0 mm	8.5 mm
Trailing edge	3.1 mm	2.9 mm	3.3 mm	0.0 mm	0.0 mm	0.0 mm	3.4 mm	0.0 mm
web	62.9 %	65.8 %	68.1 %	0.0 %	0.0 %	0.0 %	49.6 %	0.0 %
	8.7 mm	8.8 mm	7.8 mm	0.0 mm	0.0 mm	0.0 mm	7.2 mm	0.0 mm
Leading edge	3.6 mm	2.6 mm	3.2 mm	0.0 mm	0.0 mm	0.0 mm	2.0 mm	0.0 mm
web	55.2 %	57.4 %	51.9 %	0.0 %	0.0 %	0.0 %	54.9 %	0.0 %
	8.4 mm	6.9 mm	7.2 mm	0.0 mm	0.0 mm	0.0 mm	7.0 mm	0.0 mm

Table C.4. Element total thickness, 0° fibre fraction and core thickness for blade sections extending from 45 to 60 m - Optimized PA-6/glass one web and two web blade designs subjected to stiffness, strength and buckling constraints.

Blade section	PA-6/glass blades						Epoxy/glass blades	
	2 webs 0 rib	2 webs 35 ribs	2 webs 70 ribs	1 web 0 rib	1 web 35 ribs	1 web 70 ribs	2 webs 0 rib	1 web 0 rib
Upper surface	5.1 mm	3.9 mm	4.0 mm	2.8 mm	4.1 mm	6.4 mm	2.7 mm	4.5 mm
leading edge	56.8 %	58.4 %	56.8 %	53.2 %	56.6 %	57.2 %	58.7 %	56.5 %
skin	8.5 mm	7.7 mm	7.9 mm	9.3 mm	8.0 mm	8.7 mm	6.7 mm	8.4 mm
Upper surface	87.8 mm	86.9 mm	86.9 mm	82.4 mm	85.4 mm	86.9 mm	84.3 mm	82.1 mm
spar cap	96.0 %	97.1 %	97.4 %	97.5 %	97.1 %	95.3 %	96.8 %	96.4 %
	9.1 mm	8.5 mm	8.7 mm	9.5 mm	9.1 mm	10.5 mm	7.3 mm	8.8 mm
Upper surface	3.2 mm	2.1 mm	2.1 mm	3.5 mm	3.1 mm	3.5 mm	3.1 mm	3.5 mm
trailing edge	55.6 %	53.0 %	49.9 %	42.9 %	50.2 %	57.2 %	56.9 %	61.3 %
skin	15.4 mm	14.8 mm	12.4 mm	21.1 mm	16.7 mm	14.1 mm	13.3 mm	20.5 mm
Lower surface	6.3 mm	4.7 mm	4.8 mm	3.9 mm	5.6 mm	9.0 mm	4.1 mm	5.5 mm
leading edge	61.3 %	61.0 %	59.0 %	62.7 %	61.7 %	63.4 %	68.2 %	60.4 %
skin	8.6 mm	7.8 mm	8.1 mm	7.6 mm	8.1 mm	8.8 mm	6.9 mm	8.4 mm
Lower surface	83.7 mm	85.1 mm	85.4 mm	81.3 mm	82.9 mm	84.8 mm	83.1 mm	81.4 mm
spar cap	95.7 %	97.0 %	97.4 %	97.6 %	96.8 %	94.1 %	96.4 %	96.3 %
	9.0 mm	8.6 mm	8.8 mm	7.4 mm	8.8 mm	10.2 mm	7.1 mm	8.7 mm
Lower surface	3.1 mm	2.1 mm	1.9 mm	2.3 mm	2.5 mm	3.1 mm	2.6 mm	2.4 mm
trailing edge	64.7 %	66.5 %	63.5 %	78.3 %	75.9 %	70.7 %	71.2 %	65.1 %
skin	8.1 mm	5.8 mm	5.8 mm	11.9 mm	9.5 mm	7.0 mm	8.3 mm	9.5 mm
Middle	0.0 mm	0.0 mm	0.0 mm	4.3 mm	6.0 mm	6.7 mm	0.0 mm	4.6 mm
(single) web	0.0 %	0.0 %	0.0 %	48.6 %	44.9 %	57.1 %	0.0 %	55.9 %
	0.0 mm	0.0 mm	0.0 mm	8.2 mm	7.8 mm	8.4 mm	0.0 mm	8.1 mm
Trailing edge	4.2 mm	3.4 mm	3.9 mm	0.0 mm	0.0 mm	0.0 mm	3.4 mm	0.0 mm
web	55.8 %	58.5 %	54.3 %	0.0 %	0.0 %	0.0 %	45.3 %	0.0 %
	8.6 mm	7.7 mm	7.9 mm	0.0 mm	0.0 mm	0.0 mm	6.5 mm	0.0 mm
Leading edge	4.3 mm	3.8 mm	4.0 mm	0.0 mm	0.0 mm	0.0 mm	2.8 mm	0.0 mm
web	51.8 %	51.3 %	51.9 %	0.0 %	0.0 %	0.0 %	49.4 %	0.0 %
	8.7 mm	7.9 mm	8.1 mm	0.0 mm	0.0 mm	0.0 mm	7.0 mm	0.0 mm

Table C.5. Element total thickness, 0° fibre fraction and core thickness for blade sections extending from 60 to 75 m - Optimized PA-6/glass one web and two web blade designs subjected to stiffness, strength and buckling constraints.

Blade section	PA-6/glass blades						Epoxy/glass blades	
	2 webs 0 rib	2 webs 35 ribs	2 webs 70 ribs	1 web 0 rib	1 web 35 ribs	1 web 70 ribs	2 webs 0 rib	1 web 0 rib
Upper surface	4.2 mm	3.7 mm	3.9 mm	2.9 mm	4.3 mm	5.8 mm	2.5 mm	4.0 mm
leading edge	53.8 %	55.8 %	55.5 %	54.6 %	56.3 %	57.9 %	53.2 %	53.8 %
skin	9.0 mm	8.4 mm	8.6 mm	8.1 mm	8.7 mm	9.2 mm	7.7 mm	8.8 mm
Upper surface	50.9 mm	50.8 mm	50.7 mm	48.6 mm	49.9 mm	50.2 mm	49.4 mm	47.9 mm
spar cap	92.3 %	94.9 %	94.9 %	95.6 %	94.2 %	90.7 %	94.7 %	93.7 %
	9.2 mm	8.7 mm	8.9 mm	8.3 mm	9.1 mm	10.1 mm	7.9 mm	9.0 mm
Upper surface	3.3 mm	2.1 mm	2.2 mm	1.9 mm	2.6 mm	4.0 mm	2.0 mm	2.7 mm
trailing edge	61.4 %	59.0 %	57.5 %	54.5 %	59.5 %	60.5 %	65.1 %	59.3 %
skin	7.7 mm	6.9 mm	6.7 mm	10.5 mm	8.2 mm	7.9 mm	7.9 mm	8.7 mm
Lower surface	5.3 mm	4.9 mm	4.9 mm	4.1 mm	5.6 mm	7.9 mm	3.5 mm	5.0 mm
leading edge	59.2 %	61.9 %	59.6 %	62.3 %	61.3 %	61.2 %	61.4 %	59.3 %
skin	9.1 mm	8.6 mm	8.7 mm	8.2 mm	8.8 mm	9.3 mm	7.9 mm	8.9 mm
Lower surface	49.0 mm	49.2 mm	49.6 mm	47.5 mm	48.6 mm	47.6 mm	48.0 mm	46.7 mm
spar cap	92.2 %	94.8 %	94.9 %	95.2 %	94.0 %	90.2 %	94.7 %	93.6 %
	9.3 mm	8.7 mm	9.0 mm	8.1 mm	9.2 mm	10.2 mm	7.9 mm	9.0 mm
Lower surface	3.7 mm	2.6 mm	2.7 mm	2.1 mm	2.8 mm	4.7 mm	2.5 mm	2.9 mm
trailing edge	64.6 %	64.9 %	62.3 %	71.0 %	66.1 %	64.6 %	67.4 %	63.0 %
skin	7.7 mm	6.5 mm	6.8 mm	8.9 mm	7.7 mm	8.0 mm	6.4 mm	7.4 mm
Middle	0.0 mm	0.0 mm	0.0 mm	6.5 mm	7.2 mm	8.5 mm	0.0 mm	6.1 mm
(single) web	0.0 %	0.0 %	0.0 %	35.8 %	45.0 %	52.7 %	0.0 %	51.1 %
	0.0 mm	0.0 mm	0.0 mm	7.9 mm	8.6 mm	9.1 mm	0.0 mm	8.8 mm
Trailing edge	4.9 mm	4.6 mm	4.8 mm	0.0 mm	0.0 mm	0.0 mm	3.5 mm	0.0 mm
web	52.7 %	53.4 %	53.4 %	0.0 %	0.0 %	0.0 %	51.5 %	0.0 %
	9.1 mm	8.4 mm	8.6 mm	0.0 mm	0.0 mm	0.0 mm	7.8 mm	0.0 mm
Leading edge	5.0 mm	4.8 mm	4.9 mm	0.0 mm	0.0 mm	0.0 mm	3.8 mm	0.0 mm
web	48.9 %	48.0 %	48.4 %	0.0 %	0.0 %	0.0 %	47.4 %	0.0 %
	9.2 mm	8.7 mm	8.8 mm	0.0 mm	0.0 mm	0.0 mm	8.1 mm	0.0 mm

ACKNOWLEDGEMENTS

I would first like to thank people of the two institutions where I have spent the last decade. At the École technologie supérieure (Montréal, Canada), thanks to Richard MacDonald, Tony Wong, Claude Olivier, Yves Beauchamp, Paul Gely and numerous other colleagues. You have all been very patient and supportive, either before, during or after my three year stay in the Netherlands. At the Delft University of Technology, thanks to Gijs van Kuik who answered the phone when I first called seeking for a PhD project. Our first discussion triggered a terrific chain of events that led to this PhD. Thanks to Adriaan Beukers and his group for an unforgettable stay at DPCS. Extra special thanks to Harald Bersee. I am very grateful that you took me under your wing at one point and teamed me up with Kjelt. It gave significance to my work and made my two last years at DPCS much more rewarding than the first one.

Related to the work presented in this thesis, I would like to thank Olivier, Jonathan, Karine, Jean-François, Bart and other students who have contributed to the experimental work. Thanks to Fred van Keulen and Marten Jan de Ruiter (Structural Optimization and Computational Mechanical Group, TUDelft) and to Louis-Charles Forcier for their contribution to the structural design optimization work. Finally, thanks to all members of the technical staff of DPCS (Sebastiaan, Hans, Niels, Berthil, François, Serge and all the others) and non-technical staff (special thanks to Lisette: thanks for taking good care of all these Québec kids!). Completing the thesis would have not been possible without the help of Julie, Teun and François (Dutch translation), Tahira (my Beadle's office representative!), Jon, and Alexis (cover page) and others that I might miss.

On a personal level, thanks to Darko, Kjelt, Tahira, Patricia, Giovanni, Sebastiaan, Valeria, Witchuda, Paolo, Rogier, Kyle, and others "Delft friends" that I am forgetting for the fantastic time spent in the Netherlands. A special thought goes to Darko and Kjelt with whom I was lucky enough to build a friendship that survived after I left Delft. Thanks to all my hometown friends and family members. Your support and understanding helped me go the distance!

Last but not least, my love goes to Estelle. Without your love and support in every step of the way, not even half of this would have been possible.

ABOUT THE AUTHOR

Simon Joncas was born July 27th, 1971, in Montréal, Québec, Canada. After completing a college degree in pure and applied sciences (1988-1991) and a one year technical program in Mechanical Engineering Technology (1991-1992), he was accepted at École de Technologie Supérieure (ETS) (Montréal, Canada) where he completed a degree in Mechanical Engineering (1992-1996). He then pursued a Master's degree at the Mechanical Engineering department of the same institution from 1998 to 2000.

His student years at ETS were marked by his heavy involvement in different engineering projects through which he developed his leadership and design and manufacturing engineering skills. He was team leader of ETS' Human Powered Submarine team from 1993 to 1997 and also team leader of the Helios project (Human Powered Helicopter) during his Master's study.

As from 1996, he was given the chance to lecture difference courses at the Mechanical Engineering department and the Automated Manufacturing department of ETS. This experience confirmed his passion for teaching which eventually led him to be hired as an assistant professor at ETS (2002 to now).

By being supported financially by his institution for a three year period (2003-2006), he was given the opportunity to start a PhD at the Design and Production of Composites Structures (TUDelft, Netherlands). Since his return to ETS in 2006, his time is shared between teaching and pursuing research in fields related to wind energy and composite material and design.

LIST OF PUBLICATIONS

This thesis is based on the following publications:

- 1- Beauchamp, M.A., **Joncas S.**, Bersee, H.E.N., *Vacuum Infused Anionic Polyamide-6 Composites: The Development of a Recycling Strategy*, SAMPE 2010, Seattle, Washington, May 2010.
- 2- Forcier, L-C, **Joncas, S.**, *New Structural Design for Large Wind Turbine Blades Using Structural Optimization Techniques*, 51st AIAA/ASME/ASCE/AHS/ASC Structures, Structural Dynamics, and Materials Conference, Orlando, Florida, April 2010.
- 3- van Rijswijk, K., **Joncas S.**, Malek, O.J.A., Bersee, H.E.N., Beukers, A., *Vacuum Infused Thermoplastic Composites for Wind Turbine Blades*, 27th Riso International Symposium On Material Science, Roskilde, Denmark, September 2006.
- 4- **Joncas S.**, van Rijswijk, K., Thibault-Liboiron, K., Bersee, H.E.N., Beukers, A., *Mechanical Properties of Vacuum Infused Anionic Polyamide-6 Glass-fiber Composites: A Benchmark Study*, 27th SAMPE Europe International Conference and Forum, Paris, France, March 2006.
- 5- **Joncas S.**, van Rijswijk, K., Charron, J.F., Bersee, H.E.N., Beukers, A., *Interfacial Shear Strength Properties of Vacuum-infused Anionic Polyamide-6 Glass-Fiber Composites*, 47th AIAA/ASME/ASCE/AHS/ASC Structures, Structural Dynamics and Materials Conference, Newport, Rhode Island, May 2006.
- 6- van Rijswijk, K., **Joncas, S.**, Bersee, H.E.N., Bergsma, O.K., Beukers, A., *Sustainable Vacuum-Infused Thermoplastic Composites for MW-Size Wind Turbine Blades - Preliminary Design and Manufacturing Issues*, ASME Journal of Solar Energy Engineering, Vol. 127, No. 4, November 2005, p. 570-580.
- 7- van Rijswijk, K., **Joncas S.**, Bersee, H.E.N., Beukers, A., Picken, S.J., *Controlling the Reaction Rate of Anionic Polyamide-6 for Vacuum Infusion of Composite Wind Turbine Blades*, 15th International Conference on Composite Materials (ICCM-15), Durban, South Africa, June 2005.
- 8- **Joncas S.**, Lemay, J., Bergsma, O.K., Bersee, H.E.N., Beukers, A., *Topography Optimization for Maximum Buckling Loads of Wind Turbine Blade Sandwich Panels*, 15th International Conference on Composite Materials (ICCM-15), Durban, South Africa, June 2005.
- 9- van Rijswijk, K., **Joncas, S.**, Bersee, H.E.N., Bergsma, O.K., Beukers, A., *Vacuum Infused Fibre Reinforced Thermoplastic MW Size Wind Turbine Blades: A Cost Effective Solution?*, AIAA/ASME Wind Energy Symposium 2005, Reno, Nevada, January 2005.

- 10- **Joncas S.**, Bergsma O.K., Beukers A., *Power Regulation and Optimization of Offshore Wind Turbines Through Trailing Edge Flaps Control*, AIAA/ASME Wind Energy Symposium, Reno, Nevada, January 2005.
- 11- **Joncas, S.**, de Ruiter, M.J., van Keulen, F., *Preliminary Design of Large Wind Turbine Blades using Layout Optimization Techniques*, 10th AIAA/ISSMO Multidisciplinary Analysis and Optimization Conference, Albany, New York, August 2004.

NOMENCLATURE

Abbreviations

AFP	automated fiber placement
ATL	automated tape laying
APA-6	anionic polyamide-6
ASTM	American Society for Testing and Materials
BEM	blade element-momentum
CLT	classic lamination theory
CSM	chopped strand mat
DAM	dry-as-molded
DPCS	Design and Production of Composite Structures
DOC	degree of conversion
DSC	differential scanning calorimetry
DUWIND	Delft University Wind Energy Research Institute
DWT	Danish Wind Technology
EOG50(N)	50 year recurrence extreme direction change (negative)
EOG50(P)	50 year recurrence extreme direction change (positive)
EPFL	École Polytechnique Fédérale de Lausanne
EU	European Union
EWM	extreme wind speed model
EWS(HN)	extreme wind shear (horizontal negative)
EWS(HP)	extreme wind shear (horizontal positive)
EWS(V)	extreme wind shear (vertical)
FE	finite element
FRP	fiber reinforced polymer
GFRP	glass fiber reinforced polymer
GMT	glass mat thermoplastic
HPA-6	hydrolytically polymerized polyamide-6
IEA	international Energy Agency
ILSS	interlaminar shear strength
EPFL	École Polytechnique Fédérale de Lausanne
IGCC	integrated gasification combined cycle
LCA	life-cycle analysis
MAN	Maschinenfabrik Augsburg-Nürnberg
MBB	Messerschmidt-Bölkow-Blohm
MIT	Massachusetts Institute of Technology
PA-6	polyamide-6
PA-12	polyamide 12
PA-66	polyamide 66
PBT	polybutylene terephthalate
PEEK	polyetheretherketone
PEI	polyetherimide
PET	polyethylene terephthalate
PMMA	polymethylmetacrylate
PP	polypropylene

PPS	polyphenylene sulfide
RBE	rigid body element
RH	relative humidity
RIM	reaction injection molding
RMC	residual monomer content
RPM	rotation per minute
RTM	resin transfer molding
SCI	structural Composite Industries
SEM	scanning electron microscopy
SIMP	solid Isotropic Material with Penalization
SMC	sheet molding compound
TFT	transverse Filament Tape
TGA	thermal Gravimetric Analyser
TPC	thermoplastic composites
VI	vacuum infusion
WTGS	wind turbine generator system

Greek symbols

α	local slope of the deflection curve [rad]
α_{att}	attack angle [°]
α_i	induced angle of attack [°]
Ω	rotor rotational speed [rot/min]
ΔH_{100}	100% crystalline enthalpy [J/g]
ΔH_m	matrix melting enthalpy [J/g]
σ_{tens}	tensile stress [Pa]
δ_1	deflection at blade element 1 [m]
δ_i	deflection at blade element I [m]
δ_n	deflection at blade element n [m]
δr	blade element width [m]
$\epsilon_{failure}$	strain at failure
ψ	azimuth angle [°]
κ_β	hinge-spring constant [N/m]
λ	tip speed ratio/buckling factor
ω_{NR}	non-rotational natural frequency [rad/s]
ω_R	rotational natural frequency [rad/s]
ρ	density [g/cm ³]
$\rho_{amorphous}$	amorphous phase element density [g/cm ³]
$\rho_{crystal}$	crystalline phase element density [g/cm ³]
ρ_e	element density
ρ_f	fiber density [g/cm ³]
ρ_{M-comp}	measured composite density [g/cm ³]
ρ_r	resin density [g/cm ³]
ρ_{T-comp}	theoretical composite density [g/cm ³]
τ_{12}	principal shear strength [Pa]
v_f	fiber volume content [%]
v_v	void content [%]

Symbols

a	axial induction factor
a'	angular induction factor
c	chord [m]
C	compliance
C_d	drag coefficient
C_l	lift coefficient
C_{max}	maximum chord [m]
C_T	thrust coefficient
C_{T1}	thrust coefficient at $a=1$
C_p	power coefficient
C_w	weighted compliance
dA	specific area [m ²]
dF	elemental force [N]
dQ	elemental torque [Nm]
dr	blade element width [m]
dT	elemental thrust [N]
E_1	longitudinal elastic modulus [Pa]
E_2	transverse elastic modulus [Pa]
EI	flexural rigidity [Nm ²]
E_{tens}	tensile modulus [Pa]
f	load vector [N]
F	failure index/radial force []/[N]
F_{tip}	tip loss factor
F_{root}	root loss factor
G_{12}	in-plane shear modulus [Pa]
I_b	out-of-plane blade mass moment of inertia [kg/m ²]
I	cross-sectional area moment of inertia [m ⁴]
M	bending moment [Nm]
m_r	resin mass percentage [%]
m_f	fiber mass percentage [%]
$m_{monomer}$	monomer mass percentage [%]
$m_{amorphous}$	amorphous phase mass percentage [%]
$m_{crystal}$	crystalline phase mass percentage [%]
K	stiffness matrix
P	power
R	rotor radius [m]
r	radius [m]
S_2^C	transverse compressive strength [Pa]
S_1^C	longitudinal compressive strength [Pa]
S_1^T	longitudinal tensile strength [Pa]
S_2^T	transverse tensile strength [Pa]
S_{12}	in-plane shear strength [Pa]
T	residue
T_m	melt temperature [°C]
$T_{process}$	processing temperature [°C]
T_{pol}	polymerization temperature [°C]

Nomenclature

V	wind speed/shear force/volume [m/s]/[N]/[m ³]
$V_{\text{ini.design}}$	initial design domain volume [m ³]
V_{in}	cut-in wind speed [m/s]
V_{out}	cut-out wind speed [m/s]
w_a	axial induced velocity [m/s]
w_i	weighing factor
W_{comp}	composite weight [g]
W_{disc}	weight of circular sample [g]
W_{monomer}	monomer weight [g]
W_f	fiber weight [g]
w_t	tangential induced velocity [m/s]
X_c	degree of crystallinity

